



University of Udine  
Polytechnic Department of Engineering and Architecture

ADVANCED LATTICE AND POROUS STRUCTURES FOR  
AM PRODUCT OPTIMIZATION

Doctoral dissertation of:

Federico Scalzo

Supervisor:

Prof. Marco Sortino

This dissertation is submitted for the degree of Doctor of  
Philosophy in Industrial and Information Engineering  
XXXII Cycle

2020



*“Truth is ever to be found in simplicity, and not in the multiplicity and confusion of things”*

*Isaac Newton*



# SUMMARY

The present work aims at favoring development of strategies useful for innovative high - performance mechanical components design. One of the most promising but not yet adequately explored strategies to achieve this goal are lattice / porous structures to be used as structural or filler materials to increase performance in terms of stiffness to weight ratio and enhanced vibration damping. To fill this knowledge gap, static and dynamic behavior of SLM-manufactured lattice structures made in AlSi10Mg aluminum alloy and 316L austenitic stainless steel have been thoroughly investigated; in particular, the study allowed to observe the effect of lattice's unit cell geometry and overall size variation on its mechanical properties, focusing on damping performances. Acquired knowledge allowed to develop a versatile methodology that can be applied to assess the mechanical properties of different kinds of lattice / porous structures, facilitating FE models calibration, creation of homogenization methods and mathematical models useful for lattices static and dynamic behavior rapid estimation. The development of an innovative tool for in-process measurement of cutting forces that develop in milling, drilling and grinding, integrating specially designed lattice structures, represents a practical case study useful to assess the feasibility of exploiting lattice structures to enhance mechanical components performances. Transversal expertise gained with respect to the SLM process, design and optimization of mechanical components and lattice structures, allowed to develop and validate an innovative methodology for rapid production of small-sized lattice structures (Patent Pending). An appropriate experimental campaign allowed to identify optimized process parameters, suitable for the production of lattices using the proposed methodology. The proposed method enhances the overall manufacturing process efficiency; moreover, since it allows substantial savings in terms of time and costs it has both scientific and industrial relevance.



# ACKNOWLEDGEMENTS

Un ringraziamento speciale va alla mia famiglia per il supporto e la fiducia incondizionati, fondamentali per il raggiungimento di questo traguardo. Ringrazio i colleghi, che si sono rivelati ottimi compagni di viaggio in grado di rendere meno pesanti le lunghe giornate di lavoro, condividendo idee e pause caffè. Ringrazio tutti i collaboratori con cui ho avuto il piacere di lavorare, in molte occasioni il vostro supporto è stato molto utile per raggiungere in maniera rapida ed efficiente gli obiettivi prefissati. Ringrazio il Prof. Marco Sortino e il Prof. Giovanni Totis per i consigli e il supporto fornito, utili alla realizzazione di questo elaborato.





# CONTENTS

|   |            |
|---|------------|
| <b>SUMMARY</b>  | <b>i</b>   |
| <b>ACKNOWLEDGEMENTS</b>   | <b>iii</b> |
| <b>LIST OF FIGURES</b>  | <b>xi</b>  |
| <b>LIST OF TABLES</b>   | <b>xxi</b> |
| <b>INTRODUCTION</b>   | <b>1</b>   |
| <b>1 AM FOR METALS AND ADVANCED DESIGN AND MANUFACTURING OF MECHANICAL COMPONENTS</b> | <b>5</b>   |
| 1.1 AM processes for metals . . . . .   | 7          |
| 1.1.1 Summary of AM for metals main operations . . . . .                              | 8          |
| 1.1.2 AM for metals main features and applications . . . . .                          | 9          |
| 1.1.3 AM for metals processes classification . . . . .                                | 11         |
| 1.1.4 Laser Sintering - LS . . . . .  | 12         |
| 1.1.5 Laser Metal Deposition - LMD . . . . .  | 15         |
| 1.1.6 Laser Melting - LM . . . . .  | 17         |
| 1.1.7 LM materials and properties . . . . .   | 19         |

---

|          |   |           |
|----------|---|-----------|
| 1.1.8    | LM process parameters . . . . .   | 22        |
| 1.1.9    | Physical phenomena . . . . .  | 26        |
| 1.1.9.1  | Laser-powder interaction and melt pool characteristics . . . . .            | 26        |
| 1.1.9.2  | Powders particles size distribution and morphology . . . . .                | 30        |
| 1.1.9.3  | Thermo-mechanical phenomena and microstructure . . . . .                    | 31        |
| 1.1.9.4  | Mechanical properties and common defects of LM manufactured parts . . . . . | 33        |
| 1.2      | DfAM and structural optimization . . . . .                                  | 35        |
| 1.2.1    | DfAM: exploit the advantages of AM technologies . . . . .                   | 37        |
| 1.2.2    | DfAM: design and manufacturing constraints . . . . .                        | 42        |
| 1.2.3    | DfAM for LM - applications . . . . .  | 47        |
| 1.3      | State of the art on lattice and porous structures . . . . .                 | 51        |
| 1.3.1    | Lattices and porous structures geometries . . . . .                         | 53        |
| 1.3.2    | Manufacturing constraints and mechanical properties . . . . .               | 55        |
| 1.3.3    | Dynamic behaviour of lattice structures . . . . .                           | 60        |
| 1.4      | Conclusions . . . . .   | 64        |
| <b>2</b> | <b>INVESTIGATION ON MECHANICAL PROPERTIES OF LATTICE STRUCTURES</b>         | <b>67</b> |
| 2.1      | AlSi10Mg specimens design and DoE . . . . .                                 | 68        |
| 2.1.1    | Lattice topology, geometry and material selection . . . . .                 | 69        |
| 2.1.2    | Specimens FEA and sizing . . . . .  | 71        |
| 2.2      | AlSi10Mg DoE specimens manufacturing . . . . .                              | 75        |
| 2.2.1    | AlSi10Mg specimens SLM manufacturing . . . . .                              | 75        |

---

|       |  |     |
|-------|--|-----|
| 2.2.2 | AlSi10Mg specimens geometrical measurements . . . . .                      | 77  |
| 2.3   | AlSi10Mg specimens dynamic behaviour assessment . . . . .                  | 79  |
| 2.3.1 | FRF measurement: impact test analysis . . . . .                            | 79  |
| 2.3.2 | Experimental setup and procedures . . . . .                                | 81  |
| 2.3.3 | Data acquisition and analysis . . . . .                                    | 83  |
| 2.3.4 | AlSi10Mg DoE conclusions . . . . .   | 87  |
| 2.4   | Stainless Steel specimens dynamic behaviour assessment . . . . .           | 88  |
| 2.4.1 | Stainless Steel specimens design and DoE . . . . .                         | 88  |
| 2.4.2 | Stainless steel DoE specimens manufacturing . . . . .                      | 90  |
| 2.4.3 | SS 316L specimens geometrical measurements . . . . .                       | 93  |
| 2.4.4 | FRF measurement: experimental setup and procedure . . . . .                | 94  |
| 2.4.5 | Experimental results analysis . . . . .                                    | 98  |
| 2.4.6 | 316L DoE conclusions . . . . .   | 101 |
| 2.5   | Specimens 1D-3D hybrid FEM model . . . . .                                 | 102 |
| 2.6   | Beam-like specimens dynamic behaviour mathematical model . . . . .         | 106 |
| 2.7   | Innovative mini dynamometer for in-process cutting forces data acquisition | 115 |
| 2.7.1 | Dynamometer design and optimization . . . . .                              | 115 |
| 2.7.2 | Core / central plate design . . . . .                                      | 118 |
| 2.7.3 | Static parts and interface with the machine tool . . . . .                 | 119 |
| 2.7.4 | Optimized dynamometer manufacturing and assembly operations .              | 120 |
| 2.7.5 | Optimized dynamometer dynamic identification . . . . .                     | 124 |
| 2.8   | Conclusions . . . . .  | 125 |

|          |   |            |
|----------|---|------------|
| <b>3</b> | <b>METHODOLOGY FOR STATIC AND DYNAMIC LATTICE AND POROUS STRUCTURES PROPERTY ASSESSMENT</b>       | <b>129</b> |
| 3.1      | Specimen design and DoE . . . . .   | 130        |
| 3.1.1    | Lattice type, geometry and material selection . . . . .   | 130        |
| 3.1.2    | Specimens geometry and experimental set-up design . . . . .                                       | 131        |
| 3.1.3    | Selection of factors and levels for 3 <sup>rd</sup> DoE . . . . .                                 | 132        |
| 3.2      | Manufacturing of 3 <sup>rd</sup> DoE . . . . .  | 138        |
| 3.3      | Static and Modal analysis . . . . .   | 141        |
| 3.3.1    | Static analysis experimental setup and measurements . . . . .                                     | 141        |
| 3.3.2    | Modal analysis experimental setup and measurements . . . . .                                      | 143        |
| 3.3.3    | Data analysis and results . . . . .   | 144        |
| 3.4      | Conclusions . . . . .   | 151        |
| <b>4</b> | <b>INNOVATIVE METHODOLOGY FOR FAST SLM MANUFACTURING OF LATTICE AND POROUS STRUCTURES</b>         | <b>153</b> |
| 4.1      | Geometry and process design for lattice and porous structures . . . . .                           | 154        |
| 4.2      | Innovative methodology for design and manufacturing of lattices . . . . .                         | 158        |
| 4.2.1    | Generation of the simplified lattice / porous structure geometry . . . . .                        | 159        |
| 4.2.2    | SLM process design and manufacturing for simplified lattice / porous structure geometry . . . . . | 160        |
| 4.3      | DoE for methodology validation . . . . .  | 163        |
| 4.3.1    | Specimens design . . . . .  | 164        |
| 4.3.2    | DoE factors and levels selection . . . . .  | 164        |
| 4.3.3    | Specimens SLM manufacturing . . . . .   | 165        |

|  |            |
|--|------------|
| <b>CONTENTS</b>  | <b>ix</b>  |
| 4.3.4 Morphological characterization and surface roughness analysis . . .    | 166        |
| 4.3.5 Optimized process parameters . . . . .                                 | 178        |
| 4.4 Conclusions . . . . .  | 182        |
| <b>5 CONCLUSIONS AND FUTURE WORK</b>   | <b>185</b> |
| <b>LIST OF ABBREVIATIONS</b>   | <b>193</b> |
| <b>LIST OF SYMBOLS</b>   | <b>197</b> |
| <b>APPENDICES</b>  | <b>199</b> |
| 1 3 <sup>RD</sup> DOE'S SPECIMENS MAIN STATIC AND DYNAMIC PROPERTIES . . . . | 200        |
| 2 SIMPLIFIED 3D MODEL METHODOLOGY: DOE FACTORS AND LEVELS . .                | 202        |
| 3 OPTIMIZED SLM PROCESS PARAMETERS . . . . .                                 | 209        |
| <b>REFERENCES</b>  | <b>211</b> |



# LIST OF FIGURES

|      |   |    |
|------|---|----|
| 1.1  | Summary of AM process chain main steps [12] . . . . .   | 9  |
| 1.2  | Classification of AM for metals processes depending on laser source – feed-stock material interaction . . . . .                           | 11 |
| 1.3  | Schematic illustration of SLS machines main components [18] . . . . .   | 12 |
| 1.4  | Microstructure of Cu-based powder after LS [20] . . . . .   | 14 |
| 1.5  | Microstructure of LS-processed HSS powders [21] . . . . .   | 14 |
| 1.6  | Schematic illustration of LMD machines main components [22] . . . . .   | 15 |
| 1.7  | Schematic illustration of LM machines main components [32] . . . . .  | 18 |
| 1.8  | Micrographs of cross sections of LS and LM processed Stainless Steel [33] . . . . .   | 18 |
| 1.9  | Summary of LM main process parameters . . . . .   | 23 |
| 1.10 | Absorptivity as a function of wavelength of various metals [36] . . . . .   | 23 |
| 1.11 | Examples of LM scanning strategies [37] . . . . .   | 24 |
| 1.12 | Image of LM main process parameter [38] . . . . .   | 25 |
| 1.13 | Effect of surface tension gradient on Marangoni flow [40] . . . . .   | 27 |
| 1.14 | Liquid on solid wetting and simplified 3D view of melt pool highlighting transition from half cylinder to sphere (balling) [41] . . . . . | 28 |

|   |    |
|---|----|
| 1.15 Summary of physical phenomena occurring during LM [42] . . . . .   | 29 |
| 1.16 Typical defects of LM process [43] . . . . .   | 29 |
| 1.17 Metallographic cross sections of 316L single tracks evidencing keyhole phenomenon [44] . . . . .                             | 30 |
| 1.18 Residual thermal stresses and deformation due to thermal cycle [45] . . . . .  | 31 |
| 1.19 Cantilever specimens for plastic deformation estimation (LAMA FVG™) . . . . .  | 32 |
| 1.20 SEM micrographs of LM manufactured part made of AlSi10Mg, CoCrMo and SS 316L [46] . . . . .                                  | 32 |
| 1.21 Stress-strain curves of specimens built parallelly or perpendicularly to build direction [48] . . . . .                      | 33 |
| 1.22 Crack growth, preferential grain orientation and morphology for different build orientation and HIP treatment [49] . . . . . | 34 |
| 1.23 Fracture surfaces for crack propagation parallel to the build direction (b) or perpendicular (a) [50] . . . . .              | 34 |
| 1.24 Sections of conventional (left) and conformal cooling channels (right) [56] . . . . .  | 37 |
| 1.25 Comparison between conventional and conformal cooling channels heat distribution [12] . . . . .                              | 38 |
| 1.26 TO examples: aerospace bracket and bike stem (LAMA FVG™) . . . . .   | 38 |
| 1.27 Example of “all-in-one” surgical-guide system [59] . . . . .   | 39 |
| 1.28 AM acetabular hip prosthesis: lattice structure enhances bone ingrowth [60] . . . . .  | 40 |
| 1.29 Example of TO variable density lattice structure [62] . . . . .  | 40 |
| 1.30 LM-manufactured LEAP engine fuel nozzle [65] . . . . .   | 41 |
| 1.31 Examples of non-assembly joints [66] . . . . .   | 41 |
| 1.32 DfAM interior shelling of a tool [12] . . . . .  | 42 |
| 1.33 Staircase effect due to layer-by-layer material addition typical of AM [68] . . . . .  | 43 |



---

|      |   |    |
|------|---|----|
| 1.34 | Effect of feature positioning on manufacturability and surface roughness [69]                                     | 43 |
| 1.35 | Surface roughness enhancement with laser re-melting [70] . . . . .  | 44 |
| 1.36 | Warping effect due to unsupported overhang [71] . . . . .   | 45 |
| 1.37 | Evaluation of AM manufacturability for different cooling channel cross sections [12] . . . . .                    | 45 |
| 1.38 | Unsupported overhangs (a) and bridges (b) benchmarks [12] . . . . .   | 46 |
| 1.39 | LM-manufactured horizontal holes without supports benchmark [12] . . . .  | 46 |
| 1.40 | Examples of benchmarks for sloping angles, accuracy and manufacturability of small feature testing [34] . . . . . | 47 |
| 1.41 | Hydraulic manifold external shape and integrated channels [12] . . . . .  | 48 |
| 1.42 | Hydraulic manifold DfAM multi-objective optimization [12] . . . . .   | 49 |
| 1.43 | Bike stem starting geometry and design space definition (LAMA FVG™) . .   | 50 |
| 1.44 | Bike stem testing conditions - ISO 4210-5:2014 . . . . .  | 50 |
| 1.45 | Bike stem TO result (LAMA FVG™) . . . . .   | 51 |
| 1.46 | SLM-manufactured titanium alloy optimized bike stem (LAMA FVG™) . .   | 51 |
| 1.47 | Stress-strain curve for bending dominated cellular structures [73] . . . . .                                      | 53 |
| 1.48 | Bending dominated cellular structures collapse. (a) plastic (b) elastomeric (c) brittle [74] . . . . .            | 54 |
| 1.49 | Stress Stress-strain curve for stretch dominated cellular structures [73] . . .                                   | 54 |
| 1.50 | Examples of lattices topologies and corresponding Maxwell number [76] . .   | 55 |
| 1.51 | Inconel 625 cantilever lattice struts manufacturability [77] . . . . .  | 56 |
| 1.52 | Uniaxial compression stress-strain responses of Inconel 625 specimens [77]  | 57 |
| 1.53 | Ti6Al4V and AlSi12Mg cantilever lattice struts manufacturability [76] . . . .                                     | 57 |

|   |    |
|---|----|
| 1.54 AlSi12Mg BCC unit cell CT and optical microscopy of vertical and inclined struts [76] . . . . .                              | 58 |
| 1.55 Stress-strain chart of AlSi12Mg lattice structures [76] . . . . .  | 59 |
| 1.56 CAD model of 316L specimen integrating BCC lattice [64] . . . . .  | 61 |
| 1.57 BCC lattice dynamic test experimental setup [64] . . . . .   | 62 |
| 1.58 Stress-Strain cycles at 10Hz (a), damping capacity as a function of stress (b) [64] . . . . .                                | 62 |
| 1.59 SLM-manufactured Ti6Al4V gear with TO cellular lattice infill [87] . . . . .   | 63 |
| 1.60 Frequency spectrum of standard (a), cellular lattice (b) and cellular lattice with polymeric filler (c) gears [87] . . . . . | 64 |
| 2.1 Beam-like specimens' geometry (LAMA FVG <sup>TM</sup> ) . . . . .   | 71 |
| 2.2 Example of specimens FEM: BCs and tetrahedral mesh . . . . .  | 73 |
| 2.3 Total displacement contour plot – specimen B . . . . .  | 73 |
| 2.4 Three-dimensional view of specimens and masses inside the build volume .  | 76 |
| 2.5 As-built SLM-manufactured AlSi10Mg specimens and masses . . . . .   | 76 |
| 2.6 1 <sup>st</sup> repetition AlSi10Mg specimens after separation from the build platform  | 77 |
| 2.7 Macroscopic defects of AlSi10Mg specimens (TD: thermal deformation, CC: inert gas filter cleaning cycle) . . . . .            | 78 |
| 2.8 Comparison between measured and nominal AlSi10Mg struts diameters . .   | 79 |
| 2.9 Pulse testing experimental setup . . . . .  | 83 |
| 2.10 Example of inductive probe calibration procedure . . . . .   | 84 |
| 2.11 Frequency response and associated coherence function – C <sub>2</sub> specimen . . .   | 85 |
| 2.12 Modal analysis results for AlSi10Mg specimens . . . . .  | 86 |

---

|   |     |
|---|-----|
| 2.13 Specimens cross section: arrangement of the dust containment walls . . . . .                           | 90  |
| 2.14 Virtual build platform – 316L specimens . . . . .  | 91  |
| 2.15 As-built SLM-manufactured SS 316L specimens and masses . . . . .                                       | 92  |
| 2.16 1 <sup>st</sup> repetition 316L specimens after separation from the build platform . . . . .           | 92  |
| 2.17 Comparison between measured and nominal SS 316L struts diameters . . . . .                             | 94  |
| 2.18 Experimental set-up - SS 316L C specimen . . . . .   | 96  |
| 2.19 Frequency response and associated coherence function – B <sub>1</sub> specimen . . . . .               | 96  |
| 2.20 Specimens compliance measurement – alternative method . . . . .  | 97  |
| 2.21 Specimens deformed shape measurement – 2D laser scanner . . . . .                                      | 97  |
| 2.22 316L specimens modal analysis results – without additional mass . . . . .                              | 100 |
| 2.23 316L specimens modal analysis results – with additional mass . . . . .                                 | 101 |
| 2.24 A specimen hybrid 1D-3D FEM model . . . . .  | 103 |
| 2.25 A specimen displacement contour plot – hybrid FEM model . . . . .                                      | 103 |
| 2.26 A specimen first mode shape – hybrid FEM model . . . . .   | 104 |
| 2.27 Comparison between FEM and experimental results – 316L specimens . . . . .                             | 104 |
| 2.28 Comparison between FEM (with correction factor) and experimental results<br>– 316L specimens . . . . . | 105 |
| 2.29 Beam-like specimen geometry and dimensions . . . . .   | 106 |
| 2.30 Simplified beam-like specimen model . . . . .  | 107 |
| 2.31 Forces and moments acting on the solid section of the specimen . . . . .                               | 108 |
| 2.32 Specimen's deformed shape and dimensions . . . . .   | 108 |
| 2.33 Optimized Rayleigh $\beta$ coefficient for different kind of specimens . . . . .                       | 114 |

|   |     |
|---|-----|
| 2.34 Comparison between calculated and experimental A specimen's FRF . . . . .  | 114 |
| 2.35 High performance mini dynamometer exploded view (LAMA FVG <sup>TM</sup> ) . . . . .  | 116 |
| 2.36 Kistler 9016B4 sensors and reference systems orientation (Kistler) . . . . .   | 117 |
| 2.37 Optimized dynamometer - preload system section . . . . .   | 117 |
| 2.38 Optimized dynamometer central plate – reference geometry . . . . .   | 118 |
| 2.39 Virtual assembly of the dynamometer with the HAAS TR160 rotary table . . .   | 119 |
| 2.40 Virtual build volume – optimized dynamometer's central plates . . . . .  | 120 |
| 2.41 As-built optimized dynamometer's central plates . . . . .  | 121 |
| 2.42 Support cracking, upper face deformation and lattice detail view . . . . .   | 121 |
| 2.43 Central platform's upper face milling – HAAS VF-2TR . . . . .  | 122 |
| 2.44 Coupling plate machining . . . . .   | 123 |
| 2.45 Dynamometer: fully operational cutting forces measurement system . . . . .   | 123 |
| 2.46 Comparison between dynamometers with and without lattice infill: FRF co-<br>herence, amplitude and phase . . . . .                     | 124 |
| 3.1 Specimens static and dynamic behaviour assessment – experimental setup  | 131 |
| 3.2 Example of specimen integrating type A lattice structure, with and without<br>additional mass . . . . .                                 | 132 |
| 3.3 3 <sup>rd</sup> DoE factors levels combinations scheme . . . . .  | 134 |
| 3.4 FBCCZ lattices geometric accuracy assessment - beam diameter equal to: a)<br>0.4 mm b) 0.35 mm c) 0.3 mm d) 0.25 mm e) 0.2 mm . . . . . | 134 |
| 3.5 FBCCZ lattices geometric accuracy assessment - lattice's surface . . . . .  | 135 |
| 3.6 FBCCZ lattices geometric accuracy - inclined beams diameter correction . . .  | 136 |

---

|      |   |     |
|------|---|-----|
| 3.7  | FBCCZ lattices geometric accuracy assessment - lattice's surface after correction . . . . . | 136 |
| 3.8  | FBCCZ lattices geometric accuracy assessment – effective beam section . . .                 | 137 |
| 3.9  | FBCCZ lattices geometric accuracy assessment – section measurement . . .                    | 137 |
| 3.10 | FBCCZ lattices geometric accuracy assessment – beam section surface . . .                   | 138 |
| 3.11 | 3 <sup>rd</sup> DoE's specimens positioning on build platform . . . . .                     | 139 |
| 3.12 | 3 <sup>rd</sup> DoE's specimens SLM 3D printing as-built result . . . . .                   | 140 |
| 3.13 | 3 <sup>rd</sup> DoE's specimens SLM 3D printing - detail views . . . . .                    | 141 |
| 3.14 | 3 <sup>rd</sup> DoE's specimens static compliance assessment – experimental set-up .        | 142 |
| 3.15 | 3 <sup>rd</sup> DoE's specimens static compliance assessment – data acquisition . . . .     | 143 |
| 3.16 | 3 <sup>rd</sup> DoE's specimens frequency response assessment – experimental set-up         | 143 |
| 3.17 | 3 <sup>rd</sup> DoE's samples static compliance – FRF vs load cell estimated values . . .   | 144 |
| 3.18 | Effect of specimens' compliance variation on damping ratio . . . . .                        | 145 |
| 3.19 | Comparison between damping ratio " $\zeta$ " and damping coefficient "c" . . . .            | 146 |
| 3.20 | Aspect ratio effect on damping ratio " $\zeta$ " . . . . .                                  | 146 |
| 3.21 | Lattice's cells number variation effect on damping ratio " $\zeta$ " . . . . .              | 147 |
| 3.22 | Damping ratio " $\zeta$ " with respect to lattice's cross-section . . . . .                 | 147 |
| 3.23 | Damping ratio " $\zeta$ " with respect to unit cell's size . . . . .                        | 148 |
| 3.24 | Distribution of damping ratio values and mathematical models surfaces . .                   | 150 |
| 4.1  | FBCCZ solid model and section of the watertight surface . . . . .                           | 155 |
| 4.2  | Example of layer obtained after slicing operation . . . . .                                 | 156 |

---

|      |   |     |
|------|---|-----|
| 4.3  | Comparison between conventional exposure strategy (a) and Single Exposure Strategy or Laser Spot Welding (b) [99] . . . . .                                 | 157 |
| 4.4  | Comparison between layers obtained after slicing applying the conventional exposure strategy (left - contour) and the SES / LSW (right - points) [99] . . . | 157 |
| 4.5  | Graphical User Interface (GUI) lattice / porous structure generator . . . . .   | 159 |
| 4.6  | Summary of key features of proposed methodology for fast SLM manufacturing of small sized lattice and porous structures . . . . .                           | 163 |
| 4.7  | Proposed methodology validation - specimens geometry . . . . .  | 164 |
| 4.8  | SLM 3D print of specimens obtained starting from the 3D simplified model  | 166 |
| 4.9  | Experimental set-up for measurements with 3D optical profilometer . . . . .   | 166 |
| 4.10 | Beams diameter measurement with 3D optical profilometer . . . . .   | 167 |
| 4.11 | Beams roughness measurement with 3D optical profilometer . . . . .  | 168 |
| 4.12 | Vertical and inclined beams diameter variation – grouping variable: spot diameter . . . . .   | 169 |
| 4.13 | Absolute difference between vertical and inclined beams diameter - grouping variable: spot diameter . . . . .   | 169 |
| 4.14 | Vertical and inclined beams diameters vs power, scan speed and spot size .  | 170 |
| 4.15 | Scatterplots of beams' diameters as a function of power and spot diameter .   | 172 |
| 4.16 | Distribution of vertical and inclined beams diameters and mathematical models surfaces (linear regression) . . . . .  | 173 |
| 4.17 | Distribution of vertical and inclined beams diameters and mathematical models surfaces (non-linear regression) . . . . .                                    | 174 |
| 4.18 | Surface roughness vs power, scanning speed and spot diameter . . . . .  | 175 |
| 4.19 | Distribution of surface roughness and mathematical model surface (linear regression) . . . . .  | 176 |
| 4.20 | Example of intensity profile of a Gaussian laser beam . . . . .   | 177 |

---

|   |     |
|---|-----|
| 4.21 Distribution of surface roughness and mathematical models surfaces (non-linear regression) . . . . . | 178 |
| 4.22 Reference specimen's surface roughness measurement . . . . .   | 179 |
| 4.23 Modified reference specimen's surface roughness measurement (no contour)                             | 180 |
| 4.24 Scatterplot of satisfactory process parameters combinations . . . . .                                | 180 |
| 4.25 Beams diameter and surface roughness of satisfactory process parameters combinations . . . . .       | 181 |





# LIST OF TABLES

|      |  |     |
|------|--|-----|
| 1.1  | AM metal alloys and applications . . . . .   | 11  |
| 1.2  | Absorptivity of metal powders at Nd:YAG and CO <sub>2</sub> laser wavelengths [36] . . | 22  |
| 2.1  | AlSi10Mg material properties [92] . . . . .  | 72  |
| 2.2  | Summary of characteristics of designed specimens . . . . .                             | 74  |
| 2.3  | Detail views of AlSi10Mg lattice structures . . . . .                                  | 78  |
| 2.4  | Pulse testing tools and sensors technical specs . . . . .                              | 82  |
| 2.5  | Inductive probe calibration results – AlSi10Mg specimens . . . . .                     | 84  |
| 2.6  | Comparison between experimental and FEA modal analysis results . . . . .               | 85  |
| 2.7  | ANOVA of damping ratio vs cell dimension and fill ratio – AlSi10Mg specimens           | 87  |
| 2.8  | AISI 316L material properties [95] . . . . .   | 89  |
| 2.9  | Detail views of SS 316L lattice structures . . . . .                                   | 93  |
| 2.10 | Inductive probe calibration results – SS 316L specimens . . . . .                      | 95  |
| 2.11 | 316L specimens resonance frequency and compliance – no additional mass                 | 98  |
| 2.12 | 316L specimens resonance frequency and compliance – with additional mass               | 99  |
| 2.13 | ANOVA of damping ratio vs cell dimension and fill ratio - 316L specimens .             | 101 |

|   |     |
|---|-----|
| 2.14 Geometrical and physical parameters for mathematical model application .                   | 113 |
| 2.15 Modal analysis results – reference central plate . . . . .                                 | 119 |
| 3.1 3 <sup>rd</sup> DoE factors and levels . . . . .  | 130 |
| 3.2 Comparison between 3D and hybrid 3D FE models results . . . . .                             | 133 |
| 3.3 3 <sup>rd</sup> DoE factors and levels - numerical values . . . . .                         | 133 |
| 3.4 FBCCZ lattices geometric accuracy assessment - beam diameter measurement                    | 135 |
| 3.5 Comparison between lattice and full-cross section specimens damping ratio                   | 149 |
| 3.6 Estimated values of linear regression models $\beta$ coefficients . . . . .                 | 149 |
| 4.1 Time required to manufacture lattice structures with different methodolo-<br>gies . . . . . | 161 |
| 4.2 ANOVA of vertical beams diameter vs power, scanning speed and spot size .                   | 171 |
| 4.3 ANOVA of inclined beams diameter vs power, scanning speed and spot size                     | 171 |
| 4.4 Estimated values of linear regression models $\beta$ coefficients - diameters . . .         | 172 |
| 4.5 Non-linear regression models $\beta$ coefficients - diameters . . . . .                     | 173 |
| 4.6 ANOVA surface roughness vs power, scanning speed and spot size . . . . .                    | 175 |
| 4.7 Estimated values of linear regression models $\beta$ coefficients - roughness . . .         | 176 |
| 4.8 Non-linear regression models $\beta$ coefficients - roughness . . . . .                     | 178 |

# INTRODUCTION

Additive Manufacturing Technologies - AMT are an innovative category of production processes that allows the creation of three-dimensional objects through layer-by-layer material addition. Additive Manufacturing technologies have undergone rapid development over the last decade. The technological development in the field of control electronics, laser sources and materials has allowed the creation of new, more reliable and economical production methods and machines that favoured AMT diffusion. The designer who is about to create or optimize mechanical components of diverse industrial sectors has greater design freedom when AMT are involved. Geometric complexity and limitations related to traditional manufacturing technologies do not constitute a problem for AMT, facilitating designer's work by means of design constraints reduction and greater opportunities to focus on performance enhancement. AMT could be exploited for a wide range of applications. Initially, Additive Manufacturing - AM techniques were used only for rapid prototyping which allowed the creation of three-dimensional models to be used during the design phases for product development and for pre-production trials. Technological and material development has allowed a significant improvement of the mechanical properties of components produced with AM technologies making it possible to manufacture end-use products. Among application sectors, aerospace, medical (e.g. medical implants, dental restorations), automobiles, energy and art are those that could benefit more from AMT exploitation. Although AM is based on the simple concept of layer by layer material addition, there are many possible applications, with different degrees of sophistication to meet diverse needs: rapid prototyping for product development, production of highly customized products, industrial tooling, production of small lots, generation of high-performance components not achievable with traditional technologies. AM technologies could be advantageous in many cases, offering the possibility of creating, customizing, optimizing and repairing products by redefining production methods and strategies. The workflow is similar for all AMT: the virtual model of the object to be created is generated using a 3D modelling software (Computer Aided Design - CAD), obtained model could be optimized before proceeding with production process design (e.g. build job design, slicing); afterwards, layer by layer manufacturing process could start using raw materials of various types (e.g. powders, polymers, photopolymers, sheets of raw material).

As previously stated, additive technologies allow designing objects with very complex geometries without significantly affecting process design, costs and the time needed for production. It is therefore easier to design and produce components obtained through structural optimization or exploit integration of tailor-made porous/lattice structures to achieve tuneable optimized mechanical properties.

To take full advantage of AMT design freedom, development of methodologies and design rules for high-performance, high added value AM components design is critical. Different strategies could be applied to achieve this goal, for example: methodologies that involve the use of Topological Optimization - TO in conjunction with Design for Additive Manufacturing - DfAM allowing to obtain lightweight structures characterized by excellent stiffness to weight ratios or strategies exploiting lattice / porous structures with tuneable static and dynamic characteristics to be used as high performance structural or filler materials. The development of innovative methodologies using the strategies described above requires in many cases the use of AMT due to the geometric complexity of the designs obtained.

Among all AMT, technological development has allowed the creation and diffusion of Selective Laser Melting - SLM; this represents one of the most interesting additive technologies from the engineering point of view as it allows the production of substantially ready-to-use metallic components, being able to replace parts normally produced by subtractive technologies. Moreover, SLM is the best option to manufacture optimized mechanical components designed using the strategies described before, since dealing with highly optimized designs it is quite important to obtain mechanical performances comparable or superior to those achievable by means of subtractive technologies or even forging.

The AM sector is experiencing a phase of strong expansion and development, many technological aspects are still under investigation and there are no consolidated guidelines available yet. Considering the overall picture, the present work aims to favour the development of strategies useful for the design of innovative AM high-performance mechanical components.

One of the most promising yet unexplored strategies for achieving this goal are lattice / porous structures to be used as structural or filler materials to increase performance in terms of stiffness to weight ratio and enhanced vibration damping. To fill this knowledge gap, static and dynamic behaviour of lattice structures are thoroughly investigated; in particular, the study focuses on the effect of lattice's topology and geometry variation on its mechanical properties. In order to obtain the data required for lattice's mechanical properties characterization, appropriate experimental campaigns have been conceived and implemented (Design of Experiments - DoE), allowing to gather useful data to characterize aluminium and stainless steel SLM-manufactured lattice structures.

The gathered expertise on lattice structures allowed to develop an innovative tool for in

process measurement of cutting forces generated during milling, drilling and grinding operations. The key feature of this measuring system is the SLM-manufactured main platform which integrates lattice structures to increase overall performance. The development of this high-performance dynamometer represents a practical case study useful to assess the feasibility of exploiting lattice structures designed as high-performance fillers to improve the dynamic performance of a mechanical component.

To develop a methodology useful to characterize static and dynamic behaviour of different types of lattice / porous structures, a further experimental campaign was devised allowing to observe the effect of lattice's size variation on its mechanical properties. The elaborated methodology can be applied to characterize different kinds of lattice /porous structures, helping in Finite Element - FE models calibration and creation of mathematical models useful for static and dynamic properties estimation.

Taking advantage of the gained expertise, in the last chapter an innovative methodology for rapid design and production of small-sized lattice / porous structures is described; this innovative approach significantly enhances lattice / porous structures design and production phases efficiency, guaranteeing substantial savings in terms of time and costs.

The dissertation is divided into four chapters, a brief summary of each one is reported below.

In the first chapter, a solid knowledge base about the state of the art related to AM technologies for metals, DfAM and structural optimization techniques and lattice / porous structures is achieved. The SLM technology, physical phenomena governing the process and materials are studied in detail. Structural optimization and DfAM techniques, particularly useful for the design of high-performance SLM-manufactured components, are analysed. Ample space is dedicated to the state of the art on lattice / porous structures, acquiring information on different topologies and geometries, design rules and mechanical properties. Some case studies demonstrating the potential of joint use of AMT, topological optimization and lattice / porous structures are reported.

The second chapter describes two experimental campaigns, designed to characterize the mechanical properties of lattice structures made of AlSi10Mg aluminium alloy and austenitic 316L stainless steel. Design and production phases of SLM-manufactured beam-like specimens integrating the lattice structures to be analysed are exposed; furthermore, the creation of a particularly efficient FE model for the simulation of parts integrating lattice structures is documented. Thus, measurements useful to determine geometric characteristics, static and dynamic behaviour of the individual specimens are performed. Experimental data analysis allowed to assess the static and dynamic properties of different kind of lattices. Results obtained are exploited to develop a high performance in-process cutting forces measurement system, whose main component is an innovative dynamometer integrating lattice structures. Design, production, assembly and testing phases are illus-

trated, demonstrating the possibility of exploiting lattice structures as high-performance fillers.

In the third chapter the effect of the lattice's size variation (i.e. unit cell's number) on its static and dynamic behaviour is investigated. DoE's conception and planning, specimens and experimental set-up design, manufacturing, measurements acquisition and data analysis are reported. The experimental campaign made it possible to identify a versatile methodology, appropriate for property assessment of different kinds of lattices, useful to obtain enough data for FE models calibration or creation of mathematical models for lattice / porous structures behaviour prediction.

In the fourth chapter an innovative methodology for rapid manufacturing of small-sized lattice / porous structures (Patent Pending) is illustrated. To validate this methodology, a special DoE has been conceived; the investigation required SLM-manufacturing and analysis of a large number of specimens. Obtained data allowed to develop mathematical models to predict geometric characteristics and surface roughness of lattices produced with the above methodology, as well as the identification of optimized SLM process parameters.

In the last chapter a summary of the work carried out is provided, offering suggestions on possible future work and promising paths to be investigated.

## **Chapter 1**

# **AM FOR METALS AND ADVANCED DESIGN AND MANUFACTURING OF MECHANICAL COMPONENTS**

Additive Manufacturing Technologies (AMT), in particular those based on Powder Bed Fusion (PBF), allow the production of complex or customized components, reducing design constraints connected to conventional production processes and eliminating the need for expensive special tools and molds. AM processes are quite different from the traditional ones, instead of removing material from raw-parts the three-dimensional part is the result of the layer-by-layer addition of material. This unique feature represents a fundamental advantage since geometrical complexity is no longer a disadvantage and even very intricate parts can be made in one step. The geometric constraints and the design rules typical of traditional production processes (e.g. circular cross section straight holes, no internal cavities, blanks in the form of plates, blooms and tubes) are no longer an impediment for the designer. The possibility of making preassembled mechanisms makes it possible to reduce assembly operations and the integration of multiple functions in the same component helps to reduce the total number of parts that compose it. Furthermore, AM processes are well suited to on-demand production of components and spare-parts potentially very different from each other, allowing the reduction of spare parts warehouses and ensuring prompt supply, even in remote areas. These advantages and development of new AM technologies favoured their exploitation for the production of high-performance components in the aerospace, biomedical, automotive and industrial fields. In the aerospace field applications are countless, for example GE for its LEAP engine was able to create a complex geometry injector which is printed in a single solution, consistently reducing the parts to be assembled and the number of welds; at the same time optimization of structural parts allowed a significant cost reduction [1]. In the biomed-

ical field, PBF technologies have made it possible to improve performance in terms of osseointegration, biocompatibility, simplicity and rapidity in creating dental implants, prostheses and surgical instruments customized according to the patient's anatomy [2]. AM technologies are used for the production of high efficiency heat exchangers and for the construction of nozzles and swirlers of complex geometry, built with high temperature resistant materials; these features allow performance increase while extending component lifetime reducing system downtime. Automotive industry uses AM technologies for the production of prototypes, development of high-performance components for racing, manufacturing and repair of industrial hardware and molds. Thanks to recent technological advances, PBF technologies are a tool that is currently used by companies that exploit the most advanced manufacturing processes to increase competitiveness and performance of their products. This objective was achieved thanks to the development of cheaper and more efficient industrial laser sources, improved powder preparation processes, increased availability of materials and last but not least the availability of low-cost high-performance computing systems. The development of AM technologies for metals, started within university and industrial research laboratories, has demonstrated the possibility of integrating these technologies within the productive process of important industrial realities, where innovation is the key to maintain and improve competitiveness. To date, a set of guidelines and regulations for the certification of components made using AM techniques for metals has not yet been developed, in most cases the certification systems are designed for the specific case, requiring a considerable amount of time and resources. A deeper understanding of the properties of metal powder feedstock used for production with PBF technology, mechanical and microstructural properties of as-built and heat treated materials is essential to produce defect-free components with mechanical properties equal to or greater than those obtainable with traditional production processes.

In the beginning additive manufacturing processes were created to meet the typical needs of rapid prototyping, which involves the production of components useful for the design phase but with insufficient mechanical characteristics for in production use. The recent development of PBF technologies has introduced the possibility of manufacturing prototypes and components of complex geometry, impossible to achieve with traditional technologies; furthermore, these components are suitable for use in operating conditions thanks to high-level mechanical properties. The physical phenomena that occur during the production process significantly influence the microstructure and therefore also the mechanical properties in terms of anisotropy, residual stress and presence of defects such as inclusions and porosity. These issues, typical of PBF processes, must be carefully considered when the application requires good fatigue performances [3]. The development of PBF technologies is based on the knowledge previously acquired for welding and laser cladding technologies. Previous knowledge has been a good starting point, but it is not sufficient to accurately describe the physical phenomena of PBF processes with the aim of achieving process optimization. The progress in this sector has been significant and the expertise on additive processes for metals has grown considerably, proof of this is the



growing number of reviews and publications dealing with microstructural, mechanical and process characterization [4]–[10].

The following paragraphs analyse in detail the characteristics of AM production processes for metals, microstructural analysis and mechanical properties of different kinds of materials. As previously specified, PBF technologies have many similarities with traditional welding techniques. For this reason, the extensive knowledge acquired in the field of welding and metallurgy is of great help to study and analyse the physical phenomena that occur during metal AM processes. Moreover, another field of fundamental importance for industrial applications, is the study on manufacturability of materials suitable for AM. The analysis of PBF processes and the study of materials properties are very important for understanding the physical phenomena at micro-scale and macro-scale level that influence this type of processes; this knowledge is fundamental for every researcher eager to give his contribution in the innovative, fast evolving field of AM technologies.

## 1.1 AM processes for metals

Additive Manufacturing (AM) is the term used to define a group of technologies that, starting from the CAD (Computer Aided Design) 3D model of an object, allow the layer-by-layer manufacturing of ready-to-use components. Unlike traditional machining processes, which involve the removal of material, AM is based on the layer-by-layer shaping and consolidation of feedstock material. This group of technologies stems from the development of Rapid Prototyping (RP) and Rapid Manufacturing (RM) techniques. The first AM technologies for metals were conceived in the 70s, but due to the technological limitations of the time the first functioning AM machines were made in the 80s. Early stage machines exploited the Selective Laser Sintering (SLS) process and were used for the production of conceptual prototypes. In the mid-90s, technological advance led to the development of the Selective Laser Melting (SLM) technique that allows the creation of prototypes and components ready for use [11].

The study of additive technologies for metals in the last decade was focused on the creation of technologies capable of producing objects of complex geometry that cannot be made in any other way, using metal alloys and Metal Matrix Composites (MMC), very useful to satisfy the demands of aerospace, automotive and biomedical high-tech sectors.

To create objects with mechanical properties capable of satisfying the minimum requirements for industrial use, a suitable laser source is required. In commercial AM machines, CO<sub>2</sub>, Nd:YAG and high-power fiber lasers are used. The most modern AM machines use fiber lasers with powers between 200 W and 2000 W; advantages of this type of energy source are high optical quality, compactness, reliability and ease with which it is possible to direct the spot in the desired position. There are three main types of industrial level

laser-based AM processes for metals: Laser Sintering (LS-SLS), Laser Melting (LM-SLM) and Laser Metal Deposition (LMD). The nomenclatures used to define these three categories could change depending on the specific type of technology, geographical area or manufacturer of the equipment. Only laser-based AM processes for metals are analyzed, being of interest for the investigation reported in the following chapters of this work.

### **1.1.1 Summary of AM for metals main operations**

The main operations required to complete an AM for metals process are summarized below [11].

1. 3D model generation using CAD software: modern design techniques both for AM and traditional manufacturing processes use CAD (Computer-Aided-Design) software to create a 3D solid or surface model of the part to be produced. The three-dimensional representation of the object is the first necessary step to be able to complete the 3D printing process.
2. 3D model to STL conversion: the different types of CAD software use proprietary and neutral formats for saving 3D models, ensuring data interchange. In the field of AM technologies, the standard format chosen for the representation of 3D models is the STL (STereoLithography). The choice of this type of format is due to the simple data structure that facilitates its creation, manipulation and processing. The conversion from CAD model to STL involves the transformation of the solid model to a three-dimensional representation of the surface of the object. In particular, object's surface is discretized through the use of triangles; therefore, vertices coordinates and normal vector of each triangle are saved in the STL file. A clear disadvantage of this type of file format is connected to the use of planar elements (triangles) that cannot accurately describe curved surfaces. It is possible to discretize the surface more accurately by increasing the number of triangles, but this leads to a corresponding increase in the calculation time and size of the STL file. Furthermore, very large files negatively affect the time required for the fulfilment of AM pre-process operations.
3. Build process design and STL slicing: the third step, which is fundamental for the success of the AM production process, involves the correction of the STL file, positioning of the parts inside the build volume and slicing. Most pre-processing software integrate these functions, allowing STL file correction, positioning, creation of support structures and slicing. The positioning phase is particularly critical because it influences mechanical properties and manufacturing time. AM processes for metals allow the production of ready-to-use parts characterized by an anisotropic crystalline structure, for this reason the mechanical properties are not uniform and are generally lower along the axis parallel to the build direction. The

building time is proportional to the number of layers needed to produce the object; therefore, it is convenient to look for the position that reduces the occupied height along the Z axis (build direction). The positioning also influences the quantity and type of supports to be used. Support structures are added immediately after positioning and are useful to guarantee the success of the process and the geometric accuracy of some types of features. In particular, they are used in case of undercut surfaces, cavities, holes and thin surfaces. After positioning and support generation, it is possible to proceed to slice the STL model, creating the individual layers that will have to be processed by the AM machine. The thickness of these layers generally varies between tens and hundreds of micrometers and is generally thinner in the case of LS / LM powder-bed technologies while it is thicker for powder-fed LMD.

4. Part production with AM for metals: depending on the type of production process and the material chosen, suitable process parameters are set, generally suggested by the machine manufacturer. After the operator has performed job and machine preparation, the object is created by layer-by-layer addition of material, according to the instructions created in the slicing phase. An advantage of AM processes for metals is that of not requiring the supervision of the operator during the production process.
5. Postprocessing operations: the finished piece is removed from the machine, then separation from build platform and removal of support structures are carried out. If necessary, heat treatments, sandblasting, tumbling or machining are performed. Figure 1.1 summarizes the main steps of AM process chain.

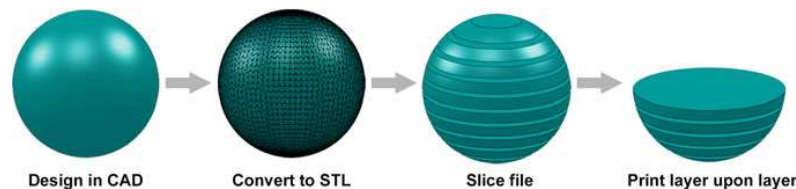


Figure 1.1: Summary of AM process chain main steps [12]

### 1.1.2 AM for metals main features and applications

AM for metals technologies development requires in-depth knowledge in the field of material science, mechanical engineering and laser technology. The technological development of the last twenty years has allowed to reach a level of maturity that can guarantee reliability, accuracy, speed and costs compatible with industrial use. The peculiar characteristics of AM technologies for metals are listed below [13].

1. Wider design freedom: mechanical designers are not forced to respect the production constraints typical of traditional manufacturing technologies. The geometry of

the object to be manufactured can be complex, without impacting significantly the complexity of process design and production phases. In particular, huge tool magazine or special tools are not required. Furthermore, product development is simpler and faster, being able to produce different kind of prototypes efficiently.

2. Faster production speed: the process design phase is leaner and faster than that required for a traditional production process; extra time is saved since no dedicated tools, equipment or molds are required.
  
3. Improved cost saving: with AM technologies it is possible to design a component that can then be produced independently of the production site, the only constraint being the presence of a machine suitable for the purpose. The ultimate goal is to eliminate the need to physically ship the component to the customer, exploiting local production sites, saving time and money. The reduction of the spare parts warehouse and the possibility of rapidly creating equipment, represent an additional economic advantage. With AM technologies for metals, part is built layer-by-layer starting from metal powders feedstock material. Material and energy waste are therefore an insignificant component compared to what occurs with traditional production technologies, constituting an advantage both from an economic and environmental point of view.

AM metal technologies are now used in many industrial sectors. In particular, industrial sectors already exploiting AM technologies for metals are aerospace, automotive, biomedical, industrial and military. In the aerospace field it is often used for the creation of parts with complex geometry, optimized from a structural point of view or made of hardly machinable materials, difficult to produce with other technologies [1]. As a matter of fact, the object obtained at the end of the AM process is substantially ready for use, requiring in some cases only some localized processing. The automotive industry exploits the technology for the production of prototypes, equipment, molds and high-performance components for the racing sector [14], [15]. AM technologies are perfect for biomedical applications, allowing the rapid creation of personalized surgical tools and prosthetic implants designed on the basis of the patient's anatomy. The advantages of AM are also used to reduce prosthesis mass, while ensuring biocompatibility and osseointegration. In particular, it is possible to integrate specific porous structures inside the prosthesis, with the aim of reducing the stress shielding phenomenon, weight and maximizing osseointegration [2], [16]. In the military field, the applications are multiple and concern rapid prototyping, high performance heat exchangers, lightweight high-performance parts. Table 1.1 summarizes additive manufacturing metal alloys and associates them with their respective application field [4].

Table 1.1: AM metal alloys and applications

|                          | Al | Maraging steel | Stainless steel | Ti | CoCr | Ni alloys | Precious metals |
|--------------------------|----|----------------|-----------------|----|------|-----------|-----------------|
| <b>Aerospace</b>         | ✓  |                | ✓               | ✓  | ✓    | ✓         |                 |
| <b>Medical</b>           |    |                | ✓               | ✓  | ✓    |           | ✓               |
| <b>Energy, oil, gas</b>  |    |                | ✓               |    |      |           |                 |
| <b>Automotive</b>        | ✓  |                | ✓               | ✓  |      |           |                 |
| <b>Marine</b>            |    |                | ✓               | ✓  |      | ✓         |                 |
| <b>Tools &amp; molds</b> |    | ✓              | ✓               |    |      |           |                 |
| <b>Consumer products</b> | ✓  |                | ✓               |    |      |           | ✓               |

### 1.1.3 AM for metals processes classification

AM for metals technologies allow the production of complex-shaped components starting from various types of powder feedstock materials. There are different types of AM production processes and each of them differs from the others depending on materials, application fields, machines and process characteristics. AM for metals process specific characteristics, determine the microstructural and mechanical properties of the material produced, influencing whether a certain technique is suitable or not for the application under investigation.

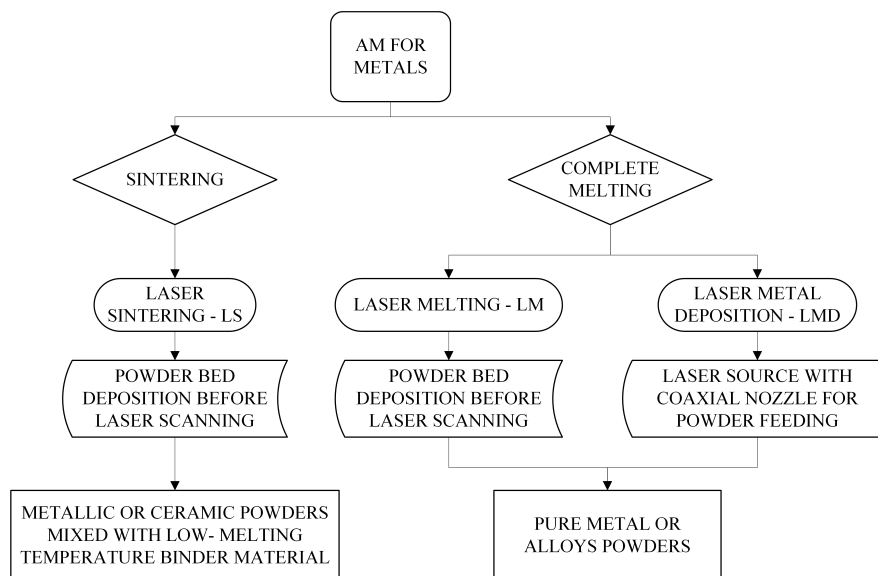


Figure 1.2: Classification of AM for metals processes depending on laser source – feedstock material interaction

AM for metals processes can be divided into three main categories, depending on the raw material supply mechanism (powder bed deposition or powder injection via coaxial nozzle) and on the type of phenomenon that creates the bond between individual metal par-

ticles (sintering or complete fusion); literature review evidenced that these three macro-categories are defined in different ways. In this chapter the terms, Laser Sintering (LS - SLS), Laser Melting (LM - SLM) and Laser Metal Deposition (LMD) will be used [11]; a graphical representation of this classification is shown in Figure 1.2.

### 1.1.4 Laser Sintering - LS

The first laser-based AM for metals technology to be developed was Laser Sintering (LS). This is a technique that involves the layer-by-layer deposition of powder raw material, falling into the category of powder bed deposition processes. The manufacturing process takes place by means of a laser source which melts the low melting elements of the binder and causes powder sintering. Different types of laser sources are used as heat sources in LS machines, for example the most common are fiber lasers, Nd:YAG and CO<sub>2</sub> [17]. The laser source type significantly affects physical phenomena that occur during powder sintering. In case of AM processes for metals that use optical heat sources, such as lasers, the amount of energy that actually reaches the powders is it is a key factor of the process; it must be taken into consideration that the amount of energy that reaches the powder bed depends on the absorptivity of the material at the wavelength of the laser source, therefore laser source type plays a key role in AM for metals processes physics. Figure 1.3 shows the typical layout of SLS machines. The main components are the laser source, the mechanism that contains and spreads powders in the form of thin layers, the device that monitors and regulates the oxygen level in the production chamber, the powder preheating system and the control unit.

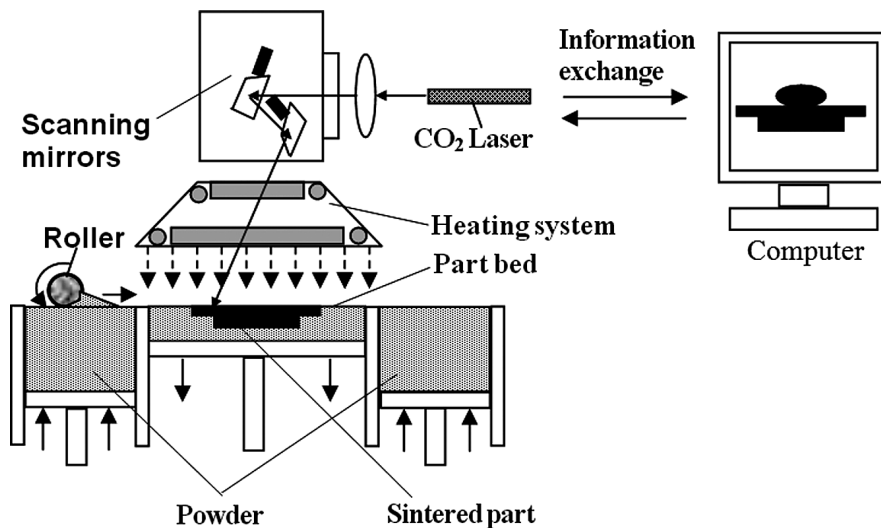


Figure 1.3: Schematic illustration of SLS machines main components [18]

Laser Sintering AM processes generally involve the following steps [17]:

1. A thin layer of powder is first deposited on the building platform, generally the first layer is deposited under operator supervision, therefore the machine can handle automatically following ones. The operator has also to take care of manual positioning and levelling of the building platform.
2. Depending on the type of material to be processed, the working chamber is filled with an appropriate inert gas, to minimize the oxidation phenomena that occur during the process.
3. Every layer is selectively scanned to achieve sintering by means of a laser heat source, guided by a series of galvanic mirrors, according to the 3D model geometry.
4. The process proceeds layer-by layer, powder deposition and laser scanning are repeated until completion.

The scanning of the powder bed proceeds at such a speed that the exposure time of the single particle is in the order of milliseconds. For this reason, the heat supply is very rapid and therefore the only possible sintering mechanism is partial melting and subsequent rapid solidification. Laser Sintering is suitable for consolidation of a great variety of materials: metals, polymers, metal-polymer and metal-ceramic mixtures [17]. In most cases, if metal powders are used, it is essential to use a binder to obtain sintering. Furthermore, to obtain a good sintering it is necessary to determine powders characteristics and optimal process parameters [19]. Metallic materials used for LS processes are multi-component mixtures, composed of three types of materials: metal powders with a high melting point, used as structural component; metal powders with low melting point, used as binder; a small amount of fluxing agents or deoxidizers. In some cases, binder material could be a polymer, removed at the end of the process by heat treatment. The possibility of using different kinds of materials and easily recycle non-sintered powders reducing to a minimum the waste of material, are the main advantages of this type of technology. However, the oxidative phenomena, the limits on dimensional accuracy and mechanical properties, are critical disadvantages of this type of technique. Dimensional accuracy depends on the average size of powder particles used as feedstock material. The oxidation can be eliminated by reducing process chamber oxygen content through controlled inert gas flow injection [17]. The LS process parameters must be chosen to provide enough energy to melt the binder, while the structural part of the multi-component powders remains solid. The sintering process success depends on particles wettability and on capillary forces that determine the positioning of the solid particles inside the liquid bath during solidification phase. An example of the result of the sintering of multi-component copper-based powders, made of pure copper and pre-alloyed SCuP, is reported in Figure 1.4.

Observing Figure 1.5, it is possible to distinguish the SCuP acting as binder, having a low melting temperature, and the copper acting as structural metal, having higher melting

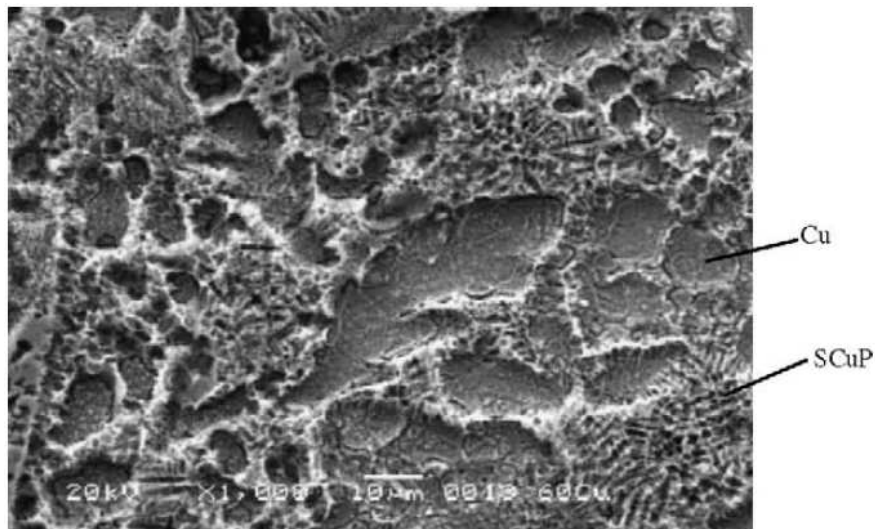


Figure 1.4: Microstructure of Cu-based powder after LS [20]

temperature. A peculiarity of pre-alloyed powders is that they exhibit a mushy zone when transition between solid and liquid state occurs. The LS process parameters are optimized to reach mushy zone temperature, then sintering takes place exploiting the phenomena that occur when solid and liquid phases coexist. Liquid flows, wetting solid particles and grain boundaries, favouring solid particles distribution and densification. Figure 1.5 shows a Scanning Electron Microscope (SEM) image of HSS powders before and after the LS process; it is possible to observe along grain boundaries a microstructure that confirms the formation of the liquid phase during the LS process.

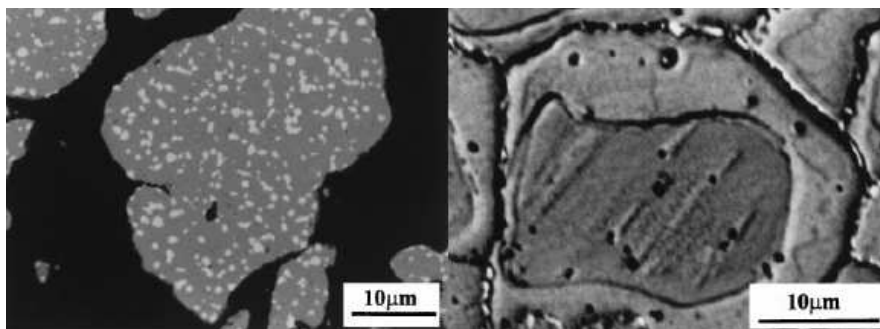


Figure 1.5: Microstructure of LS-processed HSS powders [21]

To achieve optimal sintering, the process parameters must be precisely controlled and optimized. However, this is very difficult as the process is very fast and can be significantly influenced by small local changes in process conditions. For these reasons, it is not uncommon the occurrence of poor densification, uneven microstructure and low mechanical properties; to reduce these problems, it is possible to perform furnace post-sintering, using infiltrating elements with low melting temperature or Hot Isostatic Pressing (HIP) treatment [11].



### 1.1.5 Laser Metal Deposition - LMD

Laser Metal Deposition (LMD) technology shares the same manufacturing principles of other additive technologies for metallic materials. Compared to the LS and LM processes, however, there is a fundamental difference in the LMD technique, consisting on the different powder-supply mechanism. In LS and LM processes, metal powders are spread over the building platform before laser scanning, whereas LMD powder delivery system consists of a nozzle coaxial to the laser heat source. Metal powders are conveyed through the nozzle thanks to a gas delivery system that ensures a controlled flow of the gas-powder mixture. The laser source is placed in the center of the nozzle and it is focused through a system of lenses in order to facilitate material addition over the workpiece. A computerized axis control system moves the laser head and coaxial nozzle assembly to produce the geometry resulting from previous CAD modelling and slicing operations. The production process proceeds layer by layer, up to the realization of the 3D component. Modern LMD machines can integrate multi-axis control systems, multi-material powder supply systems and in-process control systems. This type of technique is suitable for the production of complex geometry components, overhauling of mechanical parts subjected to wear (e.g. molds) and anti-corrosion anti-wear coatings deposition [22]. The main components of LMD systems are visible in Figure 1.6.

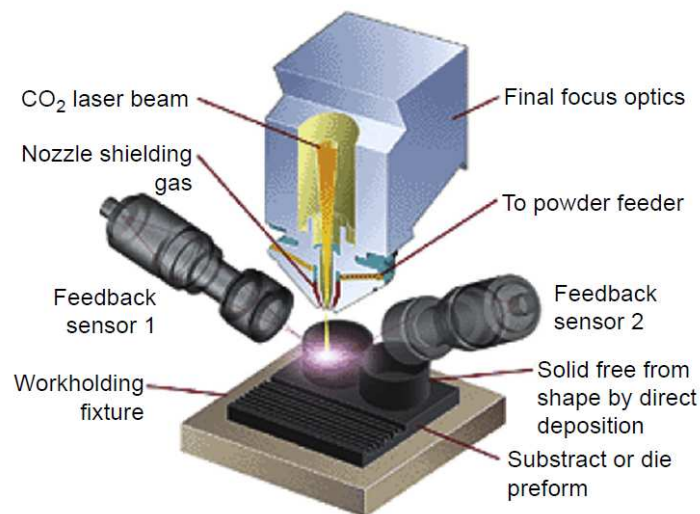


Figure 1.6: Schematic illustration of LMD machines main components [22]

The core of the system is the nozzle coaxial to the laser source: an inert gas flows through the nozzle ensuring powder delivery and at the same time guaranteeing protection against oxidative phenomena. Inert gas flow is a fundamental parameter since it has to be set to guarantee a sufficient flow of powder-gas mixture without disturbing the melt pool formation. The realization of the three-dimensional object takes place thanks to a computerized six-axis movement system. Nozzle's trajectories are defined by means of a Computer Aided Manufacturing (CAM) tool for AM, starting from the CAD model. CAM software in-

tegrating process simulation and collision detection help the designer avoiding unwanted contacts between nozzle and solid sections of the model. Optical systems to set up work-piece reference point have been developed to facilitate the production of small parts with complex geometry. Knowledge of the physical phenomena occurring during the process has allowed the development of closed-loop control systems that exploit high-speed sensors to measure the conditions of the melt pool and optimize process parameters in real time, in order to obtain optimal mechanical properties and geometrical accuracy [22]. Investigation of physical phenomena affecting the melt pool is of fundamental importance for LMD optimization. Metal powders, injected through the nozzle, are melted by means of the laser source, causing the formation of the melt pool on the solid substrate; optimizing and controlling the process parameters to obtain a constant melt pool geometry combined with a small Heat Affected Zone (HAZ), helps to improve process performances. Moreover, fine control of LMD process parameters allows to obtain materials characterized by different kinds of microstructures and thermo-mechanical properties. The effect of the process parameters on the characteristics of the melt pool have been studied both from the experimental and analytical point of view [23]–[28]. It is important to note that LMD process involves a first heating cycle of the material, which leads to melting and subsequent solidification, followed by re-heating cycles due to the layer-by-layer nature of the process. The thermal history of each individual part of the component influences the microstructure and determines the magnitude of residual thermal stresses that cause permanent deformations and unwanted delamination. In-process temperature, inert gas flow speed and melt pool geometry monitoring can provide useful data to understand process physics, helping to create mathematical models to predict microstructure and the resulting mechanical properties. The most common LMD alloys are those suitable for aerospace and energy industry, where optimal thermal and mechanical performances are required, namely titanium, stainless steel and nickel alloys. As previously mentioned, LMD technology can be used to produce 3D objects but the potential of the technology can also be exploited for repairs or for coatings deposition. Restoration of parts subject to wear is an application of great interest for aerospace and energy industries. LMD technique is particularly suitable for compressor / turbine blades overhauling. Dimensional accuracy and mechanical properties obtainable thanks to the control and positioning systems described previously, ensure the production of parts that could require only marginal post-processing operations such as grinding or shot peening [29], [30]. LMD industrial application includes refurbishing of gas turbines, shafts worn contact surfaces, seals or other parts that cannot be repaired using conventional welding techniques. The possibility of depositing new layers of material above an existing substrate facilitates manufacturing of wear and corrosion resistant coatings even on complex geometry objects. In particular, this opportunity is very convenient for repairing die, molds and coatings of mechanical parts in general. An advantage over LS and LM techniques consists in the capability of depositing different materials for every portion of the same part; this feature can be exploited to create components with tailored mechanical and thermal properties, optimized according to design constraints, in order to obtain the desired performances [22].

### 1.1.6 Laser Melting - LM

The desire of companies, research centers and engineers to produce components with good mechanical characteristics, low porosity, without the need to perform time-consuming post-treatments has led to the development of Laser Melting technology. This type of technology satisfies the need to produce objects with characteristics similar or superior to those obtainable with traditional manufacturing technologies. LM has many points in common with LS, the main difference consists in the mechanism exploited to obtain the solid part: LM is based on complete melting and solidification whilst LS on sintering. A thin layer of metal powders is spread over the build platform, then the laser source selectively scans the surface causing powder bed melting. The build platform is lowered by the selected layer thickness and a new layer of powder is spread over. These steps are repeated until the object is completed. The sequence of operations just described, justify the use of Selective Laser Melting (SLM) as an alternative name to define this kind of AM process. Laser's trajectories depend mainly on the three-dimensional geometry of the object to be produced and selected scanning strategy. Likewise to LS technology, the oxygen content in the process chamber is controlled through the use of inert gas (generally Argon or Nitrogen) in order to avoid oxidation and use reactive materials without risk of fire or explosion. The inert gas flow helps keeping the laser's field of view clean, conveying the fumes deriving from the melting process towards the filtering system. Therefore, it is important that the inert gas flow inside the build chamber is uniform, in order to favour fumes removal and improve overall process quality. Another important parameter is the powder layer's thickness. Using powders with low average particle size it is possible to reduce the thickness of the layer, thus managing to better discretize the surfaces of the object to be produced by reducing the staircase effect. At the same time, it is important to ensure that the layer thickness is uniform throughout the process; to achieve this, various powder distribution and levelling systems have been developed. In particular, there are systems that release a controlled quantity of powders through a tank placed at a higher level than the construction platform, or systems where a volume similar to the building chamber is filled with powders and the bottom height is adjusted to provide the right amount of feedstock material. Powders are then evenly distributed thanks to a roller or wiper blade. Coating systems are designed to maximise powder flowability, minimizing shear stress on the previous layer and reducing the formation of powder agglomerates [11], [31]. Figure 1.7 reports a scheme of LM machines main components. The development of LM technology, involving the complete fusion of powders, has been made possible thanks to technological development in the field of lasers and powder production. High-power lasers with smaller spots, powders with low average particle size and more precise distribution systems to reduce layer thickness have been developed. Technological improvement in these sectors has allowed to develop the LM technology to the point of obtaining materials with excellent microstructural and mechanical properties. Parts with a density close to 99.9% can be obtained without the need for post treatments (infiltration, post-sintering, HIP), a big advantage over LS technology [11].

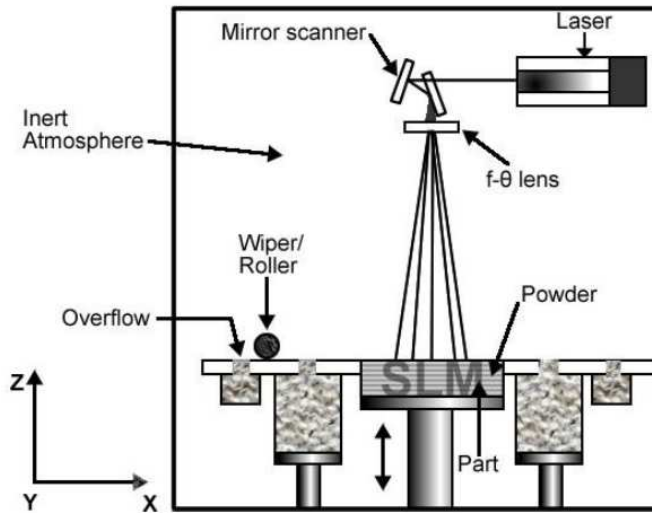


Figure 1.7: Schematic illustration of LM machines main components [32]

Kruth et al. [33] examined microstructure, mechanical properties and geometric accuracy corresponding to different kinds of machines, using LS and LM processes. The study highlights the different material's characteristics that can be obtained through LS exploiting Liquid Phase Sintering (LPS) compared to LM that relies on complete melting. In the first case, the polymeric coating of powder grains, liquefied by the laser beam, acts as a binder for structural stainless-steel grains; a post heat treatment is required to eliminate the polymer and achieve sintering using a bronze-based infiltrant. In the second case, near full density is reached thanks to powders complete melting. Figure 1.8 shows two micrographs taken from cross sections of LS-processed (left side) and LM-processed (right side) parts. Residual porosity can be identified as black spots. The light-coloured zones in the sample of LS-processed part (left side) correspond to the bronze infiltrant surrounding the dark stainless-steel (SS) particles.

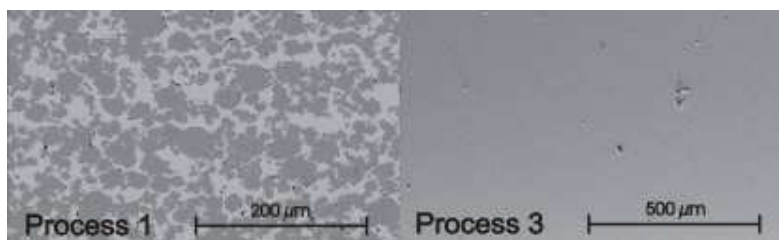


Figure 1.8: Micrographs of cross sections of LS and LM processed Stainless Steel [33]

The analysis of the results obtainable in terms of microstructural homogeneity, densification rate and surface smoothness of LM-processed parts under optimal processing conditions underline a significant improvement upon those of LS-processed parts. A further advantage of LM technology consists in the possibility of processing non-ferrous materials such as titanium, aluminium and copper [5], [34], [35]. LS technology cannot handle

these materials since the supplied energy does not allow the formation of a sufficient liquid phase, causing balling and incomplete sintering. On the other hand, the complete fusion mechanism of LM takes place providing a higher amount of energy, facilitating melt pool instability phenomena. For example, common types of problems related to instability are the balling effect that causes the formation of spherical agglomerates near the melt pool and the keyhole effect that causes the formation of porosity. Furthermore, accumulation of thermal stresses due to rapid heating and subsequent cooling, leads to permanent plastic deformation of the component with the risk of cracks and delamination [31]. For this reason, it is very important to optimize process parameters to reduce porosity, thermal stress, improve surface finish, mechanical properties and ensure dimensional accuracy.

### 1.1.7 LM materials and properties

The list of materials suitable for LM is very long, however the most used are steel, titanium, nickel, aluminium and cobalt chrome alloys. These materials are suitable for processes where heat is supplied through a laser source like LM and can satisfy the needs of most industrial applications. The availability of ytterbium-doped fiber laser sources has allowed the use of an increasing number of metal powders, thanks to the possibility of using increasing energy densities in order to obtain an optimal LM process. The characteristics of main alloys are summarized below:

- Steel alloys are particularly interesting because they guarantee high mechanical performances and allow the use of structural optimization and porous structures to reduce mass and design high-performance components. The most used steel alloy is the 316L austenitic stainless steel which has excellent mechanical properties and corrosion resistance, making it suitable for a wide variety of applications since it can replace materials obtained with traditional manufacturing technologies. The 316L stainless steel, not being reactive, does not require the use of inert atmospheres for its handling, but benefits from the reduction of the oxygen content in the process chamber in order to reduce the oxidation phenomena at high temperature. Studies have been carried out to verify the printability of tool steel, in particular the M2 and H13 alloys, obtaining results that confirm the processability with LM machines. Maraging steels are under investigation as they are particularly suitable to produce mold inserts, often characterized by complex geometries that require many hours of process design and production when manufactured with classic technologies. Recently, iron-based intermetallics are under investigation to obtain particular mechanical properties such as high microhardness, ductility and lightness. LM-manufactured steel alloys have relative densities greater than 99% when process parameters are optimized. For some alloys the relative density is lower and is around 90%, the increase in porosity generally occurs when the alloy has a higher carbon

content. Mechanical properties are comparable or superior to those of materials obtained with traditional technologies, while ductility and fatigue life in general are lower; this is due to the fine microstructure of LM-manufactured materials, possible generation of porosity and defects. The surface roughness of the components obtained from steel alloy feedstock material is between 5 and 10 microns; therefore, to obtain lower surface roughness values further finishing operations are required. Steel alloys produced with LM technology are used to produce components for the medical industry, lightweight components, tools and heat exchangers; below are some examples. It is worth recalling that LM technology is costly, suggesting its application when it is not possible to achieve the desired result with traditional technologies; for example, customized parts for the medical industry, components with conformal cooling channels that maximize heat exchange, optimized lightweight high performance structures or special tools. For medical applications it is very important to be able to obtain a customized component based on the patient's anatomy or tailor-made on the basis of surgical needs. This is possible with LM technology since lead time is short, design freedom is high and parts are substantially ready for use. It is also possible to create porous structures to facilitate osseointegration or variable porosity to reduce stress shielding. Being able to realize complex geometries and integrated cooling channels, it is easy to think of applications where it is important to maximize heat transfer; an application of great impact consists in the production of cooled inserts for molds, that would help achieving reduced cycle time and improved quality of the finished product. Moreover, manufacturing of micro heat exchangers consisting of thin walls up to 0.1 mm is simplified by the design freedom typical of LM technology. Another interesting application concerns the use of lattice / porous structures, to be used as structural or filler materials for high-performance mechanical components. They consist of multiple repetition of identical unit cells and can confer lightness and variable mechanical properties; this type of structure cannot be produced with traditional technologies because of the geometric complexity and the generally small size of the individual features that compose them. They are also used in applications where it is necessary to absorb impact energy or dampen vibrations. The ability to process tool steel alloys makes it easy to create tools suitable for micro-milling characterized by very high micro-hardness.

- Titanium alloys are well suited to meet the needs of those applications that require excellent mechanical properties and lightness. The most used titanium alloy is the Ti6Al4V. Unlike steel alloys, titanium is very reactive and therefore, especially when in powder form, it must be handled and printed under an inert Argon atmosphere to avoid oxidation or danger for the operator. The relative density obtained for LM-manufactured titanium alloys is very high being over 99.5%. Mechanical properties are comparable to those measurable for non-AM parts. In the case of titanium alloys, similarly to steel alloys, the main application sectors are medical one, optimized lightweight structures and the aerospace industry. Titanium is bio-

compatible and can therefore be used to create prostheses and dental implants; it also has mechanical properties closer to those of bone than steel alloys and cobalt chromium alloys, thus helping to reduce stress shielding. Likewise steel alloys, even titanium alloys can be exploited to produce lattice / porous structures with tuneable mechanical properties and variable density to maximize mechanical performances and facilitate osseointegration. Surgical instruments and prosthesis can be made of titanium, facilitating the work of surgeons and providing the opportunity to develop new techniques and surgical tools. Given the lightness and excellent mechanical properties of titanium, aerospace and military applications are also interesting; for example, turbine vanes with integrated cooling channels or optimized brackets for civil and military aeronautical applications. Titanium is exploited also in motorsport environment to create prototypes and small series of parts optimized to guarantee the best possible performance.

- For applications that require good mechanical performances at high temperature, nickel-based alloys, such as Inconel 625, Inconel 718, Hastelloy and Nitinol are the best choice. The relative density obtainable is very high and for most alloys exceeds 99%. Mechanical properties are excellent as is the roughness that remains below 10 microns. As already mentioned, Nickel alloys are particularly suitable for applications where it is necessary to have good mechanical properties and corrosion resistance at high temperature. Furthermore, excellent fatigue and wear resistance are achieved, while weldability is good allowing to weld AM and non-AM parts. Aeronautical engines nickel-based components benefit from the use of the LM process, since performance improvement is easier. For example, benefits can be obtained for turbine blades, turbocharger rotors and turbulence generators used in combustion chambers. As with previous alloys, it is possible to create lattice / porous structures and integrated cooling channels.
- Aluminum alloys are used a lot where lightness is fundamental. The most commonly used aluminum alloy is the AlSi10Mg. Mechanical properties are good but roughness can be high. They are more difficult to print compared to the materials listed above and are easily subject to the formation of oxides if not properly stored and processed in inert gas atmosphere. Applications include lightweight components for automotive, aerospace and robotic industries.
- Cobalt chromium alloys (Co-Cr) are excellent for dental and biomedical applications where requirements in terms of biocompatibility, excellent mechanical performance, hardness and resistance to wear have to be met. Excellent results have been achieved in terms of process repeatability and dimensional accuracy, prompting an increasing number of companies to exploit LM machines for the production of dental prostheses.
- There are also studies that analyze the workability of magnesium, tungsten, copper and precious materials such as silver and gold. Magnesium powder is particularly

reactive and therefore it is essential to guarantee the perfect inertization of the process chamber. This makes the processing of this material more complex, preferring aluminum alloys. Tungsten is a very hard and fragile material, therefore it is difficult to obtain complex geometries with traditional techniques, for this reason being able to work it with LM technology is a big advantage in terms of design freedom, costs and lead time. However, poor workability associated with its high melting temperature and poor wettability are known problems. The high density of this material and the resistance to high temperatures favor its use in the aerospace and military industry. Copper is a very interesting material for applications that require excellent performance in terms of heat exchange, thanks to its high thermal conductivity; for example, inserts with integrated cooling channels and high performance micro heat exchangers. The workability of copper alloys is not optimal when using laser sources for heat supply as the absorption coefficient is low and therefore high power is required to guarantee workability. Precious materials are used to manufacture customized jewels characterized by complex geometries, without the need for ad-hoc molds; for obvious reasons, process optimization and waste minimization are desirable.

### 1.1.8 LM process parameters

LM processes optimization is a complex operation that requires the modification of a large number of process parameters. Figure 1.9 shows the main parameters grouped according to the type of system they have influence on. Process parameters can be divided into three macro categories: laser system, powder-supply system and temperature control.

Process parameters acting on the laser system determine the amount of energy that reaches the powder bed affecting geometrical, mechanical and microstructural properties. The laser wavelength has an important effect on the process and depends on the type of laser source. In fact materials absorptivity depends on the wavelength of the heat source, this is evident by observing the graph of Figure 1.10 which shows the trend of the absorptivity as a function of the wavelength for some metals.

Moreover, Table 1.2 shows some example of absorptivity for different kinds of metal powders at Nd:YAG and CO<sub>2</sub> lasers operating wavelengths (1064 nm and 10.6 μm respectively).

Table 1.2: Absorptivity of metal powders at Nd:YAG and CO<sub>2</sub> laser wavelengths [36]

| Material | Nd:YAG absorptivity [%] | CO <sub>2</sub> absorptivity [%] |
|----------|-------------------------|----------------------------------|
| Cu       | 59                      | 26                               |
| Fe       | 64                      | 45                               |
| Sn       | 66                      | 23                               |
| Ti       | 77                      | 59                               |
| Pb       | 79                      | -                                |



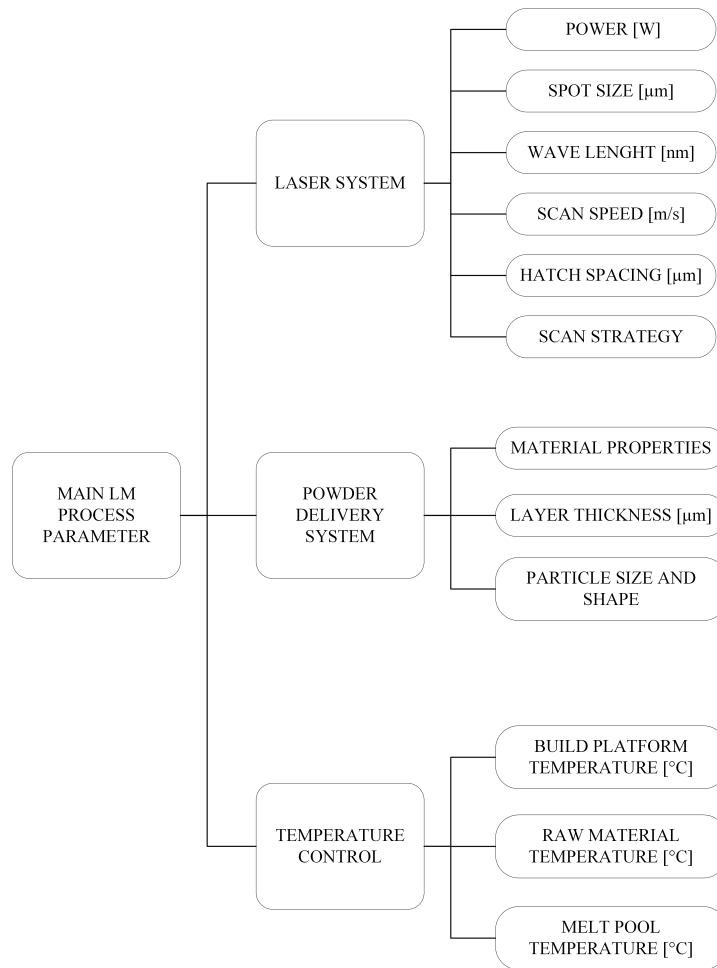


Figure 1.9: Summary of LM main process parameters

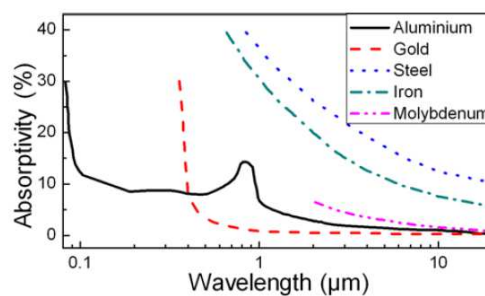


Figure 1.10: Absorptivity as a function of wavelength of various metals [36]

A high level of absorptivity is a desirable feature as it improves the efficiency and productivity of the process. LM of metal powders is more efficient with small wavelength laser sources, since it is possible to exploit better absorptivity. The wavelength also influences the minimum size of the spot due to optical diffraction limit, therefore the CO<sub>2</sub> sources are not suitable to produce small features where manufacturing resolution is a key factor. The laser source is used to transfer a sufficient amount of energy to the powder bed to ob-

tain sintering or melting. The amount of energy per unit area that reaches metal powders must exceed a certain threshold, that depends on the material; for example, aluminium and copper require a lot of energy because their reflectivity and thermal diffusivity are high. Laser power, spot and scanning speed are very important because they are the main factors that influence the amount of energy supplied to the powder bed. Yb-fiber lasers, thanks to the small wavelength, allow to obtain small spots that correspond to higher energy density compared to CO<sub>2</sub> lasers with same average power. High power lasers allow to raise scan speed increasing productivity, nevertheless some upper limitations have to be taken into account in order to avoid the decay of mechanical properties and geometrical accuracy [36]. Power, laser spot and scanning speed have a significant effect on the size of molten pool and HAZ and therefore on the thermal history of the entire component. Two other parameters that affect the thermal history are the hatch spacing and the scanning strategy, which respectively determine the overlap coefficient between individual tracks scanned by the laser and strategy used to scan the layers. The simplest scanning strategy involves the use of unidirectional single tracks scanned with constant hatch distance; examples of other scanning strategies are visible in Figure 1.11.

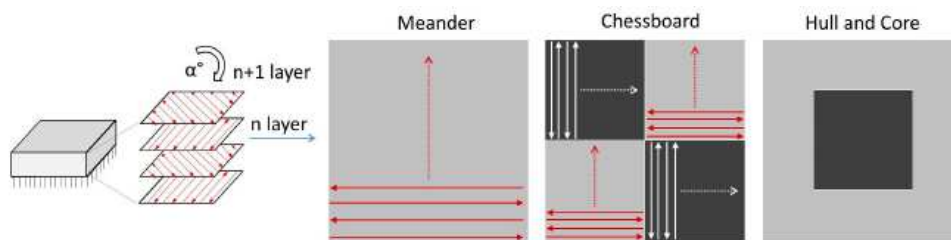


Figure 1.11: Examples of LM scanning strategies [37]

The meander strategy is the most common one and involves the use of vectors scanned in opposite directions with constant hatch distance, helping to reduce scanning time. The disadvantage of this type of strategy consists in heat accumulation and increased residual stresses in case of large area to be scanned. To reduce heat accumulation and associated thermal deformations, the area to be scanned can be divided into smaller areas scanned individually in random order with meander strategy. This approach is known as island / checkerboard strategy, since the layer is subdivided into small sub-areas similar to the checkerboard squares. Another type of strategy subdivides the layer in contour area (hull) and core area, using different parameters to obtain at the same time better surface finish and mechanical properties [37]. Process parameters that pertain to the powder-supply system are material properties such as flowability, absorptivity, melting temperature, particle shape and size and layer thickness. This last parameter is fundamental because it affects the development of the melt pool and dimensional accuracy; in fact, too high layer thicknesses prevents the formation of a uniform melt pool reducing the chances of obtaining layer-to-layer welding without porosity, moreover it also causes a pronounced staircase effect which prevents curved surfaces of the object from being reproduced correctly [4]. Build platform and raw powders chamber temperature control helps to reduce the thermal gradient during the solidification phase, allowing to reduce thermal stresses / de-

formations and delamination as well as improving the flowability of the powders, reducing at the same time unwanted moisture absorption. Melt pool temperature and shape monitoring is quite interesting for the development of quality control systems and for closed loop control systems for real time optimization of process parameters [24]. The main LM process parameters, described above, are summarized in Figure 1.12.

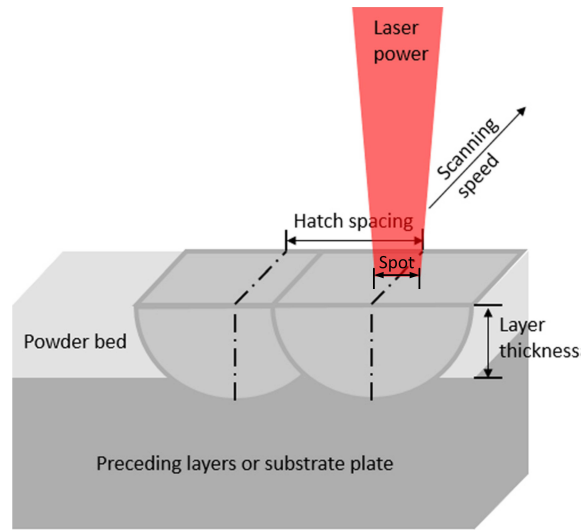


Figure 1.12: Image of LM main process parameter [38]

Using the quantities defined above, it is possible to define useful parameters to characterize the LM process [31]:

- Volumetric Energy Density (VED)

$$E_V = \frac{P}{v \cdot h \cdot t} \left[ \frac{J}{mm^3} \right] \quad (1.1)$$

where  $P$  is power [W],  $v$  is the scan speed [mm/s],  $h$  is the hatch spacing [mm] and  $t$  is the layer thickness [mm].

- Linear input energy density

$$E_I = \frac{4 \cdot P}{\pi \cdot v \cdot s^2} \left[ \frac{J}{mm^3} \right] \quad (1.2)$$

where  $s$  is the spot diameter [mm].

- Surface energy density

$$E_S = \frac{P}{v \cdot s} \left[ \frac{J}{mm^2} \right] \quad (1.3)$$

- Linear Energy Density (LED)

$$E_S = \frac{P}{v} \left[ \frac{J}{mm} \right] \quad (1.4)$$

Literature review analysis indicates that these parameters cannot describe the LM process in a satisfactory manner [39], since they don't take into account complex physical phenomena that develop during the process; therefore, they can only be used as a starting point to experimentally optimize process parameters.

### 1.1.9 Physical phenomena

The LM technology, as already specified before, involves the fusion and rapid solidification of metal powders until the desired shape is obtained layer by layer. The following paragraph will discuss the main physical phenomena concerning this type of AM process. Some hints have already been presented in the paragraph on process parameters.

#### 1.1.9.1 Laser-powder interaction and melt pool characteristics

The main physical phenomena arise from the interaction between laser source and powders. The wavelength of the laser has an important effect on the process. As already mentioned in the previous paragraph, laser sources used in LM machines changed over time starting from the CO<sub>2</sub> type borrowed from LS ( $\lambda \approx 10.6 \mu\text{m}$ ), passing to the Nd:YAG type ( $\lambda \approx 1.06 \mu\text{m}$ ) up to the Yb:YAG fiber laser. This progress has made it possible to exploit higher levels of absorptivity thanks to the reduction of the laser source wavelength, as well as greater efficiency and lifetime. As stated before, parameters that have the most significant effect on the laser-powder interaction are power, scanning speed, hatch spacing, layer thickness and absorptivity. These parameters determine the amount of energy that reaches the powder bed, for heating up and melting. The minimum amount of energy required for the LM process to occur depends on material properties. Failure to optimize process parameters causes problems related to insufficient or excessive energy supply. If the supplied energy is insufficient, for example due to too high layer thicknesses, high scanning speeds or low power, the phenomenon of balling may occur, due to an insufficient wettability of the melt pool in contact with the solid material. On the contrary, with high power, low scanning speed and layer thickness, the high amount of energy supplied leads to evaporation phenomena and generation of the keyhole effect, which are also typical of welding. The lack of hatch spacing optimization favours the formation of regular porosity between single tracks, partially fused together with inclusions of sintered or unmelt material. To describe in detail physical phenomena resulting from the laser-powder interaction, it is necessary to observe the molten pool formation phase. The energy that reaches the powder bed produces a small melt-pool; its characteristics are summarised below [31]:

- Temperature: melt pool maximum temperature is related to linear energy density;

higher laser power means higher LED and temperature, whilst higher scan speed means lower LED and temperature. Temperature gradient inside the melt pool is higher for lower conductivity material; thermal gradient increases linearly with laser power.

- Phase transition: with high laser power and low scan speed, energy density is higher and solidification phase takes more time (liquid-solid phase transition), i.e. melt pool lifetime is longer.
- Dimensions: the size of the melt pool tends to increase when the LED increases; the effect is more marked on width and length rather than on depth. The increase in scanning speed results in an increase in length and a reduction in width.
- Thermo-fluid dynamics: melt pool development is the result of multiple thermo-fluid dynamic phenomena, in particular the Marangoni flow is the predominant one. The Marangoni flow develops due to the surface tension gradient; the material flow direction is a function of the gradient sign. When the gradient of the surface tension is negative ( $\frac{d\gamma_{LV}}{dT} < 0$ ), the resulting melt pool is large but not deep, since the flow is directed from the center to the outside. On the contrary, when the gradient is positive ( $\frac{d\gamma_{LV}}{dT} > 0$ ), the melt pool is narrow and deep and the flow is directed from the outside towards the inside. The effect of the surface tension gradient on the Marangoni flow is visible in Figure 1.13.

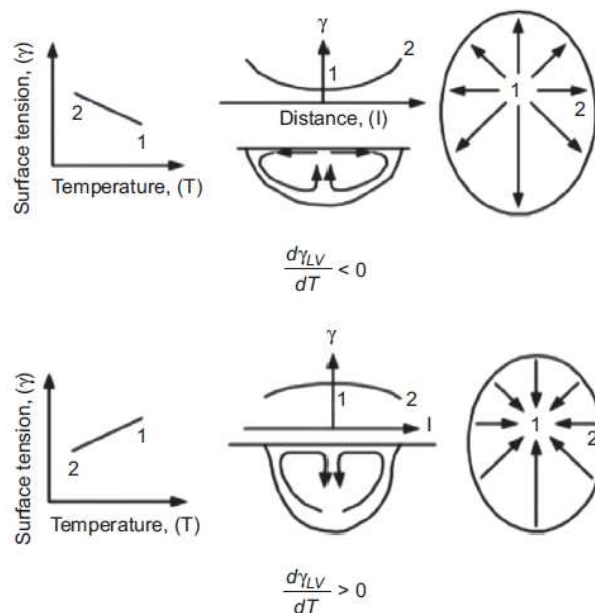


Figure 1.13: Effect of surface tension gradient on Marangoni flow [40]

- Melt pool viscosity is another parameter that affects the flow; it tends to decrease as the LED grows due to the increase in temperature. The viscosity must be low enough

to favor adhesion on the previous layer, without exceeding to avoid the balling phenomenon. The process parameter window that corresponds to the creation of a stable melt pool is narrow. Inside this window it is possible to find optimal parameters, while outside there are phenomena of instability that cause the formation of irregular tracks with an increase in porosity and surface roughness. There are two types of instability, the hydrodynamic one due to the Marangoni flow at high energy density and the capillary one caused by poor wettability. Balling and spattering phenomena are the result of melt pool instability. The balling phenomenon occurs when the melt pool struggle to wet the underlying substrate due to the surface tension, leading to spheroidization of the liquid; spheres of molten material detach from the melt pool causing the formation of irregular tracks. This phenomenon occurs especially when an oxide film forms on the previous layer, significantly reducing wettability, causing poor interlayer bonding that in combination with thermal stresses could lead also to delamination. Having established that the oxidative phenomena negatively affect the balling, it is appropriate to maintain oxygen levels lower than 0.1% in the process chamber [38]. When the balling occurs, porosity and surface roughness increase; moreover, powders deposition is less uniform due to the spherical agglomerates on the surface of the layer, this could lead to LM process failure depending on balling magnitude (i.e. balls diameter). In addition to the insufficient wettability, there are many triggers of balling: the instability of the melt pool caused by the Marangoni flow, excessive melt pool surface temperature that causes melt particles expulsion, excessive quantity of oxygen that causes oxidation and worsens wettability [31]. The balling phenomenon arises from the interaction between solid surface (S), liquid (L) and vapour (V) phases of the melt pool; Figure 1.14 shows the melt pool section, contact angle  $\theta$  between the tangent to the liquid and the solid surface corresponds to the minimum of the total free energy of the system and its value is given by the Young equation ( $\sigma_{SV}, \sigma_{SL}$  and  $\sigma_{LV}$  surface free energies). In three dimensions the melt pool can be depicted as a half cylinder, when the surface of the melt pool exceeds that of a sphere of the same volume, then balling occurs. Process parameters should be optimized in order to reduce as much as possible the length to diameter ratio of the melt pool, since with values of  $\frac{l}{d} > 2.1$  occurring of balling is highly probable (transition from half cylinder to sphere). Remaining balling can be reduced through an additional scan of the solid surface, this kind of strategy is known as surface remelting [41].

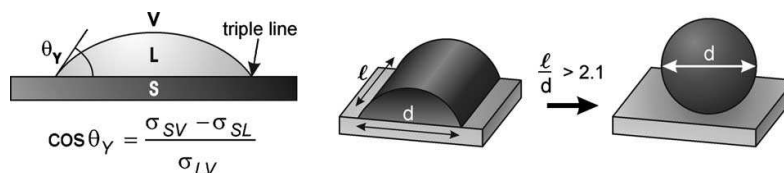


Figure 1.14: Liquid on solid wetting and simplified 3D view of melt pool highlighting transition from half cylinder to sphere (balling) [41]

- When process parameters are not optimized and supplied energy is high, overheating of the melt pool can occur; part of the metal evaporates from the melt pool and the recoil pressure causes the expulsion of droplets of molten material and unmelted particles. This type of phenomenon is called spattering. Figure 1.15 shows an image that summarize physical phenomena occurring during LM. Examples of typical defects in LM tracks are summarized in Figure 1.16.

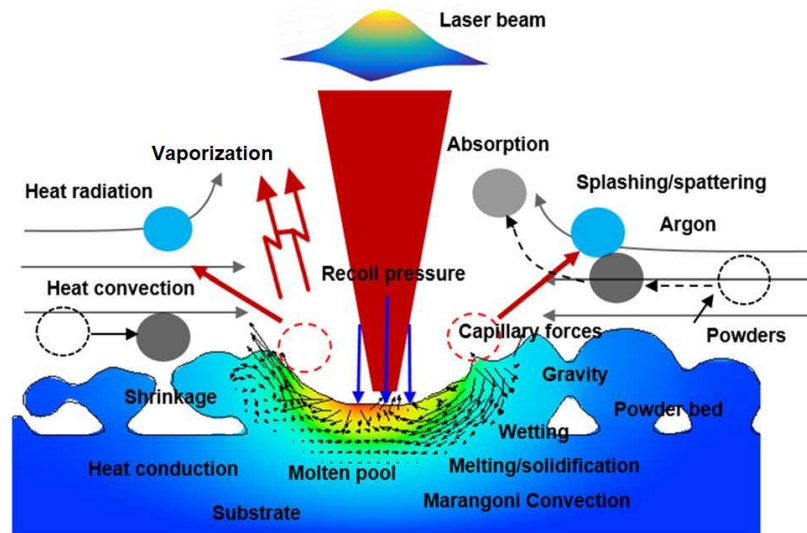


Figure 1.15: Summary of physical phenomena occurring during LM [42]

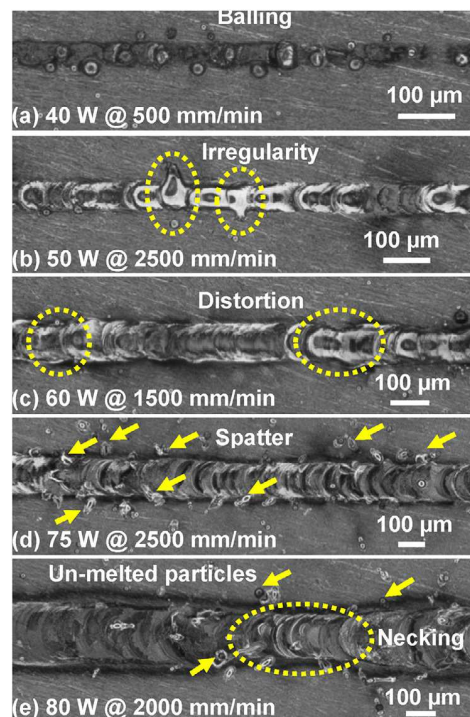


Figure 1.16: Typical defects of LM process [43]

When process parameters are optimized and therefore energy density used is in the optimal range, melt pool extends to lower layers ensuring their bond. In these conditions heat exchange takes place mainly by conduction through the material. When process parameters determine an energy density that exceeds a certain threshold, the transition from conduction to a thermal phenomenon called “keyhole-mode” occurs. High energy density causes metal evaporation and plasma formation, this involves possible development of cavities inside the melt pool that favours a more in-depth transmission of energy compared to conduction only mode. When the cavity formed by the plasma collapses, the vaporized material remains trapped forming cavities that increase the porosity of the material. Metallographic sections of Figure 1.17 show three examples of structure resulting from the execution of single tracks in 316L stainless steel with process parameters that cause the keyhole phenomenon [44].

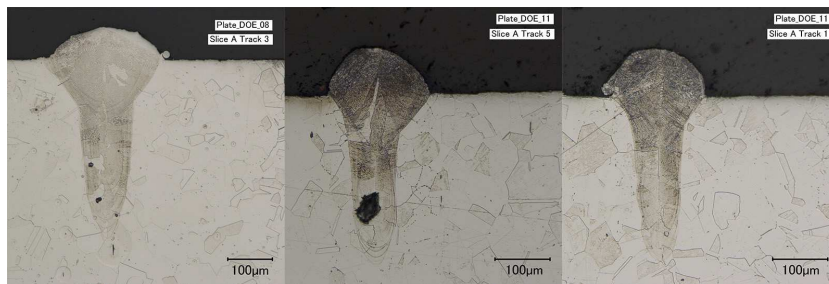


Figure 1.17: Metallographic cross sections of 316L single tracks evidencing keyhole phenomenon [44]

### 1.1.9.2 Powders particles size distribution and morphology

The size and shape of feedstock powders have an effect on the powder-laser interaction. They affect energy absorption and thermal conductivity of powder bed and flowability. Achieving a good powder deposition and a high packing density helps to obtain parts with low porosity and surface roughness as well as reducing the accumulation of residual stresses that cause undesired deformations and delamination. Achieving a high packing density depends on the shape and size of the particles; a wide particle size distribution is desirable so that smaller particles can fill the gaps left between the larger ones. Spheroidal particles improve flowability, facilitating deposition of uniform layers with a high packing density. Powders with a high percentage of non-spheroidal particles worsen the coating and the packing density, facilitating the increase of porosity. Thermal conductivity of the powder bed is closely related to the packing density; meaning that conductivity is higher for high packing density. In the paragraph dedicated to process parameters, it was emphasized that the absorptance is a very important parameter for of LM process physics. Absorptance is defined as the fraction of the energy flux incident on a surface that is absorbed by the surface. Like emissivity, absorptivity value is in the  $0 < \alpha < 1$  range. This pa-



parameter determines the efficiency of the process and constitutes a criterion to determine whether a material is suitable for LM technology or not. Metal powders have a higher absorption coefficient than solid material, this can be explained by the fact that the laser source is able to penetrate deeply exploiting the interstices between the dust particles and the multiple reflections that occur because of laser-particles interaction. This effect is more marked for highly reflective materials such as aluminium and copper. The use of finer grain size powders permits to lower layer thickness, enhancing energy absorption, requiring a lower amount of energy to obtain an optimal LM process [31], [38].

### 1.1.9.3 Thermo-mechanical phenomena and microstructure

Components made with LM technology have different mechanical and microstructural properties than those of parts obtained with traditional manufacturing technologies. The properties of materials obtained with LM are the result of their thermal history, characterized by rapid localized heating followed by equally rapid cooling, with a very high thermal gradient. The result of the considerable temperature gradients are plastic deformations due to the rapid expansion and subsequent shrinkage that occur during the thermal cycle initiated by the laser source. Heat supply gives birth to the melt pool, temperature rise causes expansion of the material followed by a rapid cooling phase which causes shrinkage constrained by the cooler solid substrate. This translates into permanent plastic deformations whose magnitude depends on the thermal gradient that develops during the cooling phase; plastic deformations are therefore higher for increasing energy density, due to higher melt pool temperature [31], [38], [45]. Figure 1.18 shows plastic deformation and residual stress development during heating/cooling cycle.

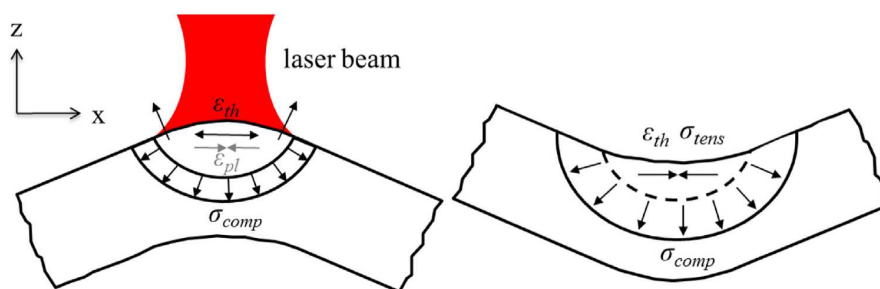


Figure 1.18: Residual thermal stresses and deformation due to thermal cycle [45]

Residual thermal stresses tend to add layer after layer during the production process, causing an increasing plastic deformation that can generate the formation of cracks and delamination. A simple method to estimate the magnitude of plastic deformations associated with residual thermal stresses, consists in the measure of maximum deformation of cantilever specimens after partial separation from the building platform, as shown in Figure 1.19.

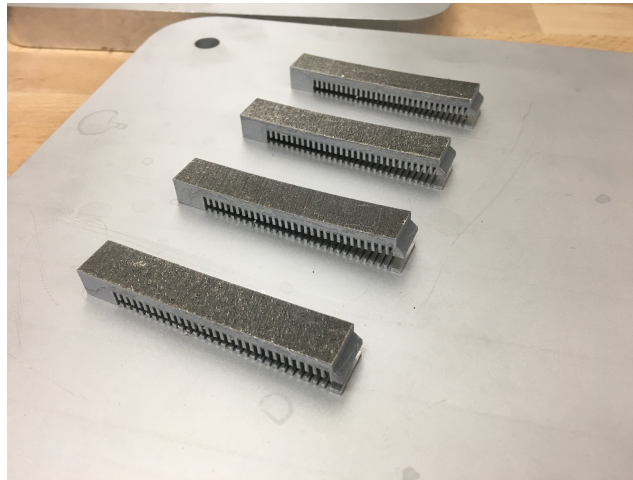


Figure 1.19: Cantilever specimens for plastic deformation estimation (LAMA FVG™)

Residual thermal stresses along the laser scanning direction are higher compared to those along the perpendicular to scanned tracks. Taking into account this result, it is possible to reduce residual stresses by adopting a scanning strategy that allows to decrease the length of scanned tracks. This kind of strategy starts from the discretization of the layer in smaller areas, scanned separately in random order by the laser source (island strategy). To reduce the impact of thermal stresses on the geometry of the printed object, it is possible to perform stress relieving heat treatments or use heated process chamber / build platform. The heat generated during the process is dissipated mainly by conduction through the solid part of the component and the build platform. This causes a directional heat dissipation, associated with growth of columnar structures along the building direction; this phenomenon can be observed for many types of metal alloys suitable for the LM process. The high thermal gradient facilitates the creation of a fine cellular metastable microstructure, due to the high nucleation speed and reduced grain size growth; this involves the generation of materials with lower ductility but with higher Ultimate Tensile Strength (UTS) than those produced with traditional processes [31], [46]. Some micrographs obtained with SEM highlighting the cellular microstructure of aluminium, cobalt chrome and stainless steel produced with LM technology are visible in Figure 1.20.

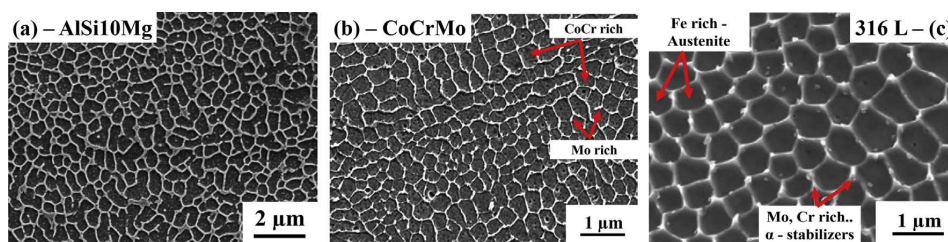


Figure 1.20: SEM micrographs of LM manufactured part made of AlSi10Mg, CoCrMo and SS 316L [46]

#### 1.1.9.4 Mechanical properties and common defects of LM manufactured parts

Mechanical properties of components made with LM technology are strongly influenced by the thermo-mechanical phenomena typical of this category of additive processes. In particular, they depend strongly on resulting microstructure, porosity magnitude and thermal post-treatments. The possible presence of porosity, especially if the average pore size exceeds a certain threshold, negatively affects mechanical properties and fatigue life, causing the reduction of the effective cross-sectional area and facilitating the nucleation and propagation of cracks. The positioning of the component in the building volume can affect its mechanical properties; this is due to the variation of the relative orientation between the features of the piece and the building direction, for this reason in most cases the parts produced with LM technology exhibit anisotropic behaviour. Generally, lower mechanical properties and ductility are to be expected when the load is directed along the build direction, since adhesion between the individual layers can be partially compromised by the presence interlayer defects such as porosity, inclusions and partially melted particles [47]. This behaviour is confirmed observing stress-strain curves of tensile tests of specimens manufactured parallelly (horizontal) and perpendicularly (vertical) to the build direction (Figure 1.21).

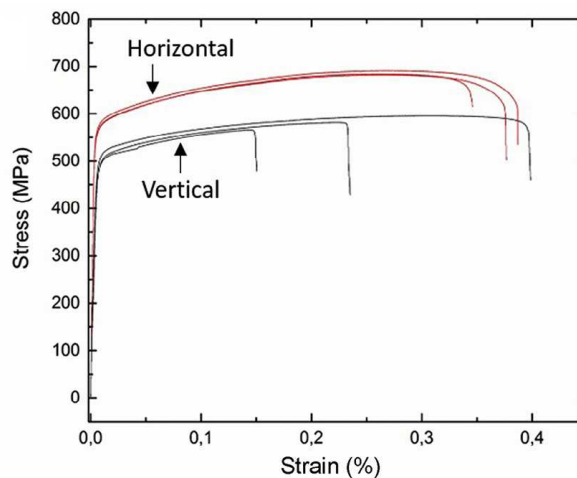


Figure 1.21: Stress-strain curves of specimens built parallelly or perpendicularly to build direction [48]

In general, given the particular microstructure, the yield strength and the UTS of materials produced with LM are equivalent or higher compared to those manufactured with traditional technologies; the ductility is lower, although thermal treatments help to reduce this shortcoming. Fatigue life is strongly influenced by the presence of defects and by the magnitude of residual thermal stresses. Fatigue cracking points are generally located in correspondence of porosity or inclusions near the surface of the component. The use of appropriate process parameters allows to obtain considerable improvements in terms of fatigue life through microstructure refinement and defects reduction [31]. Figure 1.22

shows specimens designed to study the generation and propagation of cracks and highlights microstructure's preferential grain orientation and morphology.

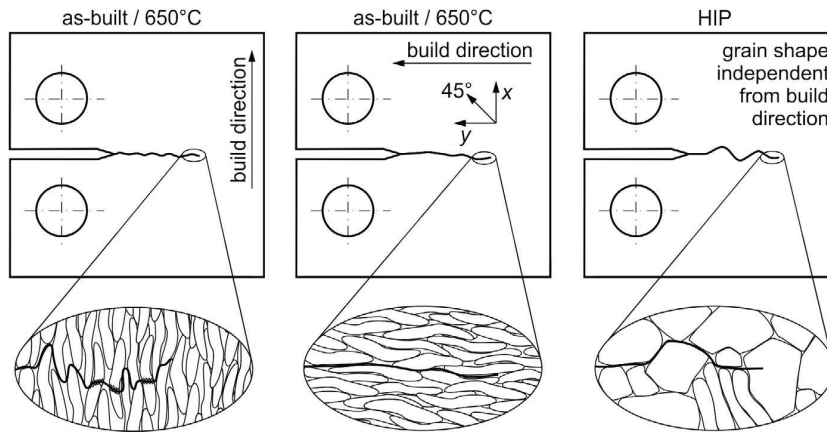


Figure 1.22: Crack growth, preferential grain orientation and morphology for different build orientation and HIP treatment [49]

The anisotropic fatigue behaviour of many materials produced with LM is justified by the different types of microstructure that are obtained depending on the build direction and on the heat treatment; the figure above shows three different cases of grain orientation and morphology. In case of crack propagation perpendicular to the build direction (X-axis Figure 1.22) the spacing between grains is small, this makes crack growth more difficult since the path along the grain boundaries is more tortuous. The material therefore has better fatigue properties when stressed along Y-axis. In case of crack propagation parallel to the growth direction (Y-axis), the grains are elongated along X-axis; the growth of the crack along the grain boundaries is therefore facilitated since the path is not tortuous, this is confirmed by the smooth fracture surface. In Figure 1.23 it is possible to observe fracture surfaces in case of crack propagation parallel to the build direction (b) or perpendicular (a) [49], [50].

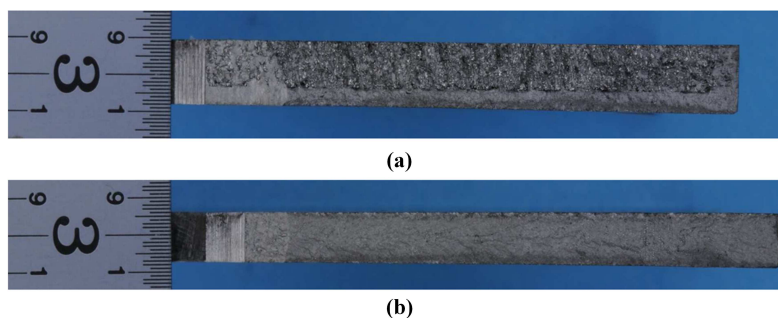


Figure 1.23: Fracture surfaces for crack propagation parallel to the build direction (b) or perpendicular (a) [50]

Mechanical properties analysis evidenced that the orientation of components with respect to the build direction has a different effect depending on whether the load is fatigu-

ing or static. Summarizing the results listed above, the specimens produced in the vertical direction have better fatigue life than those manufactured horizontally; on the contrary, in case of static loading the horizontal ones have better mechanical properties.

After analysing the effect of the microstructure on mechanical properties, it is useful to evaluate the macroscopic effects due to typical defects of the LM process. The most common defects are porosity, inclusion of unmelted or partially melted particles and formation of cracks. Main macroscopic effects are density and effective cross-section reduction and formation of crack initiation points.

The main macroscopic defects can be divided into the following categories [31]:

- **Incomplete melting:** unmelted or sintered powder particles are a common inter-layer defect, caused by insufficient energy supply or excessive hatch spacing.
- **Porosity:** residual porosity can be caused by several factors. It may be the result of evaporation of moisture absorbed by feedstock material or gaseous pores already encapsulated inside powder particles; in this case resulting pores have spherical geometry. It can be produced by the keyhole phenomenon, caused by high energy density process parameters, which generates a narrow and deep melt pool associated with formation of gases resulting from the evaporation of the material that remain trapped after melt pool collapse.
- **Unstable melting process:** Marangoni flow develops inside the melt pool, potentially causing the detachment of spheroidal particles of molten material and subsequent deposition on the solid surface of the layer. This phenomenon is common when high energy density parameters are used and leads to the formation of irregular porosity. Residual porosity and therefore relative density are strongly dependent on the energy density and on process parameters corresponding to a stable LM process. For this reason, experimental campaigns for process parameters optimization are widely adopted to improve LM process performances.

## 1.2 DfAM and structural optimization

Advanced additive technologies allowed the development of new AM machines and materials that satisfy the demand of reduced time-to-market and enhanced design freedom to customize objects without significantly impacting on production costs. Over the years, technology enhancement allowed to move from prototyping applications to production of ready-to-use components. However, in some cases AM technologies are not the best option. In fact, AM technologies, especially those for metallic materials, require the use of expensive machinery; the hourly cost of the equipment and the relative slowness of

additive processes compared to subtractive ones, in some cases lead to a sensible economic disadvantage. It is therefore critical to understand how exploit advantages of AMT to design high-performance high-quality innovative components and when it is actually convenient to use them [51]. The set of design principles, rules and constraints useful for the design of mechanical components optimized for AM is called Design for Additive Manufacturing (DfAM). For designers it is crucial to understand how AM processes work; therefore, keeping in mind advantages and disadvantages it is possible to consciously design and optimize the first prototype.

Standards providing a common knowledge base and terminology on additive technologies are being developed; for example, the ISO / ASTM 52910: 2018 standard lists requirements, guidelines and recommendations for AM product design. It can be used as a reference for AM product design, helping to define best practices in order to exploit advantages and capabilities of AM processes [52].

Design for Additive Manufacturing helps to enhance product and process optimization in order to obtain a performance and economic advantage, guaranteeing rapid product development and efficient production of high-quality components. To obtain these results it is required to simultaneously take into account design objectives and constraints, specific for selected AMT and application. DfAM gives the designer concrete tools, such as guidelines and techniques, to adapt or design from scratch mechanical parts or systems, taking into account advantages and constraints typical of the chosen AM technology. Guidelines help dimensioning the individual features that make up the object under analysis (e.g. holes, walls, undercuts, beams, relative inclinations between the parts). Moreover, they facilitate to understand the effect of design choices on the production process and therefore on quality, time and costs; they also guide in choosing the most suitable material to meet application's requirements and to choose the most suitable CAD tool to facilitate and speed up the design phase [53]. DfAM is similar to the more generic Design for Manufacturing and Assembly (DfMA), with some differences. There are many AM technologies and the guidelines may change depending on the production process chosen; nevertheless, in general constraints due to the need of ensuring coupling between multiple parts in assemblies are less important since it is possible to generate objects that integrate multiple functions, minimizing the need for assemblies.

AM production lots are small and the average production time is longer than traditional techniques; strategies to enhance product and process design must be adapted accordingly. For example, lattice / porous structures with tuneable mechanical properties are a new kind of instrument that in conjunction with Topology Optimization (TO) help generating high-performance designs consistent with the AM philosophy.

The main objective of DfAM-TO is to provide a set of tools and notions useful to guide designers in the realization of ready-to-use parts, fully exploiting advantages and capabilities of AM. The achievement of this result is essential to convince industrial players

to invest and adopt AM technologies, managing to overcome the mistrust caused by the limited availability of consistent technical and technological standards and guidelines.

### 1.2.1 DfAM: exploit the advantages of AM technologies

This paragraph briefly summarizes of AM technologies advantages that should be exploited to correctly apply DfAM. The first obvious advantage that must be exploited, is the possibility of creating objects of complex geometry without introducing penalties in terms of process design and manufacturing complexities; this is a huge advantage for mechanical designers, artisans and artists who want to improve existing designs or create innovative objects that are difficult to achieve without AM. For example, jewellery industry can produce unique and personalized products quickly and efficiently and interior designers can produce prototypes and small series of innovative furnishings and accessories by exploiting greater geometric freedom. Advantages are not limited to the aesthetic point of view but extend to products performances enhancement. For example, optimized integrated cooling channels can be designed to improve quality and performance of injection-molding process [54], [55]. In the case of injection molding, conformal cooling channels are designed to limit the distance between channels and the part to be cooled, making heat exchange more uniform and efficient; this is possible thanks to the possibility of generating channels of complex geometry that follow the profile of the surface to be cooled. Figure 1.24 shows the difference between a traditional cooling channel (cylindrical hole) and a conformal one that follows the profile of the mold.

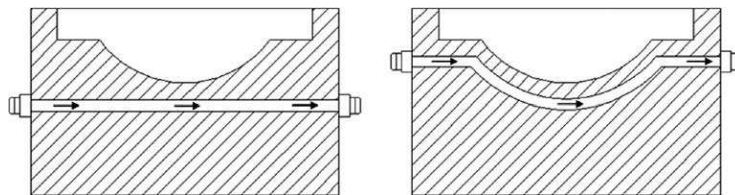


Figure 1.24: Sections of conventional (left) and conformal cooling channels (right) [56]

Industrial applications of this DfAM technique confirmed that temperature distribution is more uniform, cycle time is reduced, quality improves and waste is reduced [57], [58]. An example of heat distribution obtainable with conformal cooling channels compared with conventional ones is shown in Figure 1.25.

Another DfAM technique exploits topology optimization (TO) to generate high-performance low-mass components, reducing material and energy waste taking full advantage of AM potential. Topological Optimization is a particular type of finite element analysis which, given a starting geometry, identifies the optimal distribution of the material that maximizes performance (weight, stiffness, dynamic response...), guaranteeing the functionality of the component respecting the constraints in terms of safety factor or maximum

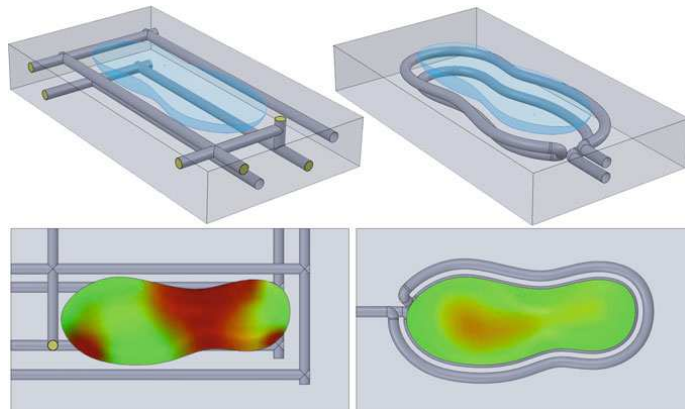


Figure 1.25: Comparison between conventional and conformal cooling channels heat distribution [12]

displacement. This type of analysis requires the definition of constraints, loads and of the so-called design space, which is the volume subject to optimization. Hence, an optimization algorithm iteratively performs Finite Element Analysis (FEA), establishing the optimal material distribution at each iteration, verifying at the same time constraints fulfillment. When the optimization criterion is satisfied, the algorithm shows the optimized geometry. TO is very powerful and is already exploited by aerospace and automotive industry, where weight reduction is a fundamental requirement to maximize energy savings and performances. Even biomedical industry uses TO to improve performances of prostheses and implants. Figure 1.26 shows two examples of TO: the first one on the left side is an aerospace bracket, the second one on the right side is a bike stem. General workflow when performing topology optimization consists of the following operations: definition of design space, loads and constraints, run TO algorithm, reshape and save optimized geometry. Optimized geometry could be further modified manually, for example to improve manufacturability, then prior to SLM prototype printing final design should be tested using FEA to check whether it is ready for production or not.

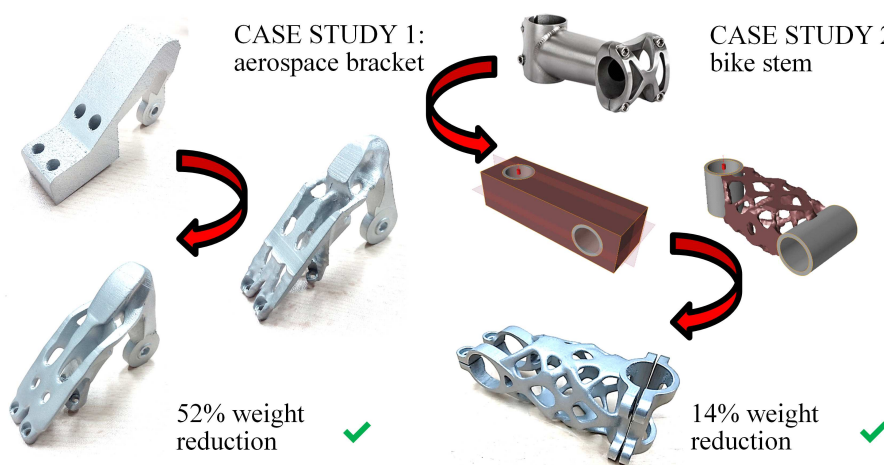


Figure 1.26: TO examples: aerospace bracket and bike stem (LAMA FVG™)



Being able to generate complex customized geometries based on the requirements of the specific project, is a further advantage when developing a product to be made with AM. Medical industry has fully exploited this advantage to create customized prostheses and implants based on the patient's anatomy; moreover, it has been used to improve surgical planning and surgical efficiency. For example, in the field of maxillo-facial surgery it is crucial to guarantee the correct positioning of the prosthesis and to minimize the biological damage resulting from the surgery. For this reason, it is possible to 3D print surgical guides designed on the basis of the patient's anatomy, in order to help the surgeon to identify the affected area, facilitating osteotomy procedure. An example of surgical guide designed on the basis of Computerized Tomography (CT) scans is shown in Figure 1.27.

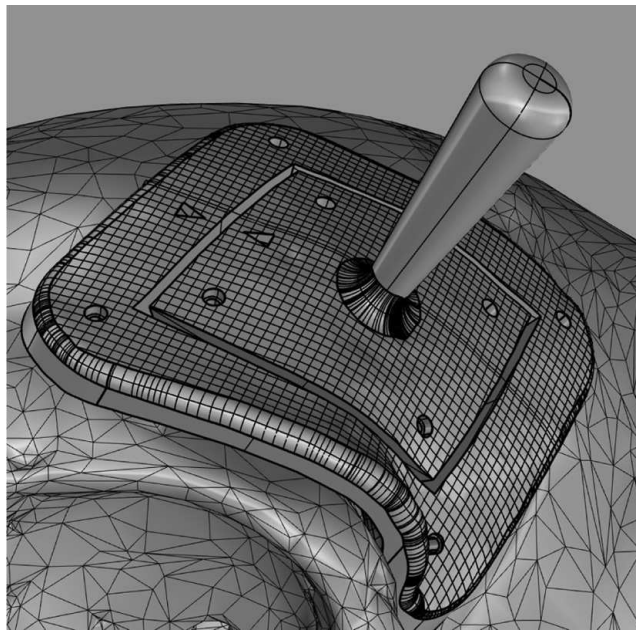


Figure 1.27: Example of “all-in-one” surgical-guide system [59]

The opportunity of using different types of materials and process parameters makes it possible to obtain parts with tuneable thermo-mechanical properties that can vary within the volume of the object itself. For example, it is possible to control porosity, microstructure and anisotropy modifying process parameters and build direction. The use of post treatments such as HIP, heat treatments and surface finishes can improve mechanical properties compared to the as-built material. Therefore, applying DfAM means choosing the best combination of material type, process parameters and post-treatments to obtain the expected result.

AM capabilities extend to the creation of textured surfaces with controlled porosity. One of the most important applications of this technique is related to the realization of medical implants that maximize osseointegration. The controlled porosity structure on the surface of the prosthesis maximizes implant fixation and bone ingrowth. An example of an acetabular hip prosthesis cup is shown in Figure 1.28.



Figure 1.28: AM acetabular hip prosthesis: lattice structure enhances bone ingrowth [60]

A further possibility that can be used for DfAM, are three dimensional lattices, obtained from the repetition of interconnected beams unit cells. This type of structure can be designed to have specific mechanical, thermal and biological properties. The most common application consists in the integration of these structures within the component to be optimized to obtain a high-stiffness lightweight design. Using these structures together with topology optimization it is possible to create variable porosity structures with point by point specific mechanical and thermal properties [61]. Uniform lattice structures, having constant cell size and fill ratio, are the most common; however, there are no limits on cell type and fill ratio of the individual unit cells of these structures. Figure 1.29 shows an example of a lattice structure with variable fill ratio and density, obtained from TO.

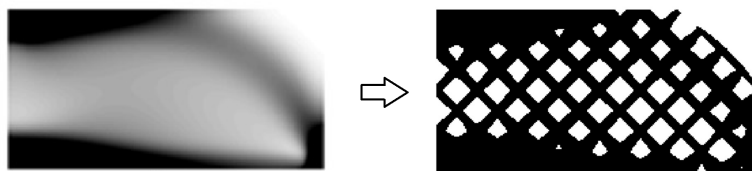


Figure 1.29: Example of TO variable density lattice structure [62]

Controlled porosity structures, obtained from the repetition of unitary cells generated by the superposition of thin walls, have similar characteristics and applications to those of lattice ones. Lattice and porous structures are used to create light but rigid objects, to increase vibration damping/isolation [63], [64] and to improve biocompatibility and osseointegration.

The additive nature of LM processes makes it possible to redesign a mechanical assembly, significantly reducing the number of parts, since it is possible to build a pre-assembled object or a completely new object that integrates all the functions of the original assembly. Main advantages are assembly operations and associated costs reduction, potential increase of performance and weight reduction. The aviation industry has used this method to reduce parts of some systems, cutting costs and improving reliability and performances. For example, GE Aviation has successfully produced the LEAP engine fuel nozzle, using LM-manufactured cobalt chrome (Figure 1.30).



Figure 1.30: LM-manufactured LEAP engine fuel nozzle [65]

Compared to the original nozzle, the one redesigned for AM is a single piece that replaces an assembly of 20 components, reducing cost and weight, eliminating joints and improved performance. Aeronautical applications are countless; companies such as Airbus, Boeing, Lockheed Martin, Rolls-Royce, Pratt and Whitney, SAFRAN Group and NASA have already developed multiple case studies and continue to invest in AM research, confirming that AM will have an important role in future aircraft manufacturing [65].

In addition to reducing assemblies' parts, one-step fabrication of ready to use assemblies with moving parts, like gears, joints and hinges, is feasible. Hence, appropriate guidelines to establish mechanical tolerances necessary to ensure relative movement between AM parts would be very important. A small clearance may prevent motion, on the other hand a large clearance may cause vibration and instability of the mechanism. Some examples of non-assembly joints are shown in Figure 1.31.

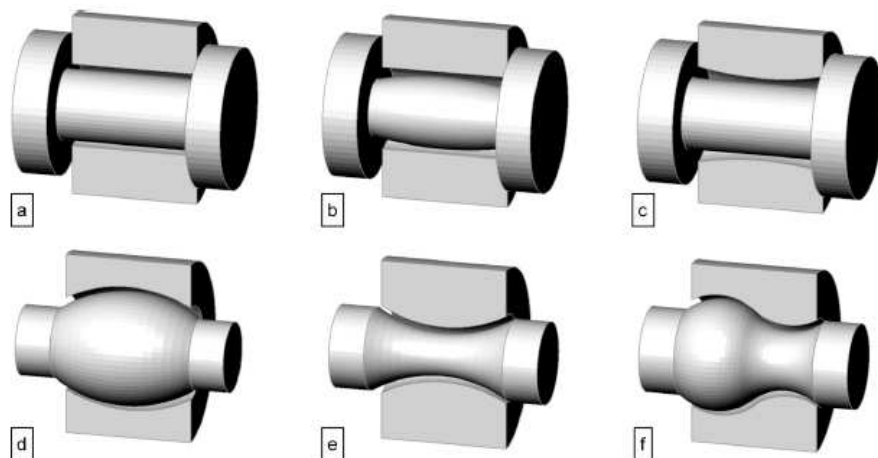


Figure 1.31: Examples of non-assembly joints [66]

Choice and optimization of the build direction is crucial, since clearance zones cannot be supported in order to avoid mechanism blocking.

A DfAM strategy that can be universally applied consists in the optimization of the part geometry by removing all the excess material. This approach is very different from the one applied for the production with Computer Numerical Control (CNC) milling machines, where it is preferred to minimize cutting operations. By minimizing the overall mass of the object, the AM production time, costs and material waste are considerably reduced. An example of this optimization strategy is shown in Figure 1.32.

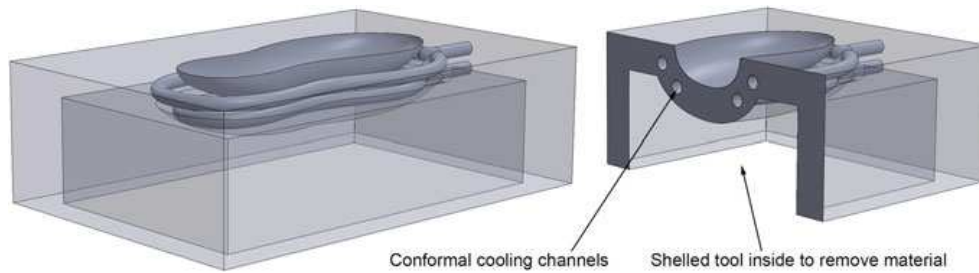


Figure 1.32: DfAM interior shelling of a tool [12]

### 1.2.2 DfAM: design and manufacturing constraints

The design freedom typical of AM technologies is remarkable but it is not unlimited. The designer must take into account limitations associated with CAD modelling tools and characteristics of the chosen AM process and material.

The creation of an accurate 3D model of the part to be produced is critical since AM production processes are automated and human intervention is minimal. Information provided to the AM machine must be correct and complete. Commercial CAD software are suitable for the design of components to be produced with traditional technologies, but do not provide adequate tools for rapid and efficient modelling of complex AM geometries. For example, generation and integration of porous or lattice structures is complex with traditional CAD and even simple task like specifying tolerances for each type of feature is not easy. Development of specific tools for the creation of complex geometries and for an efficient data exchange is necessary. A strategy used to facilitate modelling of complex parts consists on acquiring a 3D model through a laser/structured light scanner, this technique is quite useful when it is necessary to guarantee the coupling with pre-existing objects or for medical applications. New file formats are being developed in order to exchange geometry data efficiently, including 3D models with lattice structures and variable porosity materials [67].

The choice of the build direction is a relevant parameter that significantly affects the quality of the final result; DfAM guidelines specify the effect of this parameter on mechanical properties and surface finish, helping the designer to choose the best compromise without having to perform an expensive trial and error phase. The layer-by-layer addition of

material typical of AM, causes the formation of a characteristic surface roughness at the interface between the layers; this phenomenon is called staircase effect (Figure 1.33).

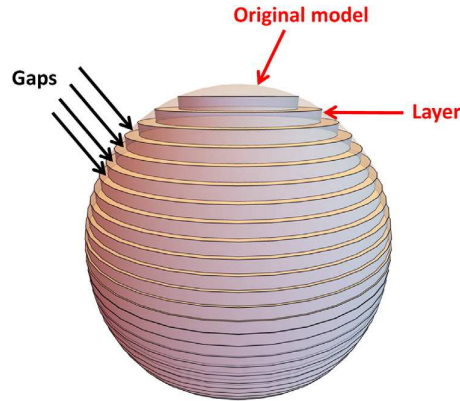


Figure 1.33: Staircase effect due to layer-by-layer material addition typical of AM [68]

In addition to increased surface roughness, defects formation that could affect fatigue life of the component is more likely at the interface between the layers. Orientation choice can help to obtain lower roughness functional surfaces, especially where post-finishing operations are not feasible. Figure 1.34 shows that when the angle between the surface and the build platform is lower, roughness increases, until the inclination is so low that correct realization of the feature is impossible; in this case better positioning of the component could be beneficial, if different positioning is not feasible support structures have to be introduced.

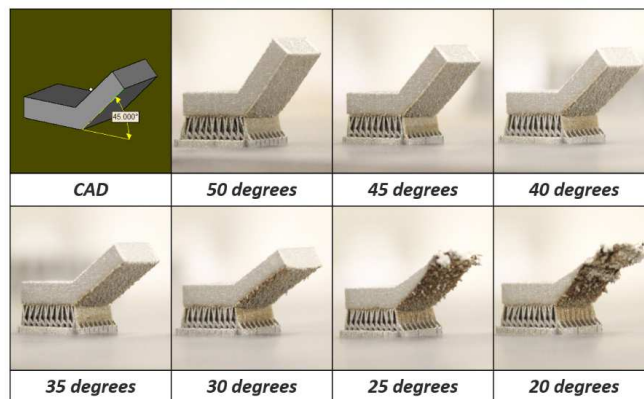


Figure 1.34: Effect of feature positioning on manufacturability and surface roughness [69]

The critical overhang angle depends on many factors, in particular on the LM material and equipment used. In general, surfaces that are inclined more than  $45^\circ$  with respect to the build platform do not require supports. If this angle is lower than  $45^\circ$  the surface roughness worsens rapidly. Inclined surfaces, not being supported by solid material, grow directly on the powder bed; hence, the laser source penetrates the powder bed causing the unwanted formation of agglomerates. This phenomenon does not happen using support structures that help dissipate heat through the build platform.

In order to obtain a better surface finish, for LM process it is possible to implement the re-melting strategy, an example is shown in Figure 1.35.

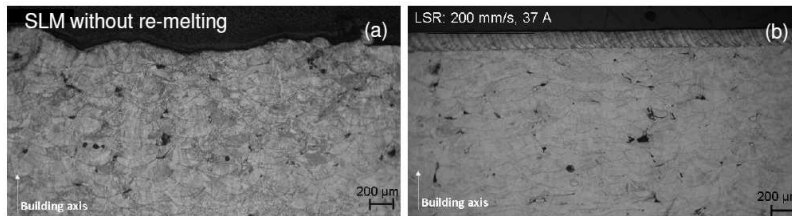


Figure 1.35: Surface roughness enhancement with laser re-melting [70]

DfAM suggests to look for the orientation of the component that allows to reduce layer's section to limit thermal stresses accumulation; moreover it suggests to find the orientation of the part that allows to avoid sudden section's variations, which could favour crack formation. Generally, the result of this strategy implies component orientations that increase the overall height and therefore the number of layers to be produced, increasing production time and costs [12].

Support structures are fundamental to ensure the success of the LM process. They are necessary to guarantee the correct adhesion between the component and the build platform, allowing easy separation at the end of the process by cutting saw or Electrical Discharge Machining (EDM). Furthermore, LM process involves the fusion and solidification of the feedstock material; due to the high thermal gradient, material undergoes a very rapid thermal cycle which determines strong residual thermal stresses. Due to thermal stresses, permanent plastic deformation accumulates causing component distortion; supports have to counteract the accumulated thermal stresses in order to avoid unwanted distortion until the stress relieving heat treatment. Supports have to maintain the shape of the component until the heat treatment, in addition to this pure mechanical function, supports act as a pathway for heat conduction in order to better dissipate the heat towards the construction platform thus reducing the accumulation of thermal stresses. DfAM guidelines suggest limiting supports use as much as possible, being waste material to be removed at the end of the process and determining an increase of supported surfaces roughness. This goal can be achieved by changing the orientation of the part in order to reduce undercuts, maximizing the number of self-supporting features; moreover, the designer have to take into account the need to effectively dissipate heat, especially near overhanging surfaces. Selecting type, dimensions and position of supports for overhanging surfaces is the most critical support generation task; thermal conductivity is considerably lower for metal powders compared to solid material, accentuating heat and residual thermal stresses accumulation. Surfaces that are inclined beyond a certain angle with respect to the build platform, called the overhang critical angle, must be supported. Figure 1.36 shows the critical angle for unsupported overhanging surfaces and the deformation caused by heat accumulation near the overhang surface.

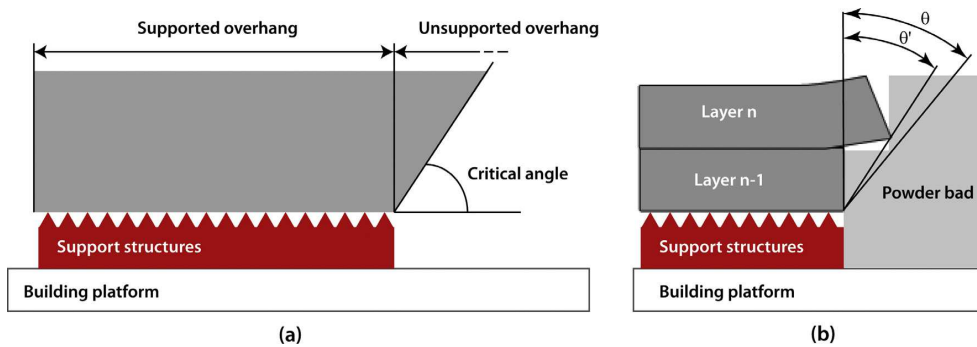


Figure 1.36: Warping effect due to unsupported overhang [71]

The choice of build direction and supports positioning significantly influence dimensional accuracy, residual deformations and surface roughness of LM-manufactured components. Therefore, it is necessary to recognize the best compromise that safeguards the most important surfaces and features, trying to minimize post-processing. Best solution is a trade-off between minimum build time, easily removable supports, good surface quality and reduced warpage [12]. At the same time, the designer must try to generate features with shapes and sizes (e.g. holes size and shape, wall thickness, gaps) that do not require the use of supports, while guaranteeing functionality; it is therefore essential to re-think and re-design traditional geometric shapes commonly used to design non-AM parts. An example of redesign for AM is shown in Figure 1.37, where cooling channels with different cross sections are compared, highlighting those suitable for AM.

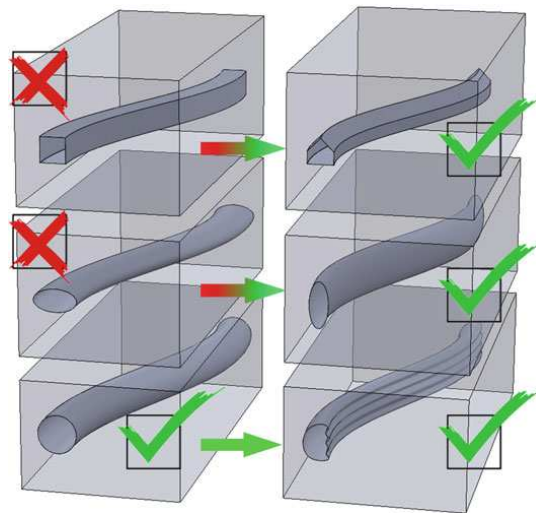


Figure 1.37: Evaluation of AM manufacturability for different cooling channel cross sections [12]

In the case of overhanging features parallel to the build platform, DfAM suggests adding support structures in order to guarantee feasibility, better accuracy and surface finish. In Figure 1.38a it is possible to observe rapid deterioration of the lower surface of the overhang; when the overhanging length is greater than 0.5 mm, supporting structures

are highly advisable. Another type of overhanging structure similar to the previous one, is composed by a surface parallel to the build platform supported by two or more fixed structures, generating a shape similar to a bridge. An example of this geometry is shown in Figure 1.38b; overhanging surfaces longer than 2 mm have to be supported.

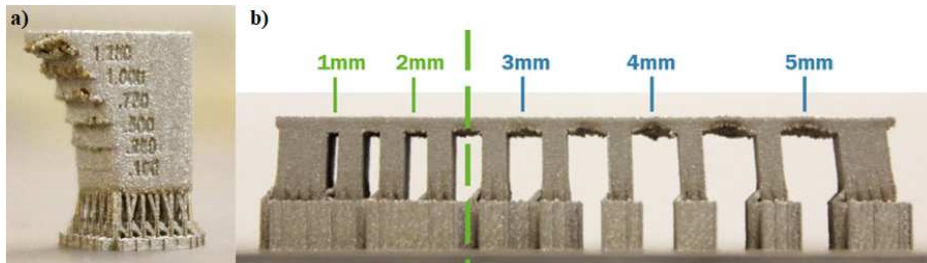


Figure 1.38: Unsupported overhangs (a) and bridges (b) benchmarks [12]

To reduce thermal stresses accumulation and stress concentration, DfAM recommends removal of sudden cross section variations, replace sharp edges with fillets and avoid designs with large masses of material.

Horizontal holes are a rather common feature, DfAM suggests using supports or modifying the hole shape if the diameter is greater than 8 mm. Common hole shapes that can be printed without the need for support material are elliptical, teardrop and diamond [12]. An example of LM-manufactured horizontal holes benchmark is shown in Figure 1.39.

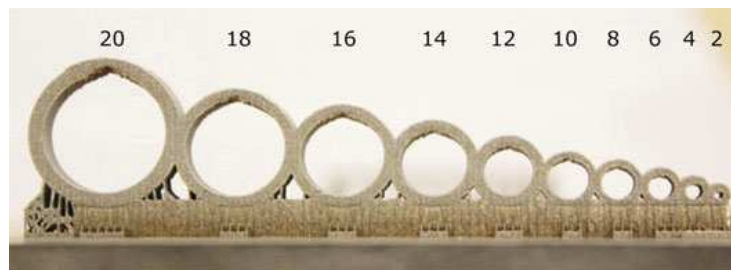


Figure 1.39: LM-manufactured horizontal holes without supports benchmark [12]

DfAM guidelines help the designer positioning parts within the construction volume. A valid strategy to improve parts quality is to orientate objects in order to avoid bulky features, like long walls, positioned parallel to the coater blade; if during recoating the coater blade meets a large obstacle, it is more likely a non-uniform powder distribution due to blade impacts with surface defects or part warpage that may cause coater displacement or damage. Rotating the part around the vertical Z axis, in some cases it is possible to minimize the recoating force exerted on already solidified parts; this is quite useful dealing with delicate features such as thin walls. Avoiding positioning parts lined up directly behind each other helps to improve layer coating uniformity and to prevent defects propagation due to coater damage. In general, parts should be positioned in order to allow uniform and gradual layer recoating.



The use of specifically designed benchmarks can help establish feature specific limits with higher accuracy compared to those suggested by DfAM guidelines. Examples of benchmarks for testing inclined surfaces quality, dimensional accuracy and manufacturability of small features are visible in Figure 1.40.

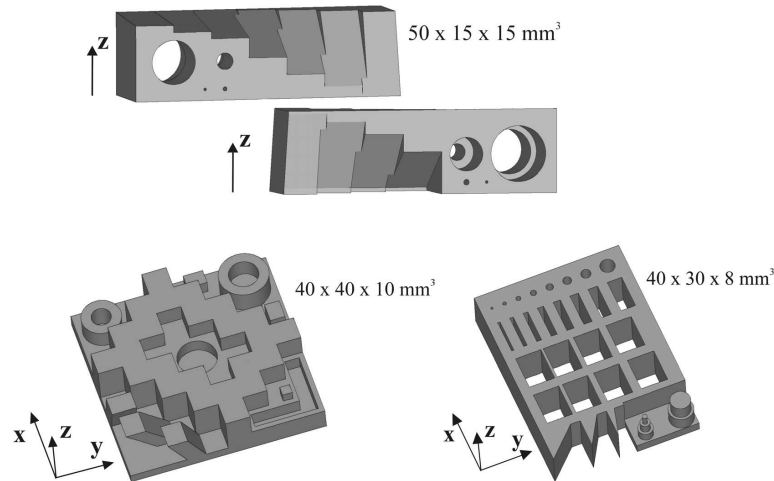


Figure 1.40: Examples of benchmarks for sloping angles, accuracy and manufacturability of small feature testing [34]

LM process offers a lot of advantages that could be exploited during design process, nevertheless quality control is quite challenging. Presence of defects or unexpected porosities have to be assessed; AM materials have different mechanical and microstructural properties compared to solid materials, for this reason specimens of as-built and heat treated materials should be tested; appropriate non-destructive methods for measurement of complex geometries, structures and internal channels have to be used [72].

### 1.2.3 DfAM for LM - applications

In previous paragraphs it has been specified several times that LM technology is slower and more expensive than conventional manufacturing technologies. When it is necessary to evaluate whether to use the LM technology to produce an object or not, it is necessary to verify whether added value due to AM design freedom justifies higher manufacturing costs. In this paragraph, some examples that demonstrate the usefulness of AM and DfAM to promote the creation of innovative high added value objects will be presented.

The first example concerns a hydraulic manifold optimization [12]. The starting geometry consists of a solid block in which holes have been drilled using a Numerical Control (NC) machine; holes interconnection forms a system of channels through which the fluid can flow (Figure 1.41).

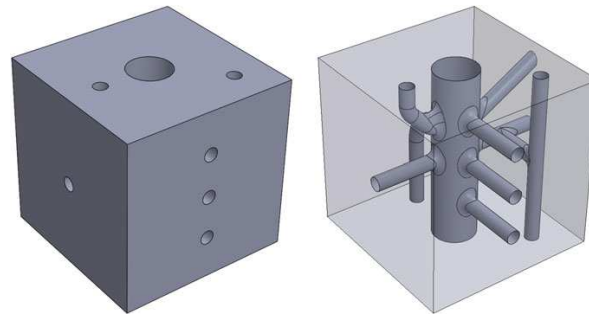


Figure 1.41: Hydraulic manifold external shape and integrated channels [12]

This item is designed to be manufactured with traditional machining processes; for this reason, operations have been designed to reduce the amount of material to be removed and to be feasible using standard tools. LM-manufacturing of massive geometries imply very high costs, due to the high number of hours needed to complete the process. Furthermore, as already specified in the paragraphs on DfAM, objects that include large full cross-sections are not suitable for AM production, since these areas are affected by residual thermal stresses accumulation that causes permanent deformations. Moreover, full-cross sections LM-manufacturing requires a lot of time that could be completely wasted if those areas do not add value to the object. One of the most important rules of DfAM is trying to avoid the production of large full cross-sections. Unlike traditional manufacturing techniques, with AM it is better to minimise the amount of material needed to produce the object, obtaining faster production and lower costs. To reduce printing costs, in addition to mass minimization by means of excess material removal, it is convenient to orient the part to decrease the overall height along the build axis, reducing layer number and therefore recoating time. This strategy has to be applied taking into account that the orientation has an effect on mechanical properties, accuracy, surface finish and positioning of supports; therefore, the optimal solution is a compromise that optimizes these aspects according to the specific case.

Considering the hydraulic manifold, the first operation to optimise the geometry for AM is excess material removal. Furthermore, it is necessary to modify the geometry in order to reduce the need for supporting structures, determining the orientation that helps to achieve this result while limiting the height along the build axis. Optimized geometry includes only the channels through which the fluid flows, removing the excess material; moreover, holes made by drilling generate sharp-edged channels, whereas LM-manufacturing allows to enhance fluid flow smoothing those areas with fillets. Part orientation influences which surfaces need to be supported. Support optimization is a compromise between supported area minimization and total height reduction, preserving accuracy and surface roughness of the most important features. If mass reduction is not a priority, it is advisable to integrate support structures transforming them into permanent features of the part, avoiding removal and post processing operations. The result of DfAM multi-objective optimization of the hydraulic manifold is shown in Figure 1.42.

|  |  |  |
|--|---|--|
|  | Solid block manifold  | Optimised DfAM manifold  |
| Scan time for hatch pattern              | 191 h 1 min 33 s  | 19 h 40 min 39 s   |
| Machine cost in metal@ \$65/h            | \$12,415.00   | \$1261.00  |
| Material weight                          | 7.411 kg  | 0.558 kg   |
| Material cost @ \$70/kg + 10% waste      | \$570.64  | \$42.96  |
| Bureau quotes for part in 316L stainless | \$15,293.82   | \$1986.25  |

Figure 1.42: Hydraulic manifold DfAM multi-objective optimization [12]

Optimized manifold AM production cost is one order of magnitude lower compared to that of the solid block manifold; this result is due to machine time reduction, thanks to the optimized geometry that significantly reduced the excess material. This case study proved that DfAM is fundamental for successful AM components design.

Bicycles used by professional cyclists and enthusiasts are optimized to reduce mass and help cyclists overcome steep slopes. The bike stem could be easily optimized and LM-manufactured, since it fits nicely inside typical LM machines build volume. Obtaining a new AM geometry mechanically equivalent to those obtained from pipe welding but lighter can be an advantage for the aforementioned categories of users. Being a component that can have a significant impact on safety, there are regulations that establish test loads (ISO 4210-5:2014) and maximum deformations allowed (ISO 4210-2:2015).

The first step consists in the generation of the starting geometry; two separate domains must be defined, the first one composed by all the parts that have to be optimized (design space) and the second one by all the regions that should remain unchanged (usually where constraints and loads are applied). The design space could be modelled as a uniform full volume that defines the maximum footprint; this choice provides maximum freedom, leaving to TO algorithm the task of calculating optimal material distribution. In the case of the bicycle stem, design space is designed with the aforementioned approach; box-shaped starting geometry is shown in Figure 1.43, where brown parallelepiped represents the design volume and grey cylinders the connection sleeves between stem and handlebar/fork.

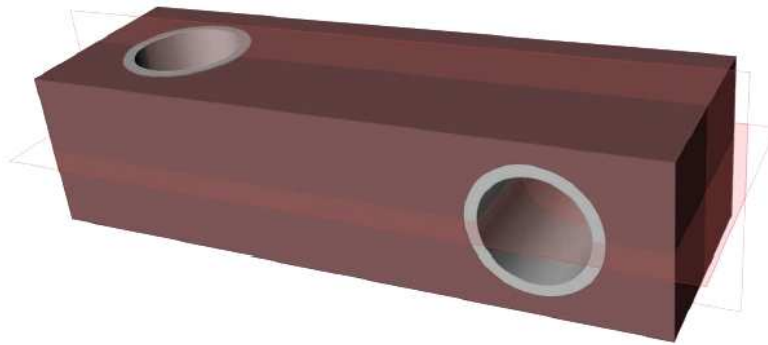


Figure 1.43: Bike stem starting geometry and design space definition (LAMA FVG™)

The second step of DfAM / TO consists in the definition of material properties (titanium alloy - Ti6Al4V) and definition of constraints and loads. As mentioned before, the ISO 4210-5:2014 standard defines test conditions for bicycle steering components; two different testing conditions have to be analysed: the first one involves an eccentric load which generates a flexion / torsion load (Figure 1.44a) and the second an inclined load (Figure 1.44b).

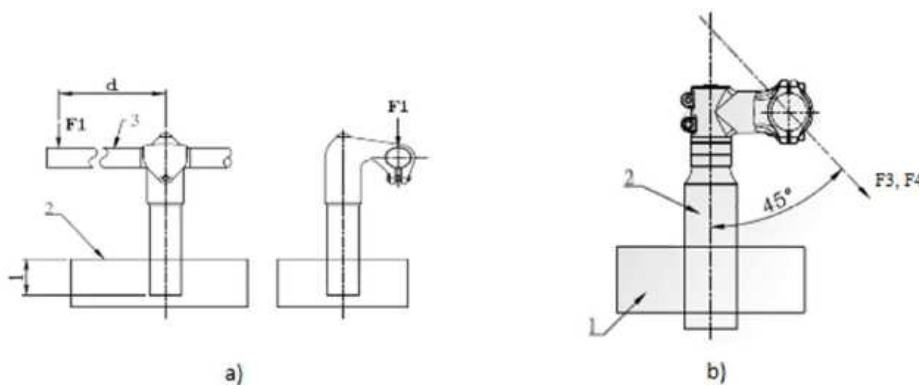


Figure 1.44: Bike stem testing conditions - ISO 4210-5:2014

The optimization problem is therefore completely defined; therefore, it is possible to proceed with TO in order to minimize mass with appropriate safety factor and displacements constraints. The resulting geometry is shown in Figure 1.45.

Using modelling tools integrated in the TO and CAD software, the optimized design is converted into a manufacturable product by wrapping obtained geometry with NURBS. Connecting sleeves have been modified to facilitate assembly and DfAM guidelines have been applied to remove excess material and minimize the need for supports (shape and size of holes, overhang angle of inclined surfaces). SLM-manufactured titanium alloy optimized bike stem is shown in Figure 1.46.

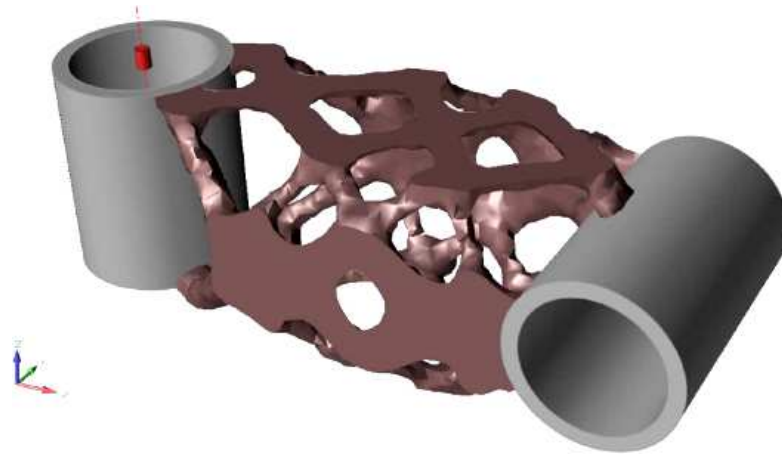


Figure 1.45: Bike stem TO result (LAMA FVG™)



Figure 1.46: SLM-manufactured titanium alloy optimized bike stem (LAMA FVG™)

### 1.3 State of the art on lattice and porous structures

In previous paragraphs AM techniques for metals have been analyzed. This category of production processes is particularly suitable for the production of mechanical components characterized by complex geometries that can guarantee high thermo-mechanical performance. In this paragraph lattice/porous structures are analyzed; these structures

are a very useful tool as they offer the chance of developing innovative functions and better thermo-mechanical properties, enhancing design freedom with respect to what could be done with solid materials. It is possible to obtain lightweight structures with high specific strength, improve vibration damping and heat exchange, enhance bio-compatibility for medical applications. Furthermore, the geometric complexity of these structures makes them particularly suitable for being produced with AM technologies.

Available scientific literature suggest the need to deepen the study on porous/lattice structures mechanical properties in order to characterize their static/dynamic behavior and evaluate their applicability for the production of lightweight, high-performance components. In light of this, the investigation of these structures is the subject of this thesis and is deepened in the following chapters.

Porous / lattice structures are formed by the ordered or stochastic repetition of unit cells; depending on the geometry of these cells the resulting porosity can be open or closed. Mechanical properties of porous / lattice structures are influenced by a large number of parameters; the main ones are unit cell shape, relative porosity, geometric parameters such as strut diameter, wall thickness and cell size and finally AM process and the material chosen. The choice of unit cell's type and geometric properties allows the designer to create structures with tailored variable properties according to the specific case needs. Lattice structures are particularly interesting since depending on their topology they exhibit bending-dominated or stretch-dominated under load behaviour. These structures are therefore suitable to be optimized to obtain the desired mechanical behaviour, point by point; for example, porous / lattice structures with high specific mechanical strength and good damping properties could be designed to fulfil requirements of specific applications. Lattice structures are easier to exploit than foams, as it is possible generate porous materials with tuneable mechanical properties. In previous paragraphs it was specified that lattice structures are very useful to obtain lightweight high-performance designs and to implement new functionalities and thermo-mechanical properties, not achievable with traditional manufacturing technologies. LM technology is the best choice for the production of lattice / porous structure, since its complex geometry, composed by the repetition of unit cells, is not a drawback. However, manufacturing constraints linked to LM process limitations must be respected. Moreover, it is necessary to assess their mechanical and fatigue properties, in order to provide designers valuable information to develop high-performance innovative products. In this paragraph hints on manufacturability constraints for lattices, in terms of feature dimensions and inclination, are given. Furthermore, an insight on testing methodology to assess lattices mechanical properties and their results is given.

### 1.3.1 Lattices and porous structures geometries

Mechanical properties of lattices are very important for designers trying to exploit them as high performance structural or filler materials. Cell topology, its characteristic dimensions, relative density (ratio between lattice density and solid material density  $\rho/\rho_s$ ) and solid material properties, significantly influence the overall mechanical properties of the porous material.

Cellular structures, like foams and lattices, can be classified according to their mechanical behaviour. In particular, it is possible to identify two different types of cellular structures species: the first, typical of foams and some types of lattices, is bending dominated while the second, typical of triangulated lattice structures, is stretch dominated [73], [74].

Figure 1.47 shows the compressive stress-strain curve of a bending dominated cell. External stress causes bending deformation of the structure. The material exhibits a linear elastic behaviour until the elastic limit is reached, afterwards the cell yields (Figure 1.48 a), buckles (Figure 1.48 b) or fractures (Figure 1.48 c). The cell deformation continues at almost constant stress, until the opposite faces of the cell come into contact causing a rapid stress increase.

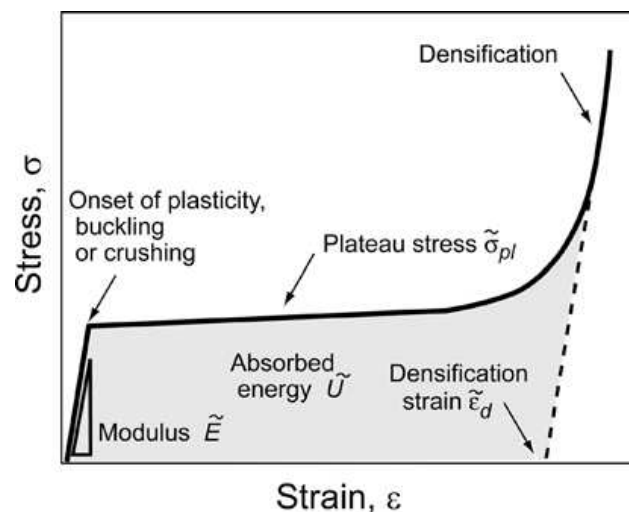


Figure 1.47: Stress-strain curve for bending dominated cellular structures [73]

The stress-strain curve for stretch dominated cellular structures is shown in Figure 1.49. External loading causes tensile or compressive stress on the members that make up the structure. Initially the material exhibits a linear elastic behaviour, hence the elastic limit is reached when one or more structure's elements yield plastically, buckle, or fracture. After initial yielding plastic buckling or brittle collapse occurs, this leads to post-yield softening. Similar to bending dominated cells, when the opposite faces of the cell come into contact there is a sudden stress increase.

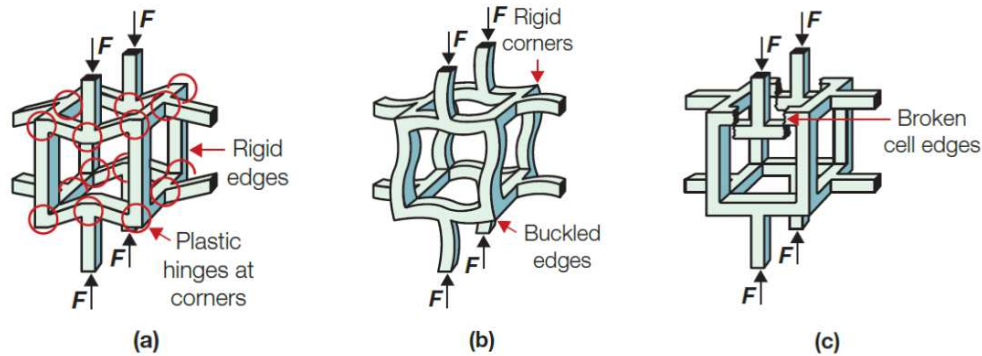


Figure 1.48: Bending dominated cellular structures collapse. (a) plastic (b) elastomeric (c) brittle [74]

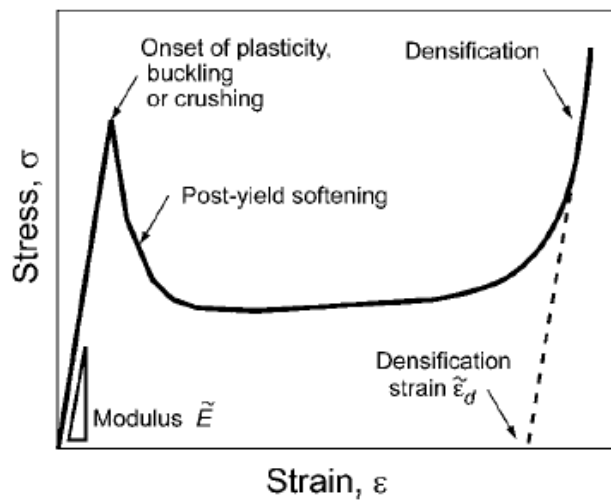


Figure 1.49: Stress Stress-strain curve for stretch dominated cellular structures [73]

Stretch dominated structures stiffness and initial collapse strength are higher compared to those of bending dominated structures with the same relative density. Therefore, stretch dominated structures are the best choice for lightweight structural applications. Bending dominated structures are useful for applications that require good energy absorption properties, having a stress-strain curve characterized by a long flat plateau [73], [74].

A parameter that can give information on the under-load mechanical behaviour of lattices having different topologies, is the Maxwell number ( $M$ ); it relates the degrees of freedom of the unit cell with the expected mechanical behaviour. This parameter, defined as in Equation 1.5 for 3D lattices, is a function of the number of beams ( $s$ ) and of connection nodes ( $n$ ) of the lattice [75].

$$M = s - 3n + 6 \tag{1.5}$$



If  $M < 0$  the lattice is under-stiff and has a bending dominated behaviour, with higher compliance and lower strength. If  $M = 0$  the lattice is just-stiff (static equilibrium) and loads acting on individual struts can be calculated analytically through equilibrium equations. The under-load behaviour is stretch dominated. If  $M > 0$  the lattice is over-stiff, since it is made up of a large number of struts. Under-load behaviour is stretch-dominated, compliance is low and strength is high. Some examples of lattice structures with different topologies<sup>1</sup> and the corresponding Maxwell numbers are shown in Figure 1.50.







|                                 | BCC   | FCCZ  | FBCCZ   | FBCCXYZ  | BCCZ  | FCC   |
|---------------------------------|---|---|---|--|---|---|
| Cell type                       |  |  |  |  |  |  |
| Struts, $s$                     | 8   | 20  | 28  | 44   | 12  | 16  |
| Joints, $n$                     | 9   | 12  | 13  | 15   | 9   | 12  |
| Maxwell number, $M$             | -13   | -10   | -5  | 5  | -9  | -14   |
| Strut aligned to load direction | No  | Yes   | Yes   | Yes  | Yes   | No  |

Figure 1.50: Examples of lattices topologies and corresponding Maxwell number [76]

The Maxwell number can help to identify the under-load behaviour of lattice structures; however, it is not sufficient since depending on the topology and loading direction, unit cell stiffness and load capacity change significantly. For example, some of the structures in Figure 1.50 with struts oriented along the Z axis, despite having a negative Maxwell number, are particularly rigid and resistant if loaded along the Z axis.

### 1.3.2 Manufacturing constraints and mechanical properties

There are numerous studies that investigate LM-manufacturability and mechanical properties of lattice structures having different topologies and geometric dimensions. Most interesting materials, from an engineering point of view, used to produce LM-manufactured lattices are titanium, aluminium, stainless steel and nickel alloys. Leary et al. [77] studied SLM manufacturability and mechanical properties of Inconel 625 lattice structures. To assess manufacturing constraints, a full factorial DoE was devised in order to analyse the effect of inclination and circular cross-section strut diameter (two factors, ten levels). Figure 1.51 shows results obtained: red indicates that production is not possible, yellow the presence of defects and green a satisfactory LM process. The 0.1 mm diameter struts were not produced due to SLM equipment limitations and horizontal structures production ( $\alpha=0^\circ$ ) fails catastrophically. For low inclination angles the downward facing surface has higher roughness than the upward one.

<sup>1</sup>BCC: Body Centered Cubic, FCC: Face Centered Cubic, BCCZ: Body Centered Cubic with Z struts, FCCZ: Face Centered Cubic with Z struts, FBCCZ: Face and Body Centered Cubic with Z struts, FBCCXYZ: Face and Body Centered Cubic with XYZ struts.

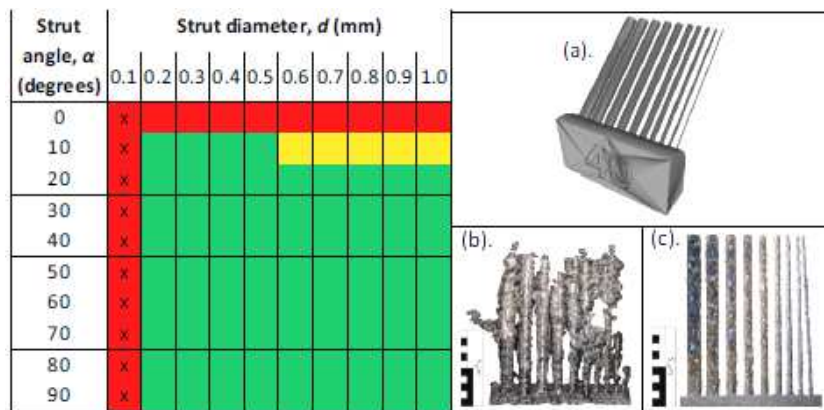


Figure 1.51: Inconel 625 cantilever lattice struts manufacturability [77]

The study proceeds with the production of full-scale lattice specimens with different topologies (BCC-BCCZ-FCC-FCCZ). Struts diameter chosen is equal to 0.3 mm, as it guarantees SLM manufacturability. Specimens relative density is higher compared to that of CAD models; this is due to undesired adhesion of powder agglomerates near the melt pool, especially in proximity of overhanging surfaces and struts intersections. For the same reason, inclined struts diameter is greater than that of struts oriented along the build direction. To assess mechanical properties and failure modes, specimens were subjected to quasi-static uniaxial compression tests. In general, Inconel 625 lattice structures have high ductility, proving to be excellent as energy-absorbing structures. Specimens incorporating FCC structures have higher compressive modulus and strength than BCC ones. The addition of struts along the build direction (Z axis) tends to enhance stiffness and mechanical strength, especially if the load is applied along Z axis; moreover, energy absorption capacity increases and is higher for FCCZ and BCCZ. BCC and FCC structures exhibit bending dominated behaviour, while BCCZ and FCCZ stretch dominated. Through the acquisition of high-resolution images during the compression test, qualitative data on failure mode and mechanical behaviour of the different topologies have been collected. All the lattices analysed show a linear behaviour for deformations up to 2%, then the BCCZ and FCCZ lattices show localized catastrophic collapses followed by densification while the BCC and FCC deformation behaviour is mostly homogeneous. These results confirm bending dominated behaviour of the BCC and FCC topologies and stretch dominated of BCCZ and FCCZ. However, this behaviour can change; in fact it has been observed the transition from bending dominated to stretch dominated behaviour when cell size exceeds a certain threshold. The stress-strain curves obtained from the uniaxial compression test of 2 mm and 4 mm unit cells lattices are shown in Figure 1.52.

Authors compared experimental results with FEA, finding that the latter is suitable for lattice structures behaviour prediction. The choice of the unit cell topology is therefore a key parameter to determine whether to favour compliance or mechanical resistance. To further finely tune the mechanical behaviour, it is possible to alter the cell size. Promising

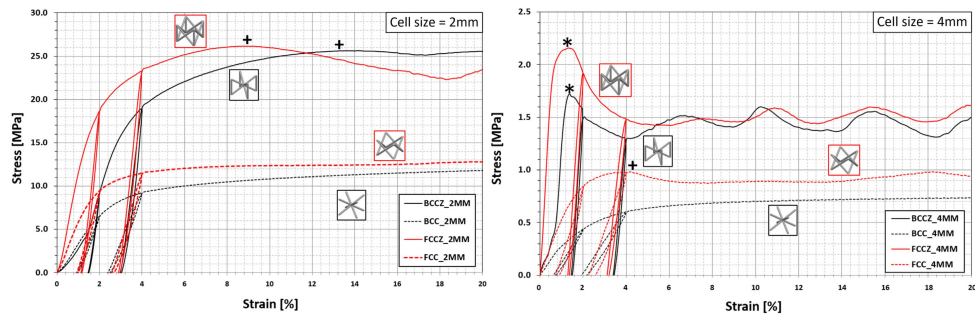


Figure 1.52: Uniaxial compression stress-strain responses of Inconel 625 specimens [77]

results obtained and poor manufacturability of Inconel by means of traditional technologies, suggest the opportunity to use AM to produce high added value products such as those integrating lattice structures.

Mazur et al. [76] performed a study similar to the previous one investigating manufacturing constraints and mechanical properties of LM-manufactured Ti6Al4V and AlSi12Mg lattice structures. As already mentioned before, LM process limitations constrain the range of feasible geometries. In the case of lattice structures, it is necessary to avoid using supports, as removal would be very complex or impossible. Therefore, to ensure manufacturability without the use of supports, unit cell's struts inclination should be limited in order to comply with the critical overhang angle limitation; moreover, the minimum diameter of circular cross-section struts depends on the specific LM equipment minimum manufacturable feature size. Authors studied manufacturing limits of Ti6Al4V and AlSi12Mg lattice structures through a full-factorial Design of Experiments (DoE); the effect of struts inclination angle and diameter on manufacturability of cantilever struts specimens was evaluated, obtaining results shown in Figure 1.53. The table illustrates manufacturability of inclined struts: green indicates geometric parameters for which the final quality of the part is excellent, yellow indicates that the struts have defects such as low surface finish but are still functional, while red indicates the structure collapse. Strut diameter has little or no influence on manufacturability of overhanging struts, except for very small diameters that cannot be reproduced due to SLM machine's limitations.

| Material        |    | Ti6Al4V |     |     |     |     |     |     |     |     |     | AlSi12Mg |     |     |     |     |     |     |     |     |     |
|-----------------|----|---------|-----|-----|-----|-----|-----|-----|-----|-----|-----|----------|-----|-----|-----|-----|-----|-----|-----|-----|-----|
| Diam. (mm)      |    | 0.1     | 0.2 | 0.3 | 0.4 | 0.5 | 0.6 | 0.7 | 0.8 | 0.9 | 1.0 | 0.1      | 0.2 | 0.3 | 0.4 | 0.5 | 0.6 | 0.7 | 0.8 | 0.9 | 1.0 |
| Angle (degrees) | 0  | L       | L   | L   | L   | L   | L   | L   | L   | L   | L   | L        | L   | L   | L   | L   | L   | L   | L   | L   | L   |
|                 | 10 | L       | L   | M   | M   | M   | M   | M   | L   | L   | L   | L        | L   | L   | L   | L   | M   | M   | M   | M   | M   |
|                 | 20 | L       | L   | H   | H   | H   | H   | H   | H   | H   | H   | L        | L   | L   | L   | L   | M   | M   | M   | M   | M   |
|                 | 30 | L       | M   | H   | H   | H   | H   | H   | H   | H   | H   | L        | L   | L   | M   | H   | H   | H   | H   | H   | H   |
|                 | 40 | L       | H   | H   | H   | H   | H   | H   | H   | H   | H   | L        | L   | L   | H   | H   | H   | H   | H   | H   | H   |
|                 | 50 | L       | H   | H   | H   | H   | H   | H   | H   | H   | H   | L        | L   | L   | H   | H   | H   | H   | H   | H   | H   |
| 90              | L  | H       | H   | H   | H   | H   | H   | H   | H   | H   | L   | L        | L   | H   | H   | H   | H   | H   | H   | H   |     |

Figure 1.53: Ti6Al4V and AlSi12Mg cantilever lattice struts manufacturability [76]

Analysing Figure 1.53 it is possible to conclude that all the topologies shown in Figure 1.50, excluding the FBCCXYZ which contains horizontal struts, could be LM-manufactured. However, if the horizontal struts are supported on both sides forming a “bridge” manufacturability is good as long as the undercut distance is below a certain threshold, as shown in previous paragraphs on DfAM. The study carries out an additional DoE to evaluate the effect of struts diameter and distance between supports on the manufacturability of horizontal struts, demonstrating their producibility when the overhanging distance does not exceed 4-5 mm. SEM images confirm dimensional accuracy and the surface roughness worsening for overhanging features. The work continues with the analysis of mechanical properties of Ti6Al4V and AlSi12Mg lattice specimens: Ti6Al4V specimens with BCC, FCCZ, FBCCZ, FBCCZ and FBCCXYZ configurations, cell dimensions equal to 2 and 3 mm and struts diameter equal to 0.3 mm; AlSi12Mg specimens with BCC, BCCZ, FCC, FCCZ and FBCCZ topologies, cubic cell size equal to 7.5 mm and strut diameter equal to 1 mm. DoE on Ti6Al4V includes 3D printing of multiple series of Ti6Al4V cubic-shaped specimens with increasing number of cells (33, 53, 73, 103). To check the coherence between as-built Ti6Al4V specimens and CAD geometries, the nominal relative density obtained from the 3D model and the actual relative density of the specimens were compared; results showed that specimens relative density is 20-30% greater than the nominal one. This last result confirms the effect of undesired adhesion of partially melted powders, concentrated near overhangs and nodes, on specimens geometry. AlSi12Mg specimens were analysed using CT and an optical microscope, highlighting an increase of downward facing overhanging surfaces roughness and of geometrical defects at the nodes (Figure 1.54).

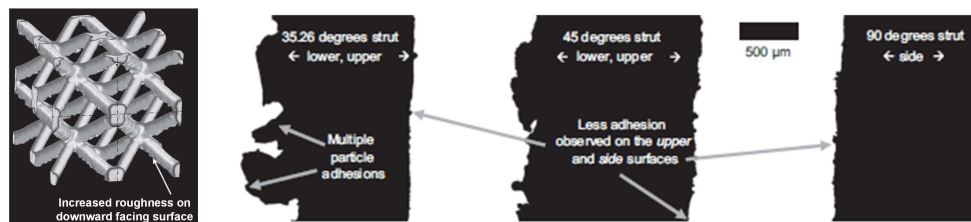


Figure 1.54: AlSi12Mg BCC unit cell CT and optical microscopy of vertical and inclined struts [76]

Then the specimens were tested with a quasi-static uniaxial compression test to assess their mechanical behaviour. Stress - strain chart for AlSi12Mg specimens is shown in Figure 1.55.

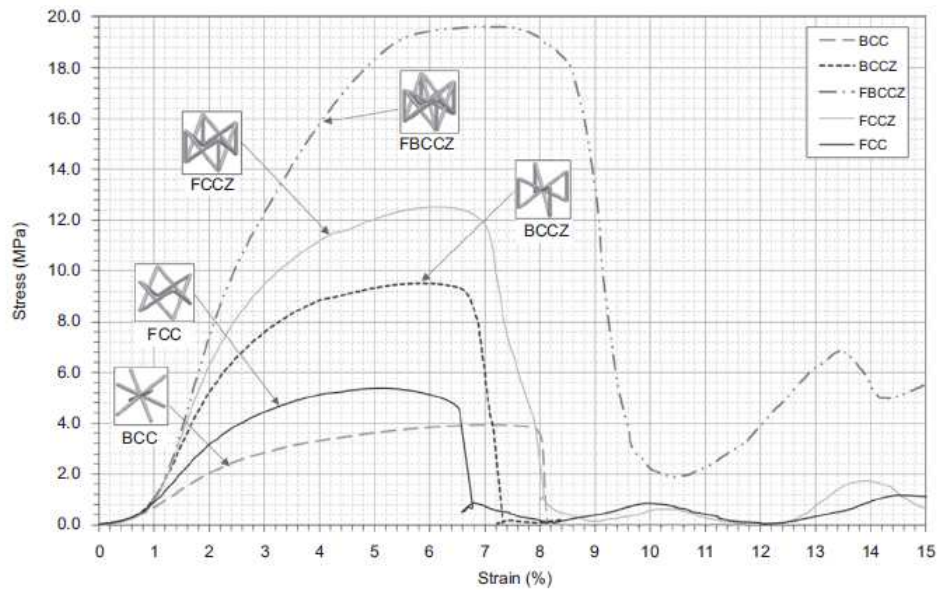


Figure 1.55: Stress-strain chart of AlSi12Mg lattice structures [76]

Images were acquired during compression tests to observe the deformation response and failure modes. Failure modes and fracture surfaces were analysed in detail with SEM images. Experimental data were compared with FEA of CT data, helping to understand deformation and fracture mechanisms and mechanical properties. Main results are listed below [76]:

- Data obtained from quasi-static uniaxial compression tests evidenced that Young's modulus is always lower than the compression modulus at 1% and 2% strain. This behavior, different from that of solid materials, is due to local plasticization and is important because it helps to avoid underestimating lattice stiffness.
- BCC specimens have the lowest compression modulus due to their under-stiff topology and bending-dominated behavior. The highest compression moduli are those of the FBCCXYZ (titanium) and FBCCZ (aluminum). The FCCZ specimens have the highest specific strength and modulus, although they have lower absolute values than the FBCCZs. This means that the FCCZ topology guarantees better performance for compressive loading when aiming at maximization of strength and stiffness-to-weight ratios.
- BCC specimens have the lowest values of absolute and specific strength. The unit cell topologies that have the highest strength values are the FBCCXYZ and FCCZ for titanium specimens whereas FBCCZ and FCCZ for aluminum ones.
- The analysis of SEM images together with those recorded during the compression tests, allowed to verify that failure modes occurred through bending of inclined struts and buckling of the vertical ones, followed by strut failure and cell collapse;

the phenomenon develops across diagonal shear bands. Under-stiff topologies, with low Maxwell number and without struts along the Z axis, such as the BCC and FCC, have demonstrated their ability to withstand large deformations before failure; these topologies are appropriated if it is necessary to guarantee high compliance. In the case of high stiffness topologies, like FBCCZ and FBCCXYZ, failure occurs by horizontal layer crushing, making them suitable as energy-absorbing structures.

- The Maxwell number is not sufficient to forecast whether a given lattice topology has bending-dominated or stretch-dominated behaviour. The analysis of uniaxial compression tests data of FCCZ and FBCCZ lattices evidenced a stretch-dominated behavior, unlike Maxwell criterion prediction. Therefore, the Maxwell criterion is not able to take into account the effect of the loading direction on cell stiffness.

Similar studies have been carried out to assess manufacturability and mechanical behaviour of lattice structures produced with LM technology using different materials (e.g. aluminium [78], [79], titanium [76], [80]–[82], stainless steel [83]–[85], cobalt chrome alloys [86]).

### 1.3.3 Dynamic behaviour of lattice structures

Lattice structures allow the production of controlled porosity materials, which can be used to design structures with point-by-point tailored mechanical properties. In the previous paragraphs some methodologies for lattices mechanical behaviour assessment and the results related to the analysis of Titanium, Aluminium and Inconel alloy lattices were analysed. A fair number of works analysing static and fatigue behaviour of LM-manufactured lattices with different topologies were already published. However, to date, there are not many publications investigating the damping behaviour of such structures, although finding a way to enhance damping is desirable for a large number of industrial applications. It has already been observed that AM technologies are particularly suitable for high performance lightweight structures manufacturing, like those obtained exploiting topology optimization; however, excess material removal and geometries containing slender features can reduce the intrinsic damping properties of the structure. The integration of lattice structures with good damping properties can therefore help to improve dynamic response of mechanical components, especially when dealing with lightweight TO structures.

Rosa et al. [64] studied the damping properties of 316L stainless steel specimens integrating lattice structures to assess if it is possible to exploit them as high-damping filler materials for mechanical components, when required by the specific application. The topology of the lattice unit cell chosen by the authors is the BCC, this choice is justified by its high structural performance and uniform under-load mechanical behaviour; moreover, BCC

topology eased design and testing of specimens to be analysed by means of a traditional universal testing machine, normally used for full cross-section specimens testing. CAD model of the rectangular cross-section specimen integrating six layers of BCC unit cells, with 4 mm sides and 1 mm circular cross-section struts diameter, is shown in Figure 1.56.

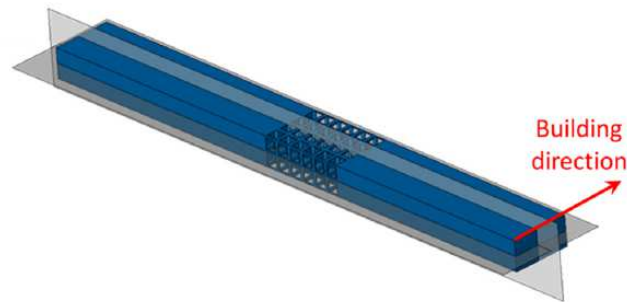


Figure 1.56: CAD model of 316L specimen integrating BCC lattice [64]

Prior to the experimental phase, the authors performed a finite element analysis in order to design specimens compatible with the universal testing machine and strain gauges limits. The FE analysis of the resulting geometry, allowed an in-detail observation of specimen's qualitative mechanical behaviour, helping to understand experimental results. In particular, FEA helped to avoid specimen's failure and to identify maximum stress and strain areas. Analysing result it was assessed that yielding begins in struts oriented along the loading direction in proximity of nodes. The elasto-plastic model chosen does not take into account the ratchetting phenomenon; hence, the yield occurs only during the first load cycle, then the behaviour is purely elastic without accumulation of plastic deformation. The chosen cyclic load amplitude has been selected to obtain high elasto-plastic deformations, responsible of energy dissipation and damping, avoiding specimen's failure. 316L stainless steel samples were manufactured by means of a SLM machine. Surface and microstructural analysis were performed by SEM. Surface roughness is high and powder adhesion is visible near overhanging surfaces. Microstructural analysis evidenced typical characteristics of SLM-manufactured materials; defects such as internal porosity and cracks at struts intersections have been noted.

Tests to measure the damping characteristics of the BCC lattice were carried out by controlling applied force and measuring the elongation with extensimeter (Figure 1.57).

Measurements were performed on lattice and full cross-section (reference) specimens, to assess the effect on damping properties. The damping effect due to internal friction was calculated in terms of delay between stress and deformation ( $\tan\delta$ ), applying loads of different amplitude and frequency. Observing hysteretic BCC specimens stress-strain curve in Figure 1.58a, it is clear that energy is dissipated during loading cycles. Moreover, as shown in Figure 1.58b, the damping capacity of BCC specimens is higher than the reference one.



Figure 1.57: BCC lattice dynamic test experimental setup [64]

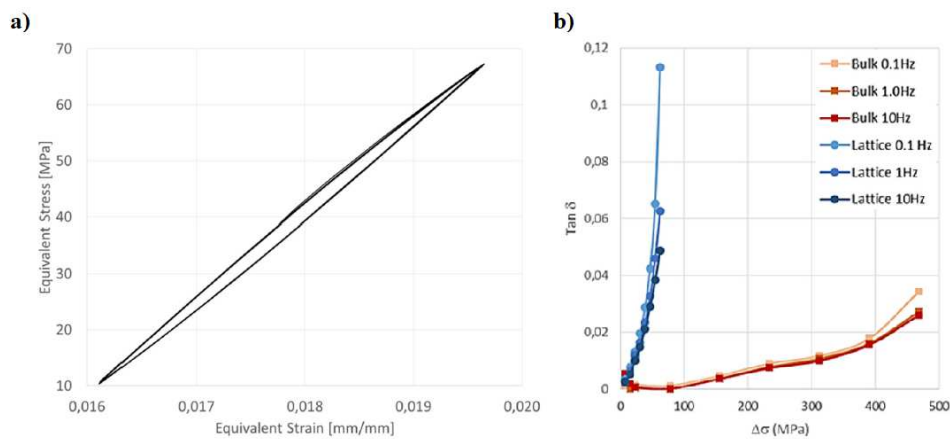


Figure 1.58: Stress-Strain cycles at 10Hz (a), damping capacity as a function of stress (b) [64]

Authors hypothesize that this behaviour may be due to amplitude dependent internal friction phenomena and micro-plasticization phenomena. Defects such as adhesions of partially melted powders and cracks could improve damping properties, worsening fatigue resistance.

Ramadani et al. [87] studied the damping effect of lattice structures through development and analysis of an optimized gear mechanism. The effect of gear body shape on vibrations induced by gear meshing was analysed. Gears are fundamental components in many mechanical systems, therefore methods to reduce vibrations and noise emitted during operation are worth to be investigated, especially for high-end industrial applications. Vibrations are caused by teeth interaction, wear, defects, torque and speed variations. The goal was to design a light-weight gear that generates a low amount of vibrations during



operation and fulfils strength and stiffness requirements. To achieve this objective, the authors choose to exploit a lattice structure as filler material. Design and optimization of lattice's topology and geometry have been performed by FEA and TO; topology optimization was set to obtain a cellular lattice structure made by cube diagonal and plane diagonal unit cells. The optimized geometry is lighter compared to the unoptimized gear, moreover mechanical requirements in terms of stiffness and strength are fulfilled, ensuring low stress levels within the cellular lattice structure. The final result was produced in Ti6Al4V with SLM technology (Figure 1.59).

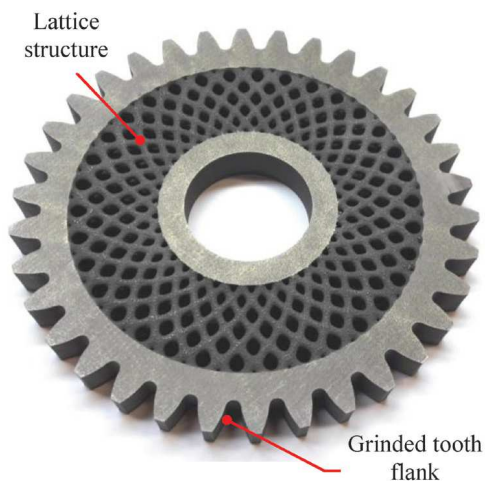


Figure 1.59: SLM-manufactured Ti6Al4V gear with TO cellular lattice infill [87]

A customized test rig has been developed to perform vibration measurements. The measurements were performed for three different gear pairs; the signal acquired from an accelerometer was sent to a data acquisition system and to a computer for data analysis. Tests were performed on a non-optimized gear and on the gear integrating the optimized cellular lattice structure; furthermore, a test was performed filling the porosity of the optimized lattice with a polymer, trying to further increase the damping effect.

To characterize the dynamic behaviour of the different types of gears, raw data of accelerations in the time domain were transformed into the frequency domain, using the Fourier Transform. The computer implementation is performed through the Discrete Fourier Transform (DFT), which is calculated with Fast Fourier Transform (FFT) that is computationally more efficient [88].

Resonance peaks are clearly visible observing the frequency spectrum, allowing the estimation of harmonic frequencies and amplitudes (Figure 1.60).

Comparing results obtained for the three different types of gears, the reduction of harmonics maximum amplitude is clear; highest amplitudes have been measured for the standard gear, while lowest for the cellular lattice gear with polymeric filler. The positive effect of optimized cellular lattice structure on the damping properties is therefore

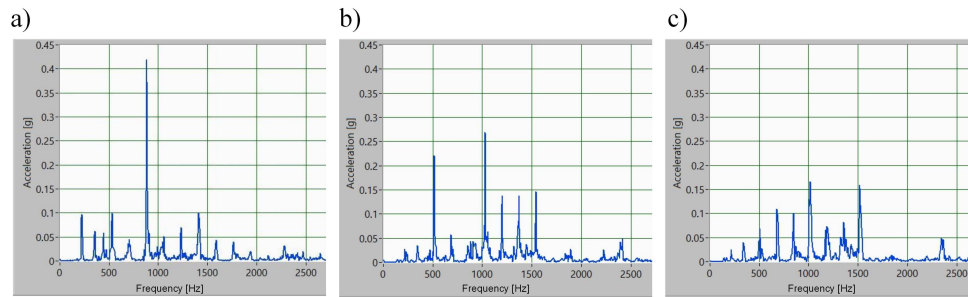


Figure 1.60: Frequency spectrum of standard (a), cellular lattice (b) and cellular lattice with polymeric filler (c) gears [87]

demonstrated; the authors hypothesize that this effect is generated by the lengthening of the path that must be travelled by pressure waves and by the fact that the propagation direction undergoes multiple changes; this improves energy dissipation due to internal friction. Polymeric fillers may further enhance vibration damping properties.

In order to characterize lattice structures' static and dynamic behaviour, theoretical background and instruments of the modal analysis have been used in the context of this work. The literature available on this topic is vast and consolidated. In order to keep the focus on the main topic of this thesis and favour an in-depth description of the experimental campaigns and data analyses, only required key point of the theoretical background are treated. If additional insights on the topic are required, see [89]–[91].

## 1.4 Conclusions

A comprehensive literature review to acquire a solid knowledge base regarding AMT for metals, DfAM, structural optimization and lattice porous structures was carried out. Particular attention was given to the SLM technology, with an in-depth study on physical phenomena governing the manufacturing process and on materials properties. Moreover, an in-depth review on state of the art regarding lattice / porous structures allowed to investigate thoroughly their geometrical, topological and mechanical properties and design rules. From the literature review the following conclusions can be drawn:

- Among AMTs for metals, the SLM technology allows the production of components having mechanical properties comparable to those of parts obtained through subtractive manufacturing technologies. Moreover, SLM allows to obtain parts of complex geometry without a negative impact on design and production phases. Therefore, the SLM technology is the best choice for the creation of high-performance components obtained through structural optimization and for the production of lattice porous structures.

- 
- The physical phenomena that develop during the production process significantly affect mechanical and geometrical characteristics of components made using SLM technology. Therefore, adequate knowledge of these phenomena and process parameters optimization are of fundamental importance.
  - DfAM techniques and structural optimization are useful tools for the design of high-performance parts that fully exploit AMT's advantages.
  - Lattice structures can be exploited as high-performance structural or filler materials, having an important role for the design of high added-value mechanical components. With respect to full density equivalent, improvements in terms of stiffness to weight ratio and vibration reduction are expected.
  - Lattice's unit cells characteristics, in terms of topology and geometry, that allow to enhance manufacturability (no need for supports) and potentially damping properties, have been identified.
  - Lack of exhaustive studies investigating static and dynamic behaviour of lattice porous structures produced with SLM technology, has been identified; therefore, filling this cognitive gap could be of scientific interest.



## **Chapter 2**

# **INVESTIGATION ON MECHANICAL PROPERTIES OF LATTICE STRUCTURES**

The analysis of the scientific literature, presented in Chapter 1, studying mechanical properties, manufacturability and damping behaviour of different kinds of lattice structures, has shown their huge potential for design and production of high-performance AM components. Vibration damping is a desirable feature for many industrial and scientific applications. Development and growing availability of new production technologies such as 3D printing, facilitates the task of the designer who wants to give objects excellent mechanical and damping properties; this objective can be achieved through appropriate design techniques, which may include the integration of particular structures in the geometry of the object under investigation. Lattice structures, as seen in the previous chapter, allow the creation of variable porosity materials whose mechanical properties can be designed and finely tuned point by point, in order to enhance stiffness to weight ratio and damping properties as required by the specific application. A fair number of publications investigating mechanical properties and manufacturability of lattice structures are already available in the literature, nevertheless few researchers have published works analysing their damping properties. The present work wants to contribute enhancing the knowledge in this field; to achieve this goal the advantages of SLM technology are exploited to produce specimens designed to assess the dynamic behaviour of some types of lattice structures. The objective is to demonstrate the usefulness of these structures to produce porous materials with good damping properties, that could be used as fillers to increase the performance of mechanical components that would benefit from reduced vibrations. Furthermore, in Chapter 3 a methodology that allows to evaluate the mechanical properties of various types of reticular structures is illustrated, in order to provide design-

ers with useful data to estimate the damping effect generated by the integration of these structures into different kinds of mechanical designs.

## 2.1 AlSi10Mg specimens design and DoE

In the first part of this paper mechanical behaviour of lattice structures has been analysed. Such structures, as previously mentioned, are generated by the ordered repetition of unit cells that form a controlled variable porosity material; the topology of these cells is the result of beams interconnection, recalling the lattice structure of high voltage pylons.

In order to assess damping properties of lattice structures, a set of appropriately designed specimens has to be produced and tested. The first phase of the study involves the selection of the unit cell topology that is believed to be best suited to be used as a damping filler for high-performance components to be produced with SLM technology. The choice of elementary cell topology is driven by the need to meet two basic requirements: obtain a structure with a good stiffness-to-weight ratio and enhance SLM manufacturability considering the process-related constraints.

A desirable feature when designing an easily SLM-manufacturable lattice unit cell topology, is a geometry that does not require supporting structures. In Chapter 1 it was observed that the SLM production of components including surfaces with inclination angle lower than the critical overhang angle is problematic, if suitable supporting structures are not contemplated [76]. When geometries that contain undercut features cannot be avoided, support structures that make printing possible and improve the result are used. Supports are designed to facilitate detachment from the piece, this goal is achieved by properly sizing their geometry, especially at the interface with the component and using process parameters that limit their mechanical properties to further facilitate removal operations. Given the nature of lattice structures, it is obvious that it is very important to design/select a unit cell topology that does not require supports to be satisfactorily produced, because their removal would be very complicated or impossible.

In order to design high-performance components suitable for SLM printing, in many cases it is desirable to reduce weight ensuring high stiffness; therefore, high stiffness unit cells should be better as filling materials for many AM applications [73], [74] and should also help achieving better damping behaviour. Main parameters that affect the mechanical behaviour of the unit cell are topology, geometry, relative density, material, and loading direction. The cell topology plays a very important role in defining the mechanical behaviour of the unit cell. In Chapter 1, the possibility of predicting the mechanical behaviour of a certain cell topology, knowing nodes and struts number and calculating the Maxwell number, was analysed. It has also been verified that this method cannot predict the effect of loading direction on the mechanical properties of the unit cell, so it is always

necessary to assess the actual mechanical response through appropriate testing.

### 2.1.1 Lattice topology, geometry and material selection

The unit cell topologies that appear to be most promising as high performance filler materials, are cubic unit cells composed by the intersection of beams arranged in different ways. These structures facilitate the task of the designer who wants to produce a variable porosity material with tuneable mechanical characteristics; design, integration and simulation phases are easier. To meet the requirements in terms of stiffness and manufacturability described previously, the unit cell topology should demonstrate high stiffness and should be SLM-manufacturable without supporting structures.

Lattice structures composed by unit cells with struts aligned along the loading direction are considerably stiffer and more resistant than other lattice types, as demonstrated by the stress-strain graphs shown in Chapter 1. Lattice manufacturability is influenced by two fundamental parameters: the inclination of the struts with respect to the build platform and the presence of overhangs. After evaluating all relevant factors, lattices composed by FBCCZ topology unit cells fit all the requirements; this kind of unit cell has excellent stiffness and does not have horizontal structures that would force to use support structures to achieve a satisfactory result. In addition to the topology, there are also production constraints related to the geometry of the lattice, in particular it is necessary to limit overhanging surfaces to enhance manufacturability and surface finish. In Chapter 1 circular cross-section struts manufacturability with respect to diameter, inclination angle and material (AlSi12Mg and Ti6Al4V) was analysed. Looking at Figure 1.53 it can be observed that to ensure aluminum alloy lattice struts manufacturability, the strut diameter should be greater than 0.4 mm; moreover, the undercut angle should be less than 30°. The latter constraint is satisfied since the minimum undercut angle of the FBCCZ cells is equal to  $\approx 35^\circ$ . Furthermore, Mazur et al. [76] observed that when the cell size of titanium alloy lattice structures exceeds 4 mm, overhanging surfaces that are perpendicular to the build direction cannot be manufactured correctly. The goal is to identify a lattice whose topology and geometry are compatible with the SLM production constraints, ensuring the manufacturability for different types of metal alloys. The lattice structure that satisfies the requirements listed above, facilitating production and integration within mechanical components, is the FBCCZ. Considering all constraints, the minimum diameter of the circular cross-section struts is set to 0.4 mm and the maximum cell size to 4 mm, this choice is the best compromise between manufacturability and mechanical characteristics of the lattice.

Topology and geometrical constraints of the lattice unit cell to be studied have been identified, some additional boundary conditions to make it easier to run the tests on the specimens and interpret the results are listed below:

- similar static compliance for all specimens
- same material and process parameters for all specimens
- specimens are designed with different unit cell dimension and aspect ratio (ratio of strut diameter to cell size)
- same experimental set-up and test conditions for all specimens

Designing specimens having similar static compliance allows an easier comparison between the different types of lattice structures, since damping behaviour is a function of the stiffness of the specimen. Analysing specimens having same material properties and similar stiffness makes it possible to evaluate in a simpler way the effect of the variation of the geometry of the unit cell on damping properties. The material chosen for the experimentation was the AlSi10Mg aluminium alloy, with good melting characteristics, suitable for SLM manufacturing technology. This alloy was chosen because it is well suited for applications where lightness is a fundamental requirement, such as for fast robotic mechanisms, where lattice structures can help improve damping properties to increase positioning accuracy. As specified in the previous paragraph, the topology and the geometry of the unit cell of the lattice were selected in order to meet the following requirements: guarantee high stiffness; reduce undercuts and eliminate the need for additional support structures, ensuring manufacturability throughout SLM process. In addition to this, cell geometry was constrained by the minimum SLM manufacturable feature size. After all these considerations, the FBCCZ structure, with a lattice strut diameter not less than 0.4 mm was selected.

To investigate the damping behaviour of the FBCCZ lattice, a full-factorial DoE on two levels for cell dimension and fill ratio was conceived. The specimens were designed as two rigid full density prisms connected by the lattice structure. The geometry was divided into three main sections, a 60 mm-high lattice FBCCZ structure, a lower base for clamping and a higher prism for the application of the external forces. The overall height is 130 mm and the size of the square cross-section lower and upper prisms is 21x21 mm. In Figure 2.1 it is possible to observe the resulting geometry, the specimens could be assimilated to beams whose central part has been replaced by the lattice structure.

As previously stated, the aim was to generate lattice specimens with different cell size and fill ratio but with similar stiffness; specimens sizing was performed iteratively by FEA using SolidWorks Computer Aided Engineering (CAE) suite. A full density square cross section sample was taken as reference. Specimens were designed in order to obtain a stiffness variation not exceeding 15% compared to the reference one.



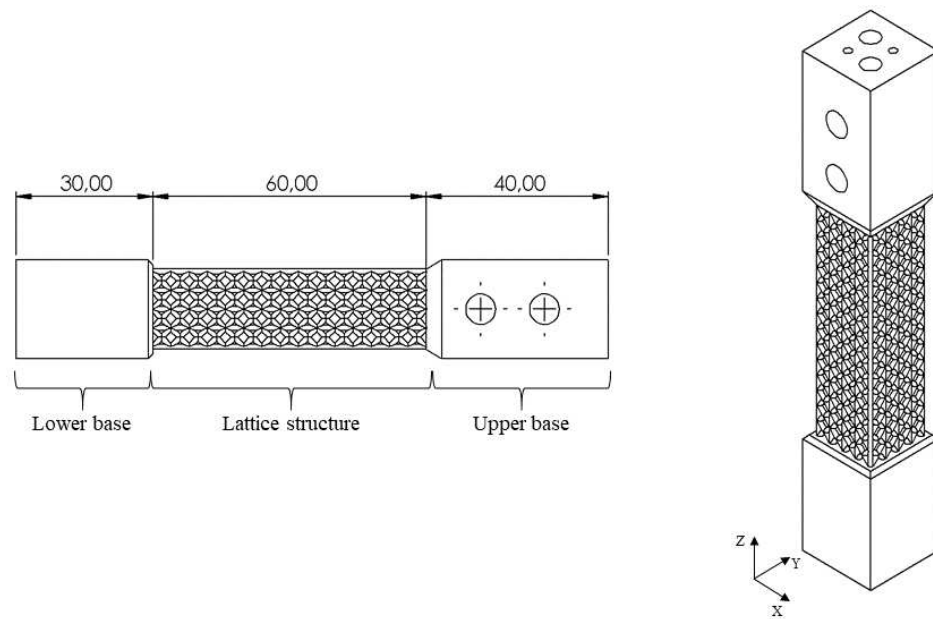


Figure 2.1: Beam-like specimens' geometry (LAMA FVG™)

### 2.1.2 Specimens FEA and sizing

The sizing of the specimens was performed by FEA; the goal was to identify the geometries that, despite having different cell size and fill ratio, had similar stiffness. The maximum sample size was fixed, as described in the previous paragraph; cell size factor levels were fixed to 2 mm and 4 mm, to obtain a lattice consisting of an entire number of unit cells and respect the manufacturing constraints described before. Additional parameters that could be modified were the number of cells on the XY plane of the lattice section and the diameter of the struts. The number of cells along X and Y axis was chosen to obtain a square cross-section. Two fill ratio values that allow to obtain specimens with different cell sizes and similar stiffness have been identified by iteratively performing linear static analyses, appropriately modifying the above parameters.

Full 3D finite element model of specimens was analysed using SolidWorks 2014; linear static analysis main steps are summarized below:

- Material properties definition
- Loads and Boundary Conditions definition
- Volume meshing
- Solution and results analysis

As previously stated, the material chosen for the trial is the AlSi10Mg aluminium alloy. Material properties of SLM-manufactured alloys are not uniform, they depend on build direction, process parameters and in general are affected by thermal history. Material properties of AlSi10Mg, obtained from the datasheet provided by the powder manufacturer (Concept Laser) are shown in Table 2.1; these values were used to create the FEA material model.

Table 2.1: AlSi10Mg material properties [92]

|  | 90° (horizontal)             | 45° (polar angle)            | 0° (upright)                 |
|--|------------------------------|------------------------------|------------------------------|
| <b>Yield Strength <math>R_{p0,2}</math></b> <sup>2</sup><br>[N/mm <sup>2</sup> ] | 211 ± 4                      | 215 ± 3                      | 205 ± 3                      |
| <b>Tensile Strength <math>R_m</math></b> <sup>2</sup><br>[N/mm <sup>2</sup> ]    | 329 ± 4                      | 346 ± 3                      | 344 ± 2                      |
| <b>Elongation</b> <sup>2</sup> [%]   | 9 ± 1 %                      | 7 ± 1 %                      | 6 ± 1 %                      |
| <b>Young's Modulus</b><br>[N/mm <sup>2</sup> ]                                   | approx. 75 · 10 <sup>3</sup> | approx. 75 · 10 <sup>3</sup> | approx. 75 · 10 <sup>3</sup> |
| <b>Thermal Conductivity <math>\lambda</math></b><br>[W/mK]                       | 120 - 180                    | 120 - 180                    | 120 - 180                    |
| <b>Coefficient of thermal Expansion</b> [K <sup>-1</sup> ]                       | 20 · 10 <sup>-6</sup>        | 20 · 10 <sup>-6</sup>        | 20 · 10 <sup>-6</sup>        |

Constraints and loads must be set appropriately before performing the calculation. To perform experimental measurements, specimens lower base has to be clamped in a vice, for this reason two opposite faces of the lower base have been fixed; translations of nodes laying on these faces are prevented, simulating the experimental set-up clamping system. The load has been applied on a small surface located at the edge of the specimens upper base; this method helps improving static compliance estimation accuracy, eliminating the effects of possible local deformations that could arise when applying concentrated loads. Afterwards, three-dimensional solid mesh has to be calculated. The meshing operation allows to obtain a discrete model that can be used for FEA. The mesh consists of tetrahedral elements; element size is variable to ensure appropriate refinement for small size features or where major stress variation is expected. In Figure 2.2 it is shown the result of the operations described above: it is possible to observe constraints and loads placement and tetrahedral mesh topology.

The finite elements model is well-defined and it is possible to calculate and analyse the results. In order to estimate the theoretical static compliance of the specimens, it is necessary to observe the results in terms of displacements. Figure 2.3 shows total displacement contour plot of the B sample.

<sup>2</sup>Tensile test according to DIN EN 50125 at 20°C

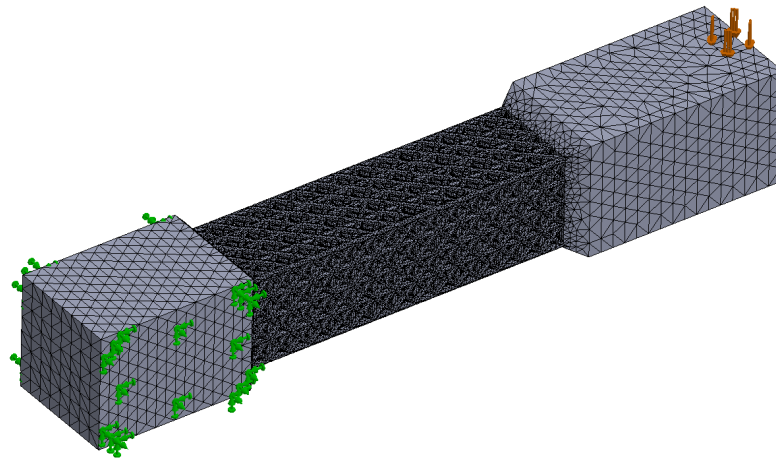


Figure 2.2: Example of specimens FEM: BCs and tetrahedral mesh

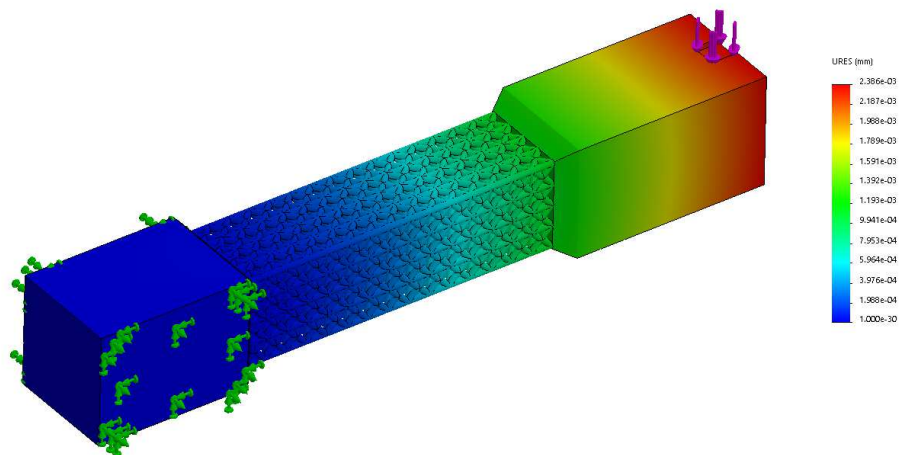


Figure 2.3: Total displacement contour plot – specimen B






The specimens' stiffness  $k$  can be calculated as the ratio of the applied load  $F$  to the associated displacement  $\delta$  (Equation 2.1).

$$k = \frac{F}{\delta} \quad (2.1)$$

Static compliance is the reciprocal of stiffness; since the applied load  $F$  is equal to 1 N, the static compliance is equal to the associated displacement. All the elements required to perform the FEA are defined, therefore it is possible to proceed with specimens sizing and DoE levels selection. Eventually, for comparison with the experimental results, the first resonance frequency of lattice specimens and full cross-section specimen were also determined by simulation. Resonance frequency is an intrinsic property of specimens

that depends on geometry, BCs, and material properties. For a simple harmonic oscillator, the resonance frequency is proportional to stiffness; therefore, since the beam-like specimens have similar stiffness, even resonance frequencies should be similar. Lattice structures geometry designed by means of FEA, DoE factors and levels, geometric and mechanical parameters are summarized in Table 2.2. Looking at stiffness values, it is clear that the design requirement in terms of maximum stiffness variation has been fulfilled. Resonance frequencies of the different specimens are similar, as should be expected for simple geometry beam-like specimens.

Table 2.2: Summary of characteristics of designed specimens

| Name                                      | A   | B   | C   | D   | E   |
|---|---|---|---|---|---|
| <b>Lattice configuration</b>              | FBCCZ   | FBCCZ   | FBCCZ   | FBCCZ   | Full cross section  |
| <b>Cell dimension [mm]</b>                | 4   | 4   | 2   | 2   | 12x12x60  |
| <b>Strut diameter [mm]</b>                | 0,8   | 1,1   | 0,4   | 0,55  | \   |
| <b>Fill ratio</b>                         | 0,2   | 0,275   | 0,2   | 0,275   | \   |
| <b>Cells along X direction</b>            | 5   | 4   | 10  | 8   | \   |
| <b>Cells along Y direction</b>            | 5   | 4   | 10  | 8   | \   |
| <b>Cells along Z direction</b>            | 15  | 15  | 30  | 30  | \   |
| <b>Total cells</b>                        | 375   | 240   | 3000  | 1920  | \   |
| <b>Stiffness [N/mm]</b>                   | 423   | 435   | 381   | 372   | 383   |
| <b>FEM 1st resonant frequency [Hz]</b>    | 625   | 623   | 569   | 573   | 568   |
| <b>Frontal view of lattice structures</b> |  |  |  |  |  |

Before proceeding with production, CAD models of the specimens were modified by creating some holes on the upper base to facilitate coupling with sensors and additional masses. Fixing additional masses to the upper base allows to observe the dynamic behaviour of the specimen as the modal mass changes. The resulting geometry is like the one already shown in Figure 2.2. CAD models of the samples, created with SolidWorks, were exported in STL format; the result is a watertight surface, tessellated into a series of small triangles. Due to the specimens' geometry complexity, it is important to use appropriate STL discretization parameters in order to achieve a sufficiently accurate and error-free model. The design of the additional masses to be mounted during the test phase, was carried out to ensure consistency with the specimens' geometry and facilitate production.

## 2.2 AlSi10Mg DoE specimens manufacturing

Specimens geometry, DoE's factors and levels are well-defined; therefore, it is possible to proceed with manufacturing process design, specimens' production and execution of measurements to evaluate printing results.

### 2.2.1 AlSi10Mg specimens SLM manufacturing

The print job was created using Materialise Magics software. Specimens were placed on the building platform in order to maximize the print quality. To achieve a good result, three main factors were taken into account: the direction of inert gas flow within the build chamber, the accumulation of SLM process-related residual stresses and the orientation of the specimens with respect to the coater blade. The inert gas inside the building chamber is extracted through a special vent, carrying the fumes and waste produced during the process towards a recirculation filtration system. The flow of inert gas is therefore directional, causing accumulation of slag in the areas of the platform that are located near the vent, increasing the likelihood of inclusion or poor surface finish. For this reason, it was chosen to place the specimens on the opposite side of the platform, obtaining the additional result of improving coating even with a low powder supply. The samples were placed vertically to take advantage of the features of the FBCCZ topology, avoiding supporting structures; furthermore, this choice helps to limit SLM process-related residual stresses, reducing the section of the individual layers to be produced. Finally, the samples were placed at an angle of 45° with respect to the coater blade, to obtain a progressive and uniform coating, enhancing powder deposition. These choices have made it possible to enhance print quality, even if this implied a long printing time (112 hours).

Specimens placement on the build platform is visible in Figure 2.4, which shows a view of the virtual build volume made with Materialise Magics software. The only supports needed for construction are those underlying the lower bases of specimens and masses, connecting components to the build platform; supports height was set to 4 mm, simplifying components separation by means of a band saw. To mitigate the effects of manufacturing defects on measurements, two samples for each combination of factors were produced, for a total of ten specimens. Specimens were randomly placed to limit the influence of position on microstructure and mechanical properties.

Specimens were manufactured by means of a Concept Laser M2 Cusing SLM metal 3D printer. The process parameters recommended by Concept Laser were applied: laser power 200 W, scanning speed 650 mm/s, spot diameter 120 μm, layer thickness 25 μm and 30% overlap between single scanning tracks. Islands exposure strategy was selected in order to reduce thermal strains as much as possible. The specimens were produced

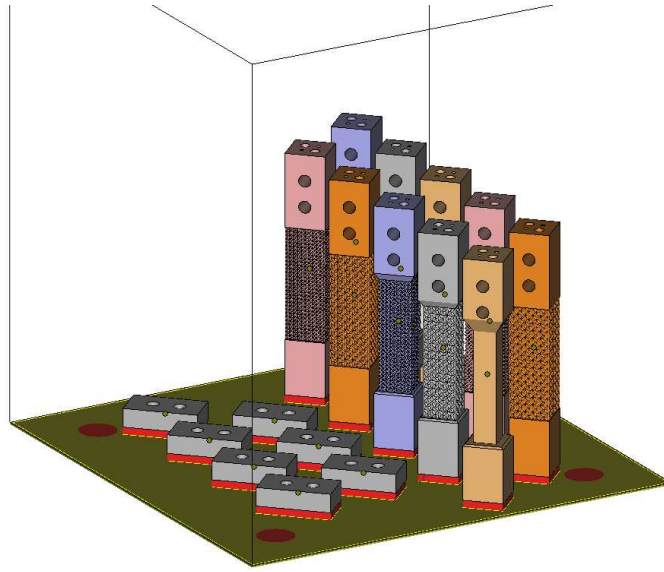


Figure 2.4: Three-dimensional view of specimens and masses inside the build volume

under an inert atmosphere of argon to reduce oxidation phenomena. Figure 2.5 shows the as-built SLM-manufactured specimens and masses while in Figure 2.6 it is possible to observe the 1st repetition specimens after separation from the build platform. The print quality was good, even if in some areas there were some powder aggregations and poor surface finish.

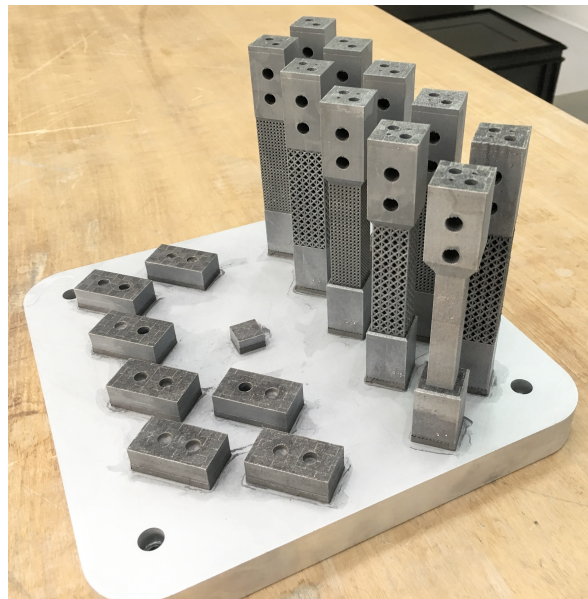


Figure 2.5: As-built SLM-manufactured AlSi10Mg specimens and masses

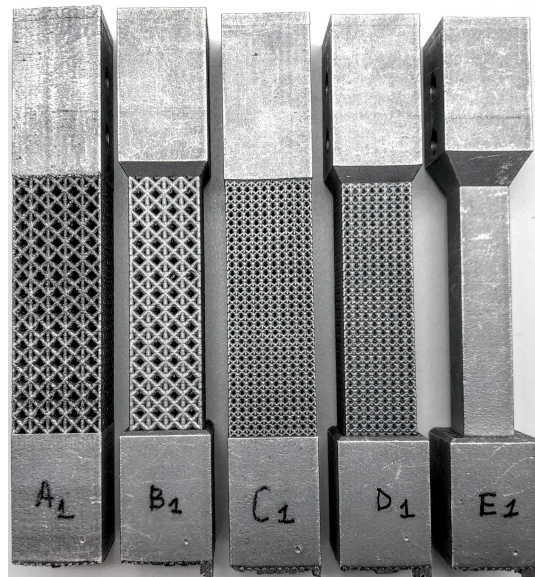


Figure 2.6: 1<sup>st</sup> repetition AlSi10Mg specimens after separation from the build platform

### 2.2.2 AlSi10Mg specimens geometrical measurements

Looking at detailed images taken by means of a Dino-Lite digital microscope, it is possible to observe that the geometry of the specimens of the first repetition in some cases differs from that of the second; detail views of the lattice structures are reported in Table 2.3. For example, geometric and surface finish variability is visible comparing 1<sup>st</sup> and 2<sup>nd</sup> repetitions of A specimens; furthermore, unwanted unmelt particles adhesion is higher for A-1<sup>st</sup>. Looking at the images it is possible to get some information about the geometry of the specimens. The A specimen has a unit cell consisting of struts with a diameter of 0.8 mm and the B of 1.1 mm; comparing A-1<sup>st</sup> and B-1<sup>st</sup> images the difference is clearly visible but comparing A-2<sup>nd</sup> with B-1<sup>st</sup> beams diameters look similar. Vertical struts diameter is smaller compared to that of inclined ones, suggesting an effect of build direction on struts geometry. This phenomenon is the result of the staircase effect and of unwanted adhesion of partially melted powders caused by the absence of supports. The D-type structure is the most critical one, given the small cell size and great fill-ratio; due to process-related limitations, the difference between CAD model and as-built lattice is the largest.

Further indications on manufacturing related issues of AlSi10Mg samples are identifiable by observing the upper base of the A-1<sup>st</sup> specimen; it is not perfectly flat due to Thermal Deformations (TD) and partially melted material aggregations that occur sporadically (Figure 2.7). No further macro deformations are detected, confirming that the vertical arrangement of the specimens is the one that gives the best result in case of FBCCZ structures. The use of purely optical measurement instruments does not allow to evaluate the level of internal porosity, nor the geometric conformity in the inner part of the specimens; the assessment of these aspects would require destructive tests or tomography.

Table 2.3: Detail views of AlSi10Mg lattice structures

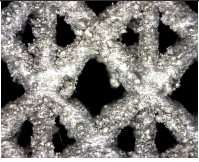
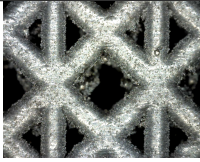
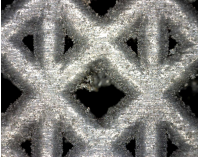
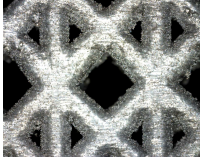
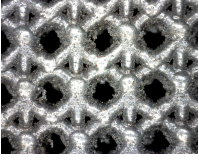
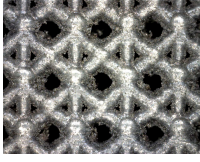
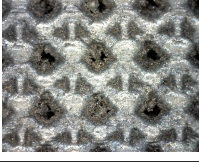
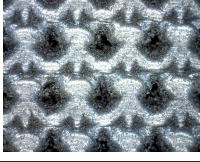
| Specimen | 1 <sup>st</sup>  | 2 <sup>nd</sup>   |
|----------|--|---|
| A        |   |   |
| B        |   |   |
| C        |   |   |
| D        |  |  |



Figure 2.7: Macroscopic defects of AlSi10Mg specimens (TD: thermal deformation, CC: inert gas filter cleaning cycle)

The specimens measurements, obtained analysing images captured with the Dino-Lite digital microscope, confirmed that inclined struts have larger diameter than the nominal value ( $D_i > D_{in}$ ), due to the limits of the manufacturing process, as shown in Figure 2.8.



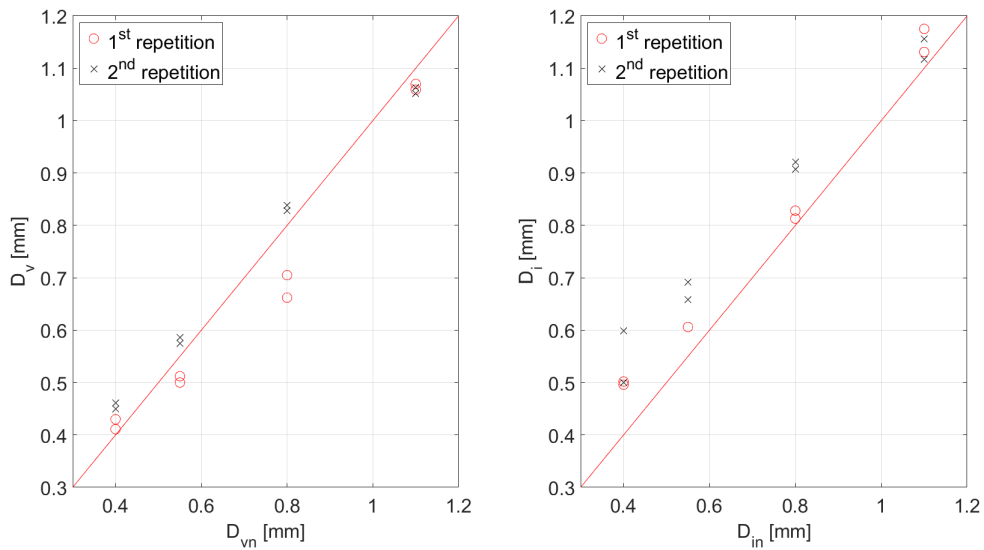


Figure 2.8: Comparison between measured and nominal AlSi10Mg struts diameters

## 2.3 AlSi10Mg specimens dynamic behaviour assessment

The purpose of the experimental analysis is to assess the dynamic behaviour of different types of specimens, focusing on damping properties granted by different types of lattices. The identification of the specimens' dynamics was accomplished by means of pulse testing procedure.

### 2.3.1 FRF measurement: impact test analysis

The frequency response of a structure can be obtained through different techniques; the two main categories are the following:

- Harmonic excitation of the system: an actuator applies sinusoidal forces with variable frequency to the system. The actuator (shaker) is generally electromagnetic or piezoelectric. The impressed force is monitored by suitable sensors (e.g. load cells) as well as the vibration (e.g. accelerometers, contact or non-contact inductive or capacitive probes). The frequency response is obtained by comparing the input (force) and the output (vibration) in the frequency domain.
- Impulsive excitation of the system: generally the impulsive force is applied by means of an instrumented hammer; the measurement of the vibrations of the system takes place through sensors positioned in one or more points. Force and vibration signals are processed in the frequency domain to obtain an estimate of the frequency

response of the structure. This approach is called "pulse testing" and it is a consolidated technique to quickly perform modal analysis [89].

Since the pulse testing technique is adequate, effective and rapid for the identification of the frequency response of beam-like specimens such as those in analysis, it has been chosen to use this approach.

As previously stated, the frequency response of a structure can be obtained through a procedure called impact test or pulse test analysis. This procedure involves the acquisition of the vibration of the structure (displacement or acceleration depending on sensor type) when an impulsive force is applied. Impulsive force can be applied by an instrumented impact hammer, while vibration can be monitored with accelerometers, inductive probes or lasers. It is convenient to repeat the procedure several times to maximize the signal coherence and minimize noise. To calculate the structure's frequency response, data should be processed according to the following sequence of operations:

- Transients corresponding to unsaturated input (hammer) and output (displacement/acceleration probes) signals are acquired, while others are discarded
- Low-pass filtering to remove acquisition-related noise
- Transient trimming in order to analyse only significant data; the number of samples to be extracted is chosen in advance in order to allow a consistent attenuation of the free oscillations of the system, capturing the transient till quasi-steady-state
- The signals are multiplied by a conversion factor that takes into account sensor sensitivity and acquisition system gain in order to obtain data expressed in terms of appropriate units
- Calculation of the  $h^{\text{th}}$  transient frequency response according to

$$W_h(j\omega) = \frac{U_h(j\omega)}{F_h(j\omega)} \quad (2.2)$$

where  $U_h(j\omega)$  and  $F_h(j\omega)$  are the Fourier transforms of the output and input signals

- Estimation of the frequency response as the average of the transients frequency responses

$$W(j\omega) = \frac{1}{N} \sum_{h=1}^N W_h(j\omega) \quad (2.3)$$

where  $N$  is equal to the number of transients acquired

- Time delay error correction in order to reduce the error due to advance or delay of the output signal with respect to the input; this allows to reduce discretization error, respecting the cause-effect principle obtaining a correct phase response

$$\hat{W}(j\omega) = W(j\omega)e^{-i\omega\tau} \quad (2.4)$$

where  $\tau$  is the time delay (positive or negative) of the same order of magnitude as the sampling interval

$$\tau = k\tau = k \frac{1}{f_s}, \quad k \approx 1 \quad (2.5)$$

where  $f_s$  is the acquisition frequency

- If the output is expressed as an acceleration, the displacement frequency response (displacement/force Fourier transforms ratio), can be calculated in the frequency domain according to

$$W(j\omega) = \frac{u(j\omega)}{F(j\omega)} = \frac{1}{(j\omega)^2} \frac{A(j\omega)}{F(j\omega)} \quad (2.6)$$

- Calculation of the coherence function associated with the frequency response

$$\gamma^2(j\omega) = \frac{|P_{uF}(j\omega)|^2}{P_{uu}(j\omega)P_{FF}(j\omega)} \quad 0 \leq \gamma^2(j\omega) \leq 1 \quad (2.7)$$

where  $P_{uu}$  and  $P_{FF}$  are the autospectral density estimates of input (force) and output (vibration), while  $P_{uF}$  is the cross power spectral density between input and output [93]. The coherence function is used to determine the frequency ranges where the frequency response is reliable. The coherence function varies between 0 and 1 and measures the linear correlation between input and output at a certain frequency. This function is lower than unity when the signal to noise ratio is not good due to external disturbances or limits of the sensors, when the system is non-linear and when the output is significantly affected by unmeasured inputs.

### 2.3.2 Experimental setup and procedures

As explained in the previous paragraph, the technique used to measure the specimens frequency response and evaluate their dynamic behaviour, is based on impulsive excitement of the system by means of an instrumented impact hammer and acquisition of induced vibration (displacement) with inductive sensors or accelerometers. This method, commonly called "Pulse Testing", is very versatile allowing to investigate the dynamic behaviour of various types of mechanical structures in a simple and rapid way.

Technical specifications of sensors and tool used to perform pulse tests, capturing data in terms of applied impulsive force and resulting transverse displacement are shown in Table 2.4.

To detect vibrations, two types of sensors, with different characteristics, were used: a triaxial accelerometer and an inductive probe. Following a preliminary series of measurements, however, it was observed that the accelerometer, which must be fixed on the specimen, alters the dynamics of the object due to the increase in vibrating mass and the dampening effect due to the connecting cable; therefore, the accelerometer was not used

for data acquisition, selecting the non-contact inductive probe. This choice penalizes the quality of the data acquired in the case of high-frequency vibrations, as the signal to noise ratio tends to deteriorate significantly. Since FEA has shown that none of the specimens have a first resonance frequency that exceeds 1000 Hz and the frequency response beyond this limit is not necessary to characterize specimens damping behaviour, eddy current probe is the best compromise. If it is necessary to measure the frequency response at high-frequency, accelerometers would guarantee better S/N ratios.

Table 2.4: Pulse testing tools and sensors technical specs

| Tool/sensor  | Manufacturer         | Model                    | Technical specs  |
|--|----------------------|--------------------------|--|
| <b>Impulse hammer (IEPE)</b>   | Dytran               | 5800B4                   | Sensitivity: 2.41 mV/N<br>Head weight: 100 g<br>Force Range ( $\pm 5$ V): 2.22 kN    |
| <b>Power Supply/Signal Conditioner (TEDS)</b>                              | Kistler              | 5134B                    | No. of channels: 4<br>Gain: 0.5 to 150   |
| <b>Eddy current sensor</b>   | Micro-Epsilon        | ES1                      | Measuring range: 1 mm<br>Resolution: 0.05 $\mu$ m                                    |
| <b>Non-contact single channel displacement measuring system controller</b> | Micro-Epsilon        | NCDT 3010-M              | Frequency response: 25 kHz   |
| <b>Triaxial accelerometer (IEPE)</b>                                       | Kistler              | 8763B100                 | Acceleration Range: $\pm 100$ g<br>Sensitivity: 50 mV/g                              |
| <b>Regulated power supply</b>  | K.E.R.T.             | /                        | Input voltage: 220 V<br>Output Voltage: 0.1 to 48 V                                  |
| <b>Data acquisition system</b>   | National Instruments | cDAQ-9178<br>2 x NI 9215 | cDAQ-9178: 8-slot NI USB rack<br>NI 9215: 4-channel analog input module (16-bit ADC) |

The lower base of the specimens was clamped in a vise and the upper one was excited using a Dytran impact hammer connected to a Kistler amplifier. Vibrations were measured by means of a Micro-Epsilon eddy current probe connected to a non-contact single channel displacement measuring system controller. Impulsive force was applied at the excitation point on upper part of specimens, while hammer signal  $F_{in}$  and vibration signal  $U_j$  were acquired. Measurements were captured in the form of analog signals, discretised and processed using a National Instruments data acquisition system (cDAQ-9178 + 2 x NI 9215) connected via USB to a PC; the sampling rate for data acquisition was 20 kHz. The software tool for pulse testing signal acquisition and in-process frequency response calculation and visualization was developed in the framework of previous research projects of the Manufacturing Technology group of the University of Udine [94]. The software communicates with the acquisition devices connected to the PC and allows the configuration of the parameters necessary for data acquisition (channel assignment, sensitivity, gain, sample rate); therefore, the acquisition begins and when the hammer signal exceeds a pre-set threshold the transient is recorded. Once the acquisition is completed, the data

is processed according to the procedure described in the previous paragraph; moreover, a graphical representation of frequency response and coherence function is available for fast evaluation. The data are saved in order facilitate further elaborations with external tools. In Figure 2.9 it is possible to observe the pulse testing setup.

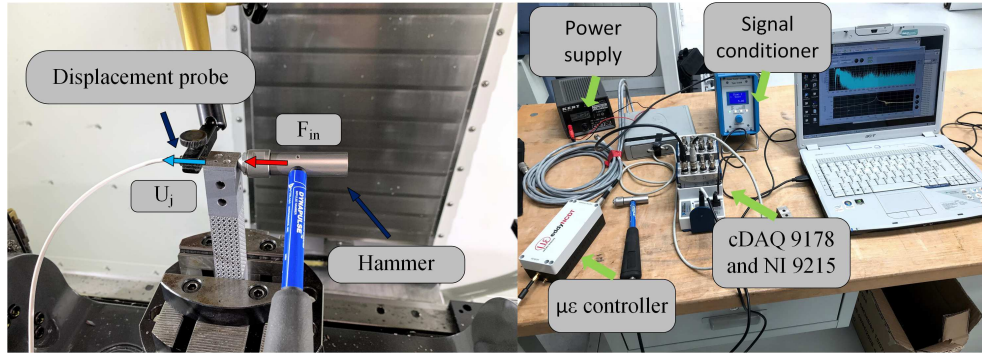


Figure 2.9: Pulse testing experimental setup

### 2.3.3 Data acquisition and analysis

The experimental set-up was organized paying attention to the relative positioning of the specimens with respect to the vise and the inductive probe. As explained in the previous paragraph, the lower base of the specimens is clamped in a vise while the impulsive force is exerted on the upper one using an instrumented hammer. The relative position of the specimen should be kept as constant as possible, even for different specimens, to prevent the positioning from significantly affecting the results. To improve the consistency of the measurements, every specimen was accurately positioned in order to have a distance of  $100 \pm 0.1$  mm between the specimen's upper base and the upper plane of the vise.

The first operation consists in the calibration of the inductive probe; this is fundamental to establish the link between the analogue signal of the inductive probe and the measured distance. The operation must be repeated for each sample, given the inevitable modification of the system when the assembly and disassembly operations are performed. After adequate positioning of the specimen in the vise, the inductive probe is placed as in Figure 2.9 in order to achieve an output of 5V; this guarantees easy measurements of both positive and negative displacements. Taking advantage of the controlled movement of the axes of the table underneath the vise, it is possible to associate controlled displacements to the inductive probe voltage variation. The calibration value  $c$  was obtained according to Equation 2.8:

$$c = \frac{v_{max} - v_{min}}{d} \quad (2.8)$$

where  $v_{max}$  and  $v_{min}$  are the maximum and minimum voltage values recorded during the controlled movement and  $d$  is the fixed displacement, see Figure 2.10.

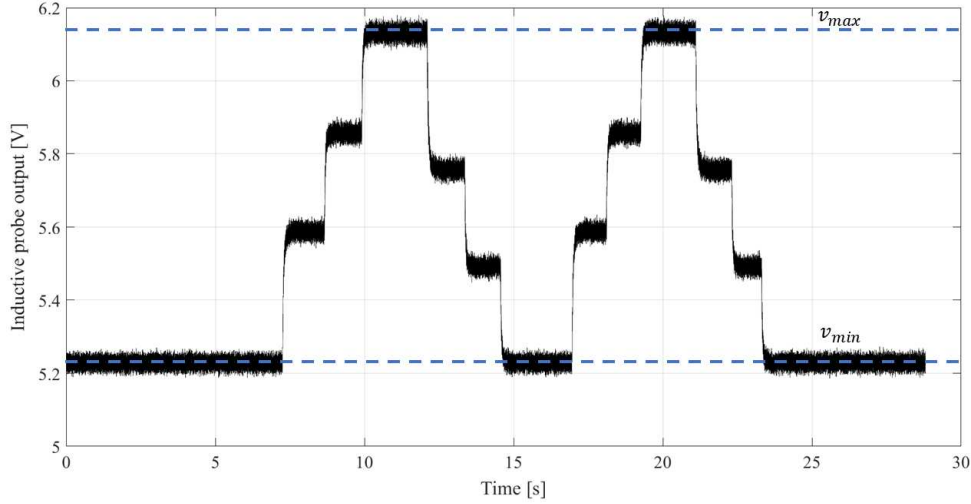


Figure 2.10: Example of inductive probe calibration procedure

The values of the calibration coefficient  $c$ , obtained by performing the aforementioned procedure for each sample before the execution of the pulse test, are shown in Table 2.5. The results obtained are consistent with expected values for aluminium.

Table 2.5: Inductive probe calibration results – AlSi10Mg specimens

| Specimen       | $v_{max}$<br>[V] | $v_{min}$<br>[V] | $d$<br>[mm] | $c$<br>[mV/ $\mu$ m] |
|----------------|------------------|------------------|-------------|----------------------|
| A <sub>1</sub> | 5.75             | 4.48             | 0.03        | 35.77                |
| B <sub>1</sub> | 6.32             | 5.22             | 0.03        | 36.87                |
| C <sub>1</sub> | 5.79             | 4.69             | 0.03        | 36.63                |
| D <sub>1</sub> | 5.66             | 4.57             | 0.03        | 36.13                |
| E <sub>1</sub> | 4.58             | 3.56             | 0.03        | 33.87                |
| A <sub>2</sub> | 4.77             | 3.74             | 0.03        | 34.33                |
| B <sub>2</sub> | 4.75             | 3.73             | 0.03        | 34.00                |
| C <sub>2</sub> | 4.38             | 3.37             | 0.03        | 33.67                |
| D <sub>2</sub> | 4.83             | 3.80             | 0.03        | 34.33                |
| E <sub>2</sub> | 4.90             | 3.88             | 0.03        | 34.00                |

Pulse tests were performed on all the specimens, repeating the measurement twice to maximize the signal coherence and minimize noise, reducing errors caused by the operator that manually exerts the impulsive force on the upper base. At the end of the procedure, data were imported and processed using MathWorks MATLAB environment. In Figure 2.11 it is possible to observe the measured frequency response for sample C2 in black and the associated coherence function in blue. Up to the first resonance frequency, the coherence function remains almost unity, for higher frequencies the signal to noise ratio deteriorates and the coherence function falls below unity.

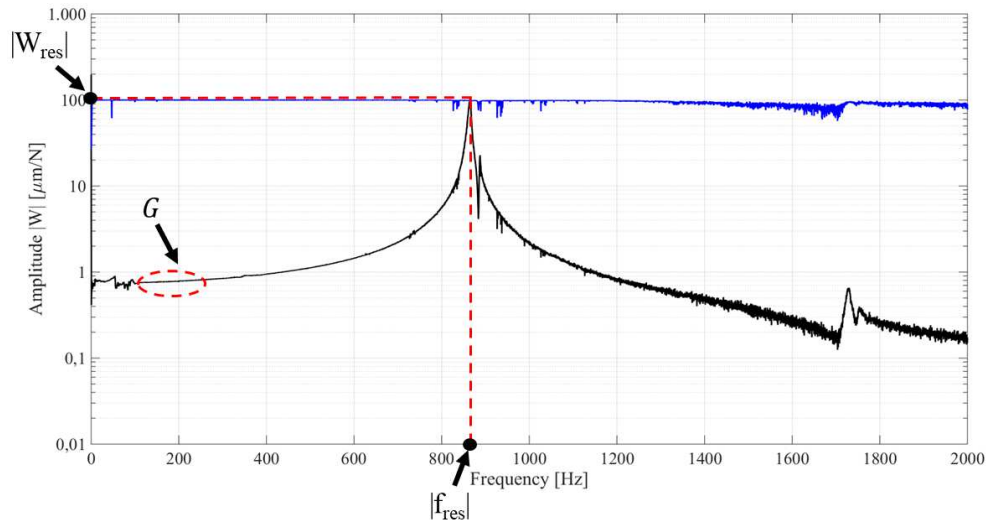


Figure 2.11: Frequency response and associated coherence function – C<sub>2</sub> specimen

From the analysis of the frequency response, it was possible to estimate the first resonance frequency and the compliance for all specimens. The comparison between the results obtained from the experimental analysis and those obtained from FEA is shown in Table 2.6.

Table 2.6: Comparison between experimental and FEA modal analysis results

| Specimen       | $f_{\text{res}}$<br>[Hz] | $f_{\text{res(FEA)}}$<br>[Hz] | $G$<br>[ $\mu\text{m/N}$ ] | $G_{\text{(FEA)}}$<br>[ $\mu\text{m/N}$ ] |
|----------------|--------------------------|-------------------------------|----------------------------|---|
| A <sub>1</sub> | 627                      | 626                           | 1.45                       | 2.36                                      |
| B <sub>1</sub> | 674                      | 623                           | 1.33                       | 2.30                                      |
| C <sub>1</sub> | 822                      | 569                           | 0.78                       | 2.63                                      |
| D <sub>1</sub> | 766                      | 573                           | 1.00                       | 2.69                                      |
| E <sub>1</sub> | 593                      | 568                           | 1.75                       | 2.61                                      |
| A <sub>2</sub> | 726                      | 626                           | 1.09                       | 2.36                                      |
| B <sub>2</sub> | 645                      | 623                           | 1.35                       | 2.30                                      |
| C <sub>2</sub> | 865                      | 569                           | 0.74                       | 2.63                                      |
| D <sub>2</sub> | 761                      | 573                           | 1.00                       | 2.69                                      |
| E <sub>2</sub> | 583                      | 568                           | 1.91                       | 2.61                                      |

Specimens sizing was performed in order to obtain samples with comparable stiffness; nevertheless, the specimens first order resonance frequency and compliance are quite different compared to those calculated with FEA. The FEA analysis is not accurate since the limits of the production process were not considered; these SLM-related limitations caused the generation of specimens with geometry and mechanical properties different from the nominal ones. As the number of cells increases, the structure stiffens (C and D specimens); this phenomenon can be explained by the fact that small unit cell size exacerbated the limitations of the SLM process, generating stiffer specimens due to the undesired adhesion of partially melted powders. This result had to be expected, due to larger diameter of the lattices struts described previously. The lattices with larger unit cell di-

mension are less affected by SLM process limitations, therefore the experimental results are closer to those obtained from FEA.

Assuming the simple harmonic oscillator model, damping ratio  $\xi$  and damping factor  $c$  were calculated. Moreover, using the Rayleigh damping model the  $\beta$  coefficient that multiplies the stiffness matrix  $[K]$  was calculated. Boxplots diagrams showing the modal analysis results are reported in Figure 2.12. The left column shows the results obtained from measurements made on both sets of specimens, while in the right one results are grouped to highlight the differences between specimens integrating lattice structures (L) and full cross section reference (F).

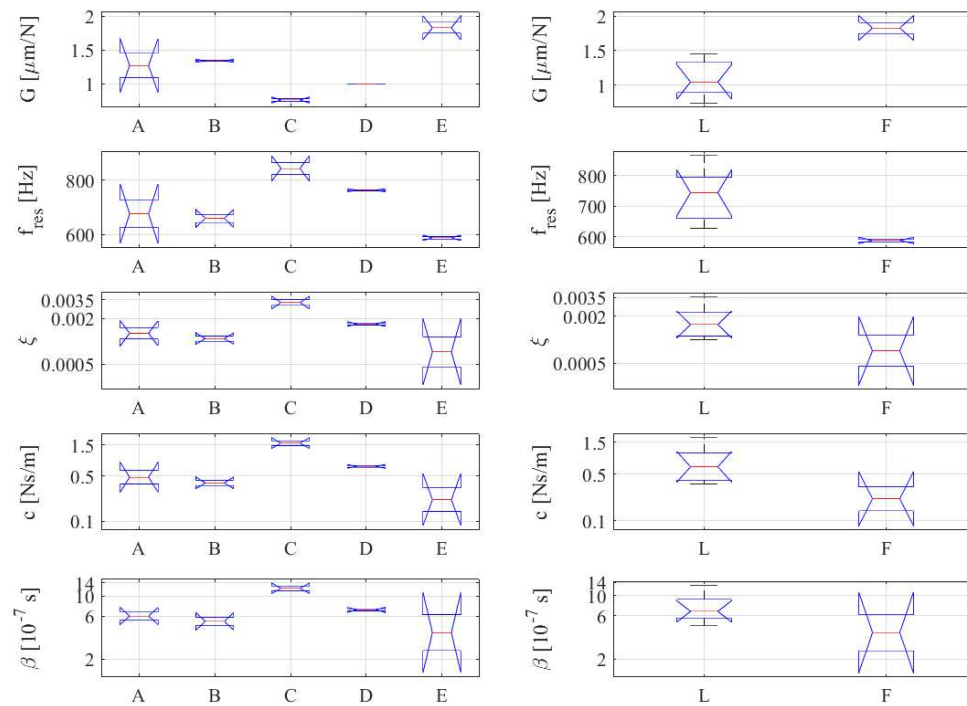


Figure 2.12: Modal analysis results for AlSi10Mg specimens

The damping ratio  $\xi$ , the damping coefficient  $c$  and the Rayleigh coefficient  $\beta$  have an opposite trend with respect to the compliance  $G$ . C and D specimens have better damping properties, but the comparison can be influenced by the fact that their compliance is lower. Comparing the results for specimens A and B with respect to the reference specimen E, having similar compliance, it is possible to conclude that specimens integrating lattice structures have better damping properties; this result is evident observing boxplot diagrams on the right side of Figure 2.12 showing comparison between damping ratio, damping factor and Rayleigh coefficient of lattices (L) vs full cross-section reference (F). Results obtained for the two repetitions of B, C and D specimens are almost coincident; on the contrary, the two series of specimens A and E demonstrated higher variability. Geometrical and modal analyses evidenced that A1 and E2 samples are the ones affected by higher defectiveness. This problem can be due to the influence of the position on the



construction platform, to the inhomogeneity of the printing process and to the stochastic phenomena intrinsic to the SLM process. An Analysis of Variance (ANOVA) was carried out on the compliance values of specimens A-B-C-D using the sample type and repetition number as factors. The result of the ANOVA show that the sample type is statistically significant (i.e. each sample type has a slightly different behaviour from the others) whereas the replicate is not significant. This latter result proves the substantial replicability of the SLM process. Lattice structures specimens have better damping properties in comparison to the full density reference specimen. Analysing the average values, the sample C is the most promising for applications requiring lightness, good stiffness and enhanced vibration damping properties. In order to evaluate the effects of cell dimension and fill ratio on damping ratio an ANOVA was carried out. The input values were the damping ratio of specimens A-B-C-D while the cell dimension and fill ratio were the factors. Analysing the results of the ANOVA, summarized in Table 2.7, it is possible to affirm that cell size has a statistically significant effect on the damping ratio. For this reason, it is confirmed that lattice configuration with smaller cell size, like C and D specimens, have better damping properties. The results obtained are promising and indicate an average improvement of the damping properties when lattices are involved.

Table 2.7: ANOVA of damping ratio vs cell dimension and fill ratio – AlSi10Mg specimens

| <b>Factor</b>         | <b>Sum Sq.</b> | <b>DOF</b> | <b>MS</b> | <b>F</b> | <b>p-value</b> |
|-----------------------|----------------|------------|-----------|----------|----------------|
| <b>Cell dimension</b> | 0.94489        | 1          | 0.94486   | 9.14     | 0.0233<0.05    |
| <b>Fill ratio</b>     | 0.32965        | 1          | 0.32965   | 3.19     | 0.1244         |
| <b>Error</b>          | 0.62029        | 6          | 0.10338   |          |                |
| <b>Total</b>          | 298.541        | 9          |           |          |                |

### 2.3.4 AlSi10Mg DoE conclusions

The experimental campaign allowed to evaluate SLM manufacturability, dimensional accuracy and dynamic behaviour of specimens integrating different kinds of lattice structures, demonstrating their great potential as high performance lightweight porous materials. Measurements performed with the optical microscope evidenced that the specimens have inhomogeneous characteristics, since struts size and surface finish are influenced by the variability of the SLM process; in particular, the factors that could influence the printing result are the position of the object in the build volume, the unwanted adhesion of partially melted powders and the stochastic phenomena typical of the SLM process. An example is represented by specimens A<sub>1</sub> and A<sub>2</sub> which, although being identical, show slight differences in size and surface finish. Nevertheless, although the printing accuracy, especially for smaller unit cells, was lower than expected due to the SLM process limitations, the repeatability was statistically good. 3D printed lattice structures in AlSi10Mg evidenced a better damping ratio, especially for sample type C, in comparison to the full density reference specimen. Results obtained by means of modal analysis of the specimens, performed by Pulse Testing, are not identical to those obtained with FEA. In partic-

ular, FEA tends to overestimate lattices compliance, especially for specimens with smaller cell size (i.e. C and D); this phenomenon occurs because the mathematical model does not take into account the limitations of the SLM process. The results obtained for specimens with larger unit cells (i.e. A and B) are excellent; the resonance frequency and compliance values obtained from the modal analysis are very close to those obtained from the FEA, making the comparison of their damping properties with respect to the full-cross section reference more accurate. The specimens having smaller cell size (i.e. C and D) have excellent damping properties, however it should be noted that they have higher stiffness with respect to the reference. The damping properties of the samples A and B are slightly lower, however there is a significant improvement in the damping ratio with respect to the reference; moreover, the stiffness of these specimens is comparable to that of the reference, therefore the excellent damping properties conferred by lattice structures can be confirmed.

These promising results suggest deepening the research in this field, studying the behaviour of lattices produced with different materials and geometries. Indeed, a better characterization of the static and dynamic behaviour of lattice elementary cells is necessary for their application as fillers of advanced mechanical components.

## **2.4 Stainless Steel specimens dynamic behaviour assessment**

The work described in the previous paragraph, focusing on the characterization of the dynamic behaviour of AlSi10Mg specimens integrating different types of lattice structures, ended with promising results that highlight the good damping properties of lattice structures. In this paragraph, the research on the dynamic behaviour of lattice structures is extended, investigating the properties of specimens made of AISI 316L stainless steel having different geometries. The possibility of exploiting unmelted metal powders as a filler material to increase the damping properties of porous / lattice structures is also investigated.

### **2.4.1 Stainless Steel specimens design and DoE**

To investigate the dynamic behaviour of stainless-steel lattice structures, a new DoE that extends the previous work is defined, choosing to study beam-like specimens integrating different types of lattice structures. Unlike what was previously done, the material under investigation is the AISI 316L stainless steel and the analysed geometries are extended, introducing some specimens that exploit unmelted powders as filler material of the porous structure. AISI 316L is an austenitic stainless steel that has high corrosion resistance and high yield strength, used in aerospace and medical fields. The main properties of this ma-

material are shown in Table 2.8. It should be remembered that material properties, as already specified before, may not be uniform, therefore the values indicated should be intended as average values.

To facilitate comparison with the results obtained for the AlSi10Mg specimens, it was decided to leave specimens geometry unmodified. This choice facilitates data acquisition, not having to substantially modify the experimental set-up and having already tested compatibility with available equipment and sensors; moreover, it is easier to compare the damping properties of lattice structures having the same geometry but made of different materials.

Table 2.8: AISI 316L material properties [95]

|   | 90°<br>(horizontal)           | 45°<br>(polar angle)          | 0°<br>(upright)               |
|---|-------------------------------|-------------------------------|-------------------------------|
| <b>Yield Strength</b><br>$R_{p0,2}$ <sup>3</sup> [N/mm <sup>2</sup> ] | 374 ± 5                       | 385 ± 6                       | 330 ± 8                       |
| <b>Tensile Strength</b><br>$R_m$ <sup>3</sup> [N/mm <sup>2</sup> ]    | 650 ± 4                       | 640 ± 3                       | 529 ± 2                       |
| <b>Elongation</b><br>[%] <sup>3</sup>                                 | 65 ± 1 %                      | 63 ± 1 %                      | 63 ± 1 %                      |
| <b>Young's Modulus</b><br>E [N/mm <sup>2</sup> ]                      | approx. 200 · 10 <sup>3</sup> | approx. 200 · 10 <sup>3</sup> | approx. 200 · 10 <sup>3</sup> |
| <b>Thermal Conductivity</b><br>$\lambda$ [W/mK]                       | approx. 15                    | approx. 15                    | approx. 15                    |
| <b>Hardness</b><br>[HRC]  | 20                            | 20                            | 20                            |

The DoE for the 316L specimens is a 2<sup>2</sup>, devised to investigate static and dynamic behaviour of beam-like specimens integrating different types of lattice structures, composed by FBCCZ unit cells. The DoE is substantially identical to that conceived for the aluminium specimens analysis. The factors are cell size and fill ratio, while levels values are the same chosen for the AlSi10Mg specimens DoE. To reduce the influence of the SLM process variability on the results, three replicates manufactured on separate build platforms have been analysed.

It should be remembered that specimens geometry and therefore DoE's factors levels were selected in order to obtain substantially constant static compliance for all the specimens; this result was achieved performing linear static and modal analyses to evaluate different geometrical configurations and combinations of factors levels.

The use of polymeric fillers to improve the damping properties of porous /lattice structures has been demonstrated by several studies, however there are no investigations that have verified the effect of unmelted powders as filler material for SLM-manufactured porous / lattice structures.

<sup>3</sup>Tensile test according to DIN EN 50125 at 20°C

To fill this knowledge gap, three lattice specimens appropriately designed in order to trap unmelted powders inside the lattice structure, were added to the DoE to investigate the effect on vibration damping. The geometry of these specimens represents the evolution of that of the C specimen which is the one that has demonstrated to have the most promising damping characteristics; lattice's cross section is composed by FBCCZ unitary cells and dust containment walls arranged in different ways. Containment walls thickness has been chosen to respect the constraint on compliance already described before; the sizing was performed by estimating the compliance with FEA.

Since the three specimens containing unmelted metal powders are variants of the C one, they are identified with the names CA, CB and CC with the second letter indicating containment baffles type. The cross section of these specimens highlights the different arrangement of the dust containment walls, Figure 2.13.

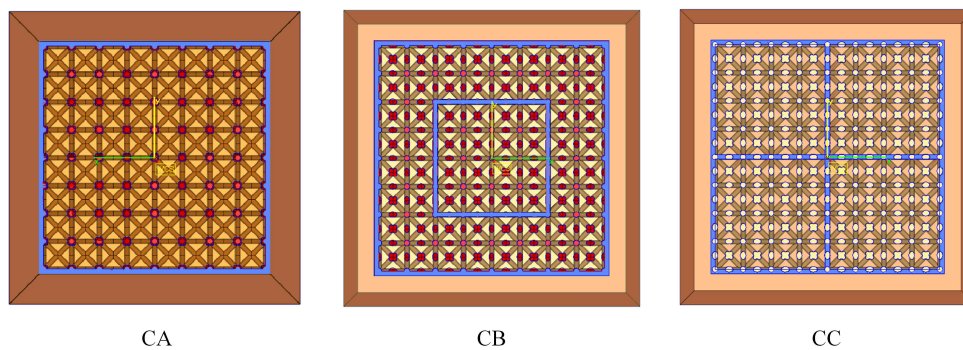


Figure 2.13: Specimens cross section: arrangement of the dust containment walls

#### 2.4.2 Stainless steel DoE specimens manufacturing

In order to proceed with 316L specimens production, it is necessary to export the 3D models in STL format and to proceed with SLM process design; specimens must be placed within the virtual build volume, making sure to create the support structures necessary to guarantee process success. Specimens STL models are composed by a very high number of triangles, therefore it is advisable to consciously choose discretization parameters to decrease errors and file size.

Materialise Magics software allows to fix errors generated in the conversion operation from 3D model to STL and subsequent supports generation; placing the specimens along the vertical direction, the need for supports is limited to the interface between build platform and specimens lower base. Specimens positioning on the build platform can influence the print result; therefore, the following factors are taken into account:

- Welding fumes aspiration takes place through a vent positioned outside the working

area; nevertheless, the side of the build platform near the vent is affected by deposits of waste carried by the fumes. Slag can adversely affect mechanical properties and surface finish, consequently it is preferable to place the specimens away from the vent.

- Specimens vertical position allows to minimize support structures, which are difficult or impossible to remove from the lattice section of the specimen, and to limit thermal stress accumulation. An horizontally positioned specimen would be affected by strong residual stresses and by the occurrence of probable consistent permanent deformations.
- The 45° specimens rotation with respect to the coater blade minimizes the chances of damage, while ensuring a gradual and uniform recoating operation.

The virtual build platform is shown in Figure 2.14, where the first and second repetitions specimens are grouped together; the simplified cross section of the three specimens containing unmelted powders is highlighted. As anticipated above, the three repetitions were produced separately and the third repetition was produced with the same positioning as the first one.

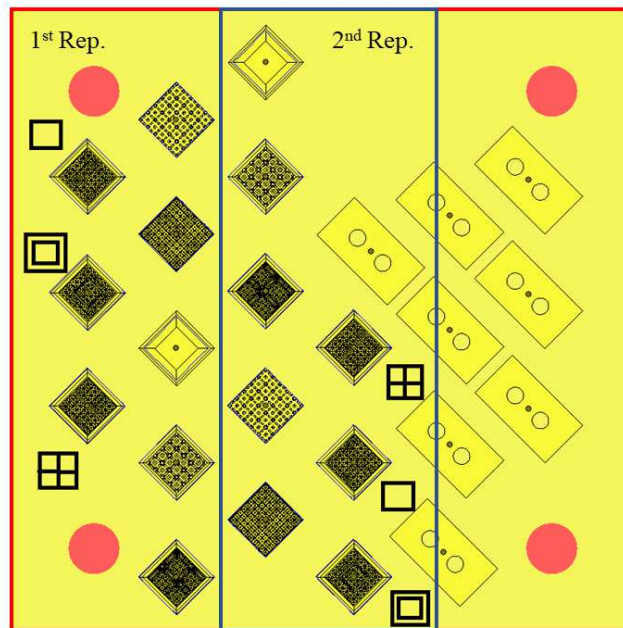


Figure 2.14: Virtual build platform – 316L specimens

Following slicing operation completion, which took several hours, the three repetitions were produced for a total of twenty-four specimens. The process parameters used are those recommended by Concept Laser: laser power 180 W, scanning speed 600 mm/s, spot diameter 120 µm, layer thickness 25 µm and 30% overlap between single scanning tracks. Islands exposure strategy was selected in order to reduce thermal strains as much

as possible. The time required to print a single platform is about four days. The result of 3D printing of the three repetitions is shown in Figure 2.15.



Figure 2.15: As-built SLM-manufactured SS 316L specimens and masses

To limit the influence of residual thermal stresses, a stress relieving heat treatment was performed as prescribed by the powder manufacturer: heat up gradually to 550°C in 3 hours, maintain temperature for 6 hours, subsequently allow the component cooling down at ambient atmosphere [95]. Mechanical tests performed on dog-bone specimens made using material and process parameters equivalent to those used in the present work have shown that material properties are substantially equivalent to those declared by the powder manufacturer and reported previously in Table 2.8. The first repetition of heat-treated specimens, separated from the build platform using a band-saw machine, are visible in Figure 2.16.

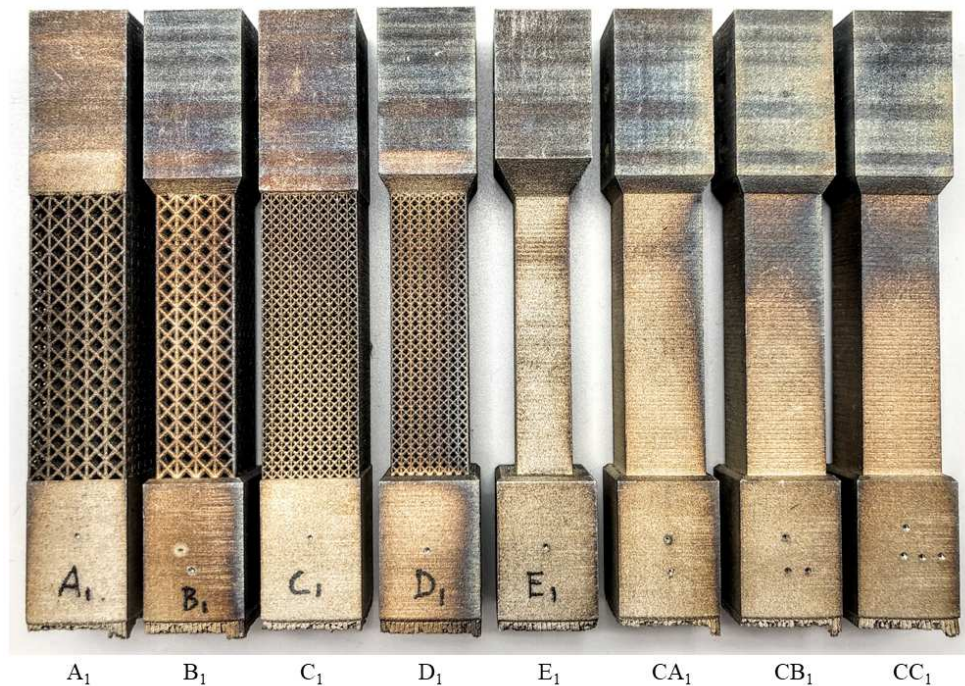
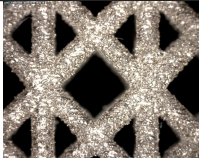

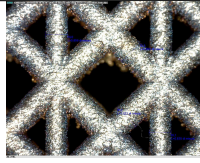
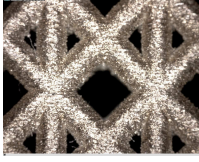

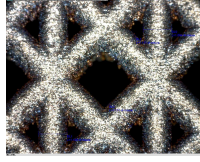
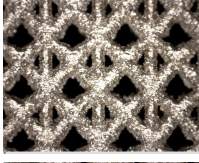
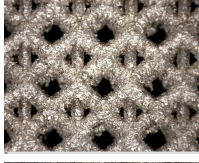
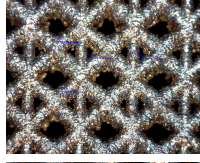
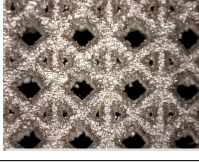
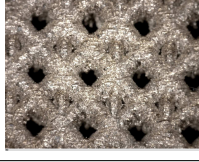
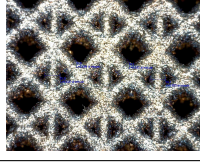


Figure 2.16: 1<sup>st</sup> repetition 316L specimens after separation from the build platform

### 2.4.3 SS 316L specimens geometrical measurements

Detail views of the lattice structures obtained performing the same procedure applied for the AlSi10Mg specimens geometry measurement are shown in Table 2.9. The lattice section is visible only for A, B, C and D specimens because CA, CB and CC specimens are closed externally to ensure metal powders containment. Comparing specimens having the same geometry (different repetition), it is clear that geometry and surface finish can be quite different. This result agrees with observations made for aluminium specimens. The print quality is inferior for lattices composed by smaller unit cells (2 mm – i.e. C and D) while the lattices composed by larger unit cells (4 mm – i.e. A and B) are well defined and are closer to the theoretical geometry. Inclined struts have larger diameter than the vertical ones despite having the same nominal size.

Table 2.9: Detail views of SS 316L lattice structures

| Specimen | 1 <sup>st</sup>   | 2 <sup>nd</sup>  | 3 <sup>rd</sup>   |
|----------|---|--|---|
| A        |   |   |   |
| B        |  |  |  |
| C        |  |  |  |
| D        |  |  |  |

Analysing the images acquired with the digital microscope, measurements of unit cells characteristic dimensions have been carried out, allowing to assess the existence of a correlation between struts diameter and their inclination with respect to the build platform. Confirming aluminium specimens DoE's results, inclined struts have larger diameter than the nominal value ( $D_i > D_{in}$ ) due to the limits of the manufacturing process, as shown in Figure 2.17.

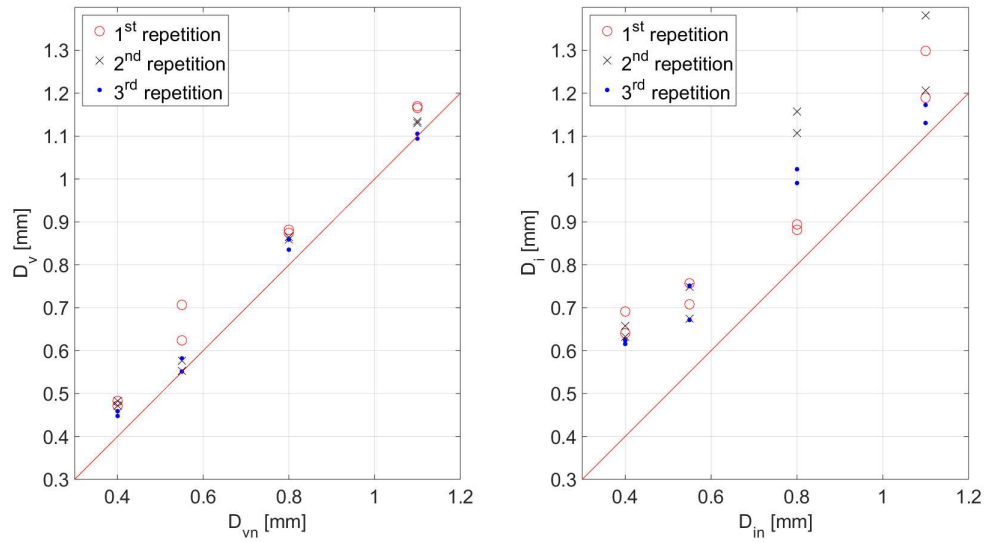


Figure 2.17: Comparison between measured and nominal SS 316L struts diameters

#### 2.4.4 FRF measurement: experimental setup and procedure

The technique and equipment used to determine the frequency response of the 316L stainless steel specimens are the same as those used for aluminium specimens. The characterization of the dynamic behaviour takes place through the pulse testing procedure, using an instrumented hammer to exert the impulsive force and an inductive probe to measure the vibrations. Signals are acquired through a dedicated National Instruments system and processed in MathWorks MATLAB.

The experimental set-up is identical to that designed to perform tests on aluminium specimens, facilitating results comparison. Specimen's positioning with respect to the vice and to the inductive probe has been kept constant as well as the excitation point; this improves the repeatability of the test and the comparability of the results, even for different specimens. The upper face of the specimen is placed at  $100 \pm 0.1$  mm from the base of the vice; specimen's lower base is constrained, allowing free vibrations of the lattice section. Inductive probe calibration, useful to establish the link between the analog output signal and the distance measured by the sensor, was performed following the same procedure previously described for aluminium specimens. The values of the calibration coefficient  $c$  obtained for the individual specimens are shown in Table 2.10.

The measurement of the frequency response through pulse testing was performed using the same techniques and equipment previously described for AlSi10Mg specimens. The frequency response measurement was performed for two different configurations:



Table 2.10: Inductive probe calibration results – SS 316L specimens

| <b>Specimen</b> | <b>v<sub>max</sub></b><br>[V] | <b>v<sub>min</sub></b><br>[V] | <b>d</b><br>[mm] | <b>c</b><br>[mV/μm] |
|-----------------|-------------------------------|-------------------------------|------------------|---------------------|
| A <sub>1</sub>  | 6.525                         | 5.593                         | 0.03             | 31.067              |
| B <sub>1</sub>  | 6.068                         | 5.17                          | 0.03             | 29.967              |
| C <sub>1</sub>  | 6.134                         | 5.233                         | 0.03             | 30.050              |
| D <sub>1</sub>  | 6.125                         | 5.228                         | 0.03             | 29.900              |
| E <sub>1</sub>  | 6.198                         | 5.296                         | 0.03             | 30.067              |
| CA <sub>1</sub> | 6.205                         | 5.301                         | 0.03             | 30.117              |
| CB <sub>1</sub> | 6.227                         | 5.322                         | 0.03             | 30.167              |
| CC <sub>1</sub> | 6.164                         | 5.260                         | 0.03             | 30.133              |
| A <sub>2</sub>  | 6.332                         | 5.420                         | 0.03             | 30.417              |
| B <sub>2</sub>  | 6.236                         | 5.330                         | 0.03             | 30.117              |
| C <sub>2</sub>  | 6.080                         | 5.179                         | 0.03             | 30.050              |
| D <sub>2</sub>  | 6.074                         | 5.179                         | 0.03             | 29.833              |
| E <sub>2</sub>  | 6.160                         | 5.258                         | 0.03             | 30.067              |
| CA <sub>2</sub> | 6.021                         | 5.125                         | 0.03             | 29.867              |
| CB <sub>2</sub> | 6.303                         | 5.394                         | 0.03             | 30.317              |
| CC <sub>2</sub> | 6.159                         | 5.256                         | 0.03             | 30.100              |
| A <sub>3</sub>  | 6.310                         | 5.397                         | 0.03             | 30.433              |
| B <sub>3</sub>  | 5.687                         | 4.820                         | 0.03             | 28.883              |
| C <sub>3</sub>  | 5.650                         | 4.788                         | 0.03             | 28.733              |
| D <sub>3</sub>  | 6.060                         | 5.166                         | 0.03             | 29.800              |
| E <sub>3</sub>  | 5.950                         | 5.060                         | 0.03             | 29.667              |
| CA <sub>3</sub> | 5.980                         | 5.060                         | 0.03             | 29.333              |
| CB <sub>3</sub> | 5.538                         | 4.682                         | 0.03             | 28.517              |
| CC <sub>3</sub> | 5.895                         | 5.005                         | 0.03             | 29.667              |

- without additional masses
- with additional masses

The difference between the two configurations is visible in Figure 2.18. The extra masses are fixed to the specimen using two bolted joints that exploit the holes on the upper base; the total additional mass is equal to 150 g.

To verify the influence of the fixing system on the measurements, the signals of a triaxial accelerometer positioned on the base of the vice, see Figure 2.18, were acquired and analysed; this allowed to exclude a significant effect of the fixing system on the measurements.

Analysing the Frequency Response Function (FRF) it is possible to estimate the compliance and first resonance frequency and amplitude, see Figure 2.19. The compliance can be estimated as the amplitude of the frequency response at  $f \approx 0$  Hz; specifically, the amplitude of the frequency response is evaluated in a range close to 0 Hz where the FRF noise is low, in the present work between 100 Hz and 150 Hz.

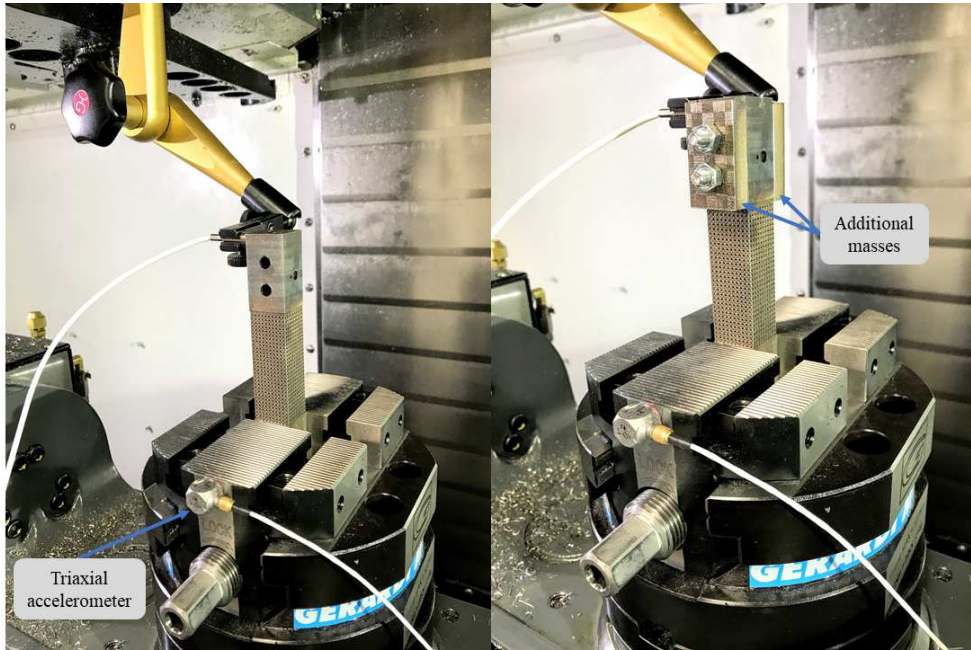


Figure 2.18: Experimental set-up - SS 316L C specimen

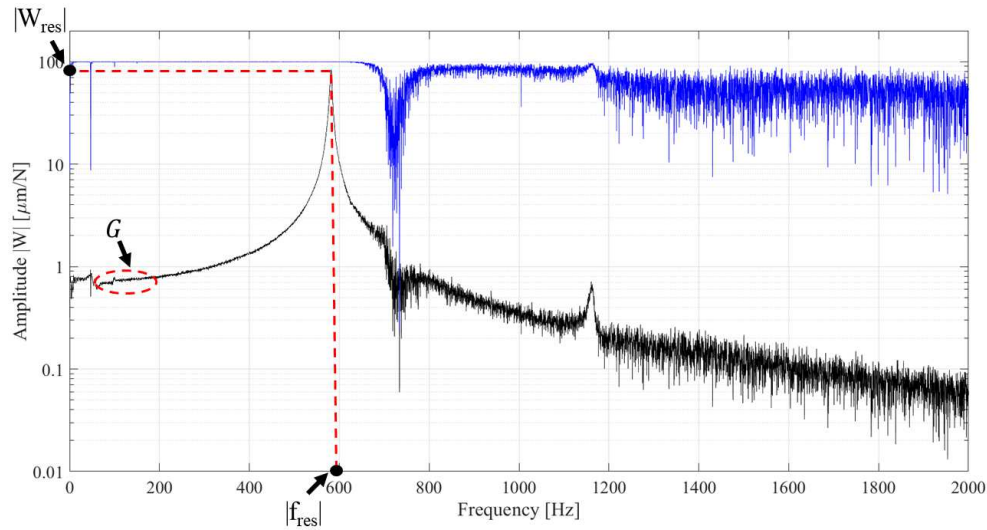


Figure 2.19: Frequency response and associated coherence function – B<sub>1</sub> specimen

To confirm compliance values estimated through frequency response analysis, verifying whether the noise at low frequencies has a significant influence on the measurement, an alternative experimental set-up was devised. The conceived test involved the application of a known static load on the specimen tip and measurement of the resulting displacement. The specimens were fixed in the vice respecting the positioning described before but rotating the A-axis of the rotary table by 90° to facilitate the application of the load. The known load was applied by means of weights ( $19.9 \pm 0.05$  kg) fixed to the specimen's

tip through a custom made interface. Specifically, using two suitably shaped plates fixed exploiting the holes on the upper base of the specimens, it was possible to apply the load near the upper edge of the same. A dial gauge positioned at the centre of specimen's tip was used to detect the displacement resulting from the application of the load. Figure 2.20 shows an example of the measurements made with this method.

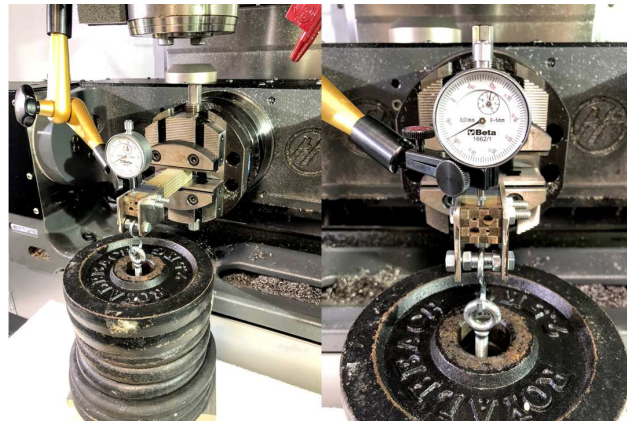


Figure 2.20: Specimens compliance measurement – alternative method

Moreover, to check if it is possible to assume that the upper base of the specimens is perfectly rigid compared to the lattice section, it is necessary to measure its deformed shape. To carry out this test, a laser profiler positioned above the upper base thanks to a special equipment is used, see Figure 2.21. A custom made bracket has been designed to connect the laser profiler to the machine tool to easily control the distance with respect to the measured surface. Measurements confirmed the hypothesis that the solid section of the upper base can be considered perfectly rigid.

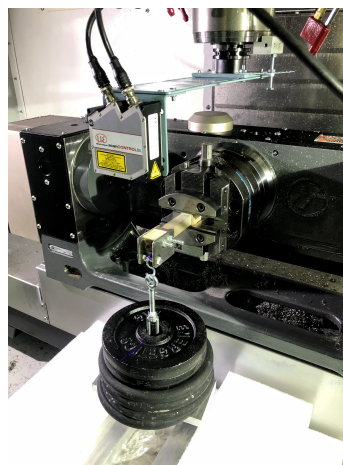


Figure 2.21: Specimens deformed shape measurement – 2D laser scanner

### 2.4.5 Experimental results analysis

The results in terms of compliance and first resonance amplitude and frequency obtained through the frequency response analysis are shown in Table 2.11 and Table 2.12 ; results are divided according to whether the measurements were made with or without additional masses. For the samples of the first and second repetition, compliance values obtained with the static method described in the previous paragraph are shown; furthermore, the compliance and resonance values of lattice specimens, obtained by FEA, are reported in order to compare them with experimental values.

Table 2.11: 316L specimens resonance frequency and compliance – no additional mass

| Specimen        | Additional mass | $f_{res}$ [Hz] | $f_{res(FEA)}$ [Hz] | $[W]_{res}$ [ $\mu\text{m}/\text{N}$ ] | $G_{(dynamic)}$ [ $\mu\text{m}/\text{N}$ ] | $G_{(static)}$ [ $\mu\text{m}/\text{N}$ ] | $G_{(FEA)}$ [ $\mu\text{m}/\text{N}$ ] |
|-----------------|-----------------|----------------|---------------------|--|--|---|--|
| A <sub>1</sub>  | No              | 548.2          | 498.29              | 135.58                                 | 0.915                                      | 1.08                                      | 1.298                                  |
| B <sub>1</sub>  | No              | 582.0          | 481.73              | 84.19                                  | 0.761                                      | 0.974                                     | 1.375                                  |
| C <sub>1</sub>  | No              | 603.5          | 439.28              | 50.79                                  | 0.703                                      | 0.871                                     | 1.683                                  |
| D <sub>1</sub>  | No              | 571.8          | 415.55              | 77.28                                  | 0.788                                      | 0.974                                     | 1.862                                  |
| E <sub>1</sub>  | No              | 550.3          | /                   | 139.82                                 | 0.941                                      | 1.18                                      | /                                      |
| CA <sub>1</sub> | No              | 543.2          | /                   | 38.73                                  | 0.980                                      | 1.02                                      | /                                      |
| CB <sub>1</sub> | No              | 544.2          | /                   | 31.67                                  | 0.877                                      | 0.974                                     | /                                      |
| CC <sub>1</sub> | No              | 543.0          | /                   | 35.40                                  | 0.865                                      | 1.02                                      | /                                      |
| A <sub>2</sub>  | No              | 596.5          | 498.29              | 41.78                                  | 0.768                                      | 0.871                                     | 1.298                                  |
| B <sub>2</sub>  | No              | 586.3          | 481.73              | 57.62                                  | 0.790                                      | 0.922                                     | 1.375                                  |
| C <sub>2</sub>  | No              | 661.9          | 439.28              | 21.19                                  | 0.594                                      | 0.717                                     | 1.683                                  |
| D <sub>2</sub>  | No              | 611.5          | 415.55              | 50.94                                  | 0.742                                      | 0.871                                     | 1.862                                  |
| E <sub>2</sub>  | No              | 533.3          | /                   | 180.81                                 | 0.982                                      | 1.18                                      | /                                      |
| CA <sub>2</sub> | No              | 573.8          | /                   | 38.55                                  | 0.806                                      | 0.974                                     | /                                      |
| CB <sub>2</sub> | No              | 571.8          | /                   | 39.50                                  | 0.791                                      | 1.02                                      | /                                      |
| CC <sub>2</sub> | No              | 569.4          | /                   | 47.19                                  | 0.805                                      | 0.974                                     | /                                      |
| A <sub>3</sub>  | No              | 604.7          | 498.29              | 62.54                                  | 0.741                                      | /   | 1.298                                  |
| B <sub>3</sub>  | No              | 578.8          | 481.73              | 99.23                                  | 0.801                                      | /   | 1.375                                  |
| C <sub>3</sub>  | No              | 636.3          | 439.28              | 39.88                                  | 0.615                                      | /   | 1.683                                  |
| D <sub>3</sub>  | No              | 574.5          | 415.55              | 97.68                                  | 0.789                                      | /   | 1.862                                  |
| E <sub>3</sub>  | No              | 542.4          | /                   | 263.22                                 | 0.942                                      | /   | /                                      |
| CA <sub>3</sub> | No              | 577.3          | /                   | 45.30                                  | 0.767                                      | /   | /                                      |
| CB <sub>3</sub> | No              | 565.4          | /                   | 46.62                                  | 0.785                                      | /   | /                                      |
| CC <sub>3</sub> | No              | 559.2          | /                   | 51.79                                  | 0.836                                      | /   | /                                      |

The specimens first order resonance frequency and compliance are quite different compared to those calculated with FEA, due to the fact that production process limits were not considered in the mathematical model; as specified before, these SLM-related limitations caused the generation of specimens with geometry and mechanical properties different from the nominal ones. Furthermore, the FEM model used to perform the simulations on steel specimens is different from that used for aluminium specimens. In order to drastically reduce calculation time and computational resources needed to perform the simulation, a simplified 1D-3D hybrid FEM model has been designed; nevertheless, it does not take into account the exact geometry of the specimen and for this reason is less accurate. This last aspect will be further examined in following paragraphs.

Table 2.12: 316L specimens resonance frequency and compliance – with additional mass

| Specimen        | Additional mass | $f_{res}$<br>[Hz] | $ W _{res}$<br>[ $\mu\text{m}/\text{N}$ ] | $G_{(dynamic)}$<br>[ $\mu\text{m}/\text{N}$ ] |
|-----------------|-----------------|-------------------|---|---|
| A <sub>1</sub>  | Yes             | 386.8             | 90.27                                     | 1.024   |
| B <sub>1</sub>  | Yes             | 415.4             | 99.30                                     | 0.844   |
| C <sub>1</sub>  | Yes             | 432.6             | 75.06                                     | 0.786   |
| D <sub>1</sub>  | Yes             | 408.5             | 56.18                                     | 0.880   |
| E <sub>1</sub>  | Yes             | 387.3             | 91.20                                     | 1.086   |
| CA <sub>1</sub> | Yes             | 387.6             | 42.24                                     | 1.090   |
| CB <sub>1</sub> | Yes             | 389.2             | 36.43                                     | 0.936   |
| CC <sub>1</sub> | Yes             | 389.5             | 43.90                                     | 0.956   |
| A <sub>2</sub>  | Yes             | 429.5             | 31.13                                     | 0.866   |
| B <sub>2</sub>  | Yes             | 418.0             | 53.75                                     | 0.888   |
| C <sub>2</sub>  | Yes             | 479.5             | 37.89                                     | 0.659   |
| D <sub>2</sub>  | Yes             | 436.5             | 75.80                                     | 0.830   |
| E <sub>2</sub>  | Yes             | 373.0             | 167.97                                    | 1.139   |
| CA <sub>2</sub> | Yes             | 409.2             | 30.62                                     | 0.916   |
| CB <sub>2</sub> | Yes             | 410.7             | 45.35                                     | 0.889   |
| CC <sub>2</sub> | Yes             | 405.7             | 51.26                                     | 0.904   |
| A <sub>3</sub>  | Yes             | 431.0             | 99.75                                     | 0.817   |
| B <sub>3</sub>  | Yes             | 407.4             | 59.28                                     | 0.877   |
| C <sub>3</sub>  | Yes             | 457.4             | 105.65                                    | 0.674   |
| D <sub>3</sub>  | Yes             | 406.0             | 50.21                                     | 0.908   |
| E <sub>3</sub>  | Yes             | 375.7             | 343.20                                    | 1.146   |
| CA <sub>3</sub> | Yes             | 409.4             | 47.46                                     | 0.866   |
| CB <sub>3</sub> | Yes             | 400.7             | 65.25                                     | 0.936   |
| CC <sub>3</sub> | Yes             | 398.2             | 61.14                                     | 0.961   |

Static compliance estimated analysing the frequency response is quite different compared to that calculated applying a known load and measuring the displacement. Compliance values estimated with the latter method are closer to those calculated with FEA, even if the difference remains consistent due to the reasons already described before. As already observed for aluminium specimens, smaller lattice unit cell's dimension is associated with higher stiffness (C and D specimens); this phenomenon is mainly due to SLM process limitations, like undesired adhesion of partially melted powders. The larger diameter of lattice's inclined struts described previously confirm process related limitations. Comparing results obtained with and without additional mass, it is clear that the mass variation significantly influences the resonance frequency. Moreover, the amplitude of the frequency response at resonance  $|W_{res}|$  of the specimens containing unmelted metal powders is smaller, suggesting that this type of filler has a significant effect on the specimens' dynamic behaviour.

As previously done, damping ratio  $\xi$  and damping factor  $c$  were calculated assuming the simple harmonic oscillator model, while  $\beta$  coefficient using the Rayleigh damping model. Boxplots diagrams showing the modal analysis results are reported in Figure 2.22; on the right column results are grouped to highlight differences between specimens integrating lattice structures (L), lattices with powder filler (POW) and full cross-section reference (F).

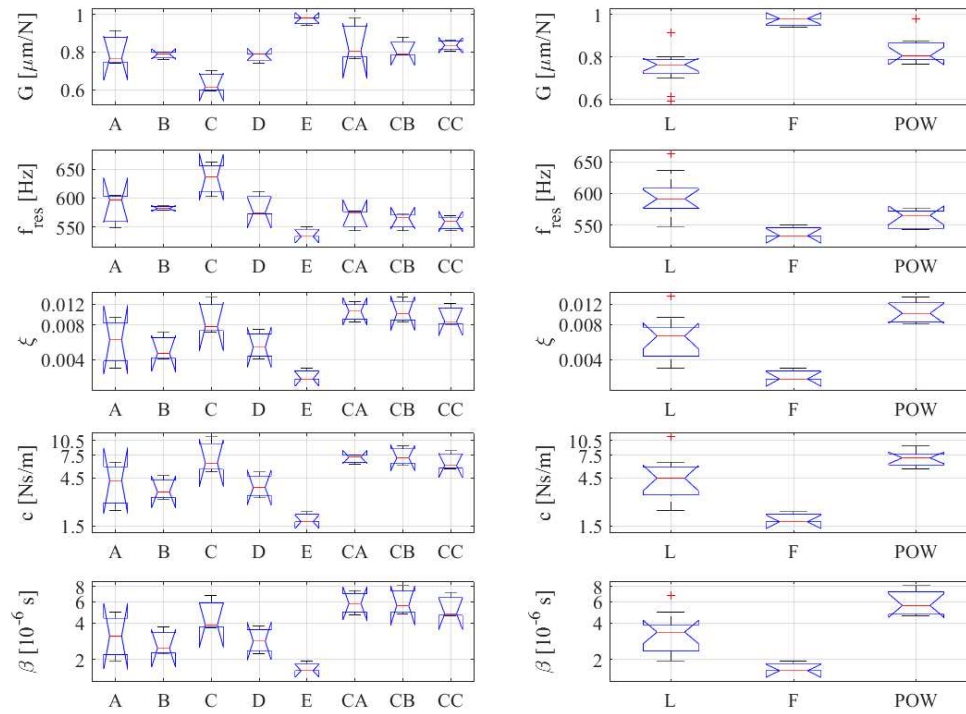


Figure 2.22: 316L specimens modal analysis results – without additional mass

Confirming the results of tests carried out on aluminium specimens, the damping ratio  $\zeta$ , the damping coefficient  $c$  and the Rayleigh coefficient  $\beta$  have an opposite trend with respect to the compliance  $G$ . Specimens incorporating lattice structures demonstrated better damping properties in comparison to the full cross-section reference specimen, but specimens that have the best damping properties are those that contain unmelt metal powders; this result is obvious observing boxplot diagrams on the right side of Figure 2.22 where specimens are grouped in order to highlight the differences between macro-categories (lattices (L), full cross-section reference (F), with unmelt metal powders (POW)). Results obtained for the three repetitions of A and C specimens are affected by higher variability, mainly due to the stochastic phenomena intrinsic to the SLM process. The C specimen is confirmed to be the most promising when enhanced vibration damping properties are required; furthermore, the results unequivocally demonstrate that unmelted metal powders contribute significantly to improve damping properties.

The results obtained from tests performed with additional masses are shown in Figure 2.23. The specimens containing unmelted metal powders are still those with the best damping properties; nevertheless, comparison between the different types of lattices is even more difficult than without additional mass. For this reason, it is preferable to consider data obtained without additional masses.

To evaluate the effects of cell dimension and fill ratio on damping ratio an ANOVA is carried out, see Table 2.13. The input values are the damping ratio of specimens A-B-C-D

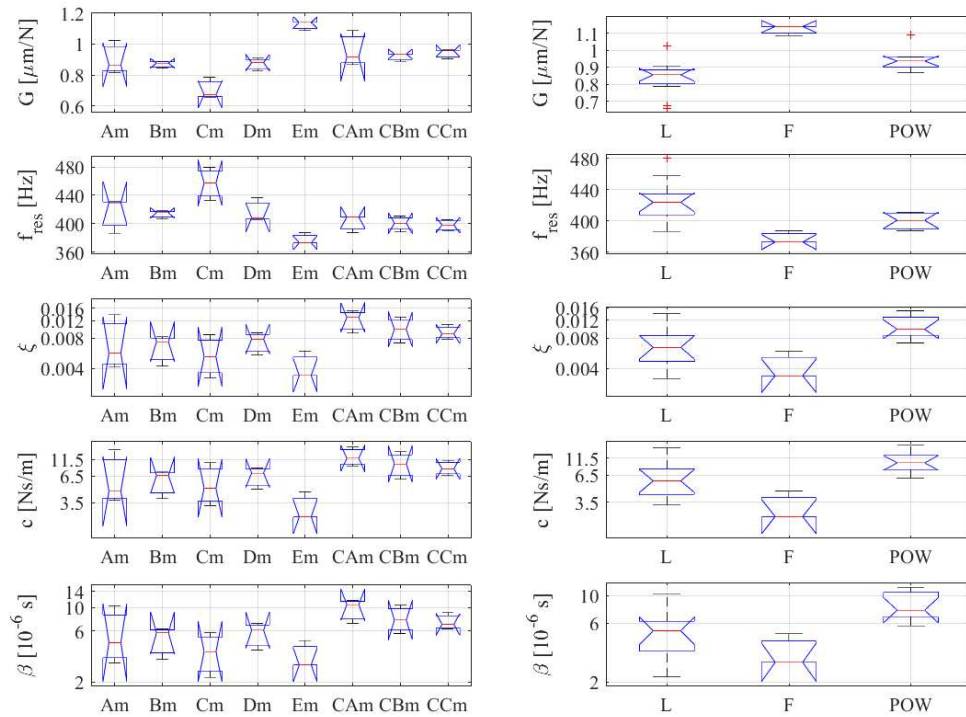


Figure 2.23: 316L specimens modal analysis results – with additional mass

while cell dimension and fill ratio are the factors. ANOVA does not allow to affirm the existence of a statistically significant effect of cell size and the fill ratio on damping ratio. It is therefore not possible to identify with certainty which type of lattice structure is the best, even if looking at the average values C-type seems to be the one that has better damping properties.

Table 2.13: ANOVA of damping ratio vs cell dimension and fill ratio - 316L specimens

| Factor                | Sum Sq. | DOF | MS      | F    | p-value |
|-----------------------|---------|-----|---------|------|---------|
| <b>Cell dimension</b> | 0.20819 | 1   | 0.20819 | 1.5  | 0.2523  |
| <b>Fill ratio</b>     | 0.33086 | 1   | 0.33086 | 2.38 | 0.1574  |
| <b>Error</b>          | 1.25205 | 9   | 0.13912 |      |         |
| <b>Total</b>          | 1.7911  | 11  |         |      |         |

### 2.4.6 316L DoE conclusions

The investigation on the dynamic properties of AISI 316L lattice structures confirms the results obtained in the previous study concerning AISi10Mg lattices. SLM manufacturability, dimensional accuracy and dynamic behaviour of specimens integrating different kinds of lattice structures have been evaluated. Measurements performed with the optical microscope confirmed that specimens lattice geometry is not homogeneous; struts size and the surface finish are influenced by SLM process variability due to unwanted adhe-

sion of partially melted powders and stochastic phenomena. Smaller lattice unit cell's dimension is associated with higher stiffness and inclined struts have larger diameter compared to vertical ones. The static compliance estimated analysing the frequency response is quite different compared to the value calculated applying a known load and measuring the displacement. Compliance values estimated with the latter method are closer to those calculated with FEA, even if the difference remains consistent. Modal mass variation significantly influences the frequency response. The amplitude of the frequency response at resonance  $|W_{res}|$  of specimens containing unmelted metal powders is smaller, suggesting that this type of filler has a significant effect on specimens dynamic behaviour. Lattice specimens have better damping properties in comparison to the full cross-section reference specimen, nonetheless those that contain unmelt metal powders are the best; the effect of cell size and the fill ratio on damping ratio is not statistically significant, nevertheless looking at the average values C-type seems to be the one that has better damping properties. An accurate characterization of dynamic behaviour and damping properties of lattice structures requires further investigations. In Chapter 3 the effect of lattice's geometry and size variation on static and dynamic behaviour have been evaluated, developing a methodology that could help characterizing different kinds of lattice / porous structures.

## 2.5 Specimens 1D-3D hybrid FEM model

Calculation time required to perform meshing and static / modal analysis of the specimens integrating lattice structures by means of a full 3D FEA is very high. If it is necessary to repeat the calculation several times to check the behaviour of different geometries and configurations, this implies a considerable allocation of time and resources.

An alternative to the full 3D analysis of lattice structures consists in the development of a hybrid 1D-3D model that uses two-dimensional elements to discretize specimens lattice section. This approach allows to considerably limit the FEM model complexity, which for lattices composed of a high number of cells may not be acceptable or compatible with available time and computing power.

The code used to develop this type of FEM model is Ansys Mechanical APDL 19.2. The lattice section of the specimens is discretized using BEAM189 elements (Timoshenko beam theory) connected to each other at elementary cell's nodes, while the two bases are discretized using SOLID186 elements. The interface between 1D and 3D elements is modelled using the contact elements TARGE170 and CONTA175, using Multipoint Constraint (MPC). To calculate the specimen's compliance, a unit load (1 N) is applied to the free end of the beam-like specimen while the lower base is fixed. The hybrid model of the A specimen is shown in Figure 2.24; the graphic representation highlights BEAM elements used for the lattice section and SOLID ones for upper and lower bases.



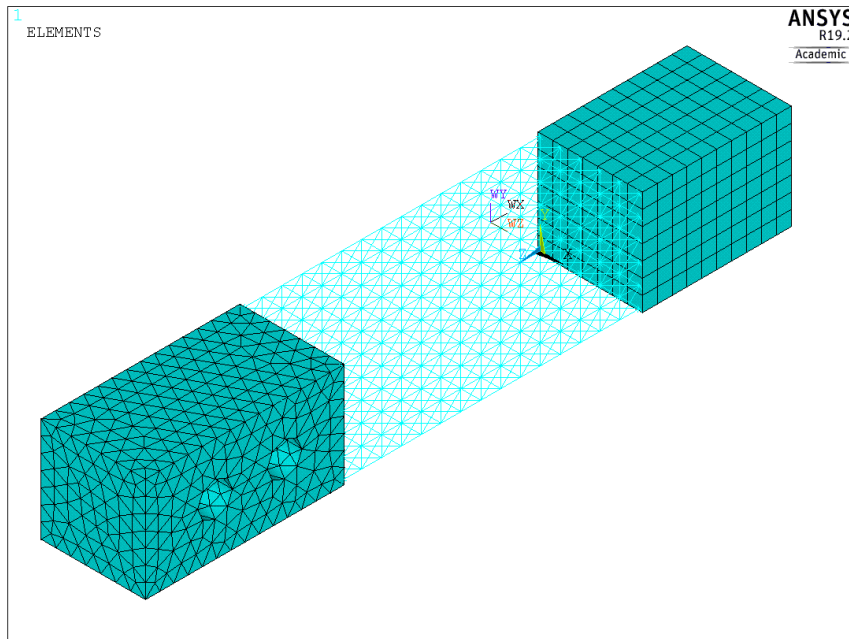


Figure 2.24: A specimen hybrid 1D-3D FEM model

The execution of linear static and modal analyses requires few minutes; the time saved is very high compared to the full 3D model, which would require several hours of calculation. Figure 2.25 shows the displacement contour plot of specimen A, useful for compliance estimation.

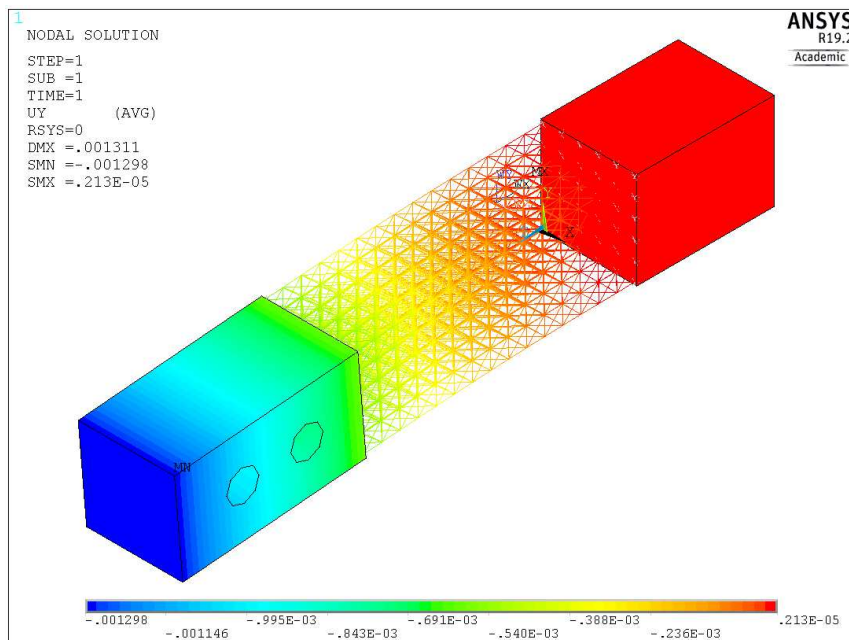


Figure 2.25: A specimen displacement contour plot – hybrid FEM model

Using the same FE model, it is possible to perform the modal analysis, eliminating the external load; for example, Figure 2.26 shows A specimen first mode shape.

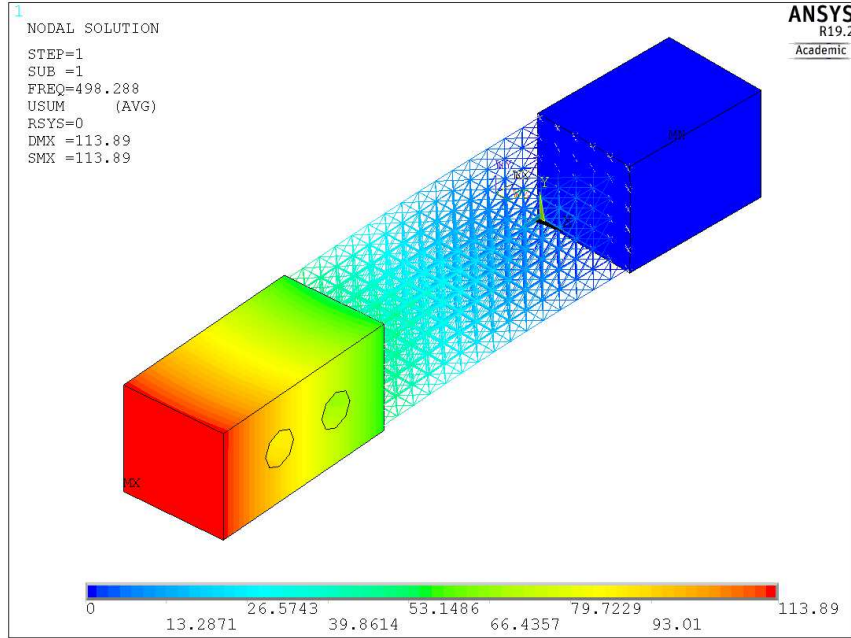


Figure 2.26: A specimen first mode shape – hybrid FEM model

Figure 2.27 shows the comparison between FEM calculated and experimental results (three replicates) in terms of compliance and first resonance frequency. The approach outlined, generally involves an underestimation of lattice’s stiffness: the lattice’s actual geometry in the areas where beams intersect (nodes) and geometric variations caused by the limits of the SLM process, which generally involve a stiffening due to unwanted adhesion of partially melted powders, are not taken into account. The model should be refined to consider the real lattice’s geometry and material properties.

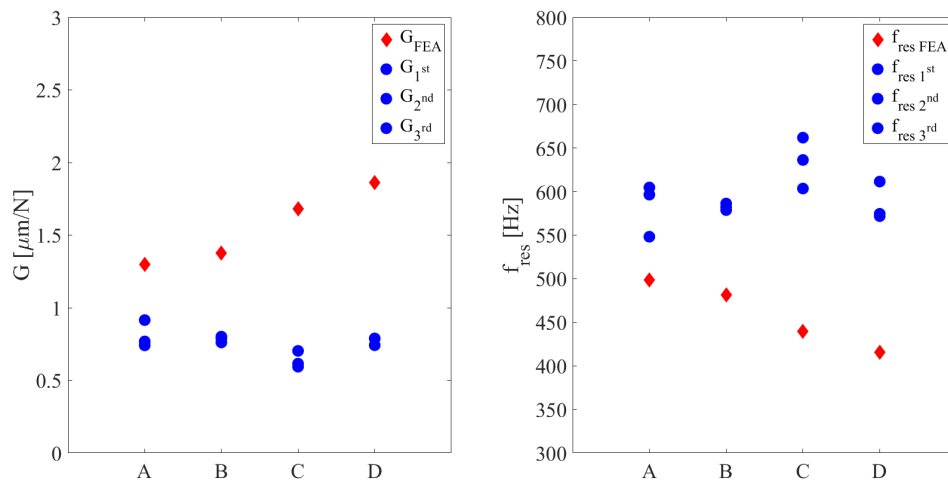


Figure 2.27: Comparison between FEM and experimental results – 316L specimens

Numerical simulations performed assuming that the lattice's geometry is identical to CAD tend to underestimate the stiffness; this is due to larger struts diameter compared to the nominal one, see Figure 2.17. This phenomenon mainly affects inclined beams, causing the production of lattices with higher stiffness and fill ratio.

If it is required to obtain a lattice's geometry close to the nominal one, literature review suggests to define appropriate correction coefficients to modify CAD nominal struts diameter in order to obtain the desired unit cell geometry [64]. In essence, changing the nominal diameter of vertical and inclined beams it would be possible to obtain the desired result at the end of SLM 3D printing process.

Applying an alternative approach, it is possible to improve simulations accuracy modifying FEM model to take into account of real struts diameters. However, this method cannot simulate undesired adhesion of partially melted metal powders at lattice nodes. To verify the effectiveness of this approach, FE model struts diameters have been modified in order to reflect the lattice's real geometry; the comparison between compliance values obtained from FEA with respect to the experimental ones is shown in Figure 2.28.

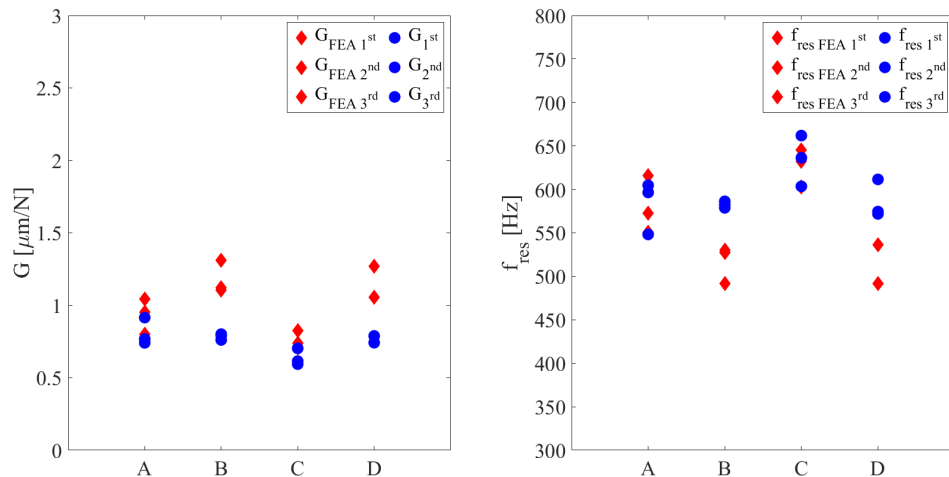


Figure 2.28: Comparison between FEM (with correction factor) and experimental results – 316L specimens

Looking at Figure 2.28 it is clear that the FEM model that takes into account the real struts diameter is more accurate than the previous one, in particular for type A and C specimens that have lower fill ratio; this result may be due to the fact that for specimens B and D, with higher fill ratio, the effect of powder agglomerates at nodes is not negligible.

## 2.6 Beam-like specimens dynamic behaviour mathematical model

In previous paragraphs the dynamic behaviour of beam-like specimens integrating lattice structures has been investigated through experimental tests and FEM simulations.

The following paragraph investigates the possibility of applying an analytical method to describe the dynamic behaviour of beam-like specimens, through the development and implementation of an appropriate mathematical model.

The goal is to develop a mathematical model to describe dynamic behaviour and damping properties of beam-like specimens; their geometry is subdivided in three distinct sections (see Figure 2.29), similarly to those analysed in previous paragraphs. The mathematical model is based on the Euler-Bernoulli beam theory. In order to calculate specimens damping properties, some fundamental parameters obtained through the analysis of the frequency response obtained experimentally, for example via pulse testing, are still required.

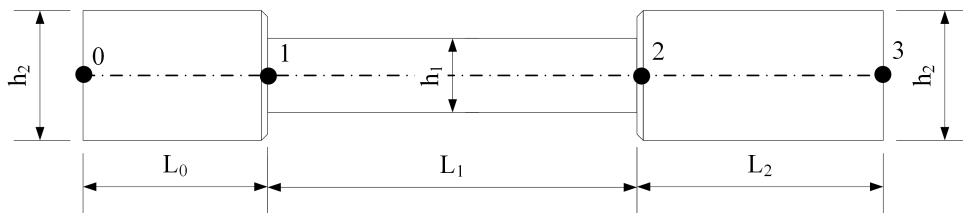


Figure 2.29: Beam-like specimen geometry and dimensions

The specimen's geometry is divided into three beam-like sections joined together, having different characteristics:

- Square full cross-section 0-1: length  $L_0$  and side  $h_2$
- Lattice section 1-2: length  $L_1$  and side  $h_1$
- Square full cross-section 2-3: length  $L_2$  and side  $h_2$

The experimental set-up chosen to determine the frequency response of the specimens used a vice to block the lower base (0-1), while the impulsive force was applied to the upper one (3) using an instrumented hammer; it is therefore reasonable to constraint all displacements and rotations at point 1 and hypothesize that the impulsive force is applied at point 3. The model can therefore be simplified, eliminating the lower base, see Figure 2.30. To further simplify the model, it is also assumed that the upper base (2-3) is perfectly rigid; this hypothesis is justified by the analysis of the specimens deformed

shape previously acquired using a laser profiler, that demonstrated that full cross-section is considerably stiffer compared to lattice section.

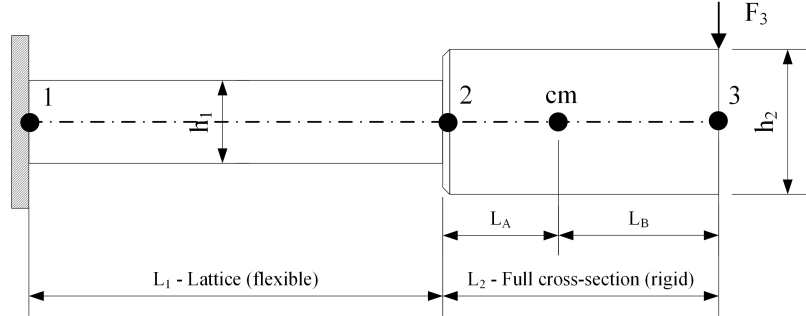


Figure 2.30: Simplified beam-like specimen model

In Figure 2.30, the center of mass of the upper base is indicated with cm, while  $L_A$  and  $L_B$  are the distances with respect to nodes 2 and 3. To take into account of the different position of the center of mass when the geometry of the upper base and the additional mass varies, the parameter  $q_1$  has been defined.

$$L_A = q_1 L_2 \quad (2.9)$$

The equation of motion that describes the behavior of the reticular section of the specimen can be expressed as:

$$\begin{aligned} & \frac{\rho_1 A_1 L_1}{420} \begin{bmatrix} 156 & 22L_1^2 & 54 & -13L_1 \\ 22L_1^2 & 4L_1^2 & 13L_1 & -3L_1^2 \\ 54 & 13L_1 & 156 & -22L_1 \\ -13L_1 & -3L_1^2 & -22L_1 & 4L_1^2 \end{bmatrix} \begin{Bmatrix} \ddot{u}_1 \\ \ddot{\phi}_1 \\ \ddot{u}_2 \\ \ddot{\phi}_2 \end{Bmatrix} + \\ & + \frac{E_1 J_1}{L_1^3} \begin{bmatrix} 12 & 6L_1 & -12 & 6L_1 \\ 6L_1 & 4L_1^2 & -6L_1 & 2L_1^2 \\ -12 & -6L_1 & 12 & -6L_1 \\ 6L_1 & 2L_1^2 & -6L_1 & 4L_1^2 \end{bmatrix} \begin{Bmatrix} u_1 \\ \phi_1 \\ u_2 \\ \phi_2 \end{Bmatrix} + [M_{rot}] \begin{Bmatrix} \ddot{u}_1 \\ \ddot{\phi}_1 \\ \ddot{u}_2 \\ \ddot{\phi}_2 \end{Bmatrix} + [C] \begin{Bmatrix} \dot{u}_1 \\ \dot{\phi}_1 \\ \dot{u}_2 \\ \dot{\phi}_2 \end{Bmatrix} \end{aligned} \quad (2.10)$$

taking into account the constraint applied at node 1 ( $u_1 = \phi_1 = 0$ ), the simplified dynamic equation is the following, where simplified matrices are identified with the subscript  $r$ :

$$[M_r] \begin{Bmatrix} \ddot{u}_2 \\ \ddot{\phi}_2 \end{Bmatrix} + [C_r] \begin{Bmatrix} \dot{u}_2 \\ \dot{\phi}_2 \end{Bmatrix} + [K_r] \begin{Bmatrix} u_2 \\ \phi_2 \end{Bmatrix} = \begin{Bmatrix} F_2 \\ M_2 \end{Bmatrix} \quad (2.11)$$

The experimental tests carried out to determine the specimens frequency response allowed to collect data in terms of displacement at node 3; therefore, it is required to re-define the Equation 2.11:

$$[M_{12}] \begin{Bmatrix} \ddot{u}_3 \\ \ddot{\phi}_3 \end{Bmatrix} + [C_{12}] \begin{Bmatrix} \dot{u}_3 \\ \dot{\phi}_3 \end{Bmatrix} + [K_{12}] \begin{Bmatrix} u_3 \\ \phi_3 \end{Bmatrix} = \begin{Bmatrix} \dots \\ \dots \end{Bmatrix} F_3 \quad (2.12)$$

to obtain this equation, it is necessary to modify the mass, damping and stiffness matrices following the steps below. Figure 2.31 shows the forces and moments that act on the solid section of the specimen (2-3).

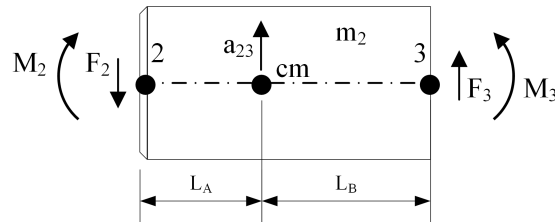


Figure 2.31: Forces and moments acting on the solid section of the specimen

The acceleration of the centre of mass is assumed equal to the average of the accelerations of the nodes 2 and 3,  $a_{23} \approx \frac{\ddot{u}_3 + \ddot{u}_2}{2}$ . The solid section of the specimen can be considered perfectly rigid, since its compliance is much lower than the lattice section; therefore, the deformation of the beam can be schematized as in Figure 2.32, where the section 2-3 is a straight line ( $\phi_2 \approx \phi_3$ ).

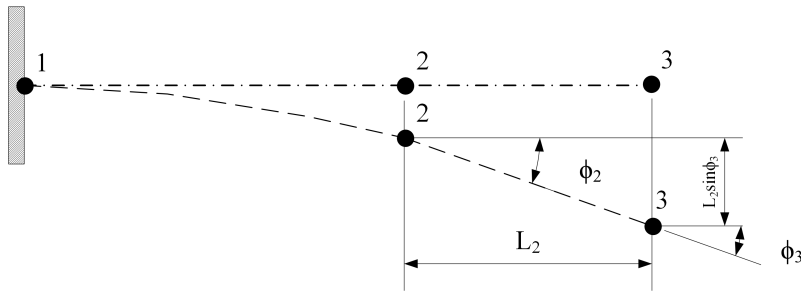


Figure 2.32: Specimen's deformed shape and dimensions

The node 2 displacement can be calculated knowing that of the node 3, assuming a small angular displacement ( $\sin \phi_2 \approx \phi_2$ ):

$$u_2 \approx u_3 - L_2 \phi_2 \quad (2.13)$$

Using the equation of translational equilibrium for the full cross-section beam it is possible to express  $F_2$  as a function of known quantities:

$$F_2 \approx F_3 - m_2 \left( \frac{\ddot{u}_3 + \ddot{u}_2}{2} \right) \approx F_3 - m_2 \left( \frac{\ddot{u}_3 + \ddot{u}_3 - L_2 \ddot{\phi}_2}{2} \right) = F_3 - m_2 \left( \ddot{u}_3 - \frac{L_2}{2} \ddot{\phi}_2 \right) \quad (2.14)$$

Similarly, using the equation of rotational equilibrium for the full cross-section beam it is possible to express  $M_2$  as a function of known quantities:

$$J_{ROT_2} \ddot{\phi}_2 = -M_2 + F_3 L_B + F_2 L_A \quad (2.15)$$

substituting Equation 2.9 and Equation 2.14:

$$J_{ROT_2} \ddot{\phi}_2 = -M_2 + F_3 (L_A + L_B) - m_2 L_A \ddot{u}_3 + m_2 \frac{L_2}{2} L_A \ddot{\phi}_2 \quad (2.16)$$

therefore:

$$M_2 = F_3 L_2 - m_2 q_1 L_2 \ddot{u}_3 + \left( m_2 \frac{L_2^2}{2} q_1 - J_{ROT_2} \right) \ddot{\phi}_2 \quad (2.17)$$

Replacing Equation 2.14 and Equation 2.17 in the Equation 2.11, the simplified equation of motion becomes:

$$\begin{bmatrix} M_r \\ C_r \\ K_r \end{bmatrix} \begin{Bmatrix} \ddot{u}_2 \\ \ddot{\phi}_2 \end{Bmatrix} + \begin{bmatrix} C_r \\ K_r \end{bmatrix} \begin{Bmatrix} \dot{u}_2 \\ \dot{\phi}_2 \end{Bmatrix} + \begin{bmatrix} K_r \end{bmatrix} \begin{Bmatrix} u_2 \\ \phi_2 \end{Bmatrix} = \begin{bmatrix} F_3 - m_2 \left( \ddot{u}_3 - \frac{L_2}{2} \ddot{\phi}_2 \right) \\ F_3 L_2 - m_2 q_1 L_2 \ddot{u}_3 + \left( m_2 \frac{L_2^2}{2} q_1 - J_{ROT_2} \right) \ddot{\phi}_2 \end{bmatrix} \quad (2.18)$$

Therefore, it is required to calculate the simplified matrices of mass, damping and stiffness, taking into account the constraint at node 1, expressing them as a function of known quantities (node 3).

The simplified mass matrix can be expressed as:

$$\begin{aligned} [M_r] \begin{Bmatrix} \ddot{u}_2 \\ \ddot{\phi}_2 \end{Bmatrix} &= \begin{bmatrix} m_{11} & m_{12} \\ m_{21} & m_{22} \end{bmatrix} \begin{Bmatrix} \ddot{u}_2 \\ \ddot{\phi}_2 \end{Bmatrix} = \begin{bmatrix} m_{11} & m_{12} \\ m_{21} & m_{22} \end{bmatrix} \begin{Bmatrix} \ddot{u}_3 - L_2 \ddot{\phi}_3 \\ \ddot{\phi}_3 \end{Bmatrix} = \\ &= \begin{bmatrix} m_{11} \ddot{u}_3 & (m_{12} - L_2 m_{11}) \ddot{\phi}_3 \\ m_{21} \ddot{u}_3 & (m_{22} - L_2 m_{21}) \ddot{\phi}_3 \end{bmatrix} = \underbrace{\begin{bmatrix} m_{11} & m_{12} - L_2 m_{11} \\ m_{21} & m_{22} - L_2 m_{21} \end{bmatrix}}_{[M_{12}]} \begin{Bmatrix} \ddot{u}_3 \\ \ddot{\phi}_3 \end{Bmatrix} \end{aligned} \quad (2.19)$$

To get an equation that has the form of the Equation 2.12, it is necessary to move the terms of the second member of the Equation 2.18 to the first; therefore, some terms of the second member have been added to the mass matrix  $[M_{12}]$ :

$$[M_{12}] = \begin{bmatrix} m_{11} + m_2 & m_{12} - L_2 m_{11} - m_2 \frac{L_2}{2} \\ m_{21} + m_2 q_1 L_2 & m_{22} - L_2 m_{21} - m_2 \frac{L_2^2}{2} q_1 + J_{ROT_2} \end{bmatrix} \quad (2.20)$$

The same procedure is applied to derive the damping and stiffness matrices,  $[C_{12}]$  and  $[K_{12}]$ :

$$\begin{aligned} [C_r] \begin{Bmatrix} \dot{u}_2 \\ \dot{\phi}_2 \end{Bmatrix} &= \begin{bmatrix} c_{11} & c_{12} \\ c_{21} & c_{22} \end{bmatrix} \begin{Bmatrix} \dot{u}_2 \\ \dot{\phi}_2 \end{Bmatrix} = \begin{bmatrix} c_{11} & c_{12} \\ c_{21} & c_{22} \end{bmatrix} \begin{Bmatrix} \dot{u}_3 - L_2 \dot{\phi}_3 \\ \dot{\phi}_3 \end{Bmatrix} = \\ &= \underbrace{\begin{bmatrix} c_{11} \dot{u}_3 & (c_{12} - L_2 c_{11}) \dot{\phi}_3 \\ c_{21} \dot{u}_3 & (c_{22} - L_2 c_{21}) \dot{\phi}_3 \end{bmatrix}}_{[C_{12}]} \begin{Bmatrix} \dot{u}_3 \\ \dot{\phi}_3 \end{Bmatrix} \end{aligned} \quad (2.21)$$

$$\begin{aligned} [K_r] \begin{Bmatrix} u_2 \\ \phi_2 \end{Bmatrix} &= \begin{bmatrix} k_{11} & k_{12} \\ k_{21} & k_{22} \end{bmatrix} \begin{Bmatrix} u_2 \\ \phi_2 \end{Bmatrix} = \begin{bmatrix} k_{11} & k_{12} \\ k_{21} & k_{22} \end{bmatrix} \begin{Bmatrix} u_3 - L_2 \phi_3 \\ \phi_3 \end{Bmatrix} = \\ &= \underbrace{\begin{bmatrix} k_{11} u_3 & (k_{12} - L_2 k_{11}) \phi_3 \\ k_{21} u_3 & (k_{22} - L_2 k_{21}) \phi_3 \end{bmatrix}}_{[K_{12}]} \begin{Bmatrix} u_3 \\ \phi_3 \end{Bmatrix} \end{aligned} \quad (2.22)$$

To consider material damping properties the Rayleigh damping model is chosen; the mass proportional coefficient is neglected as a first approximation ( $\alpha=0$ ). The  $\beta$  term models



structural or hysteretic damping, taking into account of the internal energy dissipation.

$$[C_{12}] = \beta [K_{12}] \quad (2.23)$$

The equation of motion that describes the behaviour of the beam is therefore the following:

$$[M_{12}] \begin{Bmatrix} \ddot{u}_3 \\ \ddot{\phi}_3 \end{Bmatrix} + \beta [K_{12}] \begin{Bmatrix} \dot{u}_3 \\ \dot{\phi}_3 \end{Bmatrix} + [K_{12}] \begin{Bmatrix} u_3 \\ \phi_3 \end{Bmatrix} = \begin{Bmatrix} 1 \\ L_2 \end{Bmatrix} F_3 \quad (2.24)$$

To solve this system of equations, the transition to the state-space representation is required. The state-space representation of a linear system with p inputs, q outputs and n state variables can be written in the following form:

$$\begin{aligned} \dot{x}(t) &= A(t)x(t) + B(t)u(t) \\ y(t) &= C(t)x(t) + D(t)u(t) \end{aligned} \quad (2.25)$$

where  $x(\bullet)$  is the state vector,  $y(\bullet)$  is the output vector,  $u(\bullet)$  is the input vector,  $A(\bullet)$  is the state matrix,  $B(\bullet)$  is the input matrix,  $C(\bullet)$  is the output matrix and  $D(\bullet)$  is the feedthrough matrix.

Hence, the state vector of the system under investigation can be defined as:

$$\begin{cases} x_1 = u_3 \\ x_2 = \phi_3 \\ x_3 = \dot{u}_3 \\ x_4 = \dot{\phi}_3 \end{cases} \Rightarrow \begin{cases} \dot{x}_1 = \dot{u}_3 = x_3 \\ \dot{x}_2 = \dot{\phi}_3 = x_4 \\ \dot{x}_3 = \ddot{u}_3 \\ \dot{x}_4 = \ddot{\phi}_3 \end{cases} \quad (2.26)$$

from the equation of motion, it is possible to obtain:

$$\begin{Bmatrix} \dot{x}_3 \\ \dot{x}_4 \end{Bmatrix} = \begin{Bmatrix} \ddot{u}_3 \\ \ddot{\phi}_3 \end{Bmatrix} = [-M_{12}]^{-1} [C_{12}] \begin{Bmatrix} \dot{u}_3 \\ \dot{\phi}_3 \end{Bmatrix} + [-M_{12}]^{-1} [K_{12}] \begin{Bmatrix} u_3 \\ \phi_3 \end{Bmatrix} + [M_{12}]^{-1} \begin{Bmatrix} 1 \\ L_2 \end{Bmatrix} F_3 \quad (2.27)$$

hence, the state vector is:

$$\begin{Bmatrix} \dot{x}_1 \\ \dot{x}_2 \\ \dot{x}_3 \\ \dot{x}_4 \end{Bmatrix} = \left( \begin{array}{cc|cc} 0 & 0 & 1 & 0 \\ 0 & 0 & 0 & 1 \\ \hline [-M_{12}]^{-1} & [K_{12}] & [-M_{12}]^{-1} & [C_{12}] \end{array} \right) \begin{Bmatrix} x_1 \\ x_2 \\ x_3 \\ x_4 \end{Bmatrix} + \begin{Bmatrix} 0 \\ 0 \\ [-M_{12}]^{-1} \begin{bmatrix} 1 \\ L_2 \end{bmatrix} \end{Bmatrix} \quad (2.28)$$

since the variable of interest is  $x_1 = u_3$  (displacement of node 3), the output vector can be written as:

$$y = \begin{bmatrix} 1 & 0 & 0 & 0 \end{bmatrix} \begin{Bmatrix} x_1 \\ x_2 \\ x_3 \\ x_4 \end{Bmatrix} + Du \quad (2.29)$$

since the system does not have a direct feedthrough, D is the zero matrix.

By implementing the mathematical model in MATLAB and performing data analysis, it is possible to calculate the theoretical frequency response of the system. As mentioned before, the data obtained from the analysis of the frequency response obtained by pulse testing are essential to calibrate the mathematical model. In particular, they are required to calculate the  $\beta$  coefficient. This operation is performed by comparing the experimental frequency response with that obtained from the mathematical model. The goal is to find the value of the  $\beta$  coefficient in order to obtain  $\xi_{th} = \xi_{exp}$  (theoretical damping ratio equal to the experimental one). Applying this approach, the first resonance frequency of the mathematical model deviates up to 15% with respect to the experimental value. This may be due to compliance estimation inaccuracy, caused by inaccurate positioning of the inductive probe and measurement noise. Compliance values obtained experimentally are used to calculate the equivalent Young modulus of the lattice section; therefore, an inaccurate estimate influences the accuracy of the mathematical model. For this reason, a better result can be obtained optimizing compliance values beforehand, in order to have  $f_{(res,th)} = f_{(res,exp)}$  (theoretical resonance frequency equal to the experimental one); subsequently the  $\beta$  coefficient can be calculated using the procedure described before.

The mathematical model described before can be used to characterize the behaviour of the specimens previously measured by pulse testing. Parameters necessary to calculate the theoretical frequency response are reported in Table 2.14, while the static compliance has been reported previously. The mass  $m_2$  and the correction parameter of the centre of mass  $q_1$  of the solid section have been obtained from specimens' CAD models.

Table 2.14: Geometrical and physical parameters for mathematical model application

| Specimen        | L <sub>1</sub><br>[mm] | h <sub>1</sub><br>[mm] | L <sub>2</sub><br>[mm] | h <sub>2</sub><br>[mm] | q <sub>1</sub> | m <sub>2</sub><br>[kg] |
|-----------------|------------------------|------------------------|------------------------|------------------------|----------------|------------------------|
| A               | 60                     | 20.8                   | 40                     | 21                     | 0.495          | 0.124                  |
| A <sub>m</sub>  | 60                     | 20.8                   | 40                     | 21                     | 0.478          | 0.274                  |
| B               | 60                     | 16.55                  | 40                     | 21                     | 0.507          | 0.121                  |
| B <sub>m</sub>  | 60                     | 16.55                  | 40                     | 21                     | 0.483          | 0.270                  |
| C               | 60                     | 20.4                   | 40                     | 21                     | 0.495          | 0.124                  |
| C <sub>m</sub>  | 60                     | 20.4                   | 40                     | 21                     | 0.478          | 0.274                  |
| D               | 60                     | 16.28                  | 40                     | 21                     | 0.507          | 0.121                  |
| D <sub>m</sub>  | 60                     | 16.28                  | 40                     | 21                     | 0.483          | 0.270                  |
| E               | 60                     | 12                     | 40                     | 21                     | 0.531          | 0.114                  |
| E <sub>m</sub>  | 60                     | 12                     | 40                     | 21                     | 0.493          | 0.264                  |
| CA              | 60                     | 20.5                   | 40                     | 21                     | 0.495          | 0.124                  |
| CA <sub>m</sub> | 60                     | 20.5                   | 40                     | 21                     | 0.478          | 0.274                  |
| CB              | 60                     | 20.5                   | 40                     | 21                     | 0.495          | 0.124                  |
| CB <sub>m</sub> | 60                     | 20.5                   | 40                     | 21                     | 0.478          | 0.274                  |
| CC              | 60                     | 20.5                   | 40                     | 21                     | 0.495          | 0.124                  |
| CC <sub>m</sub> | 60                     | 20.5                   | 40                     | 21                     | 0.478          | 0.274                  |

Applying the mathematical model using the coefficients specified in the table above and the data obtained from pulse testing analysis, it is possible to obtain the Rayleigh  $\beta$  coefficient. To consider the phenomena described in the previous paragraph, some of the input variables of the mathematical model must be optimized. The first step consists in experimental compliance values optimization, in order to obtain a calculated resonance frequency equal to that obtained through pulse testing ( $f_{(res,th)} = f_{(res,exp)}$ ). Subsequently, the Rayleigh  $\beta$  coefficient is optimized in order to obtain a calculated damping ratio equal to that obtained through pulse testing ( $\xi_{th} = \xi_{exp}$ ). The total number of stainless-steel specimens analysed is 24, having produced three identical replicates on separate build platforms. Figure 2.33 shows boxplot diagrams of the calculated Rayleigh  $\beta$  coefficient for different kind of specimens; on the left side (Figure 2.33 a) for specimens without additional mass, while on the right side (Figure 2.33 b) with additional mass.

The Rayleigh  $\beta$  coefficient values obtained by calibrating the mathematical model using pulse testing experimental results are different from those calculated using the simple harmonic oscillator model. However, the trend is the same and allows to confirm that lattice specimens have better damping properties with respect to the full cross section specimen. Nevertheless, it is still not possible to establish whether there is a significant effect of cell size and fill ratio on damping properties. The type C specimen is confirmed to be the one that could guarantee the best results when good stiffness to weight ratio and damping properties are required.

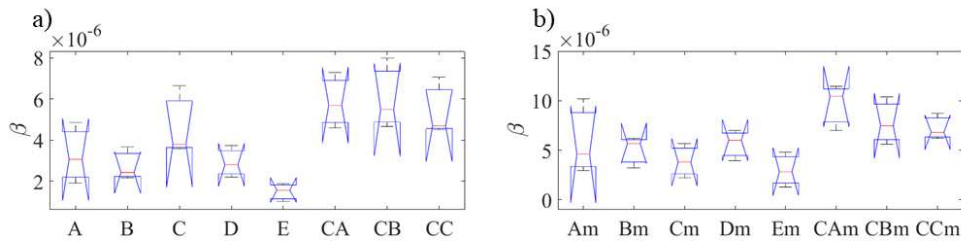


Figure 2.33: Optimized Rayleigh  $\beta$  coefficient for different kind of specimens

The behaviour of beam-like specimens is correctly described by the mathematical model. Looking at Figure 2.34, the frequency response calculated using the mathematical model, optimizing experimental compliance values in advance (blue curve), is almost identical to the experimental one (black curve); without experimental compliance values optimization, the mathematical model tends to overestimate the resonance frequency (red curve). Having previously justified the reasons that suggest performing the preliminary optimization of compliance, the mathematical model satisfactorily represents beam-like specimens behaviour.

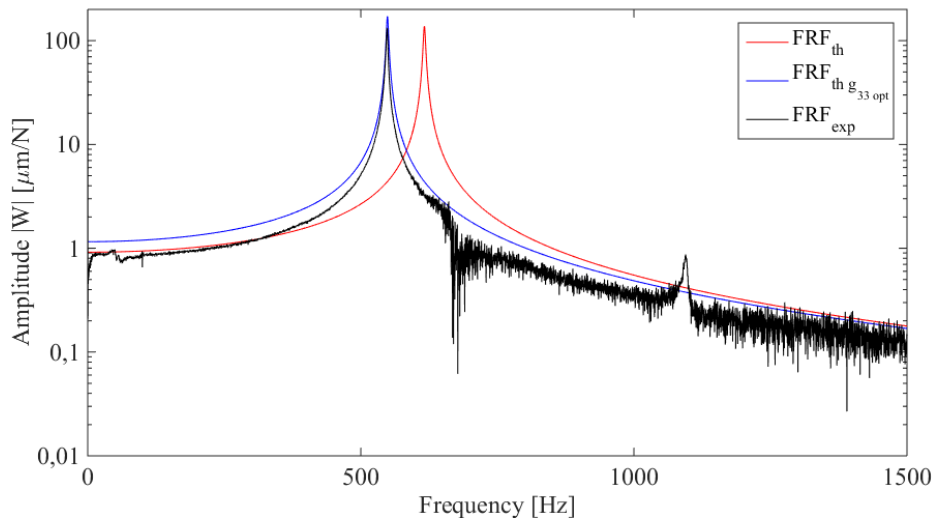


Figure 2.34: Comparison between calculated and experimental A specimen's FRF

## 2.7 Innovative mini dynamometer for in-process cutting forces data acquisition

Results obtained in previous paragraphs and some experimental studies have shown that lattice structures can be useful to generate controlled porosity materials with excellent stiffness to weight ratio and good damping properties.

In this paragraph, the possibility of concretely exploiting lattice structures to design and manufacture an optimized mechanical component that can benefit from the peculiar characteristics of these structures is investigated. Performances of some types of measuring instruments, if properly optimized, can be improved in terms of accuracy and flexibility. Lattice structures, as suggested by the experimental tests, can be used to obtain light components with good damping properties. A class of measuring instruments that could benefit from these features are dynamometers used to measure milling cutting forces. The ability to perform accurate measurements of milling cutting forces allows to achieve a more accurate and detailed characterization of the physical phenomena that occur during the cutting process, helping in the development of increasingly reliable mathematical models. It is therefore possible to better characterize materials machinability, helping in the choice of tools and optimal cutting parameters and in the development of new optimized tools. Increasing efficiency, reducing costs and ensuring high quality are important objectives of industrial interest; the development of an optimized dynamometer for the measurement of milling cutting forces can help achieve these objectives and is therefore the subject of the study reported in this paragraph. There are different types of devices suitable for cutting forces measurement, characterized by geometries and technical characteristics appropriate for different application fields. The characterization of cutting forces takes place through different techniques and sensors, exploiting deformation, displacement or acceleration measurements. The dynamometer under investigation was designed to make possible the integration with the equipment of the Advanced Mechatronics Laboratory of the University of Udine. The instrument is therefore compact and integrates the previously studied lattice structures to optimize its characteristics. The lattice chosen to perform the optimization is the type C, with 2 mm FBCCZ unit cell and 0.2 fill ratio.

### 2.7.1 Dynamometer design and optimization

As anticipated above, the mechanical component being optimized using lattice structures is a dynamometer for milling cutting forces measurement. This measuring instrument must satisfy certain constraints in order to exploit the equipment of the University of Udine and ease the development of further research campaigns.

The project is inspired to Kistler 9256C2 commercial dynamometer and uses four triaxial force sensors (Kistler 9016B4). The optimized dynamometer must be compatible with the HAAS VF-2TR milling machine of the Advanced Mechatronics Laboratory of the University of Udine and should be designed in order to obtain better performances with respect to the commercial reference.

The design phase involves the creation of three different central plates to be manufactured through SLM 3D printing:

- CAD modeling of the reference dynamometer, that does not integrate lattice structures, inspired to the design of the Kistler 9256C2 commercial dynamometer
- CAD design of the optimized dynamometer integrating the FBCCZ lattice structure
- CAD design of the optimized dynamometer integrating the FBCCZ lattice structure filled with unmelt metal powders

The exploded view that highlights the main components of the designed dynamometer is shown in Figure 2.35; the core of the measurement system are the four Kistler triaxial force sensors, the central perforated platform that allows easy fixing of the workpiece, the bolts and the rings to preload the coupled force sensors.

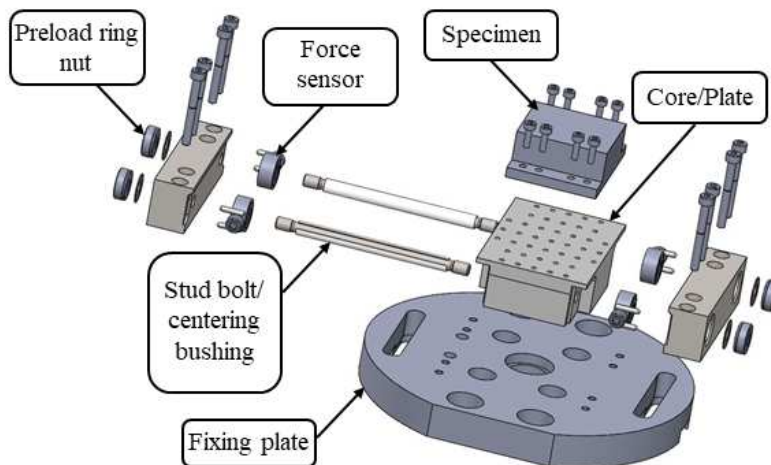


Figure 2.35: High performance mini dynamometer exploded view (LAMA FVG<sup>TM</sup>)

The chosen force sensors are piezoelectric; they are composed of three rings of piezoelectric material that detect the forces along the three directions of the orthogonal triad. The Kistler 9016B4 kit consists of two cells 9017B and two 9018B, which differ in the orientation of the reference system according to which the forces are measured; this allows the sensors to be mounted coupling them two by two as in the case under analysis. Figure 2.36 shows a detail image of the triaxial force sensor and the diagram that clarifies the orientation of the reference systems for each of the four sensors.

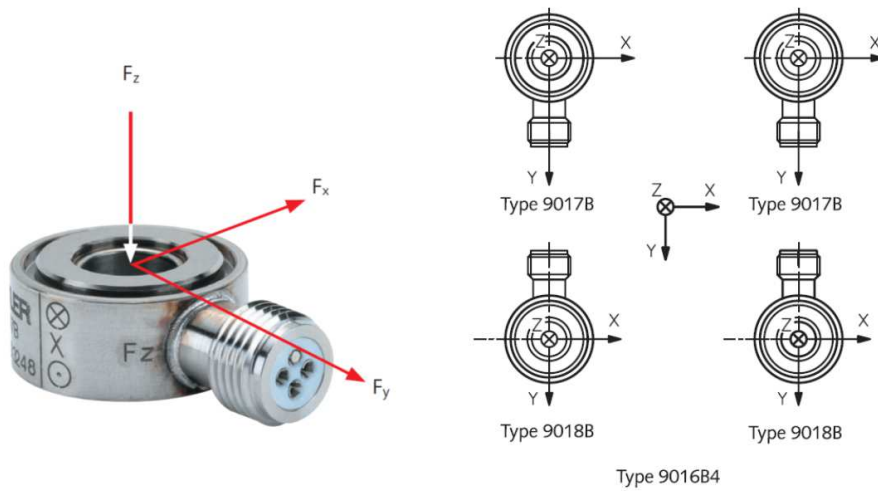


Figure 2.36: Kistler 9016B4 sensors and reference systems orientation (Kistler)

In fact, the peculiar characteristic of this type of dynamometer is the arrangement of the coupled force sensors; the piezoelectric sensors are preloaded in pairs by applying the tightening torque through the appropriate ring nuts. Figure 2.37 section highlights the elements involved in the preloading operation.

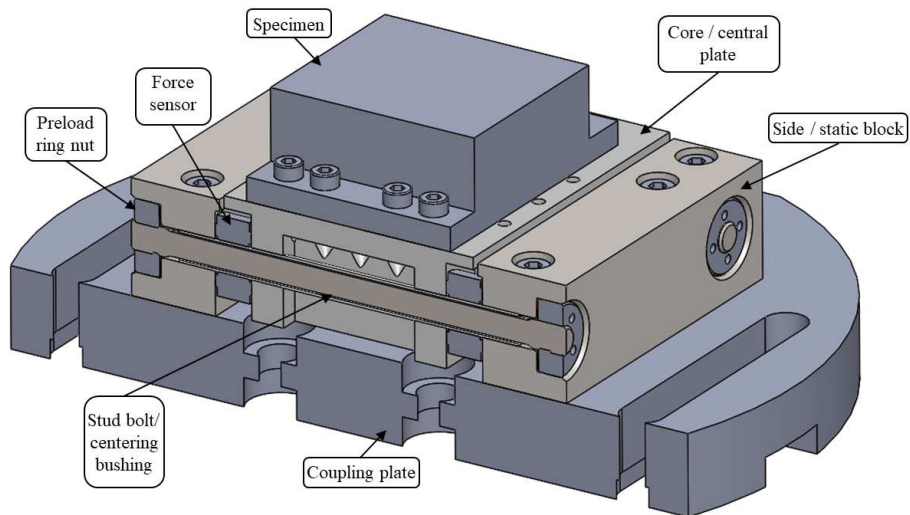


Figure 2.37: Optimized dynamometer - preload system section

This configuration is compact and makes it possible to minimize the effect of any thermal variation on acquired measurements, while ensuring a rigid coupling between the central plate and the sides of the dynamometer, increasing the instrument's passband. Particular attention was paid to the machining of the sensors coupling surfaces, to sensors alignment and preload application; these steps should be performed with care to ensure correct operation of the dynamometer. In particular, preload application is critical to obtain

a rigid no-play coupling that adequately transmits shear stresses between sensors and dynamometer structure. The preload limits the measurement range of the force sensor by a quantity equal to the value of the preload itself. Preload force varies between 20% and 70% of the maximum measurable value and is set according to the specific measurements set-up.

In the following subparagraphs the main components of the optimized dynamometer are analysed in detail.

### 2.7.2 Core / central plate design

The central platform is a fundamental part of the dynamometer, since it must ensure the fixing of the piece to be processed and adequately transfer the forces to the sensors, altering measured data as little as possible. Being the main component of the dynamometer and being responsible of transmitting cutting forces to the force sensors, optimization of this part of the dynamometer should be particularly effective. The optimization is pursued by integrating within the component the lattice structures studied in the previous paragraphs, which have shown to have excellent stiffness to weight ratio and good damping properties. The goal is to obtain a central platform integrating lattice structures, trying to maximize stiffness and minimize mass; these features allow to improve measurement performances, enhancing accuracy and obtaining a wider measuring range.

As specified above, the dynamometer being optimized is inspired to the Kistler 9256C2; exploiting the available information, the central reference platform, which does not contain lattice structures, is designed (see Figure 2.38).

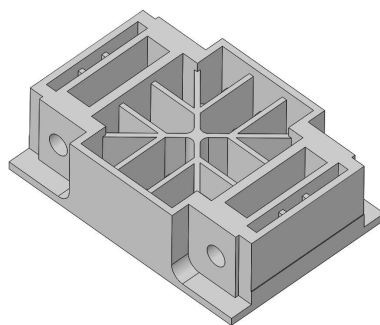


Figure 2.38: Optimized dynamometer central plate – reference geometry

Geometry is quite simple to ease the comparison of the results obtained using the three types of central plates listed before. Two out of three central platforms integrate lattice structures, for this reason the three variants of the central platform have to be manufactured using SLM 3D printing. The material chosen is a 316L stainless steel, which has excellent mechanical properties and corrosion resistance. The central reinforcement ribs



have been sized trying to maximize the value of the first resonance frequency; modal analyses have been carried out, constraining the areas in which there is rigid coupling between the sides, sensors and the central platform. The values of the frequencies of the first three normal modes, shown in Table 2.15, can be useful for a future comparison with those measured experimentally.

Table 2.15: Modal analysis results – reference central plate

| Normal mode | $f_{res}$ [Hz] |
|-------------|----------------|
| 1           | 13250          |
| 2           | 14992          |
| 3           | 15560          |

The two optimized versions of the central platform have the central section filled with a FBCCZ type C lattice (see previous paragraphs); moreover, one of the central platforms uses unmelted metal powders as filler for the lattice section.

### 2.7.3 Static parts and interface with the machine tool

The components that guarantee the connection between central platform, force sensors and the TR160 rotary table of the HAAS VF-2TR vertical machining centre are the two sides static blocks and the lower fixing coupling plate.

The two sides of the dynamometer are designed to facilitate centering and alignment operations without compromising ease of assembly. The coupling between the sides and the lower coupling plate is guaranteed by centering pins. Load cell rotation is blocked by pins inserted in the side blocks near the connectors. The lower coupling disc is fixed on the interface of the TR160 rotary table using four M10 screws. In addition, a centering pin and a feather key are used to ensure the correct alignment between the coupling plate and the interface of the TR160. The slots on the coupling plate facilitate fixing on alternative equipment. Figure 2.39 shows the virtual assembly of the dynamometer with the HAAS rotary table.

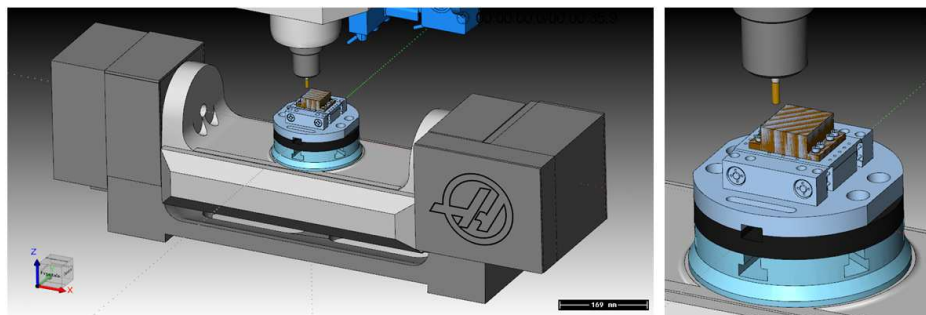


Figure 2.39: Virtual assembly of the dynamometer with the HAAS TR160 rotary table

### 2.7.4 Optimized dynamometer manufacturing and assembly operations

The three types of central platform have to be manufactured by SLM 3D printing, since the geometry of the lattice structures integrated in two of the three platforms cannot be produced with traditional manufacturing technologies. The material chosen is a 316L stainless steel, an austenitic steel whose properties have been reported in the previous paragraphs. Three distinct versions of the central platform were designed and produced: the first one, chosen as reference, has the central section filled by reinforcing ribs, the second one uses the FBCCZ type C reticular structure previously studied as central section filler, while the third one is identical to the second but uses unmelt metal powders to fill lattice porosity. After performing CAD modelling of the reference dynamometer, the model was exported to STL format to proceed with the generation of dynamometer plates incorporating the lattice structure. The FBCCZ lattice is generated in SolidWorks and is exported in STL format to integrate it with the geometry of the central plate. The actual integration between reference geometry and lattice was performed in Materialise Magics by means of Boolean operations. Central plates positioning on the build platform and supporting structures are shown in Figure 2.40; plates have been positioned to facilitate supports removal and subsequent finishing operations. In particular, the upper part of central plates is supported and have to be machined after support removal.

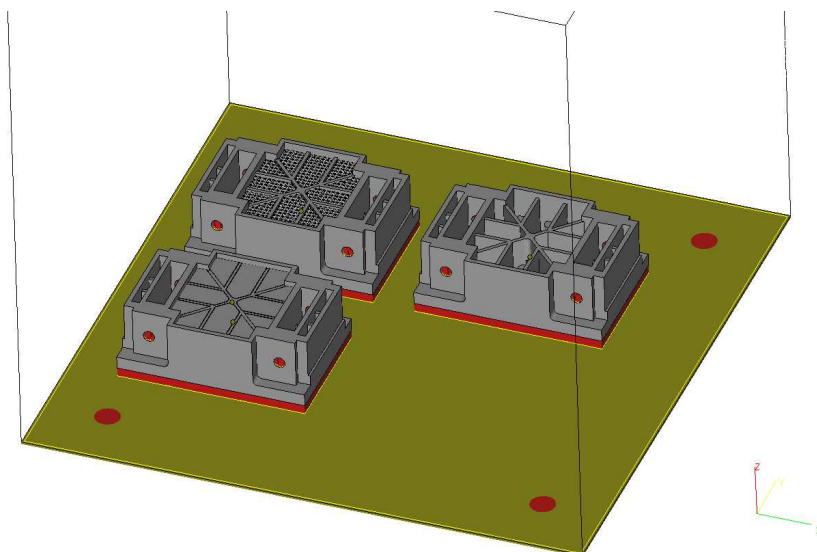


Figure 2.40: Virtual build volume – optimized dynamometer’s central plates

Appropriate machining allowance have been foreseen in the areas that must be machined at the end of printing. The process parameters chosen for SLM production are those recommended by Concept Laser for AISI 316L: power 180 W, scan speed 600 mm/s, spot diameter 120  $\mu\text{m}$ , layer thickness 25  $\mu\text{m}$ , island exposure strategy. The SLM as-built result is visible in Figure 2.41; the set of lattice specimens serves as a preliminary prototype for an additional DoE conceived to expand lattice structures characterization of the previous paragraphs, this aspect will be further discussed in Chapter 3.

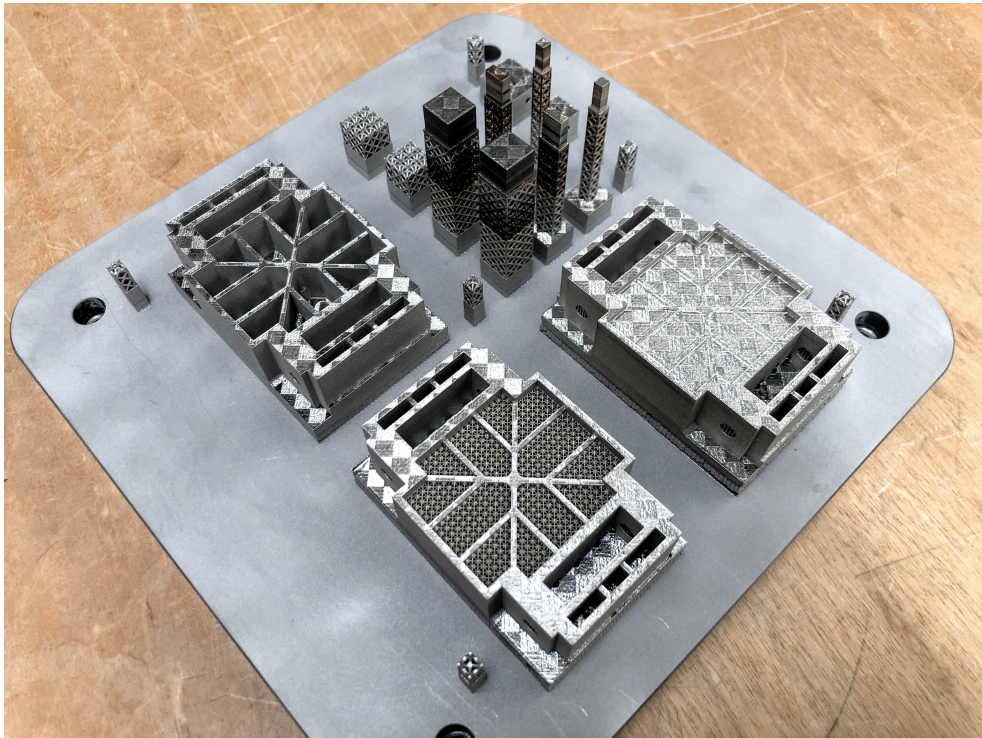


Figure 2.41: As-built optimized dynamometer's central plates

The central platforms show significant thermal deformations that mainly affect the upper face (see Figure 2.42 a); this unwanted deformation can be recovered by removing the machining allowance added during design phase to the upper face. The SLM additive manufacturing of the FBCCZ lattice integrated within the central part of the dynamometer is successful, confirming results on manufacturability obtained previously (see Figure 2.42 b). Following the stress relieving heat treatment, the components were separated from the build platform by band sawing machine.

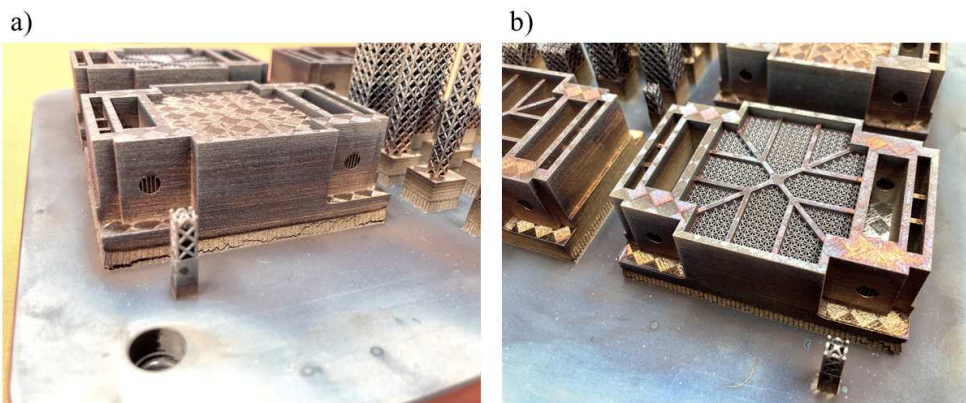


Figure 2.42: Support cracking, upper face deformation and lattice detail view

Dynamometer sides and coupling plate have been made by milling starting from blanks. The tool trajectories were generated through SolidCAM 2016 and the milling operations were performed on the HAAS VF-2TR Vertical Machining Center (VMC). Using the TR160 rotary table it is possible to perform 5-axis continuous machining; this allowed the execution of multi-placement processes without having to manually reposition the piece. Operations carried out with the aid of the VMC are briefly described below.

The three central platforms, after 3D printing, have undergone milling operations; in particular, upper face milling, contouring of the lateral faces, finishing of the coupling surfaces and through holes enlargement. Threading of the holes on the upper face was performed manually. An image of central platform's upper face milling is visible in Figure 2.43.

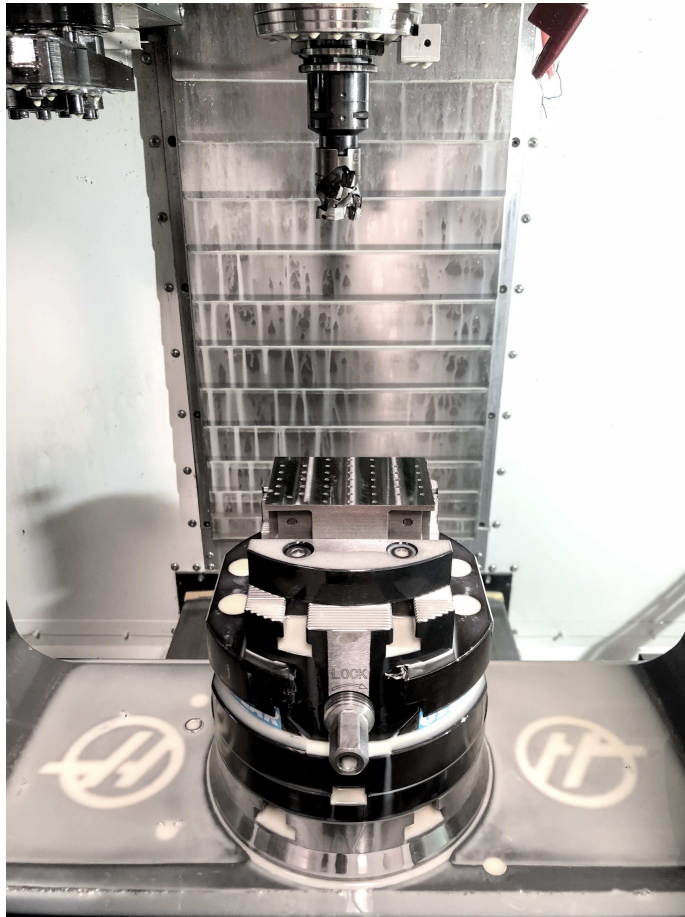


Figure 2.43: Central platform's upper face milling – HAAS VF-2TR

The lower coupling disc was created starting from an aluminium blank, the fixing of the blank is guaranteed by four M8 screws appropriately recessed (see Figure 2.44).

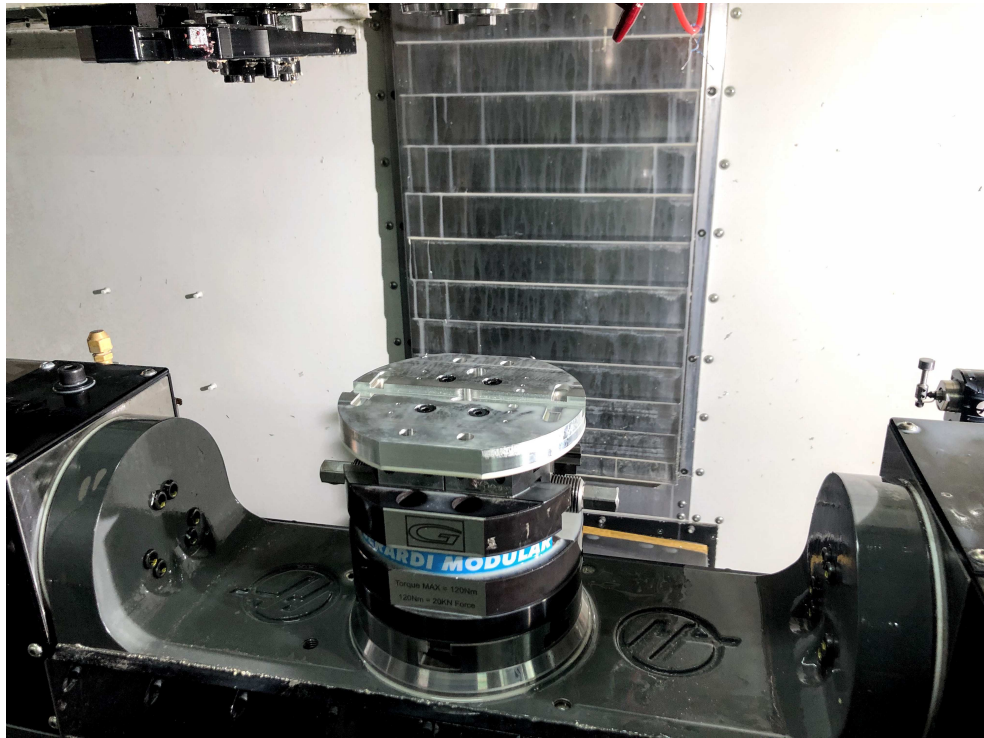


Figure 2.44: Coupling plate machining

Dynamometer's sides were obtained from a C45 steel blank. The dynamometer mounted on the HAAS VF-2TR vertical machining centre, connected to the National Instrument data acquisition system, following the application of the preload and the calibration of the force sensors, is shown in Figure 2.45.

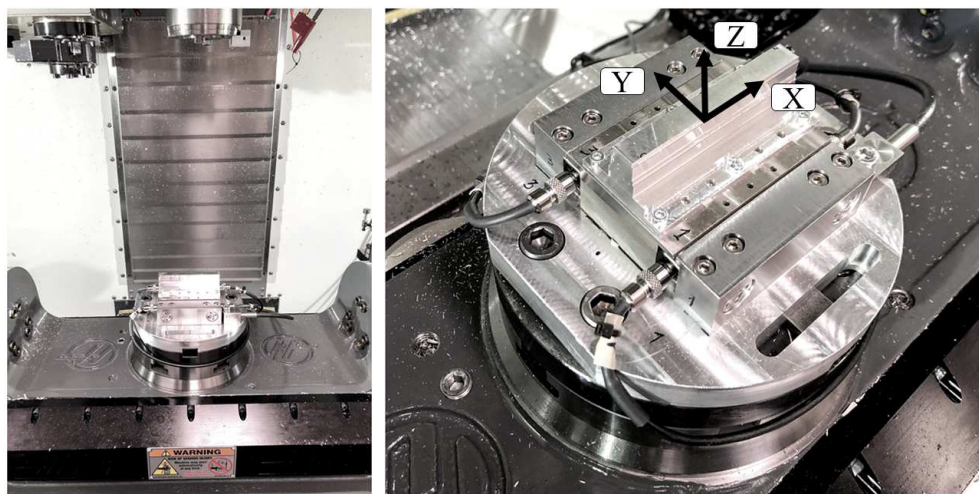


Figure 2.45: Dynamometer: fully operational cutting forces measurement system

### 2.7.5 Optimized dynamometer dynamic identification

To evaluate dynamometer's performance, preliminary tests were carried out using the different types of central platform described before. The dynamic behaviour of the dynamometer was identified using the pulse test technique. The system was excited using an instrumented hammer; the impulsive force was exerted on different points of the aluminium blank shown in Figure 2.45, along the three main directions (X, Y and Z). The input (Hammer) and the output (load cells) signals were acquired and modal analysis was performed to obtain the frequency response along the three main directions [96], [97]. The tests were performed using the standard central platform and the one with lattice infill, in order to evaluate the effect on the dynamometer's dynamic behaviour. The frequency responses obtained are shown in figure Figure 2.46.

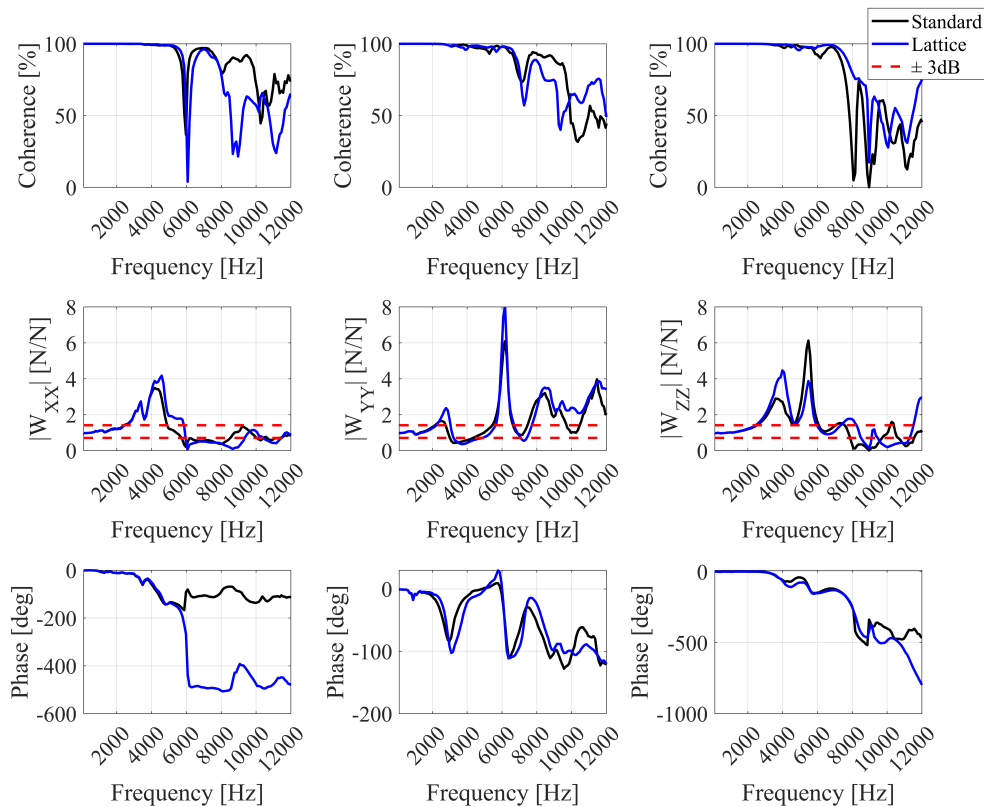


Figure 2.46: Comparison between dynamometers with and without lattice infill: FRF coherence, amplitude and phase

Comparing the standard dynamometer's FRF with that of the dynamometer with lattice infill, it can be seen that the peak amplitude of the first mode of vibration is higher for the dynamometer with lattice infill. This result is due to the central platform's mass increase, caused by the lattice infill addition. The peak amplitude of the second mode of vibration along the Z direction is lower for the dynamometer with lattice infill; this suggests the existence of a measurable damping effect due to the lattice structure, which occurs mainly

at high frequency ( $> 5\text{kHz}$ ). The frequency bandwidth of the dynamometer with lattice infill does not appear to be wider than that of the standard dynamometer, as highlighted by the  $\pm 3\text{dB}$  crossing frequencies shown in Figure 2.46; this result suggests that the measurement system's performance is not significantly affected by the lattice infill.

## 2.8 Conclusions

The in-depth analysis of the state of the art on lattice porous structures highlighted the lack of exhaustive studies investigating static and dynamic behaviour of SLM-manufactured lattices. Chapter 2 is conceived to fill this knowledge gap. Drawing inspiration from available scientific literature, the characteristics of the lattice's unit cell, in terms of topology and geometry, which allow to enhance manufacturability (no need for supports) and potentially damping properties have been identified. Thus, static and dynamic behaviour of different kinds of lattices, made of AlSi10Mg aluminium alloy and 316L austenitic stainless steel, were investigated by means of two experimental campaigns. A total of 10 aluminium specimens and 24 steel specimens were designed, manufactured and measured. Assessment of lattice's performance advantage in terms of vibration damping with respect to full density equivalent and evaluation of lattice's geometry variation effect on its properties were the main goals. Following conclusions can be drawn from the analysis of the experimental campaigns results (unless specified, results are valid for both aluminium and steel specimens):

- Measurements performed with the optical microscope evidenced that the specimens had inhomogeneous characteristics. Struts size and surface finish were influenced by the variability of the SLM process; in particular, position of the object in the build volume, unwanted adhesion of partially melt powders and stochastic phenomena typical of the SLM process affected the printing result. Nevertheless, although the printing accuracy, especially for smaller unit cells, was lower than expected due to the SLM process limitations, repeatability was statistically good.
- Analysing the SLM-manufactured lattices geometry it was possible to assess a lack of homogeneity between the nominal (CAD) and the as-built geometry; in particular, inclined beams (with respect to the build direction) diameter was greater than that of the vertical ones. This phenomenon is mainly due to undesired adhesion of partially melt metal powders affecting overhanging surfaces.
- The lack of homogeneity between CAD and as-built specimens' geometries, negatively affected accuracy of results obtained from FE simulations performed starting from the nominal CAD model.
- Measured compliance values of specimens integrating lattice structures were lower than those calculated by means of FEA. FEA tended to overestimate lattices compli-

ance especially for specimens with smaller cell size (i.e. C and D); this phenomenon occurred because SLM process limitations were not taken into account (e.g. inhomogeneity between nominal and as-built lattice's geometry).

- FEA results accuracy was improved by means of a FE model that simulates the real lattice's geometry; as-built lattices geometry was studied and appropriate factors for nominal beams diameter correction were estimated and applied.
- Calculation time and computational effort required to perform FE simulations was significantly reduced, exploiting 1D-element meshing for the specimens' lattice section.
- Specimens dynamic behaviour assessment, performed using the Pulse Test technique, showed that lattices damping properties are significantly better than those of the equivalent solid material.
- Analysing average values, the lattice's geometric configuration with the best damping characteristics is the C specimen's one, characterized by a small unit cell (2mm) and low fill ratio (0.2).
- Effect of cell dimension and fill ratio on damping ratio was assessed with ANOVA. For AlSi10Mg specimens, cell size has a statistically significant effect on the damping ratio whereas for 316L specimens it has not. Therefore, AlSi10Mg lattices with smaller cell size (i.e. C and D), have better damping properties.
- Specimens exploiting un-melt metal powders as filler of the lattice porosity demonstrated significantly higher damping properties compared to all the other specimens, suggesting that using appropriate filler materials is beneficial when optimal damping performance is desired.
- Dynamic behaviour of the beam-like specimens was described through the development and implementation of a mathematical model based on the Euler-Bernoulli theory. The mathematical model satisfactorily represents beam-like specimens' behaviour and allows to estimate Rayleigh damping  $\beta$  coefficient.

The development of an innovative measurement system allowed to investigate the feasibility of exploiting lattice structures as high-performance filler materials. The system under investigation was a dynamometer for in-process (e.g. milling, drilling, grinding) cutting forces measurement. Design and manufacturing of all system's components, whose main feature is the SLM-manufactured central platform, were carried out. Main results obtained are listed below:

- Three distinct versions of the central platform were designed, two of which integrating lattice structures to enhance stiffness to weight ratio and damping.



- External geometry of the three central platforms is the same, while the core section changes: the first one is quite similar to commercially available ones while two of them integrate the previously studied type C lattice, with and without unmelt metal powders filler. This choice guarantees platforms interchangeability and favours comparison between the results obtained using the three configurations.
- CAD modelling and FEA simulations were performed to design dynamometer's components, while manufacturing was carried out by means of CAM, SLM 3D printer and VMC.
- Minimization of thermal variation effect on measurements and rigid coupling between parts were pursued during design phase.
- SLM-manufactured central platforms had significant thermal deformations, corrected removing the machining allowance; integrated lattice was reproduced successfully.
- Dynamometer FRF analysis suggests the existence of a measurable damping effect due to the lattice structure, which occurs mainly at high frequency ( $> 5\text{kHz}$ ). Nevertheless, the frequency bandwidth of the dynamometer with lattice infill does not appear to be wider than that of the standard dynamometer; this result suggests that the measurement system's performance is not significantly affected by the lattice infill.
- No studies or commercially available systems investigated similar solutions.



## **Chapter 3**

# **METHODOLOGY FOR STATIC AND DYNAMIC LATTICE AND POROUS STRUCTURES PROPERTY ASSESSMENT**

Experimental campaigns discussed in the previous chapter have shown that lattice structures possess particularly useful features like good stiffness to weight ratio and improved damping properties. The results obtained allowed to observe the dynamic behaviour of lattice structures composed by topologically identical unit cells but with different geometry. In general, lattice structures guaranteed enhanced damping performances. Data analysis allowed to identify the unit cell geometry that maximizes the damping effect; furthermore, it was demonstrated that the use of unmelted metal powders as lattice porosity's filler significantly enhances energy dissipation, further improving the damping characteristics of the lattice.

In this chapter the investigation on the damping properties of the lattice structures is deepened. Lattices damping properties depend on their macroscopic geometry; since lattices under investigation are constituted by the repetition of unit cells, lattice's size is a multiple of cell's size. The objective is to study damping properties variation as a function of lattice's size (number of unit cells repeated along the three main directions); acquired data could be used to develop mathematical models useful for lattices damping properties estimation as well as for the development of a universal methodology for static and dynamic lattice and porous structures property assessment.

### 3.1 Specimen design and DoE

A DoE is devised to study damping properties variation as a function of lattice's geometry. Similarly to previous experimental campaigns, in order to derive lattices static and dynamic mechanical properties, specifically designed beam-like specimens are SLM manufactured and measured.

#### 3.1.1 Lattice type, geometry and material selection

The lattice geometry under investigation is chosen taking advantage of the results obtained from previous studies. The experimental campaign conceived, is an extension of the previous ones. FBCCZ unit cell's topology is selected, beams diameter and unit cell's size are equivalent to those of A and C samples described in Chapter 2. These choices allow to compare the results with those already acquired previously. Type A and C lattices have the same fill ratio, therefore comparison between specimens having the same external section is simpler having comparable stiffness. Moreover, analysing lattices having different unit cell size, it is possible to evaluate the effect of cell size variation on the damping properties of the lattice. To ensure comparability with previous experiments, the material chosen for specimens SLM production is a 316L stainless steel.

The proposed DoE is characterized by three factors and three levels for each factor. It is a full factorial DoE that requires the production of 27 specimens. Since two types of lattices with different unit cell's size are under investigation, the DoE is repeated twice, one for each cell size. The total number of specimens to be produced is therefore equal to 54. Table 3.1 shows factors and levels chosen to investigate the effect of the lattice's size on its mechanical behaviour. The factors identify the number of unit cells that make up the lattice, divided according to the three main directions (i.e.  $N_x$ ,  $N_y$ ,  $N_z$ ). Three levels for each factor are under investigation.

Table 3.1: 3<sup>rd</sup> DoE factors and levels

| Factor | Level 1   | Level 2   | Level 3   |
|--------|-----------|-----------|-----------|
| $N_x$  | $N_{x,1}$ | $N_{x,2}$ | $N_{x,3}$ |
| $N_y$  | $N_{y,1}$ | $N_{y,2}$ | $N_{y,3}$ |
| $N_z$  | $N_{z,1}$ | $N_{z,2}$ | $N_{z,3}$ |

To establish factors levels, determining the size of the lattices to be analysed, it is required to fulfil constraints due to the limitations of the equipment used to acquire the data useful for specimens static and dynamic properties estimation. In the following paragraphs, design choices about specimens' geometry and experimental set-up are analysed.

### 3.1.2 Specimens geometry and experimental set-up design

As previously stated, beam-like specimens' geometry should be designed in order to ease data acquisition; characteristics and limitations of the equipment available at the Advanced Mechatronics Laboratory of the University of Udine must be taken into account.

To determine the static compliance of the samples, a Kistler Type 9311B load cell is used; a displacement constraint is applied using a 6 mm diameter strut, measuring the reaction force (Figure 3.1 left side). Similarly to previous experimental campaigns, the pulse test technique is used to assess specimens dynamic behaviour. To facilitate measurements execution, specimens are fixed in a vise. Bearing in mind the requirements described above, specimens are designed with an upper base useful for the application of external loads and a lower base to ensure a solid grip in the vise. The size of the two bases is chosen in order to reduce printing time; moreover, specimens upper base is designed in order to allow investigation of modal mass variation effect on dynamic behaviour, by means of additional masses. The central part of the beam-like specimen integrates the lattice structure.

Figure 3.1 shows a diagram representing measurements experimental set-up and specimens' geometry.

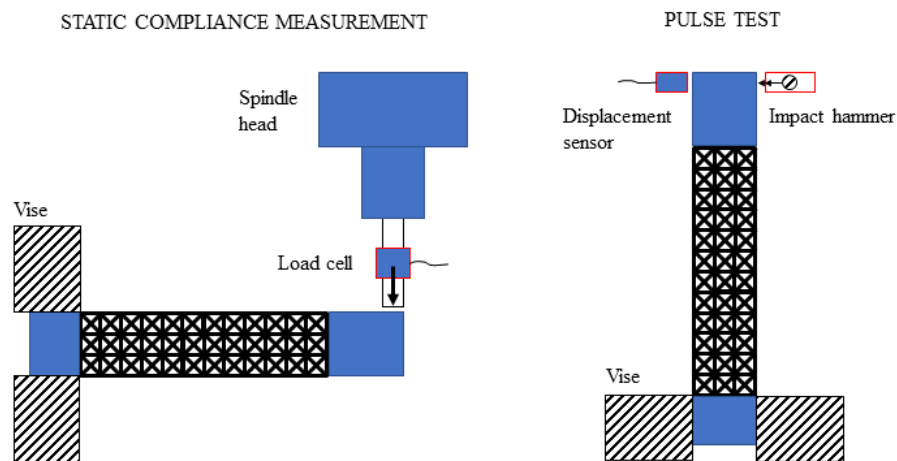


Figure 3.1: Specimens static and dynamic behaviour assessment – experimental setup

Figure 3.2 shows an example of specimen integrating type A lattice structure, with and without additional mass. Set screws are used to secure additional masses to the upper base.

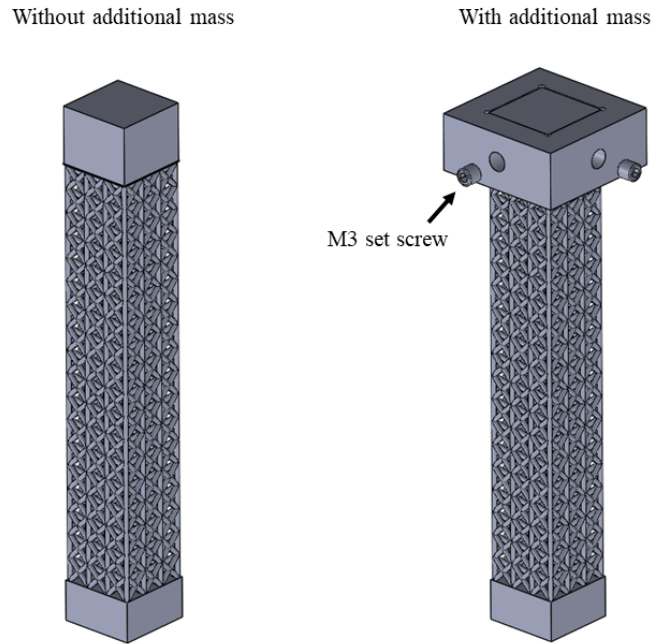


Figure 3.2: Example of specimen integrating type A lattice structure, with and without additional mass

### 3.1.3 Selection of factors and levels for 3<sup>rd</sup> DoE

In the previous paragraph the experimental set-up used to perform the measurements was analysed. To measure the displacement resulting from the application of the impulsive force applied through the instrumented hammer, an inductive probe is used. To obtain satisfactory measurements with this kind of probe it is advisable to design specimens with a first natural frequency lower than 2500 Hz. For this reason, the numerical values of the DoE's factors levels are chosen by evaluating the results obtained by FE simulations, allowing to design specimens that can be easily characterized by pulse testing, using the available equipment. As specified in Chapter 2, performing finite element simulations on 3D models of lattices made up of a considerable number of unit cells requires a lot of time and huge computational resources. Therefore, to complete the design of the specimens in reasonable time, the first resonance frequency is estimated using a 3D hybrid model similar to that described in Chapter 2; lattice's beams are discretized using 1D beam-type finite elements, allowing to reduce consistently FE model nodes. Using 1D elements to discretize the lattice, the solution obtained is less precise than that calculated using the 3D model of the entire specimen. To understand the order of magnitude of the error committed, a comparison between results obtained starting from the 3D model with respect to those obtained with the 3D hybrid model is made. Table 3.2 summarizes the results obtained: error tends to increase when cell's number increases and when unit cell's size decreases. The 3D hybrid model is a useful tool for designing lattice specimens, being aware that the results are not accurate.

Table 3.2: Comparison between 3D and hybrid 3D FE models results

| Specimen               | A1    | A2    | C1    | C2    |
|------------------------|-------|-------|-------|-------|
| $N_x$                  | 1     | 3     | 2     | 6     |
| $N_y$                  | 1     | 3     | 2     | 6     |
| $N_z$                  | 15    | 15    | 30    | 30    |
| $C_d$ [mm]             | 4     | 4     | 2     | 2     |
| $f_r$ (3D) [Hz]        | 460   | 895   | 345   | 805   |
| $f_r$ (hybrid 3D) [Hz] | 405   | 744   | 289   | 621   |
| Error [%]              | 11.95 | 16.87 | 16.23 | 22.86 |

Specimens integrating lattices of different sizes are analysed by means of FEA and factors levels shown in Table 3.3 are chosen. It has been verified that specimens first resonance frequencies are lower than 2500 Hz, facilitating measurements using the inductive probe. Since the number of beams of the lattices is very large, the 3D hybrid model was used, considerably reducing calculation time.

Table 3.3: 3<sup>rd</sup> DoE factors and levels - numerical values

| Factor | A-Level <sub>1</sub> | A-Level <sub>2</sub> | A-Level <sub>3</sub> | C-Level <sub>1</sub> | C-Level <sub>2</sub> | C-Level <sub>3</sub> |
|--------|----------------------|----------------------|----------------------|----------------------|----------------------|----------------------|
| $N_x$  | 3                    | 5                    | 7                    | 6                    | 10                   | 14                   |
| $N_y$  | 3                    | 5                    | 7                    | 6                    | 10                   | 14                   |
| $N_z$  | 12                   | 15                   | 18                   | 24                   | 30                   | 36                   |

The factors levels combinations to be analysed are clearly summarized in Figure 3.3, where  $N_z$  is fixed and resulting specimens' cross sections are schematized. It is clear that it is not required to produce 54 specimens as some of the combinations are geometrically identical; therefore, the production of 36 specimens is sufficient, 18 of which have to be measured with respect to two different orientations. Central specimen is highlighted in red as its lattice is equal to that of specimens A and C of Chapter 2, it is therefore clear that the 3<sup>rd</sup> DoE is an extension of previous experimental campaigns.

In Chapter 2 it was observed that FBCCZ lattice's inclined beams diameter is generally greater than that of vertical beams. To investigate this phenomenon and verify whether it is possible to modify the lattice's CAD model to improve geometric accuracy, a small experimental campaign is conceived. For this purpose, FBCCZ structures with a nominal beam diameter between 0.2 mm and 0.4 mm are designed and produced; five specimens, each of which with a beam diameter increased by 0.05 mm compared to the previous one, are obtained. The study is performed for lattices with 2 mm and 4 mm unit cell size, for a total of ten 316L SLM-manufactured specimens (Figure 3.4).

The average diameters of vertical and inclined beams, obtained with the 3D optical profilometer Sensofar S neoX, are shown in Table 3.4.

Moreover, images acquired with the aforementioned profilometer showing lattice's surface are reported in Figure 3.5.

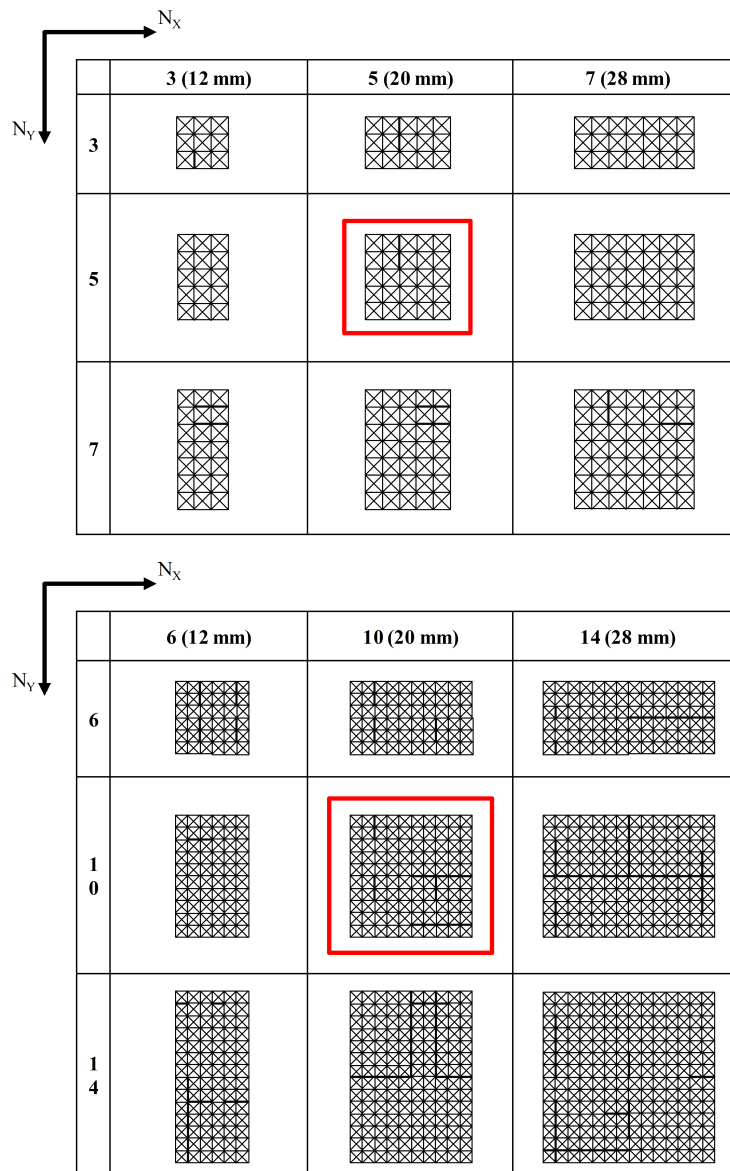


Figure 3.3: 3<sup>rd</sup> DoE factors levels combinations scheme

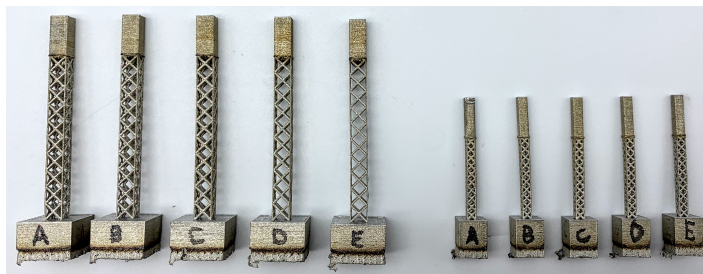


Figure 3.4: FBCCZ lattices geometric accuracy assessment - beam diameter equal to: a) 0.4 mm b) 0.35 mm c) 0.3 mm d) 0.25 mm e) 0.2 mm



Table 3.4: FBCCZ lattices geometric accuracy assessment - beam diameter measurement

|   | $C_d$ [mm] | $D_n$ [mm] | $D_v$ [mm] | $D_i$ [mm] |
|---|------------|------------|------------|------------|
| A | 2          | 0,4        | 0,41       | 0,55       |
| B | 2          | 0,35       | 0,35       | 0,46       |
| C | 2          | 0,3        | 0,34       | 0,5        |
| D | 2          | 0,25       | 0,31       | 0,41       |
| E | 2          | 0,2        | 0,26       | 0,4        |
| A | 4          | 0,4        | 0,4        | 0,52       |
| B | 4          | 0,35       | 0,35       | 0,46       |
| C | 4          | 0,3        | 0,35       | 0,51       |
| D | 4          | 0,25       | 0,3        | 0,44       |
| E | 4          | 0,2        | 0,26       | 0,43       |

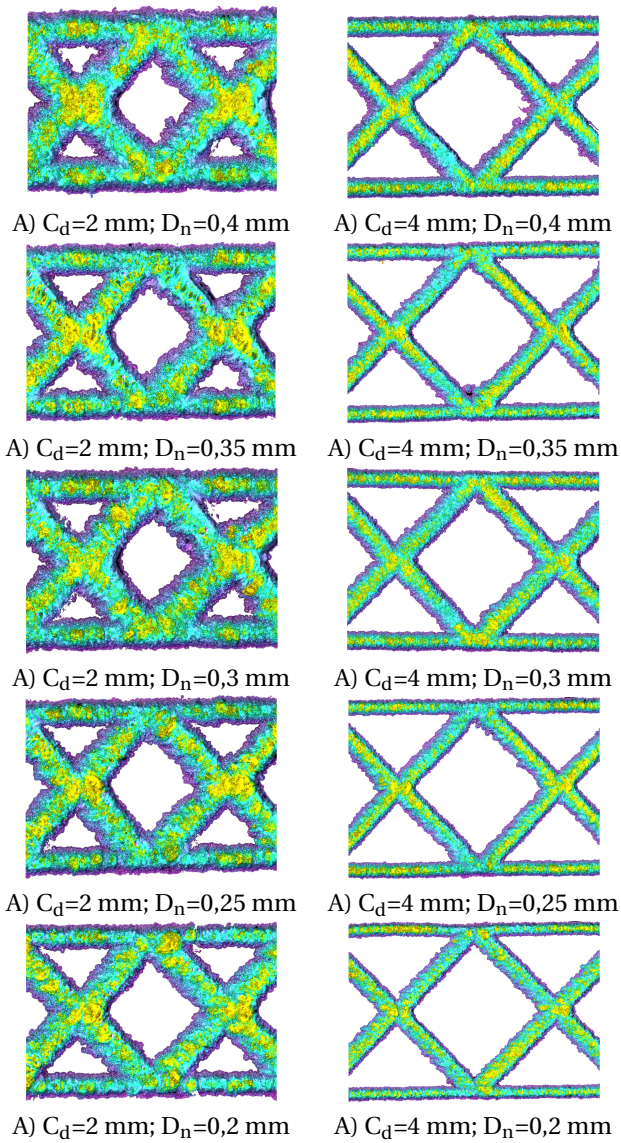


Figure 3.5: FBCCZ lattices geometric accuracy assessment - lattice's surface

Vertical beams diameter is quite similar to the nominal value while inclined beams diameter is larger. Therefore, higher geometric accuracy could be obtained by introducing a correction coefficient to reduce the CAD nominal diameter of inclined beams. Analysing values of Table 3.4, it is noticed that a uniform lattice having beams with a diameter equal to 0.4 mm can be obtained reducing inclined beams nominal diameter to 0.2 mm. In order to test this hypothesis, two specimens with nominal diameter equal to 0.4 mm for vertical beams and 0.2 mm for inclined ones are manufactured (Figure 3.6).



Figure 3.6: FBCCZ lattices geometric accuracy - inclined beams diameter correction

Comparing diameter measurements of vertical and inclined beams, it is confirmed that reducing inclined beams nominal diameter helps to increase geometric accuracy; specimens beams diameter is uniform and is very close to the nominal value equal to 0.4 mm. Observing the surface of the lattice using the Sensofar S Neox 3D optical profilometer, a sudden variation of the geometry at the intersection between inclined and vertical beams is observed (Figure 3.7); this evidence suggests the possibility that inclined beams section could be ellipsoidal rather than circular.

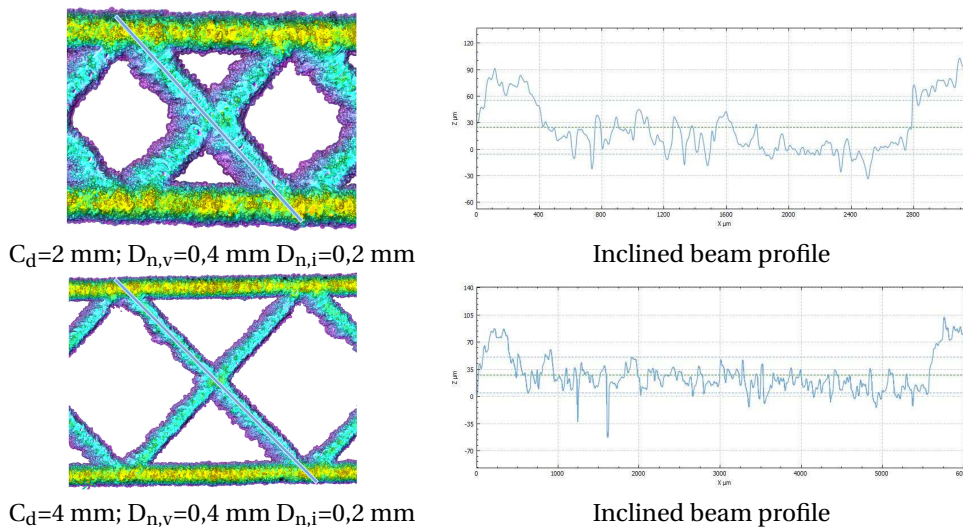


Figure 3.7: FBCCZ lattices geometric accuracy assessment - lattice's surface after correction

To investigate this phenomenon, it is required to produce specimens that allow measurement of beams sections; therefore five specimens with lattice cells sectioned along planes orthogonal to the beams axis are designed and produced (Figure 3.8). Specimens beams diameter varies between 0.2 and 0.4 mm (0.05 mm steps).



Figure 3.8: FBCCZ lattices geometric accuracy assessment – effective beam section

Vertical and inclined beams sections are measured using the experimental set-up shown in Figure 3.9.

Comparing sections measurements of the vertical and inclined beams it is clear that the latter is not circular (Figure 3.10). Inclined beam's section is elongated along the direction parallel to the build axis; this phenomenon could be due to undesired adhesion of metal particles on overhanging surfaces. Inclined beam's diameter along the direction perpendicular to the build one is close to the nominal value. The geometry of inclined beam section is therefore elliptical.



Figure 3.9: FBCCZ lattices geometric accuracy assessment – section measurement

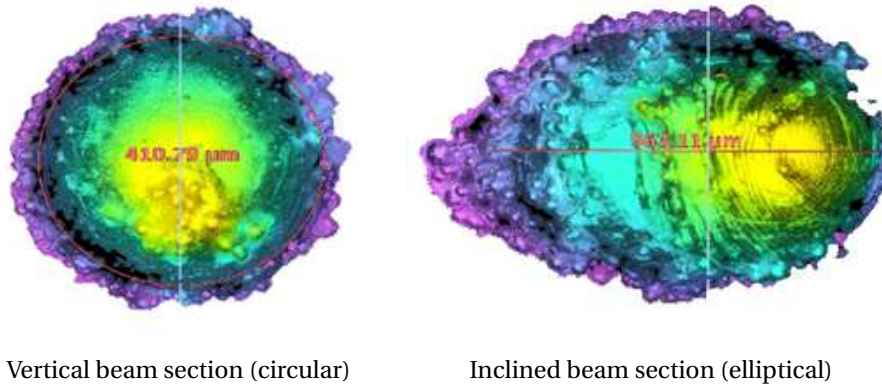


Figure 3.10: FBCCZ lattices geometric accuracy assessment – beam section surface

Results obtained suggest that it is not sufficient to apply a correction coefficient to obtain inclined beams of the desired diameter; a possible approach may be to model inclined beams with an elliptical section in order to compensate printing error along the build direction. This approach requires further studies. To ensure uniformity with previous experimental campaigns and avoid complicating three-dimensional modelling of lattices, geometric error is accepted and 3D models consisting of uniform section beams are used. This choice also has the advantage of guaranteeing the possibility of comparing the results with those of 2<sup>nd</sup> DoE. Three-dimensional modelling of the specimens integrating lattice structures requires a considerable amount of time due to the huge number of elements that make up the structure. The conversion into STL files requires a lot of time, since the number of triangles necessary to discretize the lattice geometry is significant; moreover, file's size is quite big, slowing down all the operations that must be performed before production.

### 3.2 Manufacturing of 3<sup>rd</sup> DoE

Once the specimens STL model generation phase is completed, it is possible to start performing all the operations required to be ready to start SLM 3D printing. For this purpose, Materialise Magics software is used. The first operation to be performed is the correction of errors generated during the conversion to STL file; even taking advantage of the automatic algorithm integrated into Magics, the time required to perform this operation is very long due to the very large number of triangles that make up the specimens surface. Subsequently, the specimens are positioned on the virtual build platform. Preliminary estimates of time and computational resources needed to perform slicing and 3D printing of the components suggest dividing the production on three distinct build platforms. The time required to perform the slicing of 36 specimens simultaneously is more than 15 days and production would take more than 7 days. The risk connected to the execution of such

long operations that cannot be restored in the event of interruptions (e.g. power failure) is very high. Therefore, specimens positioning is performed on three separate build platforms; specimens are subdivided according to their height, hence each build platform contains specimens of the same height. Specimens are positioned randomly to reduce the effect of the position on mechanical properties and with an angle of 45° with respect to the coater blade, to favour uniform powders distribution. Figure 3.11 shows specimens positioning for each of the three virtual printing platforms.

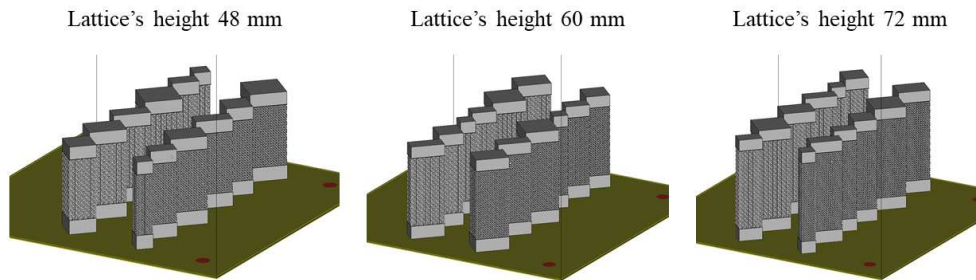


Figure 3.11: 3<sup>rd</sup> DoE's specimens positioning on build platform

It takes 4 to 5 days to slice each build platform, depending on specimens' height; obtained files define geometrical and process related characteristics of the individual layers. For each platform, files between 10 GB and 20 GB are generated; processing large files causes the slowdown of all the preliminary operations to be performed before proceeding with 3D printing. At the end of the slicing operation it is possible to proceed with the 3D SLM printing, using the generated files.

To assess whether lattice specimens have better damping properties compared to equivalent full cross-section specimens, three reference specimens have been designed similarly to what was done in Chapter 2. The points of the DoE chosen to execute the comparison are the central ones; therefore, lattice specimens chosen are those with an external section equal to 20 x 20 mm with three lattice height levels (unit cell size equal to 4 mm). The three reference specimens have a full cross-section and have been designed in order to have compliance equal to that of as-built lattice specimens.

As specified before, the material chosen for the production of the specimens is a 316L austenitic stainless steel; moreover, the SLM process parameters used are the same as those specified in Chapter 2. These choices allow the production of specimens with mechanical properties comparable to those of 2<sup>nd</sup> DoE specimens, allowing to compare the results with those obtained from previous experimental campaigns.

The SLM 3D printing process, performed using the machines already described in Chapter 2, requires 5 to 7 days depending on the specimens' height. Nearly 18 days are required to manufacture the specimens positioned on build platforms shown in the previous paragraph. In Figure 3.12a it is possible to observe the result obtained at the end of the printing phase of the first platform (specimens with 48 mm high lattice structure); the powder

layer's and specimens' surfaces are uniform, suggesting a successful SLM process. In Figure 3.12b, c and d it is possible to observe the as-built specimens.

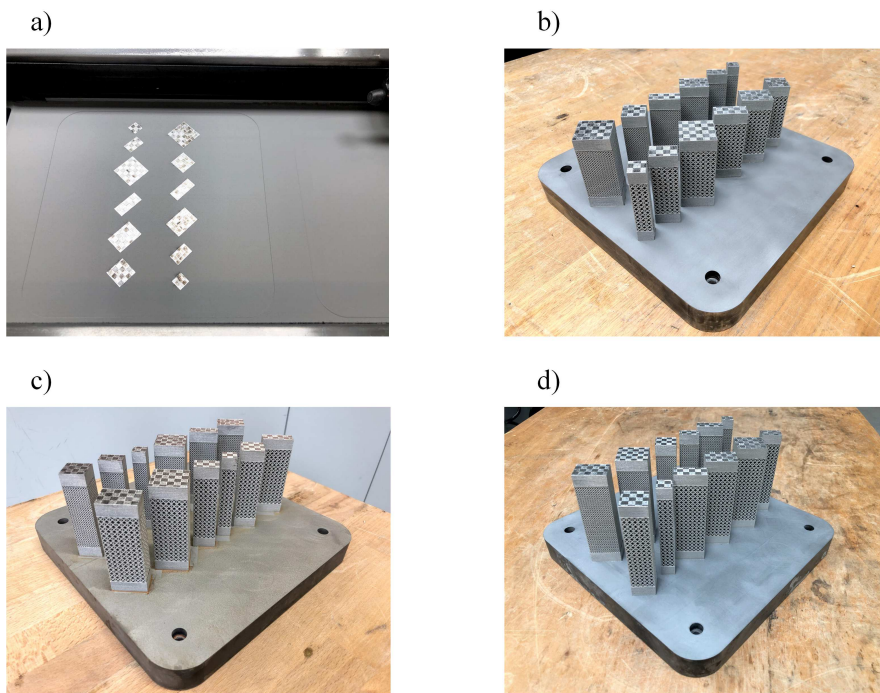


Figure 3.12: 3<sup>rd</sup> DoE's specimens SLM 3D printing as-built result

From a qualitative point of view, examining details of Figure 3.13, it is possible to observe that lattices geometry is reproduced correctly; the result is similar to that already documented in Chapter 2.

All specimens are subjected to stress relieving heat treatment; therefore, it is possible to characterize the specimens avoiding the effect of residual thermal stresses. This choice favours the exploitability of results at industrial level since it is good practice to carry out the stress relieving heat treatment of SLM-manufactured components, to eliminate the residual thermal stresses typical of this type of production process which could generate macro deformations of parts.

Heat treated specimens are separated from the build platforms using a band saw. Therefore, it is possible to perform measurements to estimate static and dynamic properties of the samples.

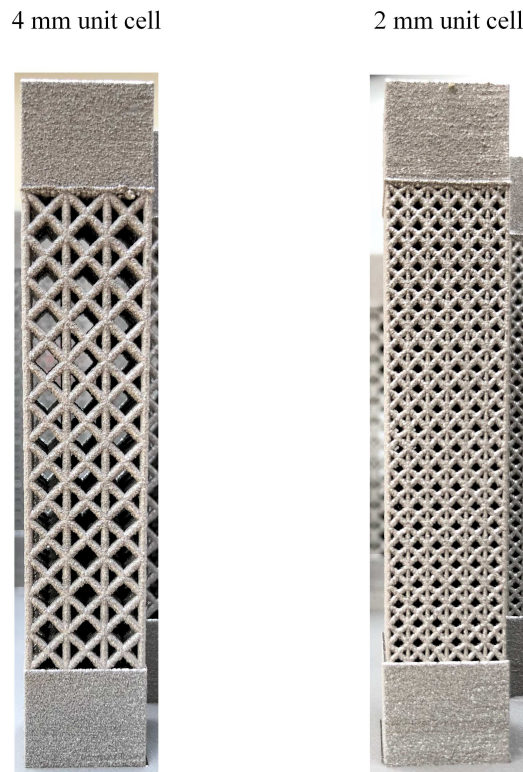


Figure 3.13: 3<sup>rd</sup> DoE's specimens SLM 3D printing - detail views

### 3.3 Static and Modal analysis

In order to proceed with specimens static and dynamic properties characterization, it is necessary to design and implement appropriate experimental set-ups, perform measurements and data analysis. The objective is to collect enough data to describe lattice specimens static and dynamic behaviour. The following paragraphs describe the procedures used to obtain static compliance and frequency response of the individual specimens. Therefore, data analysis allows to evaluate the effect of lattice geometry on static and dynamic properties and on damping performance.

#### 3.3.1 Static analysis experimental setup and measurements

To estimate the static compliance of beam-like specimens it is possible to use different methodologies. In Chapter 2, specimens' static compliance was estimated analysing the frequency response; results obtained were compared with those calculated by measuring the displacement due to the application of a known load on the specimens tip (cantilever beam - tip displacement vs tip loading). Comparing the values obtained using the two methodologies, it was observed that the static compliance estimated using the frequency

response is lower than that calculated by measuring the displacement deriving from the application of a known load.

To calculate the static compliance more accurately, a new experimental set-up is devised: it allows to measure the force that develops when a fixed displacement is applied to specimen's tip (cantilever beam - fixed tip displacement vs reaction force). The scheme that represents the main components of this experimental set-up has been reported previously in Figure 3.1, since the compatibility between experimental set-ups and specimen geometry was evaluated in the specimens' design phase.

Specimens are fixed one at a time in the HAAS VF-2TR vertical machining centre grip; 90 degrees rotation of the TR160 rotary table A axis allows to exploit the spindle head to exert a fixed deformation on the specimen tip. The displacement constraint is applied to the specimen tip using a 6 mm diameter strut connected to a Kistler Type 9311B load cell that measures the reaction force. Resulting experimental set-up is visible in Figure 3.14.

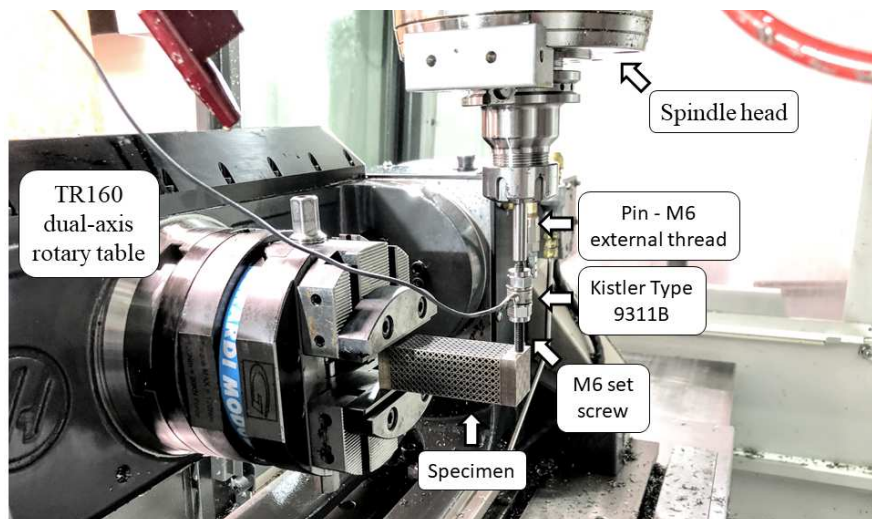


Figure 3.14: 3<sup>rd</sup> DoE's specimens static compliance assessment – experimental set-up

The load cell is connected to a Kistler Type 5073A charge amplifier connected via USB to a PC; data are acquired using ManuWare software provided by Kistler (Figure 3.15).

To improve measurement accuracy, before starting acquisition, each sample is subjected to a loading and unloading cycle to favour specimen's settlement in the vice. Then the loading and unloading cycle is performed: a fixed displacement is imposed on the specimen's tip (loading), then the unloading is performed taking note of load cell's voltage variation and corresponding displacement. VMC's Z axis moves with steps equal to 1  $\mu\text{m}$ . To mitigate the effects of backlash, during unloading phase the first displacement step is neglected.





Figure 3.15: 3<sup>rd</sup> DoE's specimens static compliance assessment – data acquisition

### 3.3.2 Modal analysis experimental setup and measurements

Similarly to previous experimental campaigns, the pulse test technique is used to assess specimens dynamic behaviour. This technique, applied to estimate the frequency response of lattice structures, is based on the impulsive excitation of the specimen's upper base by means of an instrumented hammer. Resulting vibrations are measured by an inductive probe placed near the surface of the upper base, on the same axis of the impulsive force. Specimens lower base is constrained by tightening VMC's vise jaws. Tools and equipment used to perform pulse tests and data acquisition have been already listed in Chapter 2. The resulting experimental set-up is visible in Figure 3.16.

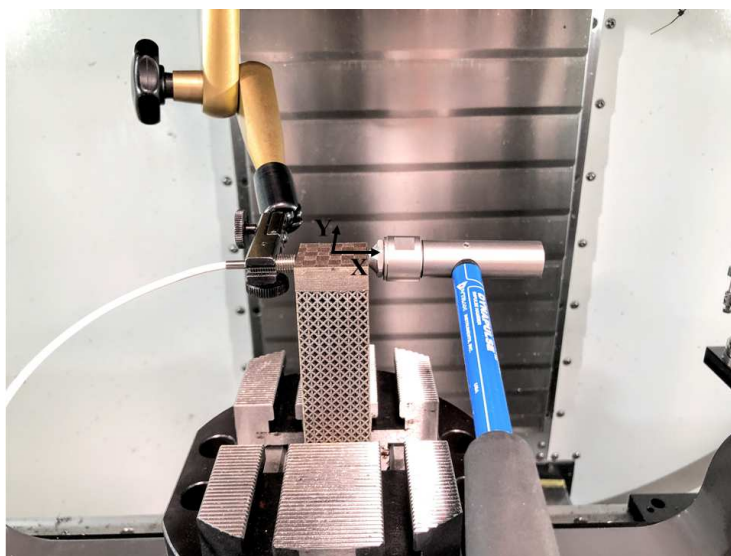


Figure 3.16: 3<sup>rd</sup> DoE's specimens frequency response assessment – experimental set-up

As previously stated, the inductive probe is suitable for measurement of medium-low frequency vibrations; therefore, the specimens have been designed with first resonance frequency lower than 2500 Hz. To study specimens with higher resonance frequencies it is required to use sensors that exploit different operating principles, for example laser interferometry. Even a triaxial accelerometer would be appropriate; however, having to be applied on the specimen it alters the dynamic response.

### 3.3.3 Data analysis and results

Data analysis was performed in MATLAB environment applying the same methodology explained in Chapter 2. The specimens' frequency response is calculated; therefore, the first natural frequency and its amplitude are gathered while the static compliance is estimated as the amplitude of the frequency response at  $f \approx 0$ . Using the simple harmonic oscillator model, specimens damping coefficient and damping ratio are estimated. The measurements were repeated twice for each sample; the average value of the results obtained are reported in Appendix 1. In Chapter 2 it was observed that specimens' static compliance values were different depending on whether the estimate was made by evaluating the frequency response or evaluating the deformation generated by the application of a known tip load. Therefore, to estimate 3rd DoE's samples static compliance the experimental set-up has been modified, as specified in the previous paragraph. In Figure 3.17 it is possible to observe the comparison between the results estimated by analysing the frequency response and those obtained using the load cell.

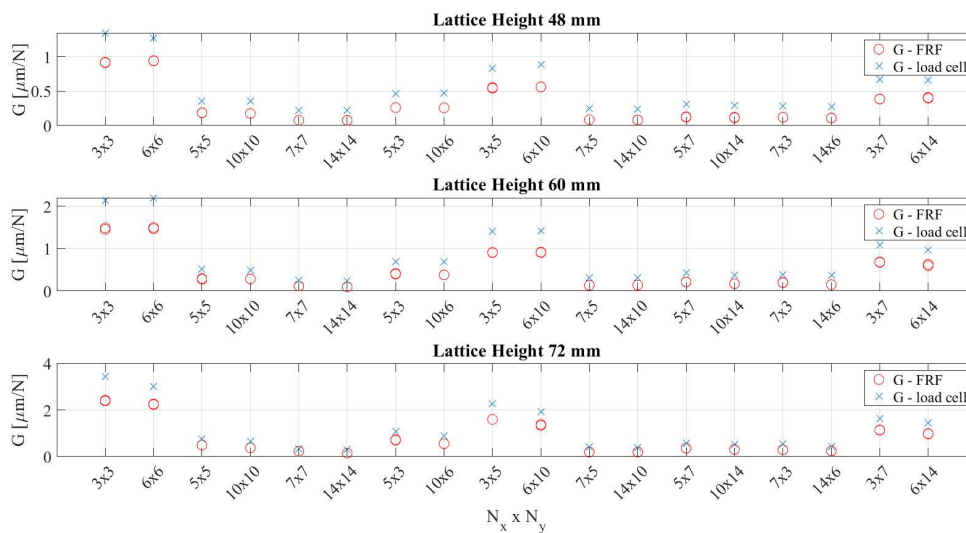


Figure 3.17: 3<sup>rd</sup> DoE's samples static compliance – FRF vs load cell estimated values

The specimen's type is indicated on the x-axis, specifying the number of cells along x-axis and y-axis, defined as in Figure 3.16. Looking at the graphs, it can be observed that specimens' compliance tends to decrease when the cross-sectional area along the load-

ing direction (x-axis) increases. The absence of trends that cannot be explained from a physical point of view confirms that measurements acquisition was performed correctly in both cases. Similarly to Chapter 2 results, the compliance estimated from the FRF is lower than that calculated by measuring with the load cell the reaction force that is generated by applying a fixed displacement to the specimen's tip. The discrepancy between the values obtained with the two methodologies can be attributed to the noise affecting the FRF at low-frequency and to the errors due to the measurement chain used to perform measurements with the load cell (i.e. mechanical tolerances and data acquisition system noise). To ensure consistency with the previous experimental campaigns, it was chosen to use the value derived from the FRF; however, it is suggested to further investigate this aspect, for example by calibrating the acquisition system using a specimen with known compliance.

Looking at Figure 3.18, the effect of compliance's variation on damping ratio " $\zeta$ " can be evaluated. Observing the values related to samples having  $N_x = N_y$ , in general the damping effect tends to increase when the compliance decreases, confirming what was observed in Chapter 2. However, analysing the data relating to the specimens with  $N_x \neq N_y$  compliance's variation effect on damping is less clear.

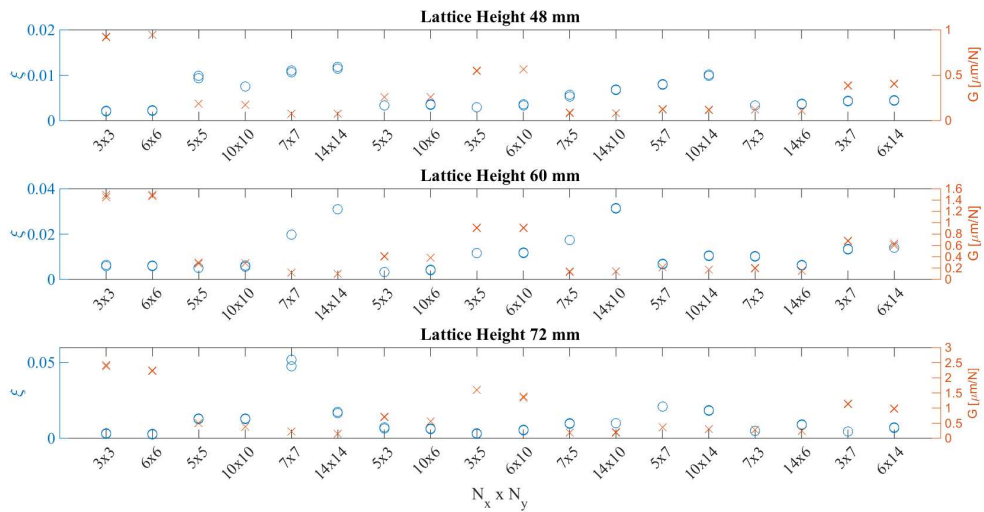


Figure 3.18: Effect of specimens' compliance variation on damping ratio

Comparing damping ratio " $\zeta$ " and damping coefficient " $c$ " values, the trend with respect to the specimen section is generally the same (Figure 3.19). Analysing data related to specimens having  $N_x = N_y$  it can be observed that the damping effect tends to grow with cross-sectional area and therefore it is proportional to unit cells number; furthermore, observing the results for specimens having  $N_x \neq N_y$ , generally the damping effect is greater when  $N_y > N_x$ . This latter result is significant taking into account that the load is applied along the x-axis.

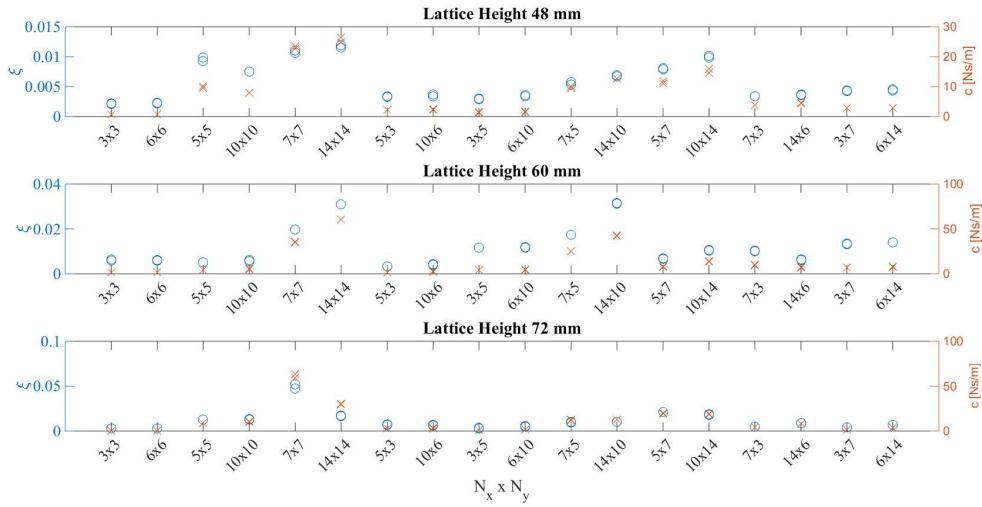


Figure 3.19: Comparison between damping ratio " $\zeta$ " and damping coefficient " $c$ "

Grouping damping ratio results on the basis of the number of cells along X and Y axis it is possible to obtain the boxplots of Figure 3.20; the damping ratio average value of the specimens having  $N_y > N_x$  is higher than those having  $N_x > N_y$ . This result is valid both for lattices composed by 4 mm and 2 mm unit cells and confirms what was observed previously.

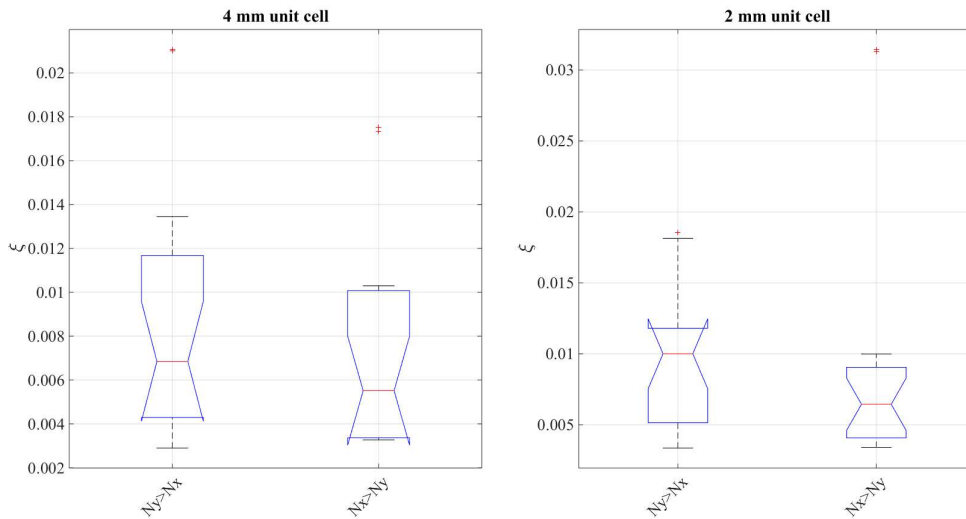


Figure 3.20: Aspect ratio effect on damping ratio " $\zeta$ "

To analyse the effect of cells number variation on the damping ratio, the results are grouped according to the number of cells along the three main directions; it is therefore possible to observe the effect of cells number variation along X, Y and Z for lattices composed by 4 mm and 2 mm unit cells (Figure 3.21).

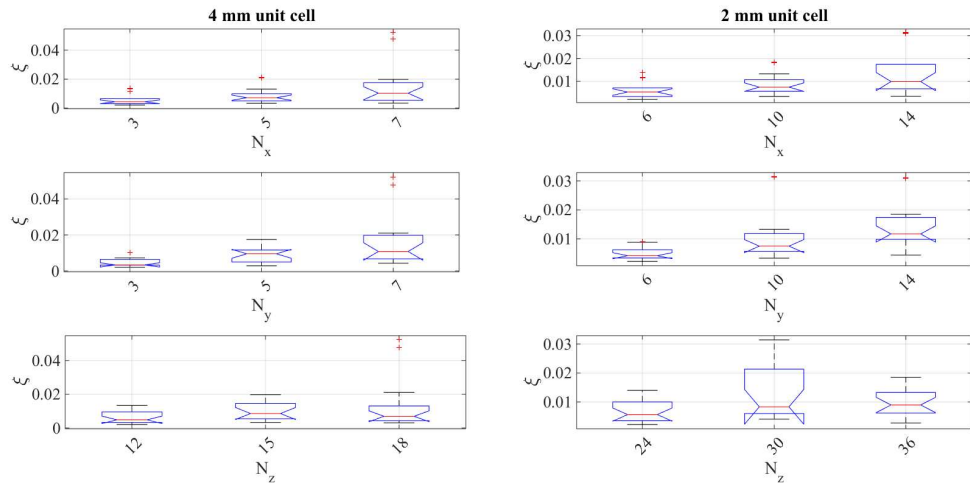


Figure 3.21: Lattice's cells number variation effect on damping ratio " $\zeta$ "

The cells number variation along X and Y directions has a significant influence on the damping ratio both for lattices composed by 4 mm and 2 mm unit cells. When the number of cells increases it also tends to increase the damping ratio. This trend is also confirmed for  $N_z$ , albeit less clearly. To evaluate the effect of cells number variation on damping ratio from a statistical point of view, an ANOVA is performed; as expected, the result obtained confirms that the individual factors as well as the interactions are significant.

To evaluate if unit cell's size variation affects damping ratio, the trend of the latter is evaluated as a function of specimens external section; in this way it is possible to compare specimens having lattice structures with the same cross-section but different unit cell size (Figure 3.22).

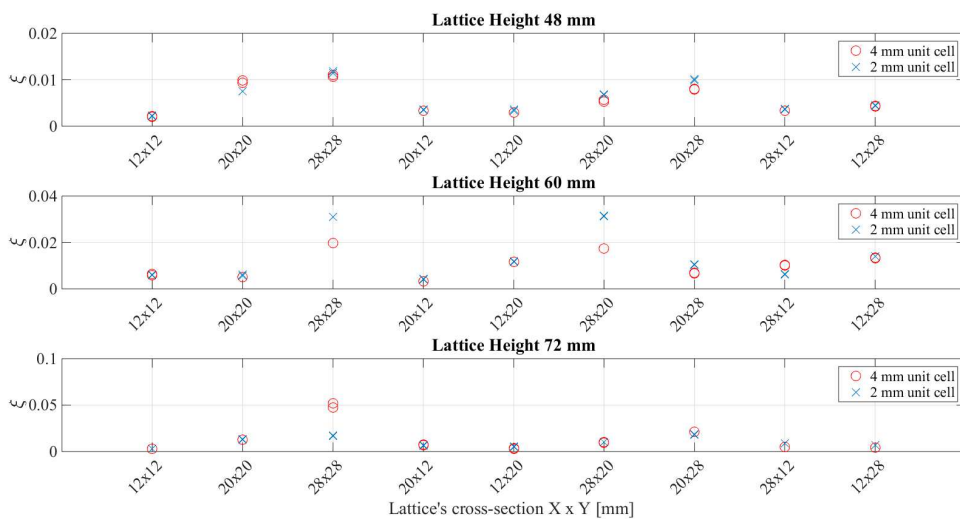


Figure 3.22: Damping ratio " $\zeta$ " with respect to lattice's cross-section

In general, considering specimens having the same section, the effect of unit cell's size variation on damping ratio is not striking; however, specimens with smaller unit cell seem to be able to guarantee slightly higher damping performance. Looking at the graph, it could be observed that in general, as the cross-section increases, the damping effect also increases; moreover, having included the results of both measurements repetitions, it is verified that repeatability is good.

To ascertain whether there is an effect, albeit small, of unit cell's size on damping ratio, results are grouped according to unit cell's size, obtaining boxplots of Figure 3.23. Comparing damping ratio's average values of the specimens with a 4 mm unit cell compared to those with a 2 mm cell, it can be observed that the latter allow to obtain a slightly better damping performance. This result suggests that lattices made up of smaller sized unit cells may be more suitable for applications where damping performance maximization is required.

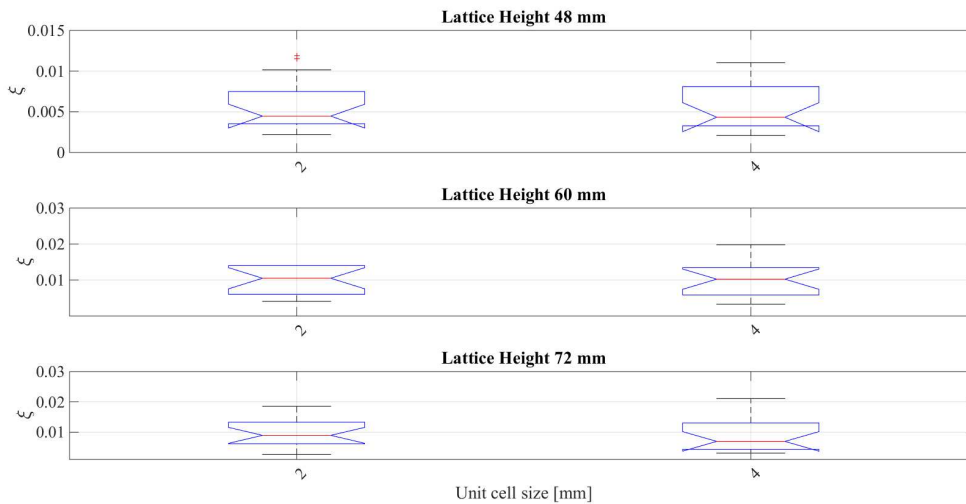


Figure 3.23: Damping ratio " $\zeta$ " with respect to unit cell's size

To confirm that lattice specimens have better damping properties than solid ones, as previously mentioned three reference specimens have been designed. These specimens have a full cross-section and have been designed in order to have compliance equal to that of lattice specimens. The lattice specimens chosen to perform the comparison are those having a 20 x 20 mm cross section, 4 mm unit cell and three lattice height levels (48-60-72 mm). The comparison between damping ratios of lattice specimens with respect to reference ones is shown in Table 3.5. Lattice specimens guarantee better damping properties; however, to confirm this result from a statistical point of view further replicates and tests are required.

Table 3.5: Comparison between lattice and full-cross section specimens damping ratio

| Type (Nx x Ny x Nz) | $\bar{\zeta}_{\text{lattice}}$ | $\bar{\zeta}_{\text{full cross-section}}$ |
|---------------------|--------------------------------|---|
| 5x5x12              | 0,0095                         | 0,0024                                    |
| 5x5x15              | 0,005                          | 0,0045                                    |
| 5x5x18              | 0,0129                         | 0,0048                                    |

To model the relationship between the number of unit cells of specimen's cross section (i.e.  $N_x$ ,  $N_y$ ) and damping ratio a linear regression was performed. ANOVA allowed to establish that statistically all factors (i.e.  $N_x$ ,  $N_y$ ,  $N_z$ ) and interactions are significant; therefore, interactions cannot be neglected. The cell's number variation along Z axis significantly changes specimen's dynamic behaviour. Therefore, data are divided according to unit cell's size " $C_s$ " and cell's along Z-axis number  $N_z$  (i.e. lattice height – " $L_h$ "). Using damping ratio as response variable and cells numbers (i.e.  $N_x$ ,  $N_y$ ,  $N_z$ ) as predictors, six mathematical models useful for damping ratio estimation are obtained by linear regression.

$$\xi_1 = \beta_1 + \beta_2 N_x + \beta_3 N_y + \beta_4 N_x N_y + \beta_5 N_x^2 \quad (3.1)$$

$$\xi_2 = \beta_1 + \beta_2 N_x + \beta_3 N_y + \beta_4 N_x N_y + \beta_5 N_x^2 \quad (3.2)$$

$$\xi_3 = \beta_1 + \beta_2 N_x + \beta_3 N_y + \beta_4 N_x^2 + \beta_5 N_y^2 \quad (3.3)$$

$$\xi_4 = \beta_1 + \beta_2 N_x + \beta_3 N_y + \beta_4 N_x N_y + \beta_5 N_x^2 + \beta_6 N_y^2 \quad (3.4)$$

$$\xi_5 = \beta_1 + \beta_2 N_x + \beta_3 N_y + \beta_4 N_x N_y + \beta_5 N_y^2 \quad (3.5)$$

$$\xi_6 = \beta_1 + \beta_2 N_x + \beta_3 N_y + \beta_4 N_x^2 \quad (3.6)$$

Estimated values of mathematical models  $\beta$  coefficients are shown in Table 3.6.

Table 3.6: Estimated values of linear regression models  $\beta$  coefficients

| $\bar{\zeta}_n$ $C_s \times L_h$ | $\beta_1$ | $\beta_2$ | $\beta_3$ | $\beta_4$ | $\beta_5$ | $\beta_6$ | $R^2$ [%] |
|----------------------------------|-----------|-----------|-----------|-----------|-----------|-----------|-----------|
| $\bar{\zeta}_1$ 4x48             | -8,19E-03 | 4,47E-03  | -4,58E-04 | 3,31E-04  | -5,26E-04 | \         | 85        |
| $\bar{\zeta}_2$ 4x60             | -5,91E-03 | 1,61E-03  | -2,19E-04 | 9,18E-05  | -1,01E-04 | \         | 98        |
| $\bar{\zeta}_3$ 4x72             | 3,21E-02  | -1,87E-02 | 5,23E-03  | 2,01E-03  | -3,55E-04 | \         | 95        |
| $\bar{\zeta}_4$ 2x48             | 3,91E-02  | -1,34E-02 | 4,40E-03  | 2,63E-04  | 6,16E-04  | -2,70E-04 | 88        |
| $\bar{\zeta}_5$ 2x60             | 6,92E-02  | -9,13E-03 | -2,46E-02 | 2,73E-03  | 1,60E-03  | \         | 91        |
| $\bar{\zeta}_6$ 2x72             | -3,17E-02 | 5,96E-03  | 1,02E-03  | -2,55E-04 | \         | \         | 90        |

Figure 3.24 shows damping ratio values distribution with respect to unit cell's number (i.e.  $N_x, N_y, N_z$ ) and the surfaces that represent mathematical models obtained by linear regression.

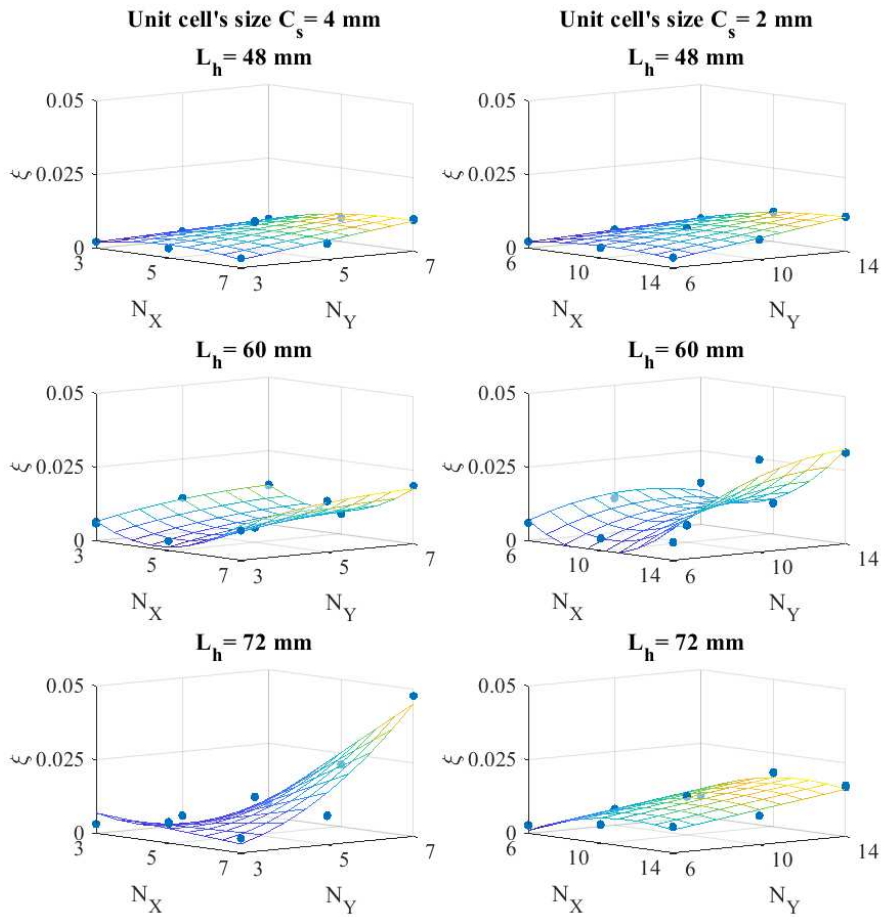


Figure 3.24: Distribution of damping ratio values and mathematical models surfaces

Observing mathematical models surfaces, it is confirmed that as the number of cells of the lattice's cross-section increases the damping effect is enhanced. These mathematical models can be useful to evaluate damping effect of lattices as a function of their size; furthermore, results obtained can be exploited for FE models calibration and development of homogenization methods.



### 3.4 Conclusions

On the basis of the results obtained from the experimental campaigns described in Chapter 2, a further in-depth study was devised to investigate static and dynamic behavior of lattices of different sizes (i.e. number of cells). A DoE developed starting from the previous ones was designed; topology and geometry of the unit cell of the lattices being studied were the same as the specimens A and C described in Chapter 2, while the number of unit cells was changed. A full factorial DoE was devised, with three factors and three levels for each factor. The variation of lattices static and dynamic properties with respect to lattice size (i.e. number of unit cells along the three main directions -  $N_x$ ,  $N_y$ ,  $N_z$ ) was under investigation. The DoE was divided in two parts, according to unit cell's size, and the central point was represented by specimens integrating lattices having dimensions equivalent to Chapter 2 A and C specimens. Using appropriate experimental set-ups, compliance and frequency response of the 36 specimens produced were obtained. Data analysis was performed allowing to evaluate lattice structures behavior according to their size; hence, exploiting data and expertise acquired by means of all the experimental campaigns investigating lattice structures properties, a generalised methodology useful to characterize static and dynamic behaviour of different types of lattice porous structures was conceived. Below, some observations and conclusions:

- Measurements execution and data analysis were facilitated optimizing specimens' geometry and DoE's factors levels by means of FEA results analysis.
- Using a 3D optical profilometer it was assessed that inclined beams cross-section was not circular. Inclined beam's section is elongated along the direction parallel to the build axis. Therefore, modifying the nominal diameter of the beam (CAD) to improve dimensional accuracy is not sufficient.
- Specimens slicing and SLM manufacturing required 13 and 18 days respectively.
- By means of adequate experimental set-ups, compliance and frequency response of 36 specimens made of 316L stainless steel were obtained, allowing to observe the effect lattice's size variation on mechanical properties.
- Specimens compliance estimated from the FRF is lower than that obtained exploiting the load cell. This problem can be connected to the noise that affects FRF's at low frequency and mechanical tolerances of the measurement chain; further investigations are necessary to improve compliance estimation accuracy.
- In general, specimens damping ratio tends to increase with stiffness and cross-sectional area. Furthermore, damping effect is enhanced when lattice's cross-section is more extended along the plane perpendicular to the applied force.
- Effect of cells number variation on damping ratio was assessed with ANOVA. All factors (i.e.  $N_x$ ,  $N_y$ ,  $N_z$ ) as well as the interactions are significant.

- It is confirmed that lattices composed of smaller unit cells can guarantee slightly better damping performance than those made up of larger cells.
- Lattice specimens had higher damping ratios compared to full cross-section equivalents.
- By means of linear regression, mathematical models useful for lattices damping properties estimation as a function of their size have been obtained. These can be used for FE models calibration, development of homogenization methods and advanced mathematical models for the prediction of lattices damping behaviour.
- Static and dynamic characteristics of porous / lattice structures could be assessed by means of the proposed method.

## **Chapter 4**

# **INNOVATIVE METHODOLOGY FOR FAST SLM MANUFACTURING OF LATTICE AND POROUS STRUCTURES**

Studies concerning lattice structures described in the previous chapters allowed an in-depth evaluation of the advantages and disadvantages related to design, optimization and production of controlled porosity materials. Furthermore, the damping properties of these structures have been investigated, contributing to improve the knowledge in an innovative field of research that was investigated by a limited number of scientific works; below is a brief summary of the aspects that highlight the potential offered by these type of structures, justifying the need to develop new strategies that facilitate and speed up their design and production. Lattice and porous structures offer the possibility of developing innovative functions and better thermo-mechanical properties, increasing design freedom compared to what is achievable with solid materials. It is possible to obtain lightweight structures with a high specific strength, improve damping properties and heat exchange, improve biocompatibility for medical applications. Lattice / porous structures are formed by the orderly or stochastic repetition of unit cells, depending on the geometry of these cells the resulting porosity can be open or closed. Mechanical properties of this kind of structures are influenced by a large number of parameters, the main ones being shape of the unit cell, relative density, geometric parameters such as beams diameter, wall thickness and cell size and material properties. The choice of unit cell type and geometry allows the creation of structures with tuneable properties calibrated according to the specific case needs. Lattice structures are particularly interesting because, depend-

ing on their topology, they exhibit different under load behaviour. This characteristic can be exploited to obtain optimized structures with point by point tuneable mechanical behaviour, helping to achieve high specific mechanical strength and good damping properties. Lattice structures are easier to exploit than foams, since it is possible to generate materials with controlled relative density and mechanical properties. SLM technology is particularly suitable to produce lattice / porous structures, since it makes it possible to produce complex geometry easily.

Therefore, considering all the aspects described above, lattice / porous structures proven to be a useful tool to design high performance mechanical components. However, some significant problems affecting the design and production phases of these structures have been highlighted. In particular, traditional CAD three-dimensional modelling methods proven to be inadequate, requiring in many cases consistent calculation times and the generation of large files; moreover, the traditional SLM scanning strategies are not optimized for the production of small-sized lattice structures, contributing to significantly increase the machine time required for production.

This chapter describes an innovative methodology for the design and production of controlled porosity lattice structures that addresses the problems described above, demonstrating the existence of important margins for improvement for design and production of these structures.

## **4.1 Geometry and process design for lattice and porous structures**

Traditional 3D CAD modelling techniques, used to design geometric models of parts to be produced with Additive Manufacturing Technologies - AMT, involve the creation of closed surface models (i.e. watertight STL); this type of 3D model is characterized by the clear distinction between the internal and external surface of the component. An example of FBCCZ lattice structure solid model and the section of the watertight surface model is shown in Figure 4.1.

The parts produced with additive technologies are the result of layer by layer material addition; in order to proceed with production, it is therefore required to define the geometry of the individual bidimensional layers that make up the object. Following the creation of the 3D model, before production phase, the surface model (generally in .stl format, which uses triangles to discretize the surface of the part) must be subjected to an operation called "slicing" which generates the geometry of the individual layers, defining contours and areas affected by the AM process. The individual layers are made by the composition of closed polygons that describe the sections of the parts to be produced;

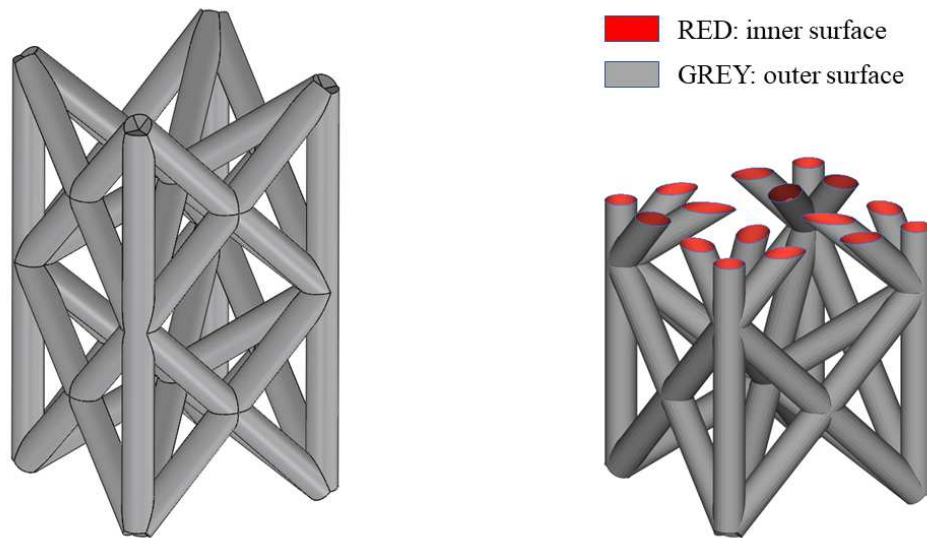


Figure 4.1: FBCCZ solid model and section of the watertight surface

curved paths are discretized using straight segments. For SLM manufacturing technology, the result of FBCCZ lattice structure slicing operation is reported in Figure 4.2; on the right side it is visible the conformation of one of the layers, the contour laser path (red) does not coincide with the actual slice contour (grey) because it is necessary to take into account the actual size of the circular spot (laser beam's diameter compensation).

It should be pointed out that most slicing software does not provide the ability to manage and produce single isolated points. In the case of the Selective Laser Melting (SLM) AM technology, the manufacturing process takes place thanks to the heat supply of a laser source that causes the selective fusion of the raw material in the form of powders and the consequent solidification, allowing the generation of the layers described above. Process parameters and in particular the circular cross-section spot diameter of the laser source can be varied within a certain range.

The creation of the three-dimensional model of the lattice structure and the conversion into a watertight surface model in many cases require huge calculation resources and long calculation times. This problem occurs because lattice structures are composed by a large number of unitary cells repeated in space and the total number of beams forming the structure is very large. This involves long times for the realization of the solid model of the structure and for the subsequent transformation into a closed watertight surface. In fact, the lattice's surface is discretized by means of a very high number of triangles, especially if beams section is circular, requiring long calculation times and the generation of large files. The watertight closed surface, as previously specified, has to be sliced; this operation requires a calculation time proportional to the number of triangles composing the surface. Therefore, the need to process large files describing surfaces composed of a

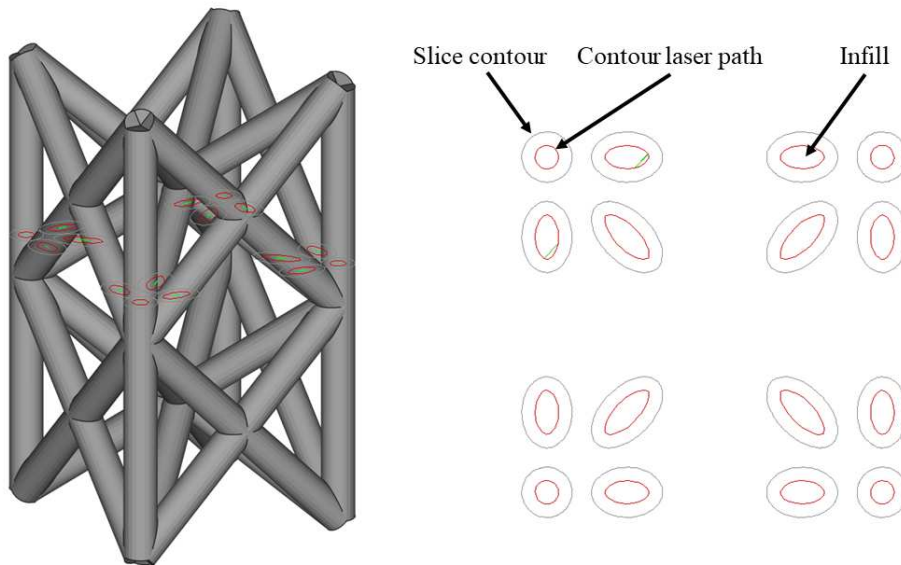


Figure 4.2: Example of layer obtained after slicing operation

very large number of triangles significantly slows down slicing operation. The result of slicing is used by the SLM machine to establish the laser trajectories used to produce the individual layers; the file obtained after slicing lattices is quite big, since it contains all the instructions for the production of contours and areas composing the lattice, therefore production process is significantly slowed down. In fact, to produce a single layer, composed of several circular / ellipsoidal sections, the laser must follow the trajectories that describe contours and internal areas of all the beams sections that make up the structure; the large number of individual trajectories to be produced contributes to slow down the production process. The problems described above highlight the weaknesses associated with design and production of lattice structures when conventional three-dimensional modelling tools and methods are used, suggesting the need to investigate new methodologies to eliminate or mitigate these problems.

Literature review evidenced some studies describing an alternative approach, named Laser Spot Welding (LSW), suitable for lattice structures manufacturing that solves some of the issues highlighted before; exploiting this type of methodology, the lattice geometry is defined layer by layer by means of points that describe the centre of the circular / ellipsoidal sections of the individual beams of the controlled porosity structure [98]–[100]. Figure 4.3 shows the comparison between conventional exposure strategy, used to manufacture the 3D watertight model of lattices, and the Single Exposure Strategy (SES) or Laser Spot Welding, which requires the geometric representation "by points". Figure 4.3a shows the conventional exposure strategy used for the production of layers obtained by slicing a complete 3D model of a cylindrical beam: two distinct groups of laser trajectories can be observed, "contour" made by the composition of segments that discretize circular / ellipsoidal sections and "infill" made by straight paths. In Figure 4.3b it is pos-

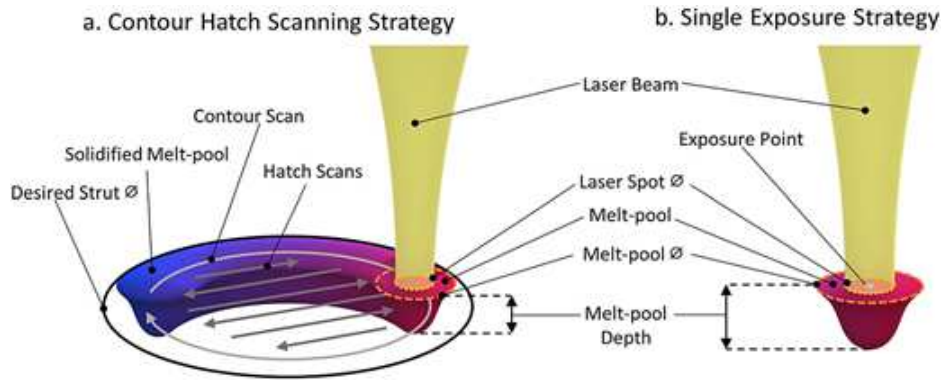


Figure 4.3: Comparison between conventional exposure strategy (a) and Single Exposure Strategy or Laser Spot Welding (b) [99]

sible to observe the LSW technique which uses a single point to define the centre of the circular section of the cylindrical beam. In the first case, the SLM process parameters are kept constant throughout the production process and geometric characteristics of the lattice such as shape and diameter of the individual beams are defined by contour and infill laser paths. When LSW is involved, the geometric characteristics are controlled modifying SLM process parameters (e.g. power, exposure time, laser spot size). Figure 4.4 shows the comparison between the layers obtained from the slicing of a lattice structure 3D model, with and without LSW technique: taking advantage of the traditional scanning strategy, the contours of the circular / ellipsoidal sections of the beams forming the structure are generated, while applying the LSW technique a series of points identifying the centres of the aforementioned sections is created.

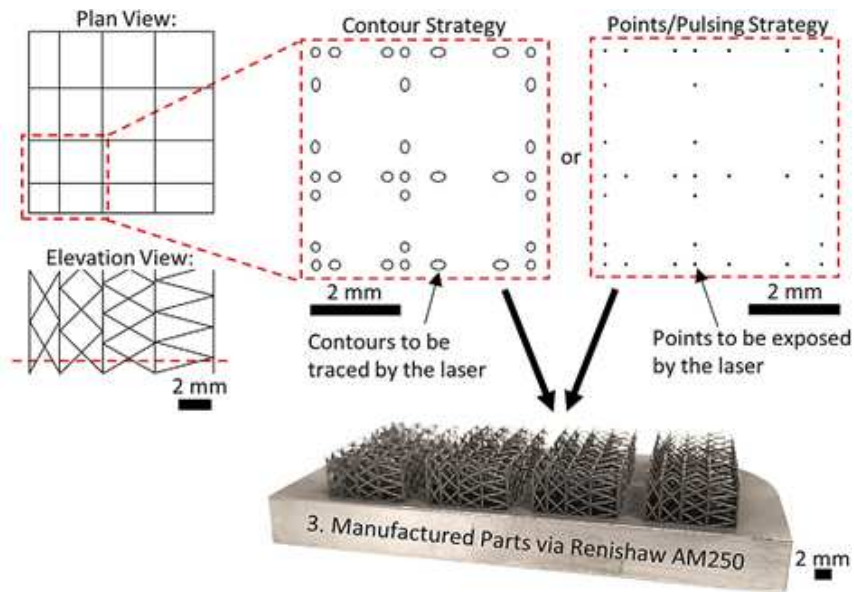


Figure 4.4: Comparison between layers obtained after slicing applying the conventional exposure strategy (left - contour) and the SES / LSW (right - points) [99]

As mentioned above, slicing and machine control software generally do not allow to manage trajectories composed by points; therefore, the LSW strategy requires the use of specifically programmed modelling tools, used for research purposes, or commercial tools that use uncommon data interchange formats (e.g. Betatype). Furthermore, the management of "point" trajectories is not universally supported by SLM machines, therefore in most cases the production of lattice structures with LSW technique is only possible if the available equipment allows direct programming of the laser trajectories. This situation is not very common when commercial equipment is involved; typically, it is possible to set a limited number of process parameters while it is mandatory to use a machine specific slicer that outputs encrypted files, making altering or defining specific trajectories impossible. In the case of non-lattice porous structures made by the repetition of complex shaped thin walls (e.g. gyroid), there are some studies that investigate the existence of optimized SLM process parameters and strategies to enhance manufacturability and their mechanical properties. It should be noted that some of the problems described previously affecting the design and production of lattice structures also occur in the case of thin-walls porous structures.

To solve problems related to the design and production of porous structures, an innovative methodology for modelling and rapid production of small-scale lattice and porous structures using SLM technique has been developed (Patent Pending). This strategy makes it possible to improve the efficiency and speed of three-dimensional modelling, slicing and production of small-sized lattice / porous structures, ensuring substantial savings in terms of calculation resources, time, design and manufacturing costs.

## **4.2 Innovative methodology for design and manufacturing of lattices**

As mentioned in the previous paragraph, generally 3D modelling of lattice / porous structures is carried out with commercial CAD software that make the design phase inefficient. There are some specific tools allowing faster lattice structures design; however, most commercial / open source software share the disadvantage of generating such structures in the form of 3D models whose surface is discretized through a mesh made up of triangles (e.g. .stl format), this causes the creation of large files that slow down design and slicing phases. The innovative methodology proposed in this chapter is of particular interest because, relying on a simplified 3D model of the lattice / porous structure to be produced, allows considerable time savings for design, slicing and manufacturing phases, while ensuring compatibility with commercial software and SLM equipment.



### 4.2.1 Generation of the simplified lattice / porous structure geometry

Details about the innovative methodology for the creation of the simplified model of lattice and porous structures, patent pending, cannot be disclosed; however, the innovative aspects, the advantages and disadvantages of the proposed methodology and some parts of the specific software developed for the creation of the simplified model are reported. It should be remembered that when lattice structures composed by circular cross-section beams are involved, the laser trajectories consist of the circular ellipsoidal contours and their infill. Similarly, in case of porous structures composed of thin walls, the laser trajectories describe the sections contours and their infill. As demonstrated by studies concerning the LSW technique described before, it is possible to exploit a simplified model of the porous structure to be produced, controlling its dimensional characteristics through SLM process parameters. The proposed methodology uses similar concepts to speed up design and production phases of lattice / porous structures, ensuring compatibility with software and commercial SLM machines.

The first step of the innovative methodology proposed for design and manufacturing of small sized lattice porous structures starts from the generation of the simplified 3D model of the structure; to perform this operation, a set of specifically designed MATLAB functions is used, unit cell's topology and lattice's size are defined and the complete structure can be generated. The topology of the unit cell used to create the lattice / porous structure is preliminarily defined through .stl files generated with commercial CAD software (e.g. SolidWorks, Inventor, etc.), with upcoming software developments it is planned to implement a function that allows direct generation of the unit cell's topology. The Graphical User Interface (GUI) of the software for lattice / porous structure generation is shown in Figure 4.5.

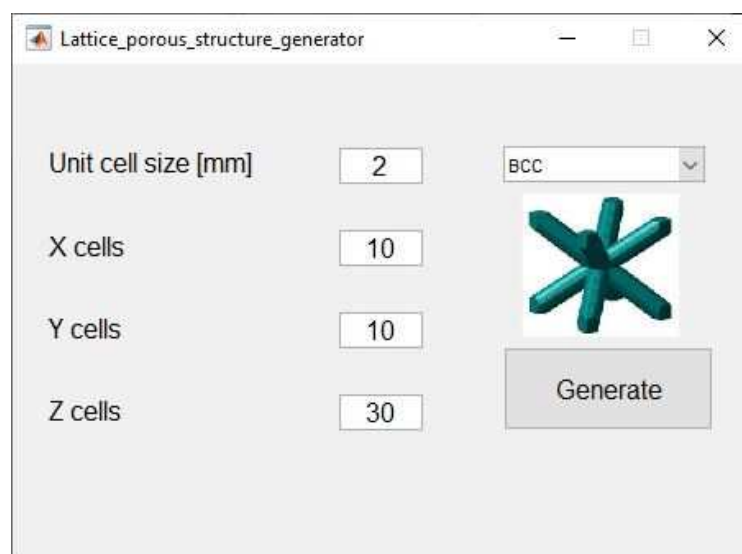


Figure 4.5: Graphical User Interface (GUI) lattice / porous structure generator


It is possible to set the size of the lattice / porous structure by choosing the number of unit cells to be repeated along the three main directions ( $N_x$ ,  $N_y$ ,  $N_z$ ) and choosing the unit cell size; the drop-down menu on the top right allows to select the unit cell type (topology). STL file generation of the entire lattice / porous structure is very rapid, allowing substantial time savings compared to the conventional methodology that involves the conversion from the 3D model to the surface model; time saving exponentially increases with the number of cells composing the structure to be generated. An example of the simplified model obtained using the proposed methodology and the aforementioned software, patent pending, cannot be included in this chapter; however, it should be noted that the file obtained at the end of the procedure, which represents the simplified three-dimensional geometry of the lattice / porous structure, is considerably more compact compared to the one obtainable starting from a solid 3D CAD model. The 3D simplified model compactness and efficiency allow considerable time savings for slicing and SLM production phases, as explained in the next paragraph.

#### **4.2.2 SLM process design and manufacturing for simplified lattice / porous structure geometry**

The simplified three-dimensional model of the lattice / porous structure has to be sliced into sections, before SLM manufacturing could start. One of the strengths of the methodology described in this chapter, is the possibility of exploiting commercially available software tools for manipulating and slicing files for additive manufacturing.

Therefore, the file obtained using the tool described in the previous paragraph can be processed with specific printing software for AM (e.g. Materialize Magics, Autodesk Netfabb, etc.). Printing process preparation and slicing can be performed using the same tools and procedures used for conventionally designed 3D components; this is an advantage as commercial SLM machines generally use proprietary slicers that generate encrypted files, not allowing direct definition of laser trajectories. It is not possible to show the result obtained from the slicing of the simplified model, being part of the innovative design method, patent pending; however, a table highlighting time savings obtainable using a simplified 3D model compared to a conventional one is reported below. Three different sized lattice structures are created in order to estimate the time required to generate the 3D model and to perform the slicing operation; these structures are composed by 2 mm FBCCZ unit cells and circular cross-section beams with 0.4 mm diameter. The three different sized lattices are shown in Table 4.1; time needed to generate the 3D model, to perform slicing and for SLM manufacturing are calculated allowing to compare values obtained starting from lattice's 3D model and simplified one. Estimation of printing time was carried out using the time estimation tool integrated on the Concept Laser M2 Cusing installed at the University of Udine.

Table 4.1: Time required to manufacture lattice structures with different methodologies



|                        |             |             |            |
|------------------------|-------------|-------------|------------|
| $N_x$                  | 2           | 5           | 10         |
| $N_y$                  | 2           | 5           | 10         |
| $N_z$                  | 15          | 15          | 15         |
| <b>3D model gen.</b>   |             |             |            |
| (3D / simp. 3D)        | 2m/<1m      | 3m/<1m      | 20m/<1m    |
| <b>Slicing</b>         |             |             |            |
| (3D / simp. 3D)        | <1m/<1m     | 4m/<1m      | 25m/<1m    |
| <b>SLM manuf. Time</b> |             |             |            |
| (3D / simp. 3D)        | 2h32m/2h27m | 3h20m/2h39m | 6h2m/3h13m |

It can be seen that the advantage in terms of time saved increases with the number of unit cells of the structure. Moreover, the printing time required for the production of lattice / porous structures is reduced if the simplified 3D model is used and the time advantage grows with the number of unit cells that make up the structure.

The main advantages and disadvantages of the proposed methodology with respect to the conventional approach that exploits the complete 3D model of the lattice / porous structure are briefly summarized below.

Advantages:

- Possibility of generating a simplified 3D model of the porous lattice structure using conventional CAD tools or specifically developed open-source (e.g. Python) or MATLAB code.
- Possibility of processing the simplified 3D model using conventional methods and software (e.g. machine specific slicer). This allows the immediate application of the method, without the need to significantly modify workflow and already consolidated CAD and CAM-AM tools.
- Significant time reduction to carry out each of the phases that make it possible to produce lattice / porous structures: creation of the 3D model, slicing, on-board printing job creation and SLM manufacturing process. The advantage in terms of time saved is proportional to the number of cells making up the lattice / porous structure.
- Possibility of creating lattice or porous structures with smaller unit cell dimensions and features (e.g. walls, beam section) compared to those obtainable starting from a complete 3D model. Furthermore, it is possible to 3D print porous structures composed by thin walls (e.g. gyroids), which cannot be produced with the LSW technique.

- Use of ad-hoc software / code to perform slicing is not required, nor are "open" SLM machines allowing input of custom-made laser trajectories. It is possible to use conventional CAD and CAM-AM tools.

Disadvantages:

- Using the simplified 3D model, it is difficult to reproduce with extreme accuracy the actual geometry of the lattice / porous structure; for example, it is not possible to accurately reproduce the ellipsoidal sections resulting from the slicing of lattice structures composed by circular cross-section inclined beams. However, generally error is small and geometric accuracy is sufficient.
- When using the simplified model, the final geometry of the lattice / porous structure depends on process parameters (power, scanning speed and laser spot size); therefore, it is necessary to adjust the aforementioned process parameters to obtain the desired geometry. Process parameters optimization requires the execution of experiments and measurements to assess geometric, microstructural and mechanical properties. Using the complete 3D model of the lattice / porous structure, generally the geometry does not depend significantly on the process parameters; therefore, it is not necessary to carry out experimental campaigns for process parameters optimization.
- In some cases, mechanical properties and surface roughness of components made starting from simplified 3D models can be influenced by the peculiar characteristics of this method. In particular, SLM manufacturing thermal history of components with small features (e.g. beams, walls) is different from that of bigger components, this could lead to a significant impact on component's properties.

Figure 4.6 summarizes the key features of the proposed method, that relies on the simplified model of the lattice / porous structure, compared to the conventional one; the results of SLM 3D printing of a lattice and a gyroid structure, made applying the two different techniques, are shown on the right side.

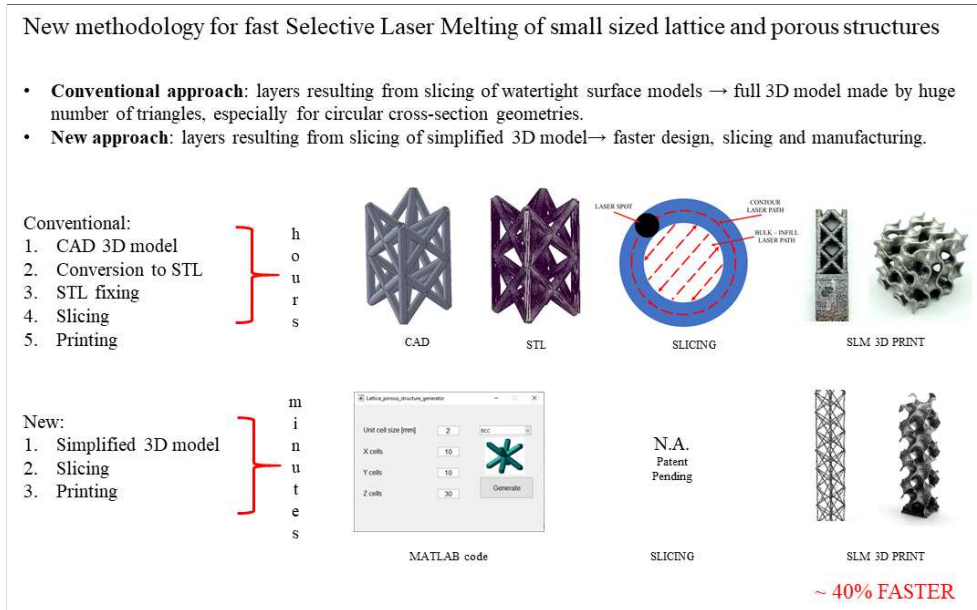


Figure 4.6: Summary of key features of proposed methodology for fast SLM manufacturing of small sized lattice and porous structures

### 4.3 DoE for methodology validation

As anticipated before, in order to produce lattice / porous structures starting from the simplified 3D model, by exploiting the innovative method described in the previous paragraph, process parameters optimization is required. When an object (e.g. a lattice) is SLM-manufactured starting from its 3D model, using the conventional scanning strategy, geometric accuracy depends mainly on laser's path. When the simplified 3D model is involved, the structure's geometry is a function not only of the laser's path but also of the combination of the main SLM process parameters (i.e. power, scanning speed, laser spot size). Therefore, optimized process parameters provided by the SLM machine manufacturer cannot be used to accurately produce the geometry of lattice / porous structures obtained starting from the simplified 3D model.

Static and dynamic mechanical properties of FBCCZ lattice structures have been studied in the previous chapters; therefore, the same geometry is chosen to test the new manufacturing method. The following paragraphs investigate the effect of the main SLM process parameters on the geometry of the FBCCZ lattice structure through an appropriate experimental campaign which required the manufacturing of 205 specimens.

### 4.3.1 Specimens design

The geometry chosen to test the innovative production methodology that involves the use of a simplified 3D model of the lattice / porous structure is the same that was investigated in the previous chapters: a lattice structure composed by FBCCZ unit cells with circular cross-section beams. The objective is to verify the effect of SLM process parameters variation on the geometry and surface roughness of this type of structure. Since the proposed methodology can be used for the production of small sized lattice / porous structures, the unit cell size is set equal to 2 mm; this cell size is equal to that of lattices analysed in previous chapters, allowing an easier comparison between obtained results. Specimens have been designed to perform measurements using the 5-axis 3D optical profilometer Sensorfar S neo installed at the University of Udine. To limit the time required for SLM manufacturing and for measurements execution, specimens' size has been reduced to a minimum. As shown in Figure 4.7, specimens are generated by the union of two unit cells along the Z direction; this choice minimized SLM manufacturing time, placing all the specimens on a single build platform and facilitated measurement operations that could be carried out semi-automatically, exploiting the entire surface of the 3D optical profilometer piece holder. The simplified 3D model of the structure was generated using the MATLAB code described before. Simplified model cannot be shown, Patent Pending.

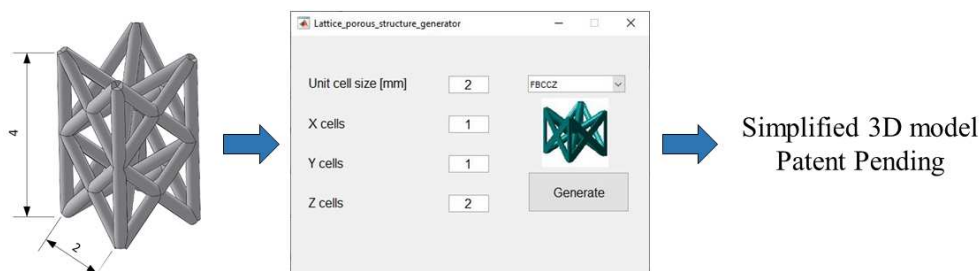


Figure 4.7: Proposed methodology validation - specimens geometry

### 4.3.2 DoE factors and levels selection

As specified before, the geometry of lattice / porous structures manufactured starting from a simplified 3D model depends on SLM process parameters. Therefore, it is necessary to find optimal process parameters that allow to correctly reproduce the geometry to be printed. For example, for lattices composed by circular cross-section beams it is possible to vary the diameter, modifying process parameters appropriately; if these parameters are not chosen wisely, the resulting geometry will not be the expected one. To investigate the effect of the main SLM process parameters on geometry and roughness of the lattice structure, an experimental campaign (Design of Experiments - DoE) has been devised. The specimen geometry is fixed, while DoE's factors and levels are listed below:

- Power [W]: 150, 200, 250, 300, 350, 400
- Scanning speed [mm/s]: 50, 100, 250, 500, 750, 1000
- Laser spot diameter [ $\mu\text{m}$ ]: 50, 100, 150, 200, 250, 300, 350, 400, 450, 500

The laser spot diameter is expected to have a predominant effect on the geometry compared to the other factors; therefore, the number of levels of this factor is greater to better assess the effect of its variation on the lattice geometry. Nevertheless, it is still possible to isolate a subset of levels that allows to identify a full factorial DoE. To investigate all possible combinations of factors levels, the total number of specimens to be produced is 360; however, to avoid problems that could cause failure of the entire production process, the experimental points where Volumetric Energy Density - VED is less than  $50 \text{ J/mm}^3$  or more than  $500 \text{ J/mm}^3$  are eliminated. By applying this precautionary criterion, the total number of specimens to be produced is 205. The table summarizing combinations of factors levels investigated is reported in Appendix 2.

### 4.3.3 Specimens SLM manufacturing

Specimens production is carried out by means of the Concept Laser M2 Cusing SLM printer installed at the University of Udine. The material chosen is a 316L austenitic stainless steel, already used to produce the lattice structures analysed in the previous chapters. Specimens positioning on the build platform and slicing operations were carried out using Materialize Magics software, which integrates Concept Laser proprietary slicer. Specimens were placed on the build platform on the basis of the VED, in order to try to isolate any problem that may occur when the supplied energy deviates significantly from the interval that identifies the optimal process window.

Figure 4.8 shows the print result and a detail that highlights the geometry of one of the specimens made using the proposed methodology; on the left side it is shown that VED tends to grow from bottom to top and from left to right. Observing the specimens, as expected, process parameters variation significantly affects lattices' geometry. The presence of specimens whose cells are partially closed, due to the excess of energy supplied and the excessive depth of the HAZ, is detected both in the upper part and in the lower part of the build platform; therefore, VED is not able to accurately describe physical phenomena that develop during the SLM process and it is not possible to use it to establish when process parameters combination will generate a defective lattice or not.

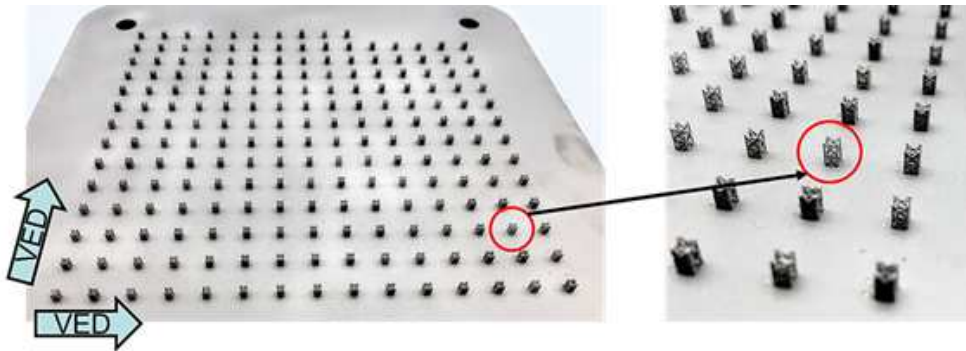


Figure 4.8: SLM 3D print of specimens obtained starting from the 3D simplified model

#### 4.3.4 Morphological characterization and surface roughness analysis

To study the effect of SLM process parameters variation on geometry and surface roughness of the lattice specimens, measurements were taken using the 3D optical profilometer Sensofar S neoX installed at the University of Udine. To facilitate and speed up measurements acquisition, a specific equipment to position all the specimens on the piece holder of the profilometer was designed and built. This equipment makes it possible to exploit profilometer's semi-automatic measurement's strategies, improving measurement speed and repeatability. The experimental set-up, shown in Figure 4.9, involves the use of a brightfield 5x objective; measurements are taken using focus variation method and High Dynamic Range (HDR) option, which helps when the intensity of the lighting varies considerably between one point and another of the sample.

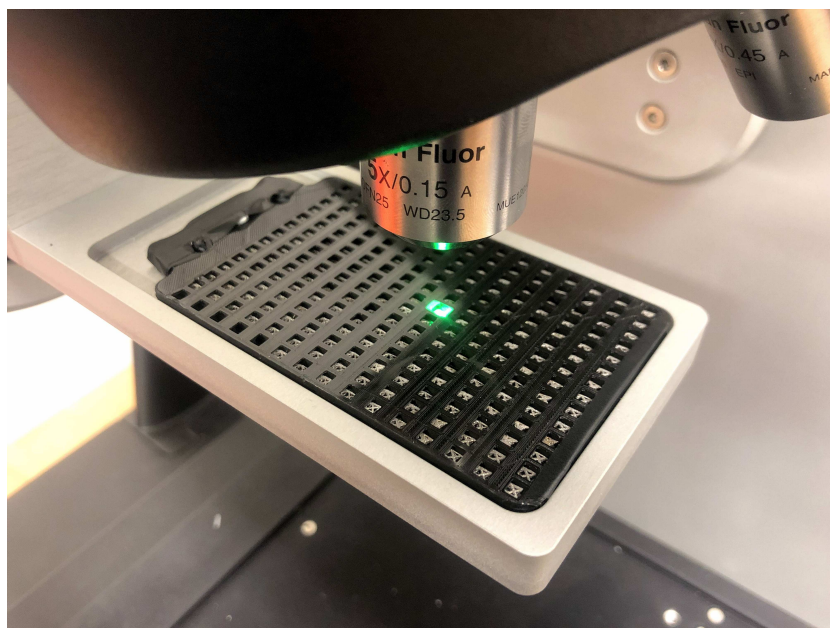


Figure 4.9: Experimental set-up for measurements with 3D optical profilometer



The SensoVIEW analysis software provided by Sensofar is used to estimate specimens' beams diameter. Before diameter estimation, acquired data were modified by applying a filter that eliminates any inclination of the specimen with respect to the horizontal plane, caused by imperfections of workpiece holder or specimen itself. Afterwards, to carry out the measurement, a section normal to beams axis was selected; hence, half of the pseudo-circular profile of the beam section was obtained, allowing beams diameter estimation. Measurements were performed to determine vertical beams' (axis along the build direction) and inclined beams' diameters; in fact, as already verified in the previous chapters, beams diameter of lattices produced with SLM technology can change according to the inclination with respect to the build direction. To limit random measurement errors due to the operator, measurements were repeated twice at different points on the sample (Figure 4.10); beams diameter is measured four times for each specimen, for a total of 820 measurements.

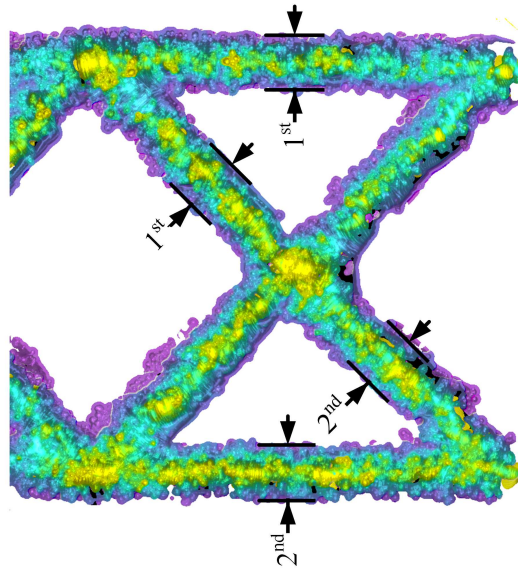


Figure 4.10: Beams diameter measurement with 3D optical profilometer

The same data set used to determine beams' diameters was used to estimate the surface roughness; as before, surface inclination was eliminated using the appropriate filter integrated in the SensoVIEW software. To estimate roughness, a section plane parallel to the beam's axis was identified, then the surface's profile was extracted and arithmetical mean deviation of the assessed profile was calculated. According to the ISO4288: 1996 standard, in case of surfaces with  $R_a$  between 2 and 10 microns, typical of components produced by SLM technology, the evaluation length should be 12.5 mm [101]. However, the size of the specimens under study limits the average profile length available for measurements to 2500  $\mu\text{m}$ . A  $\lambda_c = 2.5$  mm cut-off length, suitable to characterize surfaces produced with SLM or Electron Beam Melting (EBM) technologies when non-contact 3D optical instruments are used, is applied [102]. To calculate the mean roughness of the profile  $R_{a(2500)}$ , the following equation applies:

$$R_{a(2500)} = \frac{1}{N} \sum_{i=1}^n |y_i| \quad (4.1)$$

where  $n$  is the number of data points and  $y$  the surface height with respect to the mean line.

It is important to remember that roughness values obtained are relative to the measurement length and to the cut-off filter used. Measurements were repeated twice for each sample and the position of the section planes used to estimate roughness is shown in Figure 4.11. Evaluation length is equal to 2.5 mm ( $L_1 = L_2$ ).

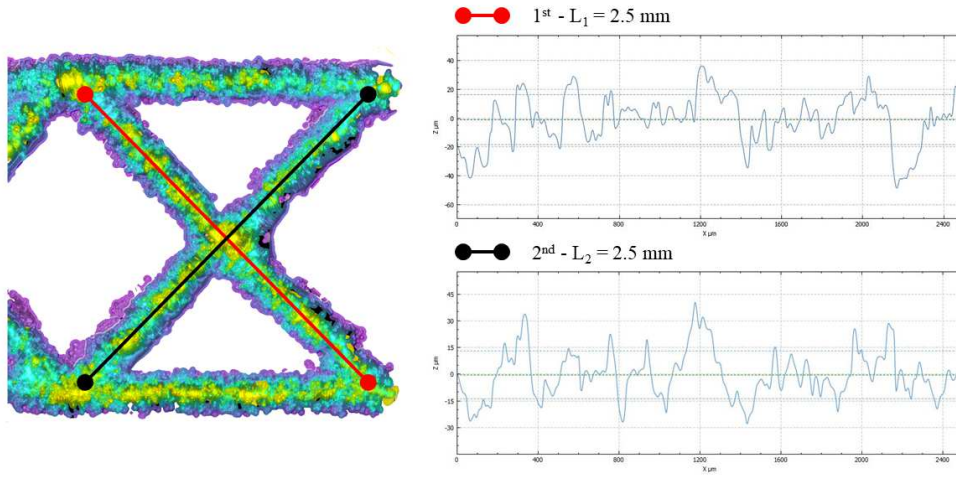


Figure 4.11: Beams roughness measurement with 3D optical profilometer

Therefore, acquired data were imported and processed in MATLAB environment. To observe the effect of SLM process parameters variation on lattice beams' diameter, acquired data were grouped according to laser spot diameter obtaining the graphs of Figure 4.12. In general, process parameters combinations corresponding to laser's spot diameters smaller than 200  $\mu\text{m}$  generated beams with larger diameter compared to that of the spot, especially for inclined beams. This phenomenon suggests that process parameters combination used for spots lower than 200  $\mu\text{m}$  correspond to excessive amounts of energy, which caused melt pool and HAZ size increase; moreover, the strong dispersion of inclined beams' diameters indicates that small variations of process parameters are linked to big diameter variations, suggesting the presence of melt pool instability phenomena. Obtained lattices are characterized by vertical beams' diameters dissimilar to those of horizontal ones and reduced cell porosity (high fill ratio). Process parameters combinations corresponding to spot diameters greater than 450  $\mu\text{m}$  show an opposite trend: generally, beams diameter is lower than that of the spot. This result suggests that supplied energy is insufficient and therefore the melt pool is small, these conditions favour the possibility of obtaining lattices with sub-optimal mechanical properties.

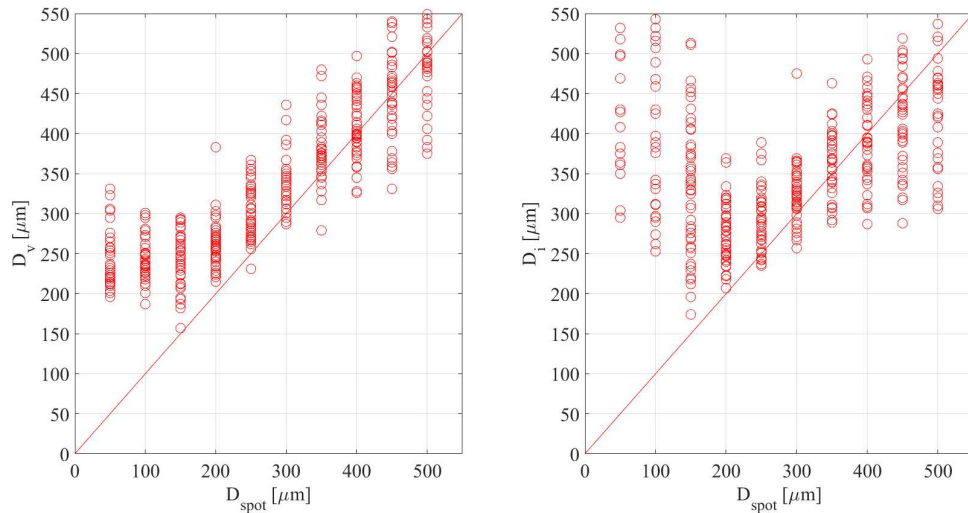


Figure 4.12: Vertical and inclined beams diameter variation – grouping variable: spot diameter

Looking at boxplot in Figure 4.13 it is clear that for laser's spots smaller than 200  $\mu\text{m}$ , vertical beams' diameter is dissimilar from that of inclined ones. This suggests that, in general, process parameters combinations chosen are outside the optimal process window since the energy supplied is excessive.

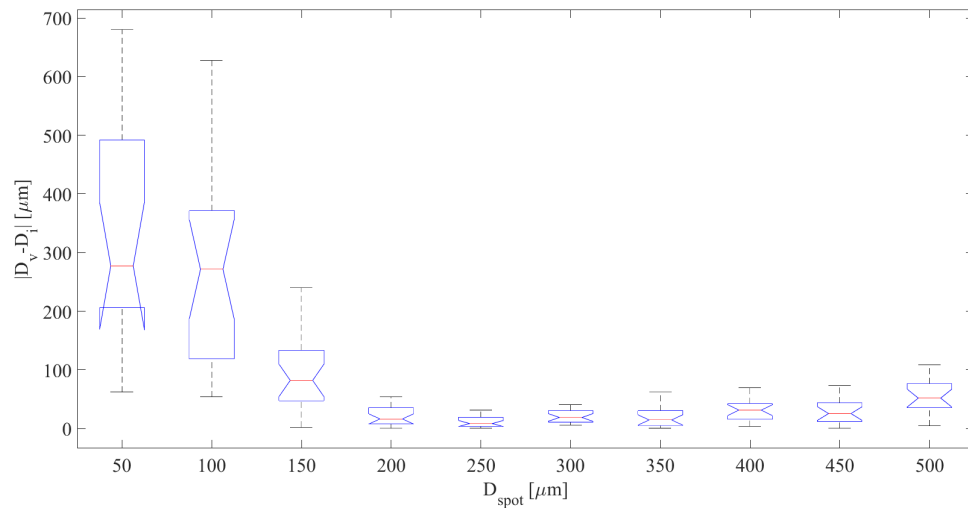


Figure 4.13: Absolute difference between vertical and inclined beams diameter - grouping variable: spot diameter

Observing the scatterplots of Figure 4.14 it is possible to evaluate the existence of possible trends that indicate the influence of one or more factors (power, speed, laser spot diameter) on the diameter of vertical and inclined beams; the data suggest that power and spot diameter have an influence on beams' diameter, while the effect of scanning speed variation is unclear. An increase of power or spot diameter corresponds to an increase

of beams' diameter. However, for spot diameters lower than 150  $\mu\text{m}$  it is noted that as the spot increases inclined beams' diameter decreases; therefore, for small spot diameters the trend is reversed due to the supplied energy excess already mentioned before.

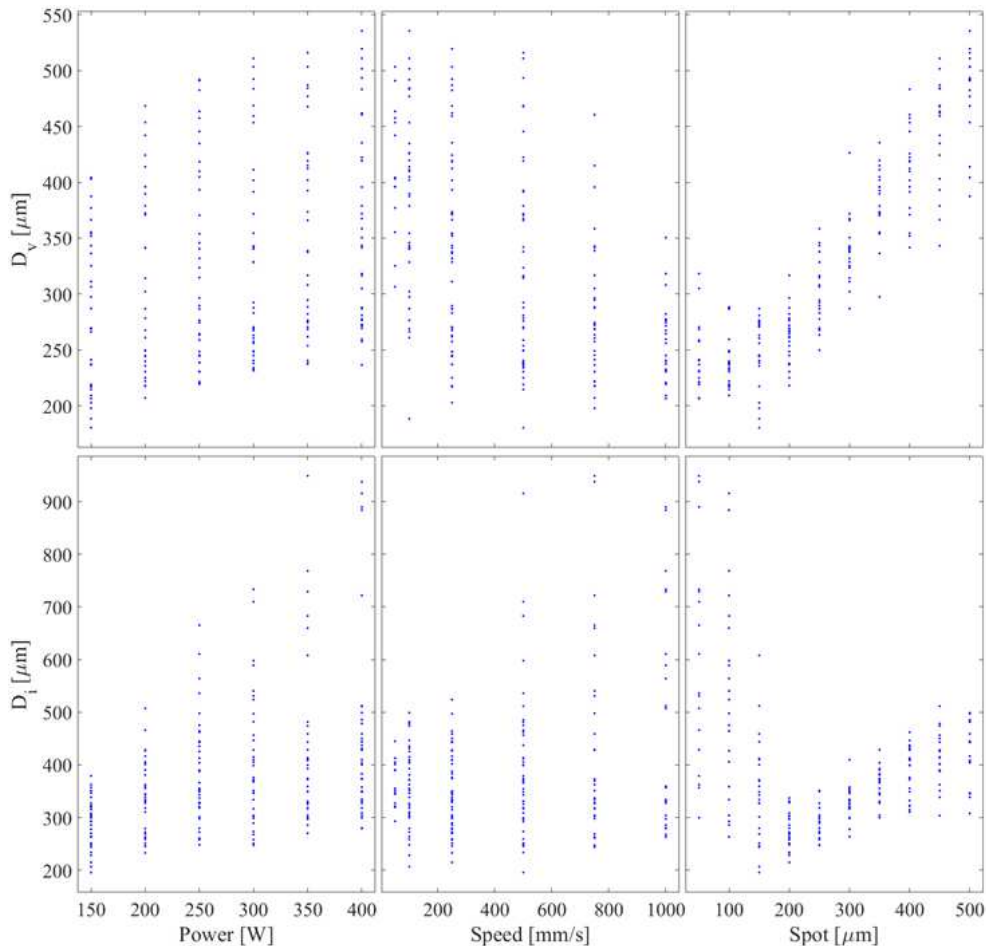


Figure 4.14: Vertical and inclined beams diameters vs power, scan speed and spot size

In order to evaluate the effect of power, scanning speed and spot diameter on vertical and inclined beams diameters an ANOVA was carried out. As specified before, chosen factors and levels do not allow to define a full factorial DoE; therefore, before executing the ANOVA, a subset of factors levels that identifies a full factorial DoE is chosen. The identified data set corresponds to the central part of the DoE, which coincides with the zone where the manufacturing process appears to be more stable. Considering the subset of the data identified as above, the ANOVA was carried out on the vertical and inclined beams diameters values using power, scanning Speed and spot diameter as factors. Results, summarized in Table 4.2 and Table 4.3, show that power and spot diameter are statistically significant whereas scanning speed is not. This latter result confirms previous observations. In general, interactions between factors are not statistically significant, except in the case of the interaction between power and spot diameter for inclined beams.

Table 4.2: ANOVA of vertical beams diameter vs power, scanning speed and spot size

| Factor             | Sum Sq.  | DOF | MS      | F     | p-value |
|--------------------|----------|-----|---------|-------|---------|
| <b>Power</b>       | 14703,9  | 4   | 3675,97 | 10,57 | 0       |
| <b>Speed</b>       | 440,3    | 3   | 146,77  | 0,42  | 0,7387  |
| <b>Spot</b>        | 29954,6  | 3   | 9984,86 | 28,72 | 0       |
| <b>Power*Speed</b> | 3666,4   | 12  | 305,53  | 0,88  | 0,5775  |
| <b>Power*Spot</b>  | 4514,3   | 12  | 376,19  | 1,08  | 0,4145  |
| <b>Speed*Spot</b>  | 7031     | 9   | 781,22  | 2,25  | 0,0532  |
| <b>Error</b>       | 8690,6   | 25  | 347,63  |       |         |
| <b>Total</b>       | 110833,6 | 68  |         |       |         |

Table 4.3: ANOVA of inclined beams diameter vs power, scanning speed and spot size

| Factor             | Sum Sq.  | DOF | MS      | F     | p-value |
|--------------------|----------|-----|---------|-------|---------|
| <b>Power</b>       | 29998    | 4   | 7499,5  | 4,83  | 0,005   |
| <b>Speed</b>       | 2848,9   | 3   | 949,6   | 0,61  | 0,6136  |
| <b>Spot</b>        | 78072,4  | 3   | 26024,1 | 16,77 | 0       |
| <b>Power*Speed</b> | 20932,6  | 12  | 1744,4  | 1,12  | 0,385   |
| <b>Power*Spot</b>  | 49709,1  | 12  | 4142,4  | 2,67  | 0,0185  |
| <b>Speed*Spot</b>  | 15989,2  | 9   | 1776,6  | 1,14  | 0,3701  |
| <b>Error</b>       | 38794,7  | 25  | 1551,8  |       |         |
| <b>Total</b>       | 276453,2 | 68  |         |       |         |

To model the relationship between beam's diameter and process parameters (DoE factors - power, scan speed and spot diameter) a linear regression was performed. The ANOVA allowed to establish that scan speed has a negligible effect on beams' diameter, therefore linear regression is performed neglecting it. Observing scatterplots of beams' diameters as a function of power and spot diameter it is possible to observe a clear trend variation when the diameter of the spot is lower than 200  $\mu\text{m}$  (Figure 4.15); this suggests that physical phenomena occurring when the spot is small are different compared to those for larger spots. This effect may be due to an excess of supplied energy for the combinations of process parameters chosen for small spots. To take into account the different behaviour that occurs for small spot diameters, the analysis was subdivided according to the spot size, obtaining two different mathematical models useful for calculating beams' diameter as a function of power and spot diameter.

Using vertical beams' diameter as response variable, power and spot diameter as predictors, mathematical models useful for vertical beams' diameter estimation were obtained by linear regression. The first model is related to spot diameters lower than 200  $\mu\text{m}$  while the second is relative to spots up to 500  $\mu\text{m}$ :

$$D_{v(s<200)} = \beta_1 + \beta_2 P + \beta_3 s + \beta_4 s^2 \quad (4.2)$$

$$D_{v(s\geq 200)} = \beta_1 + \beta_2 P + \beta_3 s + \beta_4 P s + \beta_5 P^2 \quad (4.3)$$

where P, s are power and spot diameter respectively.

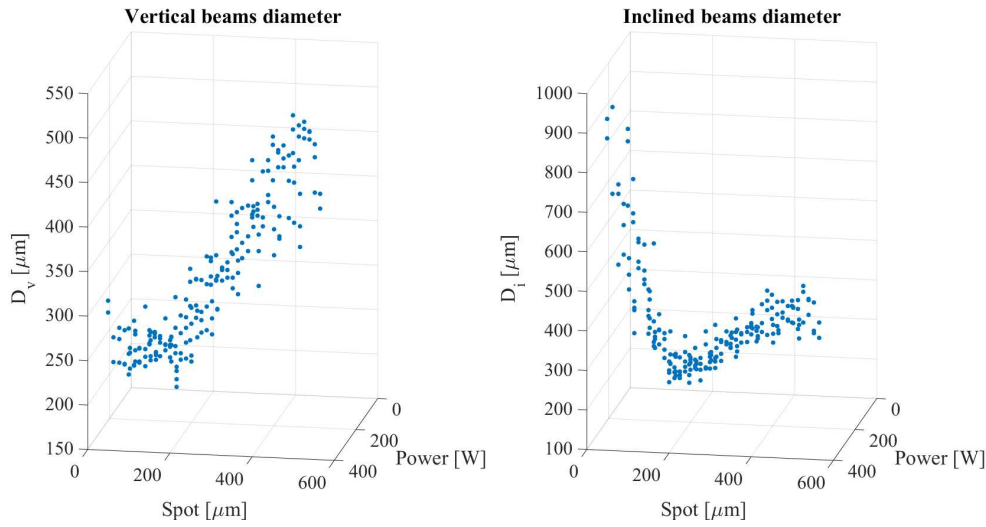


Figure 4.15: Scatterplots of beams' diameters as a function of power and spot diameter

Similarly, using inclined beams' diameter as response variable, power and spot diameter as predictors, mathematical models useful for vertical beams' diameter estimation were obtained by linear regression:

$$D_{i(s<200)} = \beta_1 + \beta_2 P + \beta_3 s + \beta_4 P s \quad (4.4)$$

$$D_{i(s \geq 200)} = \beta_1 + \beta_2 P + \beta_3 s + \beta_4 P s + \beta_5 P^2 \quad (4.5)$$

Estimated values of mathematical models  $\beta$  coefficients are shown in Table 4.4.

Table 4.4: Estimated values of linear regression models  $\beta$  coefficients - diameters

|                     | $\beta_1$ | $\beta_2$ | $\beta_3$ | $\beta_4$ | $\beta_5$ |
|---------------------|-----------|-----------|-----------|-----------|-----------|
| $D_{v(s<200)}$      | 203,0232  | 0,221181  | -0,40565  | 0,001944  | N.A.      |
| $D_{v(s \geq 200)}$ | 91,15268  | 0,334079  | 0,42297   | 0,001088  | -0,00077  |
| $D_{i(s<200)}$      | -116,171  | 3,244332  | 1,39564   | -0,01456  | N.A.      |
| $D_{i(s \geq 200)}$ | 111,1814  | 0,518947  | 0,209987  | 0,001184  | -0,00108  |

Figure 4.16 shows the distribution of vertical and inclined beams diameters with respect to power and spot diameter and the surfaces that represent the mathematical models obtained by linear regression.

Using a non-linear regression model, in some cases it is possible to obtain mathematical models that satisfactorily describe the phenomenon under examination; furthermore, they can facilitate the physical interpretation of the mathematical model.

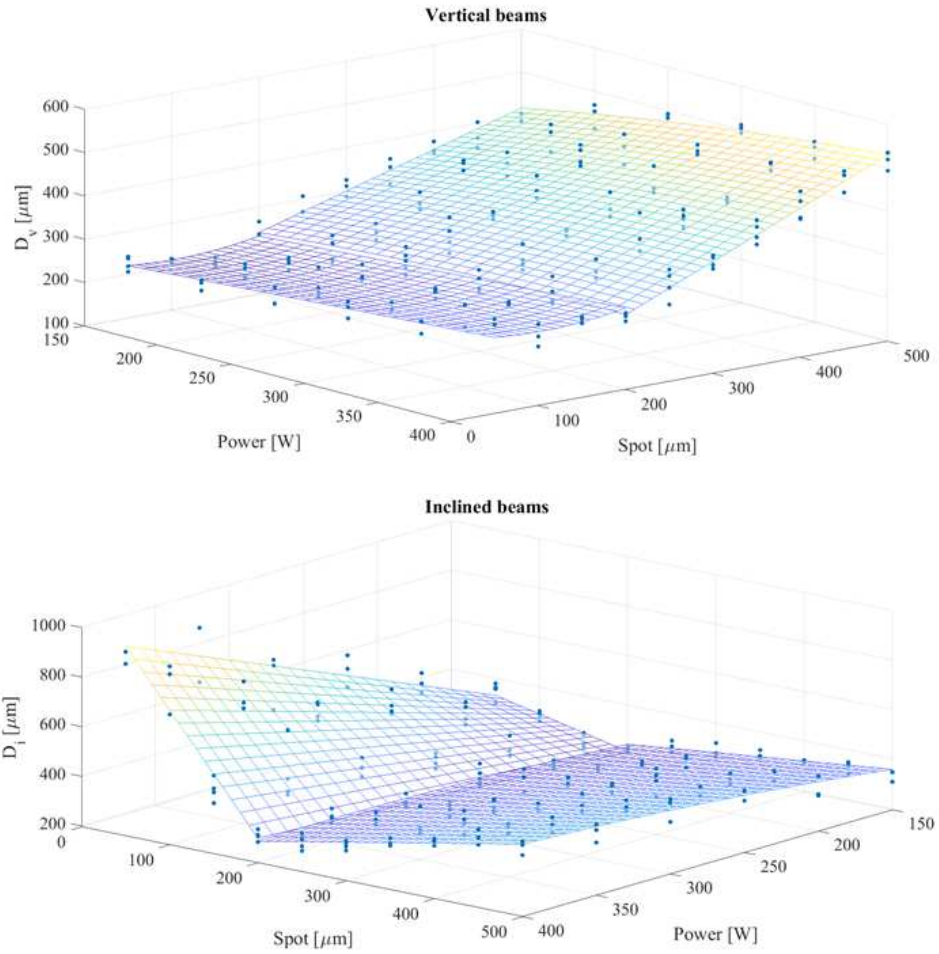


Figure 4.16: Distribution of vertical and inclined beams diameters and mathematical models surfaces (linear regression)

Applying this approach, four mathematical models expressed as below were obtained:

$$D = e^{\beta_1} P^{\beta_2} S^{\beta_3} \tag{4.6}$$

where D is vertical or inclined beams diameter.

Estimated values of mathematical models  $\beta$  coefficients are shown in Table 4.5.

Table 4.5: Non-linear regression models  $\beta$  coefficients - diameters

|                    | $e^{\beta_1}$ | $\beta_2$ | $\beta_3$ |
|--------------------|---------------|-----------|-----------|
| $D_{v(s<200)}$     | 58,7841       | 0,2325    | 0,0307    |
| $D_{v(s\geq 200)}$ | 2,6025        | 0,1943    | 0,6634    |
| $D_{i(s<200)}$     | 101,316       | 0,7572    | -0,6006   |
| $D_{i(s\geq 200)}$ | 4,4783        | 0,2479    | 0,5102    |

Beams' diameter depends on the product of power and spot diameter; when one of the two parameters increases, the diameter also increases. For inclined beams and small spot diameter ( $s < 200 \mu\text{m}$ ), beams' diameter depends on the ratio between power and spot diameter; in this case, physical phenomena developing during the manufacturing process are different and therefore, unlike previous cases, when spot diameter grows inclined beams' diameter decreases. This effect can be explained by the fact that for small spots energy supplied is quite high, thus evaporation and instability of the melt pool (e.g. keyhole) phenomena are triggered favouring HAZ depth growth; therefore, big diameter inclined beams and lattice's pores closure have to be expected. This phenomenon is attenuated when spot diameter increases.

Figure 4.17 shows the distribution of vertical and inclined beams' diameters with respect to power and spot diameter and the surfaces that represent the mathematical models obtained by non-linear regression.

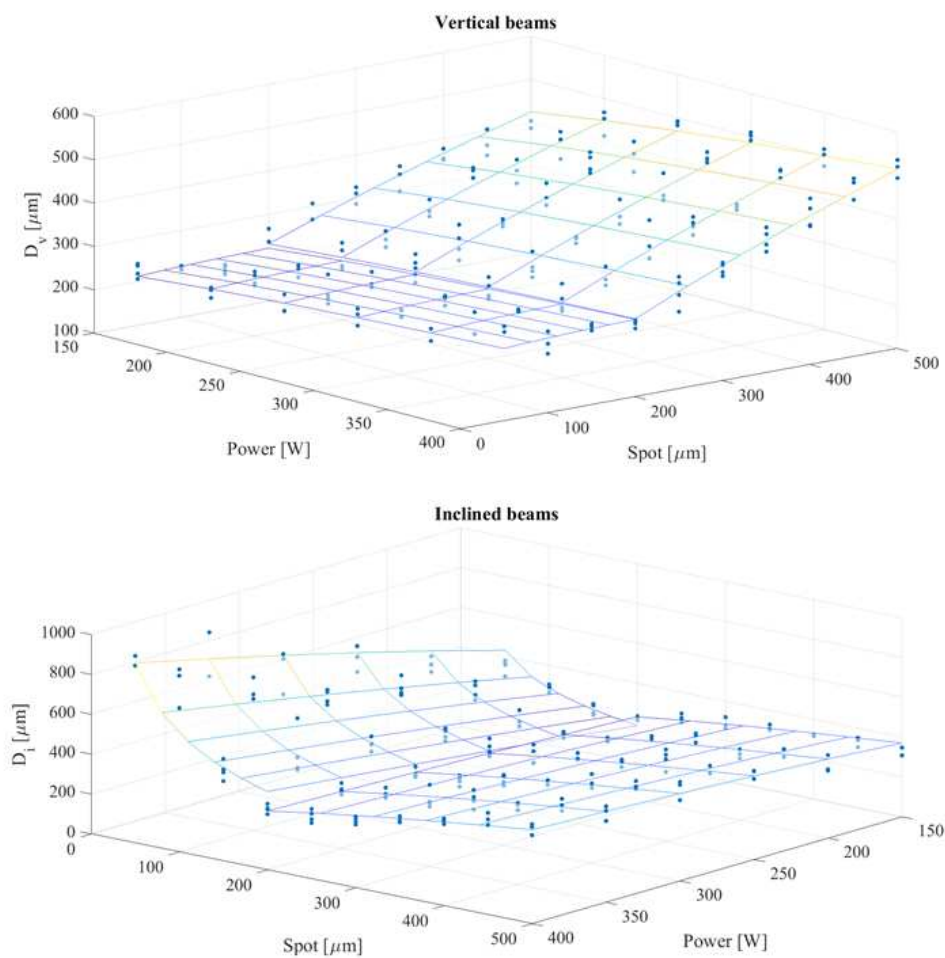


Figure 4.17: Distribution of vertical and inclined beams diameters and mathematical models surfaces (non-linear regression)



To understand the effect of SLM process parameters variation (power, scanning speed and spot diameter) on specimens' surface roughness, the data acquired using the 3D optical profilometer were imported and analysed in MATLAB environment. To check whether the individual process parameters have an influence on the surface roughness it is possible to observe the scatterplots in Figure 4.18; trends suggest that spot size has a significant influence on surface roughness, while the effect of power and scanning speed is less obvious.

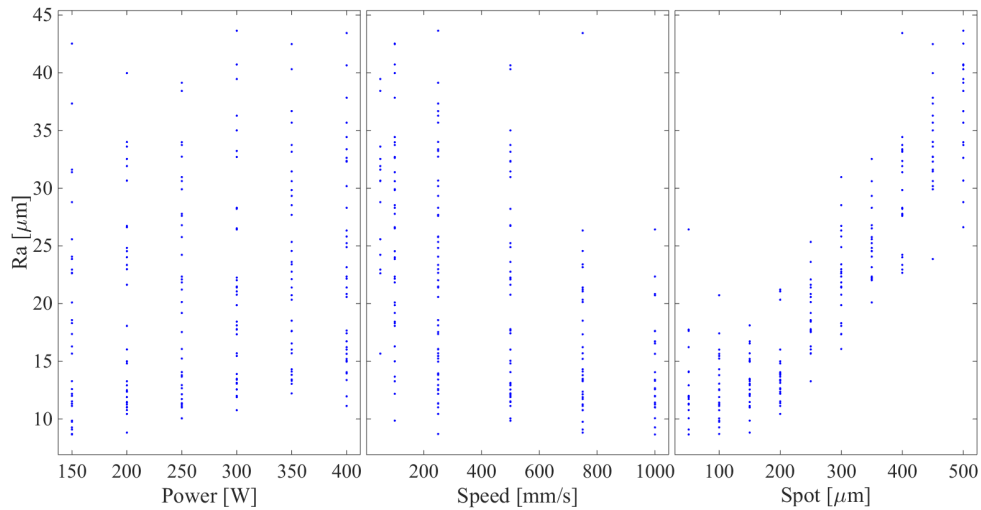


Figure 4.18: Surface roughness vs power, scanning speed and spot diameter

An ANOVA was performed to evaluate the effect, from a statistical point of view, of SLM process parameters on surface roughness. Similarly to what was been done for the analysis concerning beam diameters, before executing the ANOVA, a subset of factors levels identifying a full factorial DoE is chosen. Considering the identified subset of data, the ANOVA was carried out on surface roughness values using power, scanning speed and spot diameter as factors. Results, summarized in Table 4.6, show that spot diameter has a statistically significant effect on surface roughness whereas power and scanning speed have not. This latter result confirms previous observations. Interactions between factors are not statistically significant.

Table 4.6: ANOVA surface roughness vs power, scanning speed and spot size

| Factor             | Sum Sq. | DOF | MS      | F     | p-value |
|--------------------|---------|-----|---------|-------|---------|
| <b>Power</b>       | 66,92   | 4   | 16,731  | 2,09  | 0,1124  |
| <b>Speed</b>       | 44,23   | 3   | 14,744  | 1,84  | 0,1656  |
| <b>Spot</b>        | 417,64  | 3   | 139,213 | 17,38 | 0       |
| <b>Power*Speed</b> | 99,77   | 12  | 8,314   | 1,04  | 0,4471  |
| <b>Power*Spot</b>  | 91,63   | 12  | 7,636   | 0,95  | 0,5143  |
| <b>Speed*Spot</b>  | 111,42  | 9   | 12,379  | 1,55  | 0,1865  |
| <b>Error</b>       | 200,22  | 25  | 8,009   |       |         |
| <b>Total</b>       | 1635,63 | 68  |         |       |         |

To model the relationship between surface roughness and process parameters a linear regression was performed. Using surface roughness as response variable, power, scan speed

and spot diameter as predictors, the mathematical model useful for roughness prediction is expressed in the following form:

$$R_a = \beta_1 + \beta_2 P + \beta_3 s + \beta_4 s^2 \tag{4.7}$$

Estimated values of mathematical models  $\beta$  coefficients are shown in Table 4.7.

Table 4.7: Estimated values of linear regression models  $\beta$  coefficients - roughness

|       | $\beta_1$ | $\beta_2$ | $\beta_3$ | $\beta_4$ |
|-------|-----------|-----------|-----------|-----------|
| $R_a$ | 7,08976   | 0,017632  | -0,0006   | 0,000105  |

Figure 4.19 shows the distribution of surface roughness with respect to power and spot diameter and the surface that represent the mathematical model obtained by linear regression.

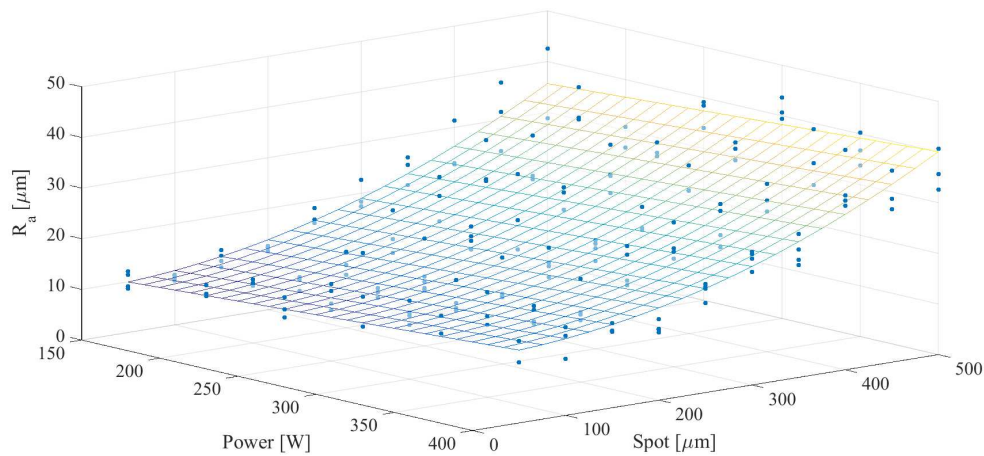


Figure 4.19: Distribution of surface roughness and mathematical model surface (linear regression)

Surface roughness increases with spot size, this phenomenon could be explained by two hypotheses. When the spot size decreases, the intensity profile of the Gaussian beam is narrower and steeper; therefore, the part of the Gaussian profile where the intensity is insufficient to guarantee an optimal process is narrower compared to when the spot is larger. Moreover, with smaller spots the transition between high and low intensity zones is faster, allowing to obtain a neat “spot contour”. Small spot diameter favours the production of lower surface roughness specimens since sintering phenomena at the spot’s edge and adhesion of partially melted metal particles are limited. Another phenomenon that can explain surface roughness rise when spot diameter increases is the hypothesis that the combinations of SLM process parameters chosen for larger spots do not provide enough energy, causing generalized sintering phenomena. The phenomena described so far can be better explained by looking at Figure 4.20, which shows the intensity profile of

a Gaussian laser beam calculated with the equation below.

$$I(r) = \frac{2P}{\pi s_r^2} e^{-2(\frac{r}{s_r})^2} \quad (4.8)$$

where P,  $s_r$  and r are power, spot radius and actual radius respectively.

The blue line shows the profile of a beam with power equal to 250 W and a spot diameter equal to 500  $\mu\text{m}$  while the red one with power equal to 150 W and spot diameter equal to 300  $\mu\text{m}$ ; the two combinations of process parameters were chosen among those of the DoE with the same VED. When the spot diameter is smaller, the maximum beam intensity is higher and the low intensity portion of the beam is less extensive.

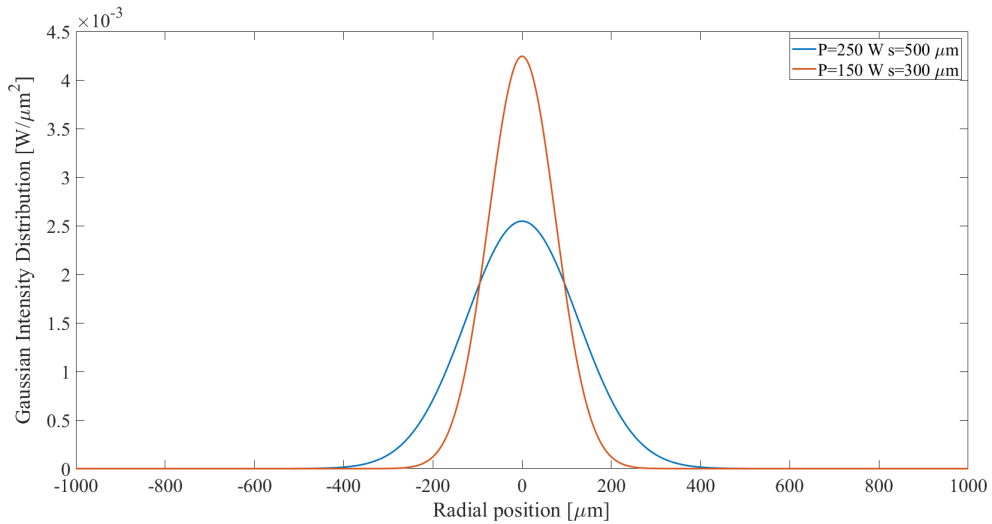


Figure 4.20: Example of intensity profile of a Gaussian laser beam

The surface roughness tends to grow slightly with power, this may be due to HAZ's depth increase and melt pool's turbulent phenomena which favour undesired adhesion of metal particles. Using a non-linear regression model, surface roughness variation as a function of power and spot diameter is expressed by the following relation:

$$R_a = e^{\beta_1} P^{\beta_2} s^{\beta_3} \quad (4.9)$$

where  $R_a$  is the surface roughness, P is power and s is spot diameter.

Using nonlinear regression, a better result is obtained subdividing the analysis according to the spot size; two different mathematical models with different  $\beta$  coefficients are obtained. Estimated values of mathematical models  $\beta$  coefficients are shown in Table 4.8.

Table 4.8: Non-linear regression models  $\beta$  coefficients - roughness

|                    | $e^{\beta_1}$ | $\beta_2$ | $\beta_3$ |
|--------------------|---------------|-----------|-----------|
| $R_{a(s<200)}$     | 1,4517        | 0,379     | 0,0195    |
| $R_{a(s\geq 200)}$ | 0,0224        | 0,1781    | 1,0311    |

For spot diameters smaller than 200  $\mu\text{m}$  surface roughness mainly depends on the power while for larger diameters spot diameter is more relevant. This result reinforces previous speculations. For small spots the energy supplied is enough to ensure metal powders fusion, however as the power supplied increases the roughness increases slightly due to the instability phenomena that occur in the melt pool and to the greater extension of the HAZ. For larger spots the roughness mainly depends on spot size since the energy supplied and the intensity profile of the Gaussian beam favour sintering phenomena.

Figure 4.21 shows the distribution of surface roughness with respect to power and spot diameter and the surfaces that represent the mathematical models obtained by non-linear regression.

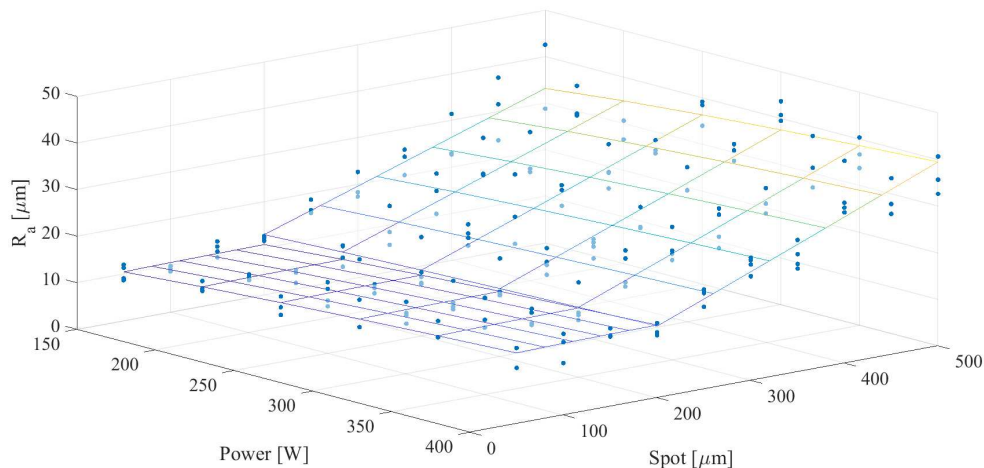


Figure 4.21: Distribution of surface roughness and mathematical models surfaces (non-linear regression)

### 4.3.5 Optimized process parameters

Analysing the results obtained in the previous paragraph it is possible to isolate the combinations of process parameters that allow to obtain FBCCZ lattices with adequate dimensional accuracy and surface roughness. To establish the limit beyond which the surface roughness becomes excessive, suggesting the possible triggering of sintering phenomena, roughness measurements are performed on a SLM manufactured reference lattice specimen. The geometry of the reference specimen is similar to that of the DoE's specimens produced starting from the simplified 3D model; the lattice section is made by circular

cross-section beams with diameter equal to 0.4 mm, five 2 mm-wide FBCCZ unit cells positioned along the build direction. Reference specimen's surface roughness measurement was carried out employing the same experimental set-up used to perform the measurements in the previous paragraph; moreover, the evaluation length and the cut-off filter are the same. Figure 4.22 shows the reference specimen during roughness measurement, the surface's map obtained and a roughness profile.

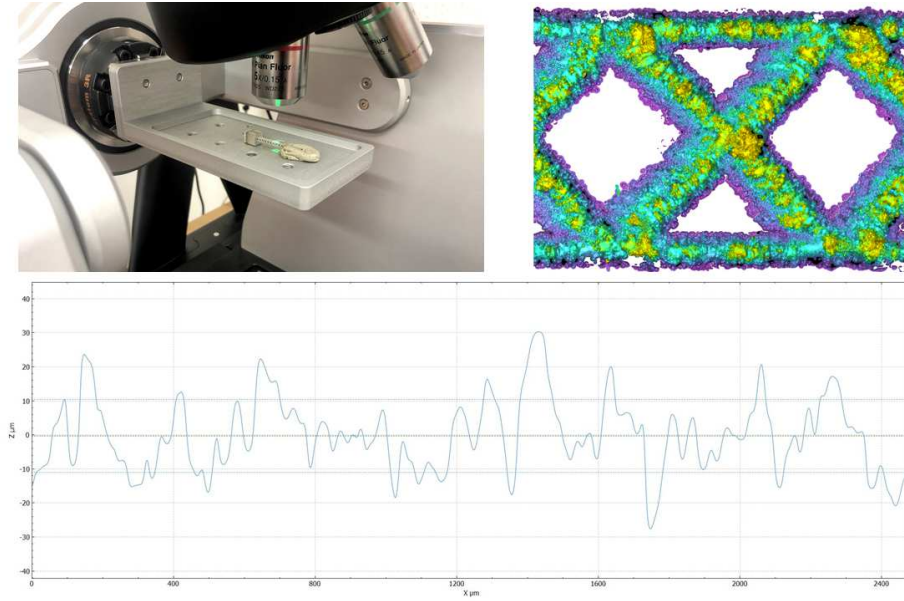


Figure 4.22: Reference specimen's surface roughness measurement

The surface roughness of the reference specimen is equal to:

$$R_{a(2500)} = \frac{1}{n} \sum_{i=1}^n |y_i| = 8,49 \mu\text{m} \quad (4.10)$$

However, it is not possible to compare this value with those obtained for the DoE's specimens examined in the previous paragraph since the scanning strategy used to manufacture them is different. Comparing specimens manufactured with the conventional scanning strategy with DoE's specimens under investigation, it is estimated that the surface roughness of the latter is, in general, two or three times greater. Therefore, the limit beyond which the roughness is considered excessive, suggesting sub-optimal manufacturing process conditions, is set equal to 20  $\mu\text{m}$ . This last consideration is confirmed by measuring the roughness of a lattice specimen identical to that of Figure 4.22, produced by eliminating the contour from the layer scanning strategy; Figure 4.23 shows roughness measurement set-up, surface's map obtained and a roughness profile. Surface roughness of the modified specimen (no contour) is equal to 16,7  $\mu\text{m}$ ; the limit beyond which the roughness is considered excessive is therefore confirmed.

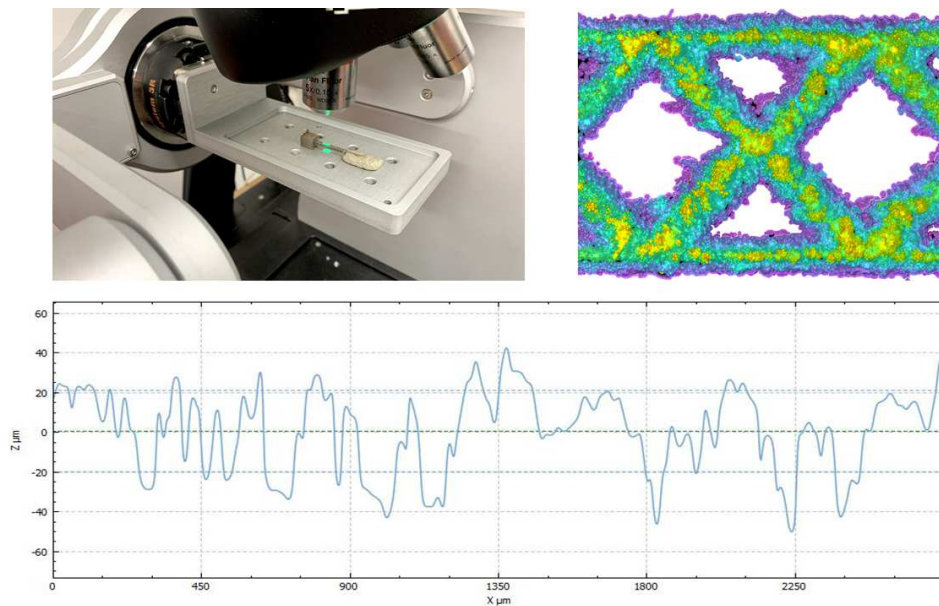


Figure 4.23: Modified reference specimen's surface roughness measurement (no contour)

To ensure optimal dimensional accuracy, only the combinations of process parameters that guarantee the production of lattices where the percentage difference between the average diameter of inclined and vertical beams is less than 20% are considered adequate. Considering the 205 SLM process parameters combinations analysed, only 44 satisfy the constraints defined above. Scatterplot showing the distribution of the identified process parameters, as a function of scanning speed, power and spot diameter, is shown in Figure 4.24.

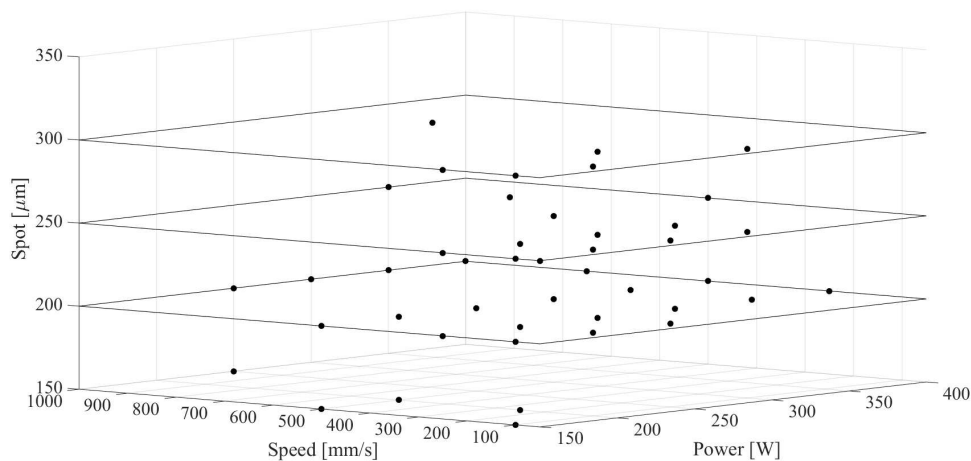


Figure 4.24: Scatterplot of satisfactory process parameters combinations

Process parameters satisfying constraints defined above have spot diameter comprised between 190  $\mu\text{m}$  and 350  $\mu\text{m}$ , suggesting the need to extend the investigation to assess the existence of process parameters combinations that allow the production of lattices having very small or millimetric sized beams.

To facilitate the choice between the identified parameters, Figure 4.25 shows the average diameter and the surface roughness associated with each parameter. The combinations of SLM process parameters identified, which allow to obtain lattice structures made starting from a simplified 3D model with satisfactory surface roughness and dimensional accuracy, permit the realization of lattices with beam's diameter comprised between 190  $\mu\text{m}$  and 350  $\mu\text{m}$ .

To identify combinations of SLM process parameters that allow the creation of lattices with larger or smaller beam's diameter, it is necessary to extend the experimental plan; some hypotheses useful for additional DoE planning can be gathered by observing the mathematical models previously obtained. To produce small diameter beams it would be convenient to investigate the combinations of process parameters with power lower than 150 W, while to obtain beams with millimetric diameter without triggering sintering phenomena, having already investigated high-power parameters, it would be interesting to consider lower scanning speeds.

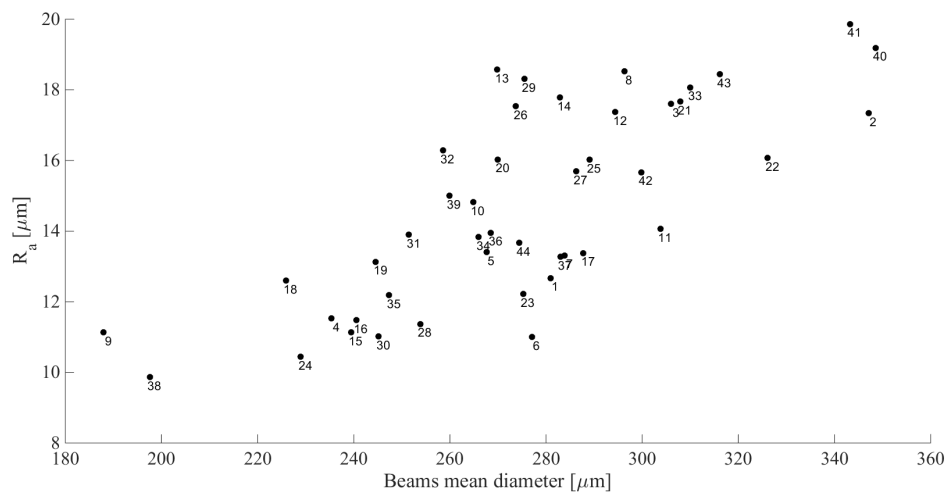


Figure 4.25: Beams diameter and surface roughness of satisfactory process parameters combinations

Appendix 3 summarizes identified combinations of process parameters and the respective values of beam's diameter and surface roughness.

## 4.4 Conclusions

In this chapter, an innovative methodology for design and manufacturing of lattice / porous structures was presented. As anticipated in previous chapters, these structures are useful to design parts with excellent stiffness-to-weight ratio and to obtain point by point tuneable mechanical properties; moreover, it has been verified that lattice structures have good damping properties allowing to enhance the performances of all those systems affected by unwanted vibrations. The study concerning the proposed methodology was created with the aim of making design and manufacturing of these structures faster and more efficient. To achieve this goal, a simplified three-dimensional model of the structure to be produced is generated using a specially designed MATLAB tool. The simplified 3D model allows to proceed with SLM process design phase and slicing using conventional software tools, granting a rapid implementation of the methodology even in industrial environments.

In order to confirm the feasibility of the proposed methodology and to verify advantages and disadvantages, a DoE conceived to study the effect of main SLM process parameters variation on geometry and surface roughness of FBCCZ lattice structures was carried out.

A total of 205 specimens were produced with different process parameter combinations. After having acquired measurements to characterize specimens' geometry and roughness, mathematical models useful for geometry and surface roughness estimation have been developed; data analysis allowed to elaborate hypotheses to correlate some macroscopic phenomena with physical phenomena occurring during the production process, helping to understand the effect of process parameters variation.

Main results are reported below:

- Process parameters combinations corresponding to spot diameters smaller than 200  $\mu\text{m}$  generated beams with larger diameter compared to that of the spot. Energy excess caused melt pool and HAZ size increase.
- The effect of power, scanning speed and spot diameter on vertical and inclined beams diameters was assessed with ANOVA. Power and spot diameter were statistically significant whereas scanning speed was not. Similarly, evaluating the effect of SLM process parameters on surface roughness it was assessed that only spot diameter had a statistically significant effect.
- Beams' diameter depends on the product of power and spot diameter; when one of the two parameters increases, the diameter also increases. Nevertheless, for inclined beams and small spot diameter ( $s < 200 \mu\text{m}$ ), beams' diameter depends on the ratio between power and spot diameter. Hence, for small spots energy supplied



is quite high, thus evaporation and instability of the melt pool (e.g. keyhole) phenomena are triggered favouring HAZ depth growth; therefore, big diameter inclined beams and lattice's pores closure have to be expected. Surface roughness increases with spot size. This latter phenomenon could be explained observing Gaussian beam intensity profile.

- Process parameters combinations that meet appropriate requirements in terms of dimensional accuracy and surface roughness were identified, allowing the immediate applicability of the proposed methodology for rapid production of FBCCZ type lattice structures with unit cell size equal to 2 mm.
- The newly designed method allows substantial time savings in the 3D model design phase and in the subsequent slicing and manufacturing phases. The simulations carried out indicate that this advantage grows rapidly with the number of unit cells that make up the lattice to be produced. Shortening the time required to produce the finished product up to over 40%, a substantial economic benefit can be obtained.



## Chapter 5

# CONCLUSIONS AND FUTURE WORK

In this thesis an in-depth study about lattice structures produced with SLM technology was carried out. The research covered aspects related to design, production and mechanical characterization of these structures. The mechanical properties of different types of lattice structures were investigated with the aim of verifying the performance advantage in terms of vibration damping with respect to full density equivalent and developing a generalized methodology for the characterization of lattice porous structures. Furthermore, an innovative methodology for design and manufacturing of small-sized lattice porous structures was developed with the aim of mitigating the problems that occur during the design and production phases of these structures, allowing savings in terms of time and costs.

A comprehensive literature review to acquire a solid knowledge base regarding AMT for metals, DfAM, structural optimization and lattice porous structures was carried out. Particular attention was given to the SLM technology, with an in-depth study on physical phenomena governing the manufacturing process and on materials properties. Moreover, an in-depth review on state of the art regarding lattice / porous structures allowed to investigate thoroughly their geometrical, topological and mechanical properties and design rules. From the literature review the following conclusions can be drawn:

- Among AMTs for metals, the SLM technology allows the production of components having mechanical properties comparable to those of parts obtained through subtractive manufacturing technologies. Moreover, SLM allows to obtain parts of complex geometry without a negative impact on design and production phases. Therefore, the SLM technology is the best choice for the creation of high-performance

components obtained through structural optimization and for the production of lattice porous structures.

- The physical phenomena that develop during the production process significantly affect mechanical and geometrical characteristics of components made using SLM technology. Therefore, adequate knowledge of these phenomena and process parameters optimization are of fundamental importance.
- DfAM techniques and structural optimization are useful tools for the design of high-performance parts that fully exploit AMT's advantages.
- Lattice structures can be exploited as high-performance structural or filler materials, having an important role for the design of high added-value mechanical components. With respect to full density equivalent, improvements in terms of stiffness to weight ratio and vibration reduction are expected.
- Lattice's unit cells characteristics, in terms of topology and geometry, that allow to enhance manufacturability (no need for supports) and potentially damping properties, have been identified.
- Lack of exhaustive studies investigating static and dynamic behaviour of lattice porous structures produced with SLM technology, has been identified; therefore, filling this cognitive gap could be of scientific interest.

Static and dynamic behaviour of different kinds of lattices, made of AlSi10Mg aluminium alloy and 316L austenitic stainless steel, were investigated by means of two experimental campaigns. A total of 10 aluminium specimens and 24 steel specimens were designed, manufactured and measured. Assessment of lattice's performance advantage in terms of vibration damping with respect to full density equivalent and evaluation of lattice's geometry variation effect on its properties were the main goals. Following conclusions can be drawn from the analysis of the experimental campaigns results (unless specified, results are valid for both aluminium and steel specimens):

- Measurements performed with the optical microscope evidenced that the specimens had inhomogeneous characteristics. Struts size and surface finish were influenced by the variability of the SLM process; in particular, position of the object in the build volume, unwanted adhesion of partially melt powders and stochastic phenomena typical of the SLM process affected the printing result. Nevertheless, although the printing accuracy, especially for smaller unit cells, was lower than expected due to the SLM process limitations, repeatability was statistically good.
- Analysing the SLM-manufactured lattices geometry it was possible to assess a lack of homogeneity between the nominal (CAD) and the as-built geometry; in particular, inclined beams (with respect to the build direction) diameter was greater than

that of the vertical ones. This phenomenon is mainly due to undesired adhesion of partially melt metal powders affecting overhanging surfaces.

- The lack of homogeneity between CAD and as-built specimens' geometries, negatively affected accuracy of results obtained from FE simulations performed starting from the nominal CAD model.
- Measured compliance values of specimens integrating lattice structures were lower than those calculated by means of FEA. FEA tended to overestimate lattices compliance especially for specimens with smaller cell size (i.e. C and D); this phenomenon occurred because SLM process limitations were not taken into account (e.g. inhomogeneity between nominal and as-built lattice's geometry).
- FEA results accuracy was improved by means of a FE model that simulates the real lattice's geometry; as-built lattices geometry was studied and appropriate factors for nominal beams diameter correction were estimated and applied.
- Calculation time and computational effort required to perform FE simulations was significantly reduced, exploiting 1D-element meshing for the specimens' lattice section.
- Specimens dynamic behaviour assessment, performed using the Pulse Test technique, showed that lattices damping properties are significantly better than those of the equivalent solid material.
- Analysing average values, the lattice's geometric configuration with the best damping characteristics is the C specimen's one, characterized by a small unit cell (2mm) and low fill ratio (0.2).
- Effect of cell dimension and fill ratio on damping ratio was assessed with ANOVA. For AlSi10Mg specimens, cell size has a statistically significant effect on the damping ratio whereas for 316L specimens it has not. Therefore, AlSi10Mg lattices with smaller cell size (i.e. C and D), have better damping properties.
- Specimens exploiting un-melt metal powders as filler of the lattice porosity demonstrated significantly higher damping properties compared to all the other specimens, suggesting that using appropriate filler materials is beneficial when optimal damping performance is desired.
- Dynamic behaviour of the beam-like specimens was described through the development and implementation of a mathematical model based on the Euler-Bernoulli theory. The mathematical model satisfactorily represents beam-like specimens' behaviour and allows to estimate Rayleigh damping  $\beta$  coefficient.

The development of an innovative measurement system allowed to investigate the feasibility of exploiting lattice structures as high-performance filler materials. The system under investigation was a dynamometer for in-process (e.g. milling, drilling, grinding) cutting forces measurement. Design and manufacturing of all system's components, whose

main feature is the SLM-manufactured central platform, were carried out. Main results obtained are listed below:

- Three distinct versions of the central platform were designed, two of which integrating lattice structures to enhance stiffness to weight ratio and damping.
- External geometry of the three central platforms is the same, while the core section changes: the first one is quite similar to commercially available ones while two of them integrate the previously studied type C lattice, with and without unmelt metal powders filler. This choice guarantees platforms interchangeability and favours comparison between the results obtained using the three configurations.
- CAD modelling and FEA simulations were performed to design dynamometer's components, while manufacturing was carried out by means of CAM, SLM 3D printer and VMC.
- Minimization of thermal variation effect on measurements and rigid coupling between parts were pursued during design phase.
- SLM-manufactured central platforms had significant thermal deformations, corrected removing the machining allowance; integrated lattice was reproduced successfully.
- Dynamometer FRF analysis suggests the existence of a measurable damping effect due to the lattice structure, which occurs mainly at high frequency ( $> 5\text{kHz}$ ). Nevertheless, the frequency bandwidth of the dynamometer with lattice infill does not appear to be wider than that of the standard dynamometer; this result suggests that the measurement system's performance is not significantly affected by the lattice infill.
- No studies or commercially available systems investigated similar solutions.

Exploiting the knowledge acquired by means of former experimental campaigns, a further investigation to assess the effect of lattice's size variation on static and dynamic behaviour was carried out; hence, exploiting data and expertise acquired by means of all the experimental campaigns investigating lattice structures properties, a generalised methodology useful to characterize static and dynamic behaviour of different types of lattice porous structures was conceived. A total of 36 316L stainless steel specimens were designed, manufactured and measured. Below, some observations and conclusions:

- Measurements execution and data analysis were facilitated optimizing specimens' geometry and DoE's factors levels by means of FEA results analysis.
- Using a 3D optical profilometer it was assessed that inclined beams cross-section was not circular. Inclined beam's section is elongated along the direction parallel

---

to the build axis. Therefore, modifying the nominal diameter of the beam (CAD) to improve dimensional accuracy is not sufficient.

- Specimens slicing and SLM manufacturing required 13 and 18 days respectively.
- By means of adequate experimental set-ups, compliance and frequency response of 36 specimens made of 316L stainless steel were obtained, allowing to observe the effect lattice's size variation on mechanical properties.
- Specimens compliance estimated from the FRF is lower than that obtained exploiting the load cell. This problem can be connected to the noise that affects FRF's at low frequency and mechanical tolerances of the measurement chain; further investigations are necessary to improve compliance estimation accuracy.
- In general, specimens damping ratio tends to increase with stiffness and cross-sectional area. Furthermore, damping effect is enhanced when lattice's cross-section is more extended along the plane perpendicular to the applied force.
- Effect of cells number variation on damping ratio was assessed with ANOVA. All factors (i.e.  $N_x$ ,  $N_y$ ,  $N_z$ ) as well as the interactions are significant.
- It is confirmed that lattices composed of smaller unit cells can guarantee slightly better damping performance than those made up of larger cells.
- Lattice specimens had higher damping ratios compared to full cross-section equivalents.
- By means of linear regression, mathematical models useful for lattices damping properties estimation as a function of their size have been obtained. These can be used for FE models calibration, development of homogenization methods and advanced mathematical models for the prediction of lattices damping behaviour.
- Static and dynamic characteristics of porous / lattice structures could be assessed by means of the proposed method.

Drawing inspiration from the acquired expertise, an innovative methodology for rapid design and SLM-manufacturing of small-sized lattice / porous structures (Patent pending) was developed. The key features of the method and the results obtained are reported below:

- A specific MATLAB tool that generates a simplified three-dimensional model of the structure to be produced was created.
- Process design, slicing and production operations can be performed using widely available free and commercial tools, enabling rapid implementation even at industrial level.

- The proposed methodology allows substantial time savings in 3D modelling, slicing and production phases. The simulations carried out indicate that this advantage grows rapidly with the number of unit cells that make up the lattice to be produced. Shortening the time required to produce the finished product up to over 40%, a substantial economic benefit can be obtained.
- A DoE, which involved the production and analysis of 205 specimens, was carried out to verify the feasibility of the proposed methodology and the effect of main process parameters on geometrical characteristics and surface roughness of lattices.
- Process parameters combinations corresponding to spot diameters smaller than 200  $\mu\text{m}$  generated beams with larger diameter compared to that of the spot. Energy excess caused melt pool and HAZ size increase.
- The effect of power, scanning speed and spot diameter on vertical and inclined beams diameters was assessed with ANOVA. Power and spot diameter were statistically significant whereas scanning speed was not. Similarly, evaluating the effect of SLM process parameters on surface roughness it was assessed that only spot diameter had a statistically significant effect.
- Mathematical models useful for estimation of lattices geometrical and surface roughness characteristics were obtained. Beams' diameter depends on the product of power and spot diameter; when one of the two parameters increases, the diameter also increases. Nevertheless, for inclined beams and small spot diameter ( $s < 200 \mu\text{m}$ ), beams' diameter depends on the ratio between power and spot diameter. Hence, for small spots energy supplied is quite high, thus evaporation and instability of the melt pool (e.g. keyhole) phenomena are triggered favouring HAZ depth growth; therefore, big diameter inclined beams and lattice's pores closure have to be expected. Surface roughness increases with spot size. This latter phenomenon could be explained observing Gaussian beam intensity profile.
- Process parameters combinations that meet appropriate requirements in terms of dimensional accuracy and surface roughness were identified, allowing the immediate applicability of the proposed methodology for rapid production of FBCCZ type lattice structures with unit cell size equal to 2 mm.

Below, a summary of results obtained is accompanied by suggestions on possible future developments.

Investigations carried out allowed to study the mechanical characteristics of lattice structures made of aluminium and stainless steel, observing their variation as a function of unit cell geometry and lattice's size. Acquired knowledge allowed to identify a generalized methodology exploitable to characterize lattice / porous structures. To improve data acquisition and assess the effect of exciting force's frequency variation on lattices dynamic



behaviour, it is possible to use a shaker in place of the instrumented hammer; in comparison to the pulse test it would be possible to have greater control over the characteristics of the applied force in terms of type, frequency, amplitude and phase. To take full advantage of acquired data it would be possible to develop homogenization methods to describe lattices properties through analytical models or help to make FE simulations simpler and faster. Dynamometer's performances could be further improved reducing central platform's mass, exploiting topology optimization and materials such as titanium alloys. Transversal expertise gained with respect to the SLM process and lattice structures, allowed to develop and validate an innovative methodology for rapid production of lattice structures (Patent Pending); investigated process parameters combinations tend to favour instability conditions when small spots are involved; therefore, to identify process parameters combinations that allow the production of small-diameter beams it is recommended to extend the experimental plan considering powers lower than 150 W. In order to obtain beams diameters greater than 349  $\mu\text{m}$  without triggering sintering phenomena, it is necessary to extend the experimental plan including scanning speeds lower than 50 mm/s.



# LIST OF ABBREVIATIONS

|         |  |
|---------|--|
| ADC     | Analog to Digital Converter                  |
| AM      | Additive Manufacturing                       |
| AMT     | Additive Manufacturing Technologies          |
| ANOVA   | Analysis of Variance                         |
| BCC     | Body Centered Cubic                          |
| BCCZ    | Body Centered Cubic with Z struts            |
| CAD     | Computer Aided Design                        |
| CAE     | Computer Aided Engineering                   |
| CAM     | Computer Aided Manufacturing                 |
| CC      | Cleaning Cycle                               |
| CNC     | Computer Numerical Control                   |
| CT      | Computerized Tomography                      |
| DfAM    | Design for Additive Manufacturing            |
| DFT     | Discrete Fourier Transform                   |
| DoE     | Design of Experiments                        |
| EBM     | Electron Beam Melting                        |
| EDM     | Electrical Discharge Machining               |
| FBCCTXZ | Face and Body Centered Cubic with XYZ struts |
| FBCCTZ  | Face and Body Centered Cubic with Z struts   |
| FCC     | Face Centered Cubic                          |
| FCCZ    | Face Centered Cubic with Z struts            |
| FE      | Finite Element                               |
| FEA     | Finite Element Analysis                      |

---

|      |                                       |
|------|---------------------------------------|
| FFT  | Fast Fourier Transform                |
| FRF  | Frequency Response Function           |
| GB   | Gigabyte                              |
| GUI  | Graphical User Interface              |
| HAZ  | Heat Affected Zone                    |
| HDR  | High Dynamic Range                    |
| HIP  | Hot Isostatic Pressing                |
| HRC  | Hardness Rockwell Cone                |
| IEPE | Integrated Electronics Piezo-Electric |
| LED  | Linear Energy Density                 |
| LM   | Laser Melting                         |
| LMD  | Laser Metal Deposition                |
| LPS  | Liquid Phase Sintering                |
| LS   | Laser Sintering                       |
| LSW  | Laser Spot Welding                    |
| MMC  | Metal Matrix Composites               |
| MPC  | Multipoint Constraint                 |
| NC   | Numerical Control                     |
| PBF  | Powder Bed Fusion                     |
| RM   | Rapid Manufacturing                   |
| RP   | Rapid Prototyping                     |
| SEM  | Scanning Electron Microscope          |
| SES  | Single Exposure Strategy              |
| SLM  | Selective Laser Melting               |
| SLS  | Selective Laser Sintering             |
| SS   | Stainless Steel                       |
| TD   | Thermal Deformation                   |
| TEDS | Transducer Electronic Data Sheets     |
| TO   | Topology Optimization                 |
| UTS  | Ultimate Tensile Strength             |
| VED  | Volumetric Energy Density             |

VMC      Vertical Machining Center



# LIST OF SYMBOLS

|             |                                   |
|-------------|-----------------------------------|
| $c$         | Damping coefficient               |
| $C_d$       | Lattice's unit cell size          |
| $D$         | Strut diameter                    |
| $E$         | Young Modulus                     |
| $EI$        | Linear input energy density       |
| $EL$        | Linear energy density             |
| $ES$        | Surface energy density            |
| $EV$        | Volumetric energy density         |
| $f_{res}$   | Firs resonance frequency          |
| $G$         | Compliance                        |
| $h$         | Hatch spacing                     |
| $J$         | Moment of inertia                 |
| $k$         | Stiffness                         |
| $P$         | Laser power                       |
| $R_a$       | Roughness                         |
| $s$         | Laser spot diameter               |
| $t$         | Layer thickness                   |
| $v$         | Laser scan speed                  |
| $ W_{res} $ | FRF amplitude at first resonance  |
| $\beta$     | Rayleigh damping Beta coefficient |
| $\delta$    | Displacement                      |
| $\lambda_c$ | Cut-off lenght for Ra estimation  |
| $\xi$       | Damping ratio                     |

|        |            |
|--------|------------|
| $\rho$ | Density    |
| $\tau$ | Time delay |



# **APPENDICES**

## 1 3<sup>RD</sup> DOE'S SPECIMENS MAIN STATIC AND DYNAMIC PROPERTIES

| $N_x$ | $N_y$ | $N_z$ | $C_d$<br>[mm] | $f_{res}$<br>[Hz] | $W_{res}$<br>[ $\mu\text{m}/\text{N}$ ] | $G$<br>[ $\mu\text{m}/\text{N}$ ] | $G$ load cell<br>[ $\mu\text{m}/\text{N}$ ] | $\xi$   | $c$<br>[Nm/s] |
|-------|-------|-------|---------------|-------------------|---|-----------------------------------|---|---------|---------------|
| 3     | 3     | 18    | 4             | 673,2             | 382,5                                   | 2,402                             | 3,424                                       | 0,00314 | 0,618         |
| 6     | 6     | 36    | 2             | 689,5             | 404,5                                   | 2,243                             | 2,997                                       | 0,00277 | 0,571         |
| 5     | 5     | 18    | 4             | 957,7             | 19,1                                    | 0,492                             | 0,757                                       | 0,01287 | 8,705         |
| 10    | 10    | 36    | 2             | 1051,2            | 14,4                                    | 0,377                             | 0,648                                       | 0,01309 | 10,530        |
| 7     | 7     | 18    | 4             | 1123,0            | 2,3                                     | 0,230                             | 0,330                                       | 0,04986 | 61,459        |
| 14    | 14    | 36    | 2             | 1225,0            | 4,3                                     | 0,147                             | 0,315                                       | 0,01705 | 30,064        |
| 5     | 3     | 18    | 4             | 994,2             | 51,4                                    | 0,714                             | 1,086                                       | 0,00695 | 3,114         |
| 10    | 6     | 36    | 2             | 1091,5            | 43,6                                    | 0,555                             | 0,891                                       | 0,00637 | 3,344         |
| 3     | 5     | 18    | 4             | 658,5             | 249,3                                   | 1,596                             | 2,268                                       | 0,00320 | 0,970         |
| 6     | 10    | 36    | 2             | 695,2             | 127,2                                   | 1,357                             | 1,916                                       | 0,00533 | 1,800         |
| 7     | 5     | 18    | 4             | 1292,0            | 9,7                                     | 0,192                             | 0,407                                       | 0,00994 | 12,720        |
| 14    | 10    | 36    | 2             | 1265,2            | 9,8                                     | 0,194                             | 0,386                                       | 0,00992 | 12,838        |
| 5     | 7     | 18    | 4             | 950,0             | 8,5                                     | 0,359                             | 0,566                                       | 0,02104 | 19,651        |
| 10    | 14    | 36    | 2             | 999,0             | 8,4                                     | 0,308                             | 0,529                                       | 0,01832 | 18,976        |
| 7     | 3     | 18    | 4             | 1313,7            | 29,1                                    | 0,293                             | 0,550                                       | 0,00503 | 4,158         |
| 14    | 6     | 36    | 2             | 1411,7            | 13,4                                    | 0,240                             | 0,442                                       | 0,00896 | 8,422         |
| 3     | 7     | 18    | 4             | 665,0             | 129,9                                   | 1,137                             | 1,619                                       | 0,00438 | 1,843         |
| 6     | 14    | 36    | 2             | 686,5             | 69,0                                    | 0,978                             | 1,445                                       | 0,00709 | 3,361         |
| 3     | 3     | 15    | 4             | 904,0             | 119,5                                   | 1,470                             | 2,131                                       | 0,00615 | 1,473         |
| 6     | 6     | 30    | 2             | 892,0             | 122,0                                   | 1,483                             | 2,197                                       | 0,00608 | 1,462         |
| 5     | 5     | 15    | 4             | 1272,5            | 28,8                                    | 0,288                             | 0,516                                       | 0,00500 | 4,345         |
| 10    | 10    | 30    | 2             | 1272,0            | 24,2                                    | 0,285                             | 0,489                                       | 0,00587 | 5,166         |
| 7     | 7     | 15    | 4             | 1506,5            | 3,0                                     | 0,118                             | 0,259                                       | 0,01980 | 35,510        |
| 14    | 14    | 30    | 2             | 1617,0            | 1,6                                     | 0,101                             | 0,246                                       | 0,03094 | 60,422        |
| 5     | 3     | 15    | 4             | 1349,0            | 60,8                                    | 0,406                             | 0,692                                       | 0,00334 | 1,940         |
| 10    | 6     | 30    | 2             | 1370,0            | 45,5                                    | 0,381                             | 0,687                                       | 0,00418 | 2,554         |

|    |    |    |   |        |       |       |       |         |        |
|----|----|----|---|--------|-------|-------|-------|---------|--------|
| 3  | 5  | 15 | 4 | 910,5  | 38,8  | 0,907 | 1,403 | 0,01168 | 4,500  |
| 6  | 10 | 30 | 2 | 892,5  | 39,1  | 0,912 | 1,421 | 0,01167 | 4,562  |
| 7  | 5  | 15 | 4 | 1600,0 | 3,9   | 0,137 | 0,317 | 0,01742 | 25,366 |
| 14 | 10 | 30 | 2 | 1655,0 | 2,3   | 0,141 | 0,313 | 0,03138 | 42,738 |
| 5  | 7  | 15 | 4 | 1297,0 | 15,6  | 0,214 | 0,427 | 0,00685 | 7,870  |
| 10 | 14 | 30 | 2 | 1373,0 | 8,3   | 0,174 | 0,366 | 0,01050 | 14,016 |
| 7  | 3  | 15 | 4 | 1675,5 | 9,7   | 0,199 | 0,392 | 0,01024 | 9,758  |
| 14 | 6  | 30 | 2 | 1845,5 | 12,1  | 0,151 | 0,364 | 0,00623 | 7,100  |
| 3  | 7  | 12 | 4 | 881,5  | 25,6  | 0,681 | 1,083 | 0,01329 | 7,043  |
| 6  | 14 | 24 | 2 | 945,0  | 22,0  | 0,614 | 0,965 | 0,01399 | 7,670  |
| 3  | 3  | 12 | 4 | 1202,5 | 214,0 | 0,919 | 1,350 | 0,00215 | 0,618  |
| 6  | 6  | 24 | 2 | 1187,5 | 208,3 | 0,943 | 1,270 | 0,00226 | 0,643  |
| 5  | 5  | 12 | 4 | 1671,5 | 9,7   | 0,186 | 0,359 | 0,00956 | 9,786  |
| 10 | 10 | 24 | 2 | 1706,0 | 11,7  | 0,176 | 0,352 | 0,00749 | 7,954  |
| 7  | 7  | 12 | 4 | 1964,5 | 3,5   | 0,076 | 0,224 | 0,01084 | 23,062 |
| 14 | 14 | 24 | 2 | 1936,5 | 3,2   | 0,075 | 0,224 | 0,01169 | 25,548 |
| 5  | 3  | 12 | 4 | 1793,5 | 39,3  | 0,261 | 0,467 | 0,00332 | 2,258  |
| 10 | 6  | 24 | 2 | 1808,5 | 36,8  | 0,259 | 0,473 | 0,00352 | 2,392  |
| 3  | 5  | 12 | 4 | 1240,0 | 93,3  | 0,549 | 0,832 | 0,00294 | 1,376  |
| 6  | 10 | 24 | 2 | 1211,0 | 81,9  | 0,564 | 0,890 | 0,00344 | 1,605  |
| 7  | 5  | 12 | 4 | 2108,0 | 7,7   | 0,085 | 0,247 | 0,00551 | 9,798  |
| 14 | 10 | 24 | 2 | 2127,0 | 5,9   | 0,080 | 0,241 | 0,00680 | 12,683 |
| 5  | 7  | 12 | 4 | 1775,0 | 7,8   | 0,125 | 0,311 | 0,00800 | 11,489 |
| 10 | 14 | 24 | 2 | 1790,5 | 5,8   | 0,116 | 0,294 | 0,01000 | 15,262 |
| 7  | 3  | 12 | 4 | 2287,5 | 18,1  | 0,121 | 0,284 | 0,00336 | 3,854  |
| 14 | 6  | 24 | 2 | 2337,0 | 15,2  | 0,110 | 0,279 | 0,00361 | 4,488  |
| 3  | 7  | 12 | 4 | 1258,0 | 44,5  | 0,386 | 0,669 | 0,00434 | 2,843  |
| 6  | 14 | 24 | 2 | 1232,5 | 45,1  | 0,404 | 0,660 | 0,00447 | 2,861  |

## 2 SIMPLIFIED 3D MODEL METHODOLOGY: DOE FACTORS AND LEVELS

| Power [W] | Scan Speed [mm/s] | Laser Spot Diameter [ $\mu\text{m}$ ] |
|-----------|-------------------|---------------------------------------|
| 250       | 1000              | 200                                   |
| 250       | 500               | 400                                   |
| 150       | 750               | 150                                   |
| 200       | 1000              | 150                                   |
| 200       | 750               | 200                                   |
| 250       | 750               | 250                                   |
| 200       | 500               | 300                                   |
| 300       | 750               | 300                                   |
| 400       | 1000              | 300                                   |
| 350       | 750               | 350                                   |
| 400       | 750               | 400                                   |
| 150       | 250               | 450                                   |
| 300       | 500               | 450                                   |
| 350       | 1000              | 250                                   |
| 350       | 500               | 500                                   |
| 250       | 500               | 350                                   |
| 150       | 1000              | 100                                   |
| 150       | 500               | 200                                   |
| 300       | 1000              | 200                                   |
| 150       | 250               | 400                                   |
| 300       | 500               | 400                                   |
| 400       | 750               | 350                                   |
| 350       | 750               | 300                                   |
| 350       | 500               | 450                                   |
| 200       | 500               | 250                                   |
| 300       | 750               | 250                                   |
| 400       | 1000              | 250                                   |

|     |      |     |
|-----|------|-----|
| 200 | 250  | 500 |
| 400 | 500  | 500 |
| 250 | 1000 | 150 |
| 250 | 750  | 200 |
| 250 | 500  | 300 |
| 150 | 250  | 350 |
| 300 | 500  | 350 |
| 350 | 1000 | 200 |
| 350 | 500  | 400 |
| 200 | 750  | 150 |
| 400 | 750  | 300 |
| 200 | 250  | 450 |
| 400 | 500  | 450 |
| 350 | 750  | 250 |
| 150 | 750  | 100 |
| 200 | 1000 | 100 |
| 150 | 500  | 150 |
| 300 | 1000 | 150 |
| 200 | 500  | 200 |
| 300 | 750  | 200 |
| 400 | 1000 | 200 |
| 250 | 500  | 250 |
| 150 | 250  | 300 |
| 300 | 500  | 300 |
| 350 | 500  | 350 |
| 200 | 250  | 400 |
| 400 | 500  | 400 |
| 250 | 250  | 500 |
| 400 | 750  | 250 |
| 250 | 750  | 150 |

|     |      |     |
|-----|------|-----|
| 250 | 250  | 450 |
| 200 | 250  | 350 |
| 400 | 500  | 350 |
| 350 | 1000 | 150 |
| 350 | 750  | 200 |
| 350 | 500  | 300 |
| 150 | 250  | 250 |
| 300 | 500  | 250 |
| 300 | 250  | 500 |
| 250 | 1000 | 100 |
| 250 | 500  | 200 |
| 250 | 250  | 400 |
| 200 | 750  | 100 |
| 200 | 500  | 150 |
| 300 | 750  | 150 |
| 400 | 1000 | 150 |
| 400 | 750  | 200 |
| 200 | 250  | 300 |
| 400 | 500  | 300 |
| 300 | 250  | 450 |
| 350 | 500  | 250 |
| 350 | 250  | 500 |
| 250 | 250  | 350 |
| 150 | 1000 | 50  |
| 150 | 500  | 100 |
| 300 | 1000 | 100 |
| 150 | 250  | 200 |
| 300 | 500  | 200 |
| 300 | 250  | 400 |
| 150 | 100  | 500 |

|     |      |     |
|-----|------|-----|
| 350 | 750  | 150 |
| 350 | 250  | 450 |
| 200 | 250  | 250 |
| 400 | 500  | 250 |
| 400 | 250  | 500 |
| 250 | 750  | 100 |
| 250 | 500  | 150 |
| 250 | 250  | 300 |
| 150 | 100  | 450 |
| 300 | 250  | 350 |
| 350 | 1000 | 100 |
| 350 | 500  | 200 |
| 350 | 250  | 400 |
| 400 | 750  | 150 |
| 400 | 250  | 450 |
| 150 | 100  | 400 |
| 150 | 750  | 50  |
| 200 | 1000 | 50  |
| 200 | 500  | 100 |
| 300 | 750  | 100 |
| 400 | 1000 | 100 |
| 150 | 250  | 150 |
| 300 | 500  | 150 |
| 200 | 250  | 200 |
| 400 | 500  | 200 |
| 250 | 250  | 250 |
| 300 | 250  | 300 |
| 350 | 250  | 350 |
| 400 | 250  | 400 |
| 200 | 100  | 500 |

|     |      |     |
|-----|------|-----|
| 150 | 100  | 350 |
| 200 | 100  | 450 |
| 400 | 250  | 350 |
| 350 | 750  | 100 |
| 350 | 500  | 150 |
| 350 | 250  | 300 |
| 300 | 250  | 250 |
| 250 | 1000 | 50  |
| 250 | 500  | 100 |
| 250 | 250  | 200 |
| 150 | 100  | 300 |
| 200 | 100  | 400 |
| 250 | 100  | 500 |
| 200 | 750  | 50  |
| 400 | 750  | 100 |
| 200 | 250  | 150 |
| 400 | 500  | 150 |
| 400 | 250  | 300 |
| 250 | 100  | 450 |
| 350 | 250  | 250 |
| 200 | 100  | 350 |
| 150 | 500  | 50  |
| 300 | 1000 | 50  |
| 150 | 250  | 100 |
| 300 | 500  | 100 |
| 300 | 250  | 200 |
| 150 | 100  | 250 |
| 150 | 50   | 500 |
| 300 | 100  | 500 |
| 250 | 100  | 400 |



|     |      |     |
|-----|------|-----|
| 400 | 250  | 250 |
| 250 | 750  | 50  |
| 250 | 250  | 150 |
| 200 | 100  | 300 |
| 150 | 50   | 450 |
| 300 | 100  | 450 |
| 350 | 1000 | 50  |
| 350 | 500  | 100 |
| 350 | 250  | 200 |
| 350 | 100  | 500 |
| 250 | 100  | 350 |
| 150 | 100  | 200 |
| 150 | 50   | 400 |
| 300 | 100  | 400 |
| 350 | 100  | 450 |
| 200 | 500  | 50  |
| 300 | 750  | 50  |
| 400 | 1000 | 50  |
| 200 | 250  | 100 |
| 400 | 500  | 100 |
| 300 | 250  | 150 |
| 400 | 250  | 200 |
| 200 | 100  | 250 |
| 200 | 50   | 500 |
| 400 | 100  | 500 |
| 250 | 100  | 300 |
| 150 | 50   | 350 |
| 300 | 100  | 350 |
| 350 | 100  | 400 |
| 200 | 50   | 450 |

|     |     |     |
|-----|-----|-----|
| 400 | 100 | 450 |
| 350 | 750 | 50  |
| 350 | 250 | 150 |
| 250 | 500 | 50  |
| 250 | 250 | 100 |
| 150 | 100 | 150 |
| 200 | 100 | 200 |
| 250 | 100 | 250 |
| 150 | 50  | 300 |
| 300 | 100 | 300 |
| 350 | 100 | 350 |
| 200 | 50  | 400 |
| 400 | 100 | 400 |
| 250 | 50  | 500 |
| 400 | 750 | 50  |
| 400 | 250 | 150 |
| 250 | 50  | 450 |
| 200 | 50  | 350 |
| 400 | 100 | 350 |
| 350 | 100 | 300 |
| 150 | 250 | 50  |
| 300 | 500 | 50  |
| 300 | 250 | 100 |
| 150 | 50  | 250 |
| 300 | 100 | 250 |
| 300 | 50  | 500 |
| 250 | 100 | 200 |
| 250 | 50  | 400 |

### 3 OPTIMIZED SLM PROCESS PARAMETERS

| ID Number | Power<br>[W] | Scan Speed<br>[mm/s] | Spot size<br>[ $\mu\text{m}$ ] | Beam diameter<br>[ $\mu\text{m}$ ] | R <sub>a</sub><br>[ $\mu\text{m}$ ] |
|-----------|--------------|----------------------|--------------------------------|------------------------------------|-------------------------------------|
| 1         | 250          | 1000                 | 200                            | 281                                | 13                                  |
| 2         | 300          | 750                  | 300                            | 347                                | 17                                  |
| 3         | 350          | 1000                 | 250                            | 306                                | 18                                  |
| 4         | 150          | 500                  | 200                            | 235                                | 12                                  |
| 5         | 300          | 1000                 | 200                            | 268                                | 13                                  |
| 6         | 250          | 1000                 | 150                            | 277                                | 11                                  |
| 7         | 350          | 1000                 | 200                            | 284                                | 13                                  |
| 8         | 350          | 750                  | 250                            | 296                                | 19                                  |
| 9         | 150          | 500                  | 150                            | 188                                | 11                                  |
| 10        | 200          | 500                  | 200                            | 265                                | 15                                  |
| 11        | 400          | 1000                 | 200                            | 304                                | 14                                  |
| 12        | 150          | 250                  | 300                            | 294                                | 17                                  |
| 13        | 150          | 250                  | 250                            | 270                                | 19                                  |
| 14        | 300          | 500                  | 250                            | 283                                | 18                                  |
| 15        | 250          | 500                  | 200                            | 239                                | 11                                  |
| 16        | 200          | 500                  | 150                            | 241                                | 11                                  |
| 17        | 400          | 750                  | 200                            | 288                                | 13                                  |
| 18        | 150          | 250                  | 200                            | 226                                | 13                                  |
| 19        | 300          | 500                  | 200                            | 245                                | 13                                  |
| 20        | 200          | 250                  | 250                            | 270                                | 16                                  |
| 21        | 400          | 500                  | 250                            | 308                                | 18                                  |
| 22        | 250          | 250                  | 300                            | 326                                | 16                                  |
| 23        | 350          | 500                  | 200                            | 275                                | 12                                  |
| 24        | 200          | 250                  | 200                            | 229                                | 10                                  |
| 25        | 400          | 500                  | 200                            | 289                                | 16                                  |
| 26        | 250          | 250                  | 250                            | 274                                | 18                                  |
| 27        | 300          | 250                  | 250                            | 286                                | 16                                  |

---

|    |     |     |     |     |    |
|----|-----|-----|-----|-----|----|
| 28 | 250 | 250 | 200 | 254 | 11 |
| 29 | 150 | 100 | 300 | 275 | 18 |
| 30 | 200 | 250 | 150 | 245 | 11 |
| 31 | 300 | 250 | 200 | 251 | 14 |
| 32 | 150 | 100 | 250 | 259 | 16 |
| 33 | 200 | 100 | 300 | 310 | 18 |
| 34 | 350 | 250 | 200 | 266 | 14 |
| 35 | 150 | 100 | 200 | 247 | 12 |
| 36 | 400 | 250 | 200 | 269 | 14 |
| 37 | 200 | 100 | 250 | 283 | 13 |
| 38 | 150 | 100 | 150 | 198 | 10 |
| 39 | 200 | 100 | 200 | 260 | 15 |
| 40 | 250 | 100 | 250 | 349 | 19 |
| 41 | 300 | 100 | 300 | 343 | 20 |
| 42 | 150 | 50  | 250 | 300 | 16 |
| 43 | 300 | 100 | 250 | 316 | 18 |
| 44 | 250 | 100 | 200 | 274 | 14 |

## REFERENCES

- [1] R. Liu, Z. Wang, T. Sparks, F. Liou, and J. Newkirk, "Aerospace applications of laser additive manufacturing", in *Laser Additive Manufacturing: Materials, Design, Technologies, and Applications*, Woodhead Publishing, 2016, ch. 13, pp. 351–371.
- [2] M. Munsch, "Laser additive manufacturing of customized prosthetics and implants for biomedical applications", in *Laser Additive Manufacturing: Materials, Design, Technologies, and Applications*, Woodhead Publishing, 2016, ch. 15, pp. 399–420.
- [3] T. M. Mower and M. J. Long, "Mechanical behavior of additive manufactured, powder-bed laser-fused materials", *Materials Science and Engineering A*, vol. 651, pp. 198–213, 2016.
- [4] T. DebRoy, H. Wei, J. Zuback, T. Mukherjee, J. Elmer, J. Milewski, A. Beese, A. Wilson-Heid, A. De, and W. Zhang, "Additive manufacturing of metallic components – Process, structure and properties", *Progress in Materials Science*, vol. 92, pp. 112–224, 2018.
- [5] J. Zhang, B. Song, Q. Wei, D. Bourell, and Y. Shi, "A review of selective laser melting of aluminum alloys: Processing, microstructure, property and developing trends", *Journal of Materials Science & Technology*, vol. 35, no. 2, pp. 270–284, 2019.
- [6] A. Adeyemi, E. T. Akinlabi, and R. M. Mahamood, "Powder Bed Based Laser Additive Manufacturing Process of Stainless Steel: A Review", *Materials Today: Proceedings*, vol. 5, no. 9, pp. 18510–18517, 2018.
- [7] S. Zhang, S. Rauniar, S. Shrestha, A. Ward, and K. Chou, "An experimental study of tensile property variability in selective laser melting", *Journal of Manufacturing Processes*, 2019.
- [8] H. Shipley, D. McDonnell, M. Culleton, R. Coull, R. Lupoi, G. O'Donnell, and D. Trimble, "Optimisation of process parameters to address fundamental challenges during selective laser melting of Ti-6Al-4V: A review", *International Journal of Machine Tools and Manufacture*, vol. 128, pp. 1–20, 2018.
- [9] A. M. Aboutaleb, M. J. Mahtabi, M. A. Tschopp, and L. Bian, "Multi-objective accelerated process optimization of mechanical properties in laser-based additive manufacturing: Case study on Selective Laser Melting (SLM) Ti-6Al-4V", *Journal of Manufacturing Processes*, vol. 38, pp. 432–444, 2019.

- [10] S. Afkhami, M. Dabiri, S. H. Alavi, T. Björk, and A. Salminen, "Fatigue characteristics of steels manufactured by selective laser melting", *International Journal of Fatigue*, vol. 122, pp. 72–83, 2019.
- [11] D. Gu, *Laser additive manufacturing of high-performance materials*. Berlin, Heidelberg: Springer Berlin Heidelberg, 2015, pp. 1–311.
- [12] O. Diegel, A. Nordin, and D. Motte, *A Practical Guide to Design for Additive Manufacturing*, ser. Springer Series in Advanced Manufacturing. Singapore: Springer Singapore, 2019.
- [13] S. A. Tofail, E. P. Koumoulos, A. Bandyopadhyay, S. Bose, L. O'Donoghue, and C. Charitidis, *Additive manufacturing: scientific and technological challenges, market uptake and opportunities*, 2018.
- [14] R. Hölker-Jäger and A. Tekkaya, "Additive manufacture of tools and dies for metal forming", *Laser Additive Manufacturing*, pp. 439–464, 2017.
- [15] D. Böckin and A. M. Tillman, "Environmental assessment of additive manufacturing in the automotive industry", *Journal of Cleaner Production*, 2019.
- [16] L. Yuan, S. Ding, and C. Wen, *Additive manufacturing technology for porous metal implant applications and triple minimal surface structures: A review*, 2019.
- [17] N. Ahmed, *Direct metal fabrication in rapid prototyping: A review*, 2019.
- [18] C. Yan, Y. Shi, and L. Hao, "Investigation into the differences in the selective laser sintering between amorphous and semi-crystalline polymers", *International Polymer Processing*, vol. 26, no. 4, pp. 416–423, 2011.
- [19] J. P. Kruth, G. Levy, F. Klocke, and T. H. Childs, "Consolidation phenomena in laser and powder-bed based layered manufacturing", *CIRP Annals - Manufacturing Technology*, vol. 56, no. 2, pp. 730–759, 2007.
- [20] H. H. Zhu, L. Lu, and J. Y. H. Fuh, "Development and characterisation of direct laser sintering Cu-based metal powder", in *Journal of Materials Processing Technology*, vol. 140, Elsevier, 2003, pp. 314–317.
- [21] H. J. Niu and I. T. Chang, "Liquid phase sintering of M3/2 high speed steel by selective laser sintering", *Scripta Materialia*, vol. 39, no. 1, pp. 67–72, 1998.
- [22] J. Mazumder, "Laser-aided direct metal deposition of metals and alloys", in *Laser Additive Manufacturing: Materials, Design, Technologies, and Applications*, Woodhead Publishing, 2016, pp. 21–53.
- [23] C. Kledwig, H. Perfahl, M. Reisacher, F. Brückner, J. Bliedtner, and C. Leyens, "Analysis of melt pool characteristics and process parameters using a coaxial monitoring system during directed energy deposition in additive manufacturing", *Materials*, vol. 12, no. 2, p. 308, 2019.
- [24] S. K. Everton, M. Hirsch, P. I. Stavroulakis, R. K. Leach, and A. T. Clare, *Review of in-situ process monitoring and in-situ metrology for metal additive manufacturing*, 2016.

- [25] F. Wirth, S. Arpagaus, and K. Wegener, "Analysis of melt pool dynamics in laser cladding and direct metal deposition by automated high-speed camera image evaluation", *Additive Manufacturing*, vol. 21, pp. 369–382, 2018.
- [26] Y. Huang, M. B. Khamesee, and E. Toyserkani, "A new physics-based model for laser directed energy deposition (powder-fed additive manufacturing): From single-track to multi-track and multi-layer", *Optics and Laser Technology*, vol. 109, pp. 584–599, 2019.
- [27] N. A. Kistler, D. J. Corbin, A. R. Nassar, E. W. Reutzel, and A. M. Beese, "Effect of processing conditions on the microstructure, porosity, and mechanical properties of Ti-6Al-4V repair fabricated by directed energy deposition", *Journal of Materials Processing Technology*, vol. 264, pp. 172–181, 2019.
- [28] W. Xiao, S. Li, C. Wang, Y. Shi, J. Mazumder, H. Xing, and L. Song, "Multi-scale simulation of dendrite growth for direct energy deposition of nickel-based superalloys", *Materials and Design*, vol. 164, 2019.
- [29] W. Wang, A. J. Pinkerton, L. M. Wee, and L. Li, "Component repair using Laser Direct Metal Deposition", in *Proceedings of the 35th International MATADOR 2007 Conference*, vol. 222, SAGE PublicationsSage UK: London, England, 2007, pp. 345–350.
- [30] T. Petrat, B. Graf, A. Gumenyuk, and M. Rethmeier, "Laser metal deposition as repair technology for a gas turbine burner made of inconel 718", in *Physics Procedia*, vol. 83, Elsevier, 2016, pp. 761–768.
- [31] S. Sun, M. Brandt, and M. Easton, "Powder bed fusion processes: An overview", in *Laser Additive Manufacturing: Materials, Design, Technologies, and Applications*, Woodhead Publishing, 2016, pp. 55–77.
- [32] A. T. Sidambe, *Biocompatibility of advanced manufactured titanium implants-A review*, 2014.
- [33] J. Kruth, B. Vandenbroucke, J. Vaerenbergh, and P. Mercelis, "Benchmarking of different SLS/SLM processes as rapid manufacturing techniques", in *Int. Conf. Polymers & Moulds Innovations (PMI), Gent, Belgium, April 20-23, 2005*, 2005, pp. 1–7.
- [34] B. Vandenbroucke and J. P. Kruth, "Selective laser melting of biocompatible metals for rapid manufacturing of medical parts", in *17th Solid Freeform Fabrication Symposium, SFF 2006*, vol. 13, Emerald Group Publishing Limited, 2006, pp. 148–159.
- [35] S. D. Jadhav, S. Dadbakhsh, L. Goossens, J. P. Kruth, J. Van Humbeeck, and K. Vanmeensel, "Influence of selective laser melting process parameters on texture evolution in pure copper", *Journal of Materials Processing Technology*, vol. 270, pp. 47–58, 2019.
- [36] H. Lee, C. H. J. Lim, M. J. Low, N. Tham, V. M. Murukeshan, and Y. J. Kim, *Lasers in additive manufacturing: A review*, 2017.

- [37] D. Koutny, D. Palousek, L. Pantelejev, C. Hoeller, R. Pichler, L. Tesicky, and J. Kaiser, "Influence of scanning strategies on processing of aluminum alloy EN AW 2618 using selective laser melting", *Materials*, vol. 11, no. 2, 2018.
- [38] C. Y. Yap, C. K. Chua, Z. L. Dong, Z. H. Liu, D. Q. Zhang, L. E. Loh, and S. L. Sing, *Review of selective laser melting: Materials and applications*, 2015.
- [39] K. G. Prashanth, S. Scudino, T. Maity, J. Das, and J. Eckert, "Is the energy density a reliable parameter for materials synthesis by selective laser melting?", *Materials Research Letters*, vol. 5, no. 6, pp. 386–390, 2017.
- [40] X. Zhou, X. Liu, D. Zhang, Z. Shen, and W. Liu, "Balling phenomena in selective laser melted tungsten", *Journal of Materials Processing Technology*, vol. 222, pp. 33–42, 2015.
- [41] J. P. Kruth, L. Froyen, J. Van Vaerenbergh, P. Mercelis, M. Rombouts, and B. Lauwers, "Selective laser melting of iron-based powder", in *Journal of Materials Processing Technology*, vol. 149, 2004, pp. 616–622.
- [42] Z. Chen, Y. Xiang, Z. Wei, P. Wei, B. Lu, L. Zhang, and J. Du, "Thermal dynamic behavior during selective laser melting of K418 superalloy: numerical simulation and experimental verification", *Applied Physics A: Materials Science and Processing*, vol. 124, no. 4, p. 313, 2018.
- [43] C. Li, Y. B. Guo, and J. B. Zhao, "Interfacial phenomena and characteristics between the deposited material and substrate in selective laser melting Inconel 625", *Journal of Materials Processing Technology*, vol. 243, pp. 269–281, 2017.
- [44] W. E. King, H. D. Barth, V. M. Castillo, G. F. Gallegos, J. W. Gibbs, D. E. Hahn, C. Kamath, and A. M. Rubenchik, "Observation of keyhole-mode laser melting in laser powder-bed fusion additive manufacturing", *Journal of Materials Processing Technology*, vol. 214, no. 12, pp. 2915–2925, 2014.
- [45] T. Simson, A. Emmel, A. Dwars, and J. Böhm, "Residual stress measurements on AISI 316L samples manufactured by selective laser melting", *Additive Manufacturing*, vol. 17, pp. 183–189, 2017.
- [46] K. G. Prashanth and J. Eckert, "Formation of metastable cellular microstructures in selective laser melted alloys", *Journal of Alloys and Compounds*, vol. 707, pp. 27–34, 2017.
- [47] A. Bača, R. Konečná, G. Nicoletto, and L. Kunz, "Influence of Build Direction on the Fatigue Behaviour of Ti6Al4V Alloy Produced by Direct Metal Laser Sintering", in *Materials Today: Proceedings*, vol. 3, Elsevier, 2016, pp. 921–924.
- [48] R. Casati, J. Lemke, and M. Vedani, "Microstructure and Fracture Behavior of 316L Austenitic Stainless Steel Produced by Selective Laser Melting", *Journal of Materials Science and Technology*, vol. 32, no. 8, pp. 738–744, 2016.
- [49] A. Riemer, S. Leuders, M. Thöne, H. A. Richard, T. Tröster, and T. Niendorf, "On the fatigue crack growth behavior in 316L stainless steel manufactured by selective laser melting", *Engineering Fracture Mechanics*, vol. 120, pp. 15–25, 2014.



- [50] P. Edwards and M. Ramulu, "Effect of build direction on the fracture toughness and fatigue crack growth in selective laser melted Ti-6Al-4 V", *Fatigue and Fracture of Engineering Materials and Structures*, vol. 38, no. 10, pp. 1228–1236, 2015.
- [51] O. Kerbrat, P. Mognol, and J. Y. Hascoët, "A new DFM approach to combine machining and additive manufacturing", *Computers in Industry*, vol. 62, no. 7, pp. 684–692, 2011.
- [52] International Organization for Standardization, *ISO/ASTM 52910:2018 - Additive manufacturing – Design – Requirements, guidelines and recommendations*, 2018.
- [53] B. Zhang, A. Goel, O. Ghalsasi, and S. Anand, "CAD-based design and pre-processing tools for additive manufacturing", *Journal of Manufacturing Systems*, 2019.
- [54] T. Wu, S. A. Jahan, Y. Zhang, J. Zhang, H. Elmounayri, and A. Tovar, "Design Optimization of Plastic Injection Tooling for Additive Manufacturing", *Procedia Manufacturing*, vol. 10, pp. 923–934, 2017.
- [55] H. S. Park and X. P. Dang, "Development of a Smart Plastic Injection Mold with Conformal Cooling Channels", *Procedia Manufacturing*, vol. 10, pp. 48–59, 2017.
- [56] K. Altaf, A. Majdi Abdul Rani, and V. R. Raghavan, "Prototype production and experimental analysis for circular and profiled conformal cooling channels in aluminium filled epoxy injection mould tools", *Rapid Prototyping Journal*, vol. 19, no. 4, pp. 220–229, 2013.
- [57] T. Evens, W. Six, J. De Keyzer, F. Desplentere, and A. Van Bael, "Experimental analysis of conformal cooling in SLM produced injection moulds: Effects on process and product quality", in *AIP Conference Proceedings*, vol. 2055, AIP Publishing LLC, 2019.
- [58] A. Armillotta, R. Baraggi, and S. Fasoli, "SLM tooling for die casting with conformal cooling channels", *International Journal of Advanced Manufacturing Technology*, vol. 71, no. 1-4, pp. 573–583, 2014.
- [59] A. Tel, F. Costa, S. Sembronio, A. Lazzarotto, and M. Robiony, "All-in-one surgical guide: A new method for cranial vault resection and reconstruction", *Journal of Cranio-Maxillofacial Surgery*, vol. 46, no. 6, pp. 967–973, 2018.
- [60] N. Kourra, J. M. Warnett, A. Attridge, G. Dibling, J. McLoughlin, S. Muirhead-Allwood, R. King, and M. A. Williams, "Computed tomography metrological examination of additive manufactured acetabular hip prosthesis cups", *Additive Manufacturing*, vol. 22, pp. 146–152, 2018.
- [61] J. Parthasarathy, B. Starly, and S. Raman, *A design for the additive manufacture of functionally graded porous structures with tailored mechanical properties for biomedical applications*, 2011.
- [62] A. Panesar, M. Abdi, D. Hickman, and I. Ashcroft, "Strategies for functionally graded lattice structures derived using topology optimisation for Additive Manufacturing", *Additive Manufacturing*, vol. 19, pp. 81–94, 2018.

- [63] W. P. Syam, W. Jianwei, B. Zhao, I. Maskery, W. Elmadih, and R. Leach, "Design and analysis of strut-based lattice structures for vibration isolation", *Precision Engineering*, vol. 52, pp. 494–506, 2018.
- [64] F. Rosa, S. Manzoni, and R. Casati, "Damping behavior of 316L lattice structures produced by Selective Laser Melting", *Materials and Design*, vol. 160, pp. 1010–1018, 2018.
- [65] L. Jyothish Kumar and C. G. Krishnadas Nair, "Current trends of additive manufacturing in the aerospace industry", in *Advances in 3D Printing and Additive Manufacturing Technologies*, Singapore: Springer Singapore, 2016, pp. 39–54.
- [66] A. Boschetto and L. Bottini, "Manufacturability of non-assembly joints fabricated in AlSi10Mg by selective laser melting", *Journal of Manufacturing Processes*, vol. 37, pp. 425–437, 2019.
- [67] E. Pei, M. Ressin, R. I. Campbell, B. Eynard, and J. Xiao, "Investigating the impact of additive manufacturing data exchange standards for re-distributed manufacturing", *Progress in Additive Manufacturing*, vol. 4, no. 3, pp. 331–344, 2019.
- [68] A. Boschetto, L. Bottini, and F. Veniali, "Roughness modeling of AlSi10Mg parts fabricated by selective laser melting", *Journal of Materials Processing Technology*, vol. 241, pp. 154–163, 2017.
- [69] E. Utley, *An Introduction to Designing for Metal 3D Printing*, <https://blogs.solidworks.com/solidworksblog/2017/06/introduction-designing-metal-3d-printing.html>, [Online; accessed 2019-06-28], 2017.
- [70] J. P. Kruth, M. Badrossamay, E. Yasa, J. Deckers, L. Thijs, and J. Van Humbeeck, "Part and material properties in selective laser melting of metals", in *16th International Symposium on Electromachining, ISEM 2010*, 2010, pp. 3–14.
- [71] F. Calignano, "Design optimization of supports for overhanging structures in aluminum and titanium alloys by selective laser melting", *Materials and Design*, vol. 64, pp. 203–213, 2014.
- [72] M. K. Thompson, G. Moroni, T. Vaneker, G. Fadel, R. I. Campbell, I. Gibson, A. Bernard, J. Schulz, P. Graf, B. Ahuja, and F. Martina, "Design for Additive Manufacturing: Trends, opportunities, considerations, and constraints", *CIRP Annals - Manufacturing Technology*, vol. 65, no. 2, pp. 737–760, 2016.
- [73] M. Scheffler and P. Colombo, *Cellular ceramics : structure, manufacturing, properties and applications*. Wiley-VCH, 2005, pp. 4–17.
- [74] M. Ashby, *Materials selection in mechanical design: Fourth edition*. Butterworth-Heinemann, 2010, pp. 328–336.
- [75] V. S. Deshpande, N. A. Fleck, and M. F. Ashby, "Effective properties of the octet-truss lattice material", *Journal of the Mechanics and Physics of Solids*, vol. 49, no. 8, pp. 1747–1769, 2001.

- [76] M. Mazur, M. Leary, M. McMillan, S. Sun, D. Shidid, and M. Brandt, “Mechanical properties of Ti6Al4V and AlSi12Mg lattice structures manufactured by Selective Laser Melting (SLM)”, in *Laser Additive Manufacturing: Materials, Design, Technologies, and Applications*, Woodhead Publishing, 2016, pp. 119–161.
- [77] M. Leary, M. Mazur, H. Williams, E. Yang, A. Alghamdi, B. Lozanovski, X. Zhang, D. Shidid, L. Farahbod-Sternahl, G. Witt, I. Kelbassa, P. Choong, M. Qian, and M. Brandt, “Inconel 625 lattice structures manufactured by selective laser melting (SLM): Mechanical properties, deformation and failure modes”, *Materials and Design*, vol. 157, pp. 179–199, 2018.
- [78] M. Leary, M. Mazur, J. Elambasseril, M. McMillan, T. Chirent, Y. Sun, M. Qian, M. Easton, and M. Brandt, “Selective laser melting (SLM) of AlSi12Mg lattice structures”, *Materials and Design*, vol. 98, pp. 344–357, 2016.
- [79] H. Lei, C. Li, J. Meng, H. Zhou, Y. Liu, X. Zhang, P. Wang, and D. Fang, “Evaluation of compressive properties of SLM-fabricated multi-layer lattice structures by experimental test and  $\mu$ -CT-based finite element analysis”, *Materials and Design*, vol. 169, 2019.
- [80] S. L. Campanelli, N. Contuzzi, A. D. Ludovico, F. Caiazzo, F. Cardaropoli, and V. Sergi, “Manufacturing and characterization of Ti6Al4V lattice components manufactured by selective laser melting”, *Materials*, vol. 7, no. 6, pp. 4803–4822, 2014.
- [81] S. Gangireddy, M. Komarasamy, E. J. Faierson, and R. S. Mishra, “High strain rate mechanical behavior of Ti-6Al-4V octet lattice structures additively manufactured by selective laser melting (SLM)”, *Materials Science and Engineering A*, vol. 745, pp. 231–239, 2019.
- [82] N. Jin, F. Wang, Y. Wang, B. Zhang, H. Cheng, and H. Zhang, “Failure and energy absorption characteristics of four lattice structures under dynamic loading”, *Materials and Design*, vol. 169, 2019.
- [83] Z. Xiao, Y. Yang, R. Xiao, Y. Bai, C. Song, and D. Wang, “Evaluation of topology-optimized lattice structures manufactured via selective laser melting”, *Materials and Design*, vol. 143, pp. 27–37, 2018.
- [84] P. Köhnen, C. Haase, J. Bültmann, S. Ziegler, J. H. Schleifenbaum, and W. Bleck, “Mechanical properties and deformation behavior of additively manufactured lattice structures of stainless steel”, *Materials and Design*, vol. 145, pp. 205–217, 2018.
- [85] O. Rehme and C. Emmelmann, “Rapid manufacturing of lattice structures with selective laser melting”, in *Laser-based Micropackaging*, F. G. Bachmann, W. Hoving, Y. Lu, and K. Washio, Eds., vol. 6107, International Society for Optics and Photonics, 2006.
- [86] S. Limmahakhun, A. Oloyede, K. Sitthiseripratip, Y. Xiao, and C. Yan, “Stiffness and strength tailoring of cobalt chromium graded cellular structures for stress-shielding reduction”, *Materials and Design*, vol. 114, pp. 633–641, 2017.

- [87] R. Ramadani, M. Kegl, J. Predan, A. Belšak, and S. Pehan, "Influence of Cellular Lattice Body Structure on Gear Vibration Induced by Meshing", *Strojniški vestnik - Journal of Mechanical Engineering*, 2018.
- [88] J. W. Cooley, P. A. W. Lewis, and P. D. Welch, "The Fast Fourier Transform and its Applications", *IEEE Transactions on Education*, vol. 12, no. 1, pp. 27–34, 1969.
- [89] D. J. Ewins, *Modal Testing: Theory, Practice and Application*. Research Studies Press, 2001.
- [90] W. Heylen, S. Lammens, and P. Sas, *Modal Analysis Theory and Testing*. 1997.
- [91] J. He and Z.-F. Fu, *Modal analysis*. Butterworth-Heinemann, 2001.
- [92] Concept Laser GmbH, *CL 30AL / CL 31AL Aluminium alloys*, [https://www.ge.com/additive/sites/default/files/2018-12/CLMAT\\_30\\_31AL\\_DS\\_EN\\_US\\_2\\_v1.pdf](https://www.ge.com/additive/sites/default/files/2018-12/CLMAT_30_31AL_DS_EN_US_2_v1.pdf), [Online; accessed 2019-02-12].
- [93] J. S. Bendat and A. G. Piersol, *Random data: analysis and measurement procedures*. John Wiley & Sons, 2011, vol. 729.
- [94] S. Belfio, "Intelligent manufacturing systems", Doctoral dissertation, (Doctoral dissertation), University of Udine, 2014.
- [95] Concept Laser GmbH, *CL 20ES Stainless steel*, [https://www.ge.com/additive/sites/default/files/2018-12/CLMAT\\_20ES\\_DS\\_EN\\_US\\_2\\_v1.pdf](https://www.ge.com/additive/sites/default/files/2018-12/CLMAT_20ES_DS_EN_US_2_v1.pdf), [Online; accessed 2019-02-12].
- [96] L. Ljung, *System Identification: Theory for the User, 2nd edition*. Prentice-Hall PTR, 1999.
- [97] G. Totis, G. Wirtz, M. Sortino, D. Veselovac, E. Kuljanic, and F. Klocke, "Development of a dynamometer for measuring individual cutting edge forces in face milling", *Mechanical Systems and Signal Processing*, vol. 24, no. 6, pp. 1844–1857, 2010.
- [98] S. Tsopanos, R. A. Mines, S. McKown, Y. Shen, W. J. Cantwell, W. Brooks, and C. J. Sutcliffe, "The influence of processing parameters on the mechanical properties of selectively laser melted stainless steel microlattice structures", *Journal of Manufacturing Science and Engineering, Transactions of the ASME*, vol. 132, no. 4, 2010.
- [99] S. Ghouse, S. Babu, R. J. Van Arkel, K. Nai, P. A. Hooper, and J. R. Jeffers, "The influence of laser parameters and scanning strategies on the mechanical properties of a stochastic porous material", *Materials and Design*, vol. 131, pp. 498–508, 2017.
- [100] E. Onal, A. E. Medvedev, M. A. Leeflang, A. Molotnikov, and A. A. Zadpoor, "Novel microstructural features of selective laser melted lattice struts fabricated with single point exposure scanning", *Additive Manufacturing*, vol. 29, 2019.
- [101] G. Pyka, G. Kerckhofs, I. Papantoniou, M. Speirs, J. Schrooten, and M. Wevers, "Surface roughness and morphology customization of additive manufactured open porous Ti6Al4V structures", *Materials*, vol. 6, no. 10, pp. 4737–4757, 2013.
- [102] A. Triantaphyllou, C. L. Giusca, G. D. Macaulay, F. Roerig, M. Hoebel, R. K. Leach, B. Tomita, and K. A. Milne, "Surface texture measurement for additive manufacturing", *Surface Topography: Metrology and Properties*, vol. 3, no. 2, 2015.